2023-09-12

Navigation Sensor Stochastic Error Modeling and Nonlinear Estimation for Low-Cost Land Vehicle Navigation

Minaretzis, Chrysostomos

UNIVERSITY OF CALGARY

Navigation Sensor Stochastic Error Modeling and Nonlinear Estimation for Low-Cost

Land Vehicle Navigation

by

Chrysostomos Minaretzis

A THESIS

SUBMITTED TO THE FACULTY OF GRADUATE STUDIES

IN PARTIAL FULFILMENT OF THE REQUIREMENTS FOR THE

DEGREE OF DOCTOR OF PHILOSOPHY

GRADUATE PROGRAM IN GEOMATICS ENGINEERING

CALGARY, ALBERTA

SEPTEMBER, 2023

Abstract

The increasing use of low-cost inertial sensors in various mass-market applications necessitates their accurate stochastic modeling. Such task faces challenges due to outliers in the sensor measurements caused by internal and/or external factors. To optimize the navigation performance, robust estimation techniques are required to reduce the influence of outliers to the stochastic modeling process. The Generalized Method of Wavelet Moments (GMWM) and its Multi-signal extensions (MS-GMWM) represent the latest trend in the field of inertial sensor error stochastic analysis, they are capable of efficiently modeling the highly complex random errors displayed by low-cost and consumer-grade inertial sensors and provide very advantageous guarantees for the statistical properties of their estimation products. On the other hand, even though a robust version exists (RGMWM) for the single-signal method in order to protect the estimation process from the influence of outliers, their detection remains a challenging task, while such attribute has not yet been bestowed in the multi-signal approach. Moreover, the current implementation of the GMWM algorithm can be computationally intensive and does not provide the simplest (composite) model. In this work, a simplified implementation of the GMWM-based algorithm is presented along with techniques to reduce the complexity of the derived stochastic model under certain conditions. Also, it is shown via simulations that using the RGMWM every time, without the need for contamination existence confirmation, is a worthwhile trade-off between reducing the outlier effects and decreasing the estimator efficiency.

Generally, stochastic modeling techniques, including the GMWM, make use of individual static signals for inference. However, it has been observed that when multiple static signal replicates are collected under the same conditions, they maintain the same model structure but exhibit variations in parameter values, a fact that called for the MS-GMWM. Here, a robust multi-signal

method is introduced, based on the established GMWM framework and the Average Wavelet Variance (AWV) estimator, which encompasses two robustness levels: one for protection against outliers in each considered replicate and one to safeguard the estimation against the collection of signal replicates with significantly different behaviour than the majority. From that, two estimators are formulated, the Singly Robust AWV (SR-AWV) and the Doubly Robust (DR-AWV) and their model parameter estimation efficiency is confirmed under different data contamination scenarios in simulation and case studies. Furthermore, a hybrid case study is conducted that establishes a connection between model parameter estimation quality and implied navigation performance in those data contamination settings. Finally, the performance of the new technique is compared to the conventional Allan Variance in a land vehicle navigation experiment, where the inertial information is fused with an auxiliary source and vehicle movement constraints using the Extended and Unscented Kalman Filters (EKF/UKF). Notably, the results indicate that under linear-static conditions, the UKF with the new method provides a 16.8-17.3% improvement in 3D orientation compared to the conventional setting (AV with EKF), while the EKF gives a 7.5-9.7% improvement. Also, in dynamic conditions (i.e., turns), the UKF demonstrates an 14.7-17.8% improvement in horizontal positioning and an 11.9-12.5% in terms of 3D orientation, while the EKF has an 8.3-12.8% and an 11.4-11.7% improvement respectively. Overall, the UKF appears to perform better but has a significantly higher computational load compared to the EKF. Hence, the EKF appears to be a more realistic option for real-time applications such as autonomous vehicle navigation.

Acknowledgements

First and foremost, I would like to express my sincerest gratitude towards my supervisor Prof. Naser El-Sheimy for his continuous support, counsel, motivation and firm belief in my research abilities and ideas. His guidance, willingness to patiently listen and answer all my questions as well as his work ethic have been a source of inspiration to me, not only as a researcher but as a person too. In addition, I am indebted to Prof. Michael G. Sideris for giving me the opportunity to come to the University of Calgary (UofC) as a Master student and for supporting my transfer to the PhD program.

My appreciation to Prof. Yang Gao and Prof. Aboelmagd Noureldin should be highlighted for accepting to be members of my supervisory committee, inspecting my thesis draft, and offering valuable comments for its refinement. Moreover, I am thankful to the Graduate Program Administrator of the Department of Geomatics Engineering, June Au Yeung, for her assistance with every procedural matter I encountered over the years.

Another very important figure during the realization of my PhD research has been Asst. Prof. Stéphane Guerrier from the University of Geneva, the creator of the Generalized Method of Wavelet Moments method. The very fruitful collaboration we have had over the last three years, his eagerness to have lengthy conversations with me regarding stochastic modeling and the concept of robustness as well as his friendship deserve a wholehearted thank you. Furthermore, through Dr. Guerrier, I had the pleasure of being introduced to the following members of his research group: Dr. Davide A. Cucci and PhD candidate Lionel Voirol. The former is acknowledged for sharing the inner workings of his navigation simulator and his cooperation on my publications, while the latter's help on matters related to high-performance cluster computing has been invaluable.

During my time in the UofC and the Department of Geomatics Engineering, I have had the opportunity to meet and work with several researchers and PhD students, each of which has helped me in at least one aspect of my research, and I would like to thank them for that. First, my gratefulness is extended to Dr. Adel Moussa for his vital help in troubleshooting my coding and for his insightful remarks. Second, Drs. Ahmed Radi and Ahmed Youssef are greatly appreciated for their tutelage in data collection and for the particularly useful discussions regarding practical aspects of navigation. In addition, Yang Jiang, Dr. Ilyar Asl Sabbaghian Hokmabadi, Dr. Yiran Luo and Dr. Mengchi Ai are acknowledged for their cooperation in common research endeavours, critical thinking and for the interesting conversations that in turn gave birth to ideas implemented in this thesis. Finally, an honorable mention is given to Dr. Wei Ding for his friendship and support in my research.

A special thank you also should be given to Drs. Dimitrios Piretzidis and Iliana Tsali. They were the first people to welcome me in Calgary, made my adjustment a lot easier and they have been two of my strongest supporters ever since. What's more, my gratitude is extended to Elpida Karantagli, Nikolaos Georgiadis and Dércia Eliana. They are my closest friends, a rock of emotional support during the last five years and the closest thing I have to a second family. Finally, and most importantly, a loving thank you from the bottom of my heart has to be given to my mother, father, and sister. Without their love and encouragement, none of this would have ever been possible.

Dedication

To the memory of my grandfather

Chrysostomos

The strongest and wisest man I have ever known

And

to my parents

Georgia and Panagiotis

Who taught me to never back down from a challenge

Table of Contents

List of Tables

List of Figures

List of Symbols, Abbreviations and Nomenclature

Symbol	Definition
$\in$	Element of
$\subset$	Proper subset of
$\mathbf{A}$	Least Squares design matrix
a	Tuning term for the M-estimator of the Empirical Wavelet Variance
a	Significance level of confidence interval
A	Azimuth angle
$\mathbf{b}_\omega$	Gyroscope measurement bias vector
$\mathbf{b}_f$	Accelerometer measurement bias vector
b_{xx}	Inertial sensor bias value
B	Bias instability coefficient estimated by the AVLR
c	Tuning term for the M-estimator of the Empirical Wavelet Variance
CI_{xx}	Confidence interval extremes (higher and lower limits)
Δt	Time/sampling interval
e	First eccentricity of the reference ellipsoid
f	Frequency
$F_{\boldsymbol{\theta}}$	Random drift generating (composite) stochastic process
f_0	Bias instability cut-off frequency
$\tilde{\mathbf{f}}^b$	Accelerometer measurement (specific force) vector
$\tilde{f}_{xx}$	Specific force measurement value
f_{xx}	True (unknown) specific force measurement value
$\mathbf{F}$	EKF dynamic matrix
g	Gravity

$G(\cdot)$	True error generating function in multi-signal calibration
$\mathbf{G}$	EKF random forcing matrix
h	Ellipsoidal height
$H(f)$	Transfer function of the MODWT Haar wavelet filter
h	MODWT Haar wavelet filter
H	Monte Carlo simulation total number
$\mathbf{H}$	EKF update design matrix
I	Identity matrix
i, j	Unitless indexes
j	Imaginary unit
j_{max}	Maximum wavelet decomposition level
J	Maximum AV curve points
k	Subscript denoting the point index from a discrete data sequence
K	Random Walk coefficient estimated by the AVLR
K	Number of available inertial sensor measurement signal replicates
$\mathbf{K}$	Kalman gain matrix
l_{GNSS}^{b}	IMU-GNSS lever-arm vector
l_{wheel}^{b}	IMU-Vehicle frame origin lever-arm
l	Sensor measurement in the context of deterministic calibration
m_{xx}	IMU axes non-orthogonalities
$\mathbf{M}_{c}$	Inertial sensor deterministic error coefficient matrix
M_{AV}	Total AV cluster number
M	Wavelet variance coefficient length
N	Data sequence size

N	White Noise coefficient estimated by the AVLR
$\mathcal{N}(...)$	Normal (Gaussian) distribution
sl	Confidence interval level
p	Number of smaller and larger values removed by the trimmed mean
p	Pitch angle
P	V-C matrix of the EKF and UKF Gaussian state PDF
q^2_{QN}	Defining parameter of the QN stochastic process
Q_z	Quantization noise coefficient estimated by the AVLR
Q	V-C matrix associate with the EKF and UKF system noise
$\mathbf{Q}_s$	Spectral densities matrix
$\mathbf{q}_s$	Spectral densities vector
q	Quaternion based on the Hamilton convention
R_{xx}	Autocorrelation
R	Drift ramp coefficient estimated by the AVLR
R_M	Meridian radius of curvature
R_N	Radius of curvature in the prime vertical
R_e	Gaussian mean Earth radius of curvature
R	V-C matrix associated with the EKF and UKF measurement noise
R	Reference signal for the inertial sensor deterministic calibration
r	Geodetic position vector
r	Roll angle
$S_{xx}(f)$	Power spectral density
$\tilde{S}_{xx}(f)$	Approximation to the power spectral density
s_{xx}	Deterministic scale factor error

S	Lower triangular square root matrix from Cholesky factorization
t	Time
t_0	Sampling time interval
τ	Shift in time
τ	Allan variance cluster time length and Haar wavelet scale
T	Data record total time span
T_{BI}	Bias instability fluctuation period
T_c	Correlation time of the GM1 stochastic process
tr	Trim level
$U(...)$	Uniform distribution
u	Control input vector
u	Error with respect to the reference navigation solution
V	UKF measurement noise vector
$\hat{v}_j^2$	Classical empirical wavelet variance value for the jth scale
$\hat{\boldsymbol{v}}$	Classical empirical wavelet variance vector
$\tilde{v}_j^2$	Robust empirical wavelet variance value for the jth scale
$\tilde{\boldsymbol{v}}$	Robust empirical wavelet variance vector
$v_j^2(\boldsymbol{\theta})$	Model-implied wavelet variance value for the jth scale
$\boldsymbol{v}(\boldsymbol{\theta})$	Model-implied wavelet variance vector
v	Velocity vector
$\overline{v}_{AWV}$	AWV estimator characteristic wavelet variance
$\overline{v}_{SR-AWV}$	SR-AWV estimator characteristic wavelet variance
$\overline{v}_{DR-AWV}$	DR-AWV estimator characteristic wavelet variance
$\boldsymbol{v}$	EKF measurement noise vector

v_n	North velocity in the n-frame
v_e	East velocity in the n-frame
v_d	Down velocity in the n-frame
v	UKF innovation sequence
$\mathbf{W}_{LS}$:	LS misclosure matrix
$\mathbf{w}$	Process/system noise vector
$W_{j,t}$	MODWT wavelet variance coefficient
w_i	Empirical wavelet variance weighting factor
w^m	Weights associated with the mean of the Gaussian state PDF, produced by the SSS-UT
w^c	Weights associated with the covariance of the Gaussian state PDF, produced by the SSS-UT
w_0	Initial weight for the SSS-UT
x(t)	Random variable
$\{x(t)\}$	Ensemble of time functions
$\boldsymbol{X_t, Y_t}$	Discrete data sequences
$\bar{\mathbf{x}}$	Mean of the Gaussian state PDF
$\mathbf{x}$	EKF absolute state vector
$\mathcal{X}$	Sigma point
$\widehat{\mathbf{X}}$	UKF absolute state vector
Y_k	Standard discrete uniform variable
$\mathcal{Z}$	Transformed SP through the nonlinear measurement model
$\mathbf{Z}$	UKF measurement vector
$\hat{z}$	UKF predicted measurements
z	Auxiliary source information inputted within the UKF

α_e Semi-major axis of the reference ellipsoid

α Scaling parameter for the SSS-UT

$\boldsymbol{\alpha}$ Acceleration vector

β_{GM1} Inverse of the GM1 stochastic process correlation time

β Scaling parameter for the SSS-UT

γ Normal gravity

γ^2_{RW} Defining parameter of the RW stochastic process

$\delta\boldsymbol{f}^b$ EKF random accelerometer bias vector

$\delta\mathbf{x}$ EKF error state vector

$\delta\mathbf{z}$ EKF measurement error vector

$\delta\boldsymbol{\omega}^b$ EKF random gyroscope bias vector

ε_k Gaussian white noise involved within the AR1 stochastic process

$\boldsymbol{\theta}$ Composite stochastic model defining parameter vector

$\boldsymbol{\theta}_i$ Defining parameter vector based on the ith signal replicate

$\boldsymbol{\theta}_0$ True (unknown) stochastic model defining parameter vector

$\widehat{\boldsymbol{\theta}}^o_{AGMWM}$ Estimated stochastic model parameter vector by the AGMWM estimator

$\widehat{\boldsymbol{\theta}}^{\dagger}_{AWV}$ Estimated stochastic model parameter vector by the AWV estimator

$\widehat{\boldsymbol{\theta}}_{MS-GMWM}$ Estimated stochastic model parameter vector by the MS-GMWM estimator

$\overline{\boldsymbol{\theta}}$ Stochastic model parameter vector estimated by the new robust multi-signal method

$\boldsymbol{\Theta}$ Stochastic model parameter space

λ Longitude

$\tilde{\lambda}$ GNSS-derived longitude

ξ^2_{AR1} Variance of the Gaussian WN involved within the AR1 stochastic process

σ^2_{xx}	Variance of a navigation state quantity
σ_0^2	A-priori variance factor in the context of the LS-based inertial sensor deterministic calibration
σ^2_{AV}	Allan variance
σ_{AV}	Allan standard deviation
σ^2_{BI}	Defining parameter of the BI stochastic process
σ^2_{GM1}	Defining parameter of the GM1 stochastic process
σ^2_{WN}	Defining parameter of the WN stochastic process
φ_{AR1}	Parameter characterizing the systematic part of the AR1 stochastic process
ϕ	Latitude
$\tilde{\phi}$	GNSS-derived latitude
$\boldsymbol{\Phi}$	EKF transition matrix
$\boldsymbol{\varphi}$	Rotation vector
χ^2	Chi-squared distribution
$\boldsymbol{\psi}$	EKF attitude error vector
ω	Weight function corresponding to the influence function
ω_e	Rotation rate of the Earth
ω_{DR}	Defining parameter of the DR stochastic process
$\tilde{\boldsymbol{\omega}}^b_{ib}$	Gyroscope measurement vector
$\hat{\boldsymbol{\Omega}}$	Weight matrix for the GLS-based GMWM optimization

Operator	Definition
$\dot{...}$	First-order time differentiation of a quantity
$\hat{...}$	Estimated quantity
$\bar{...}$	Mean
$\times$	Cross-product
$\otimes$	Quaternion product (Hamilton convention)
$...^{-1}$	Matrix and quaternion inverse
$...^{\text{T}}$	Matrix transpose
$(\cdot\times)$	Skew-symmetric representation of a vector
$\widehat{cov}(\cdot)$	Estimated covariance between two quantities
$\delta(\cdot)$	Error, correction
$\text{diag}(\cdot)$	Diagonal matrix expression of a vector
$E\{\cdot\}$	Mathematical expectation
$\mathcal{F}\{\cdot\}$	Fourier Transformation
$\lfloor\cdot\rfloor$	Floor operator
$\ln(\cdot)$	Natural logarithm
$\log_{\text{n}}(\cdot)$	Logarithm with base n
$log(\cdot)$	Logarithmic mapping in the SO(3) 3D Rotation Group
$\text{mad}(\cdot)$	Median absolute deviation
$\text{med}(\cdot)$	Median
$\text{mod}(\cdot)$	Modulo operator
$\text{rms}(\cdot)$	Root mean square
$p(...\,|\,...)$	Conditional probability distribution

Abbreviation	Definition
AccRW	Acceleration Random Walk
ACF	Autocorrelation Function
ACS	Autocorrelation Sequence
ADC	Analog-to-Digital Converter
ADEV	Allan Standard Deviation
AGMWM	Average Generalized Method of Wavelet Moments Estimator
AINS	Aided Inertial Navigation System
AR	Autoregressive Stochastic Process
ARW	Angle Random Walk
ASEE	Average Standard Estimation Error
AVLR	Allan Variance Linear Regression
AWV	Average Wavelet Variance Estimator
BeiDou	Chinese Navigation Satellite System
CI	Confidence Interval
CV-WVIC	Cross-Validated Wavelet Variance Information Criterion
DCM	Direction Cosine Matrix
DFT	Discrete Fourier Transformation
DGNSS	Differential GNSS Processing Strategy
DAccR	Drift Acceleration Ramp
DoF	Degrees of Freedom
DR	Drift Ramp
DRR	Drift Rate Ramp
DR-AWV	Doubly Robust Average Wavelet Variance Estimator
ECEF	Earth-Centered Earth-Fixed Frame

EKF	Extended Kalman Filter
EM	Expectation Maximization
FOG	Fiber-Optic Gyroscope
FT	Fourier Transformation
Galileo	European Union's Navigation Satellite System
GLONASS	GLObal NAvigation Sputnik System
GLS	Generalized Least Squares
GM	Gauss-Markov Stochastic Process
GMM	Generalized Method of Moments
GMWM	Generalized Method of Wavelet Moments
GMWMX	Generalized Method of Wavelet Moments for eXogenous Inputs
GNSS	Global Navigation Satellite System
GPS	Global Positioning System
GRV	Gaussian Random Variable
IF	Influence Function
IMU	Inertial Measurement Unit
INS	Inertial Navigation System
KF	Kalman Filter
LLF	Local Level Frame
LS	Least Squares Estimation
MC	Monte-Carlo
MEMS	Micro Electronic Mechanical Systems
MLE	Maximum Likelihood Estimator
MMSE	Minimum Mean Square Error
MODWT	Maximal Overlap Discrete Wavelet Transform

MS-GMWM	Multi-Signal Generalized Method of Wavelet Moments Estimator
NED	North-East-Down Local Level Frame
NHC	Non-Holonomic Constraint
PDF	Probability Density Function
PF	Particle Filter
ppm	Parts per Million
PPP	Precise Point Positioning Processing Strategy
PSD	Power Spectral Density
PVA	Position, Velocity, Attitude
QN	Quantization Noise
RGMWM	Robust Generalized Method of Wavelet Moments
RMSE	Root Mean Square Error
RRW	Rate Random Walk
RW	Random Walk
SEE	Standard Estimation Error
SP	Sigma Point
SPAN	Synchronous Position, Attitude and Navigation System
SPP	Single Point Positioning Processing Strategy
SR-AWV	Singly Robust Average Wavelet Variance Estimator
SSS-UT	Scaled Spherical Simplex Unscented Transformation
TV	Total Variance
UKF	Unscented Kalman Filter
UT	Unscented Transformation
V-C	Variance-Covariance Matrix
VRW	Velocity Random Walk

WN	Gaussian White Noise
WOSA	Welch's Overlapped Segmented Average
WV	Wavelet Variance
WV-AWV	AWV estimator characteristic wavelet variance
WV-SR-AV	SR-AWV estimator characteristic wavelet variance
WV-DR-AWV	DR-AWV estimator characteristic wavelet variance
WVIC	Wavelet Variance Information Criterion
ZUPT	Zero Velocity Update

Conventions

1) Matrices are denoted using upper-case letters in bold font.

2) Vectors are denoted using lower-case letters in bold font.

3) Angular rate vectors are denoted with two subscripts and one superscript like so ω_{ab}^c: 'a' indicates the frame with respect to which the rotation occurs, 'b' is the rotating frame and 'c' is the frame where the angular rate is resolved.

4) $\mathbf{R}_a^b$ denotes a Direction Cosine Matrix (DCM) that describes the transformation from frame a to frame b.

5) $\mathbf{q}_a^b$ represents a quaternion (Hamilton convention) that describes the rotation/trans-formation from frame 'a' to frame 'b'.

Coordinate Frames

Body frame (b-frame)

- Origin: origin of the mutually orthogonal IMU accelerometer triad

- X-axis: towards the forward direction (i.e., roll axis)

- Y-axis: towards the transverse direction (i.e., pitch axis)

- Z-axis: towards the vertical direction (i.e., yaw axis) to complete a right-handed frame

Inertial Frame (i-frame)

- Origin: Earth's centre of mass

- X-axis: direction of the vernal equinox

- Y-axis: orthogonal to complete a right-handed frame

- Z-axis: spin axis of the Earth (defined by the North and South celestial pole)

- Axes are non-rotating with respect to distant galaxies

Earth-Centered Earth-Fixed Frame (e-frame)

- Origin: Earth's centre of mass

- X-axis: Intersecting the mean equatorial plane and the mean Greenwich meridian plane

- Y-axis: Orthogonal to complete a right-handed frame

- Z-axis: Mean spin axis of the Earth

- Rotates with respect to the i-frame around its Z-axis at a fixed angular rate $\omega_e = 15.041$ deg/hr

Navigation frame (n-frame)

- Origin: same as the b-frame

- X-axis: tangent to geodetic meridian, pointing towards the geodetic North

- Y-axis: orthogonal to complete a right-handed frame

- Z-axis: orthogonal to the reference ellipsoid (here the WGS84 reference ellipsoid is employed)

- Identical to the NED Local Level Frame

Vehicle frame (v-frame)

- Origin: ground projection of the rear drive axle's midpoint and aligned with the roll, pitch, and azimuth axes of the vehicle (assuming a front wheel steering system)

- X-axis: towards the vehicle's longitudinal axis

- Y-axis: pointing right, along the line connecting the ground projection points of the two rear wheel centers

- Z-axis: orthogonal to complete a right-handed frame, pointing downward

Chapter One: Introduction

1.1 Background and Objectives

Inertial sensors are an integral part of modern navigation, with applications ranging from aviation and drones to vehicular and pedestrian navigation. They are the fundamental unit of the Inertial Navigation System (INS) (Groves, 2013), an autonomous system that is capable of delivering precise high frequency and short term position, velocity, and attitude (PVA) information for the moving platform they are mounted on. However, the INS standalone operation degrades rapidly with time due to the effects of random errors governing the inertial sensor measurements. In fact, this phenomenon is particularly intense when dealing with either low-cost or consumer-grade equipment, due to the fact that their observation noise is not only high leveled but also very complex structured. Therefore, to prevent the evolution of the inertial sensor stochastic errors, maintain high navigation solution quality and avoid the INS performance derailment, integration with aiding sources is required. Specifically, these aiding sources have complementary characteristics to the INS, a comparatively lower bandwidth and offer partial navigation state information (i.e., nav-aids). Here, since particular focus will be given to outdoor vehicular navigation, a characteristic example of such source is the Global Navigation Satellite System (GNSS) (Misra and Enge, 2011), incorporated in the context of strapdown inertial navigation (Titterton and Weston, 2004).

Even though the synergy between INS and GNSS is very beneficial, a challenge arises in real-life vehicular navigation situations where the latter's information is obstructed, and the former has to operate on standalone mode for a period of time. In such an occurrence, the navigation performance would be reliant on three major factors: (a) the quality of the knowledge regarding the inertial sensor random error behavior, (b) the estimation method/filter employed for the in-

formation fusion and (c) motion constraints, whose usefulness is linked with the quality of the inertial sensor noise behavior.

Currently, the latest trend in the modeling of inertial sensor random errors is the Generalized Method of Wavelet Moments (GMWM) (Guerrier et al., 2013a), which offers a stochastic analysis (statistical) framework capable of estimating the parameters of a composite stochastic model that balances the adequate description of the sensed random behavior and the simplicity of that model's structure. However, as it stands now, the identified stochastic model by the GMWM based on a single calibration signal (presumed intrinsically stationary) has room for further complexity reduction, while the whole implementation can also be improved in terms of simplicity and speed, without sacrificing the quality of the final product.

The GMWM is capable of efficiently identifying and estimating high and low frequency error terms with great accuracy. In addition, unlike the standard Allan Variance method (Allan, 1966) that has been the status quo in the navigation community for the last 15 years, it is capable of precisely identifying and quantifying multiple time-correlated error terms that affect different regions of the mid frequency spectrum. On top of that, this method includes a robust feature, which based on fundamental concepts of robust statistics, it is capable of providing some level of protection to the estimation process by reducing the impact of existent outliers within the one signal that is being utilized for the stochastic analysis (Guerrier et al., 2022). However, it can be challenging to determine whether the data at hand are contaminated with outliers or not.

On another note, it has been observed in recent studies regarding low-cost and consumer-grade inertial sensors (Radi et al., 2019), that when multiple calibration signals are collected under the exact same operating conditions, there is a certain variation in stochastic behavior from one signal replicate to another. In order to consider this phenomenon, a multi-signal stochastic

error modeling framework was proposed as well as three different estimators that are based on it (Radi et al., 2019; Bakalli et al., 2023). Nevertheless, despite the fact that the improvements it offers over the single-signal GMWM have been demonstrated in a recent study (Bakalli et al., 2023), it contains no safeguards against the influence of outliers that exist within the multiple calibration signals that are being considered by the method. In fact, the situation is more complicated in the multi-signal case since even if only a small number of signal replicates contain a significant number of outliers, that can affect not only the estimation of the composite model that describes the random error behavior but also the selection of the proper model structure.

After conducting the stochastic modeling of the inertial sensor errors, the derived knowledge has to be included within the navigation algorithm in order to allow for their recursive compensation and thus, improve the INS performance. Typically, the incorporation of such information as well as the integration of INS with other aiding sources in order to estimate the integrated navigation solution along with its corresponding uncertainty, is conducted by the means of Bayesian filtering (Haug, 2005).

The navigation problem is a real-life ever evolving system that can be observed by various sensors like the INS and GNSS systems. In the context of Bayesian filtering, the mathematical description of such system is comprised of two parts: the dynamic/kinematic or system model and the measurement model. The first one is driven by the INS due to its high bandwidth and it expresses the physics behind the motion (i.e., evolution of the navigation states over time) from the previous to the current time, while the latter relates the information from auxiliary sources (e.g., GNSS, motion constraints) to the propagated state. Furthermore, Bayesian filtering considers the navigation states (i.e., position, velocity, attitude) as random variables that can be fully

characterized by their probability distribution function (PDF) and constitute a 1st-order hidden Markov chain model (HMM), which is visually represented in Figure 1.1.
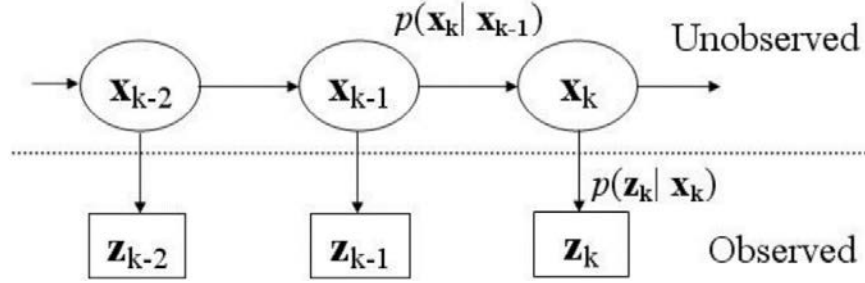
Figure 1.1: 1st-order Hidden Markov model (HMM) representation (Georgy, 2010)

Consequently, the conditional probability distribution of each state moment, considering all its past and future values, depends only on the immediately preceding moment $\left(p(\mathbf{x}_k|\mathbf{x}_{k-1})\right)$ and each independent measurement $\mathbf{z}$, observes and characterizes a single state moment of the HMM $\left(p(\mathbf{z}_k|\mathbf{x}_k)\right)$ (Rabiner and Juang, 1986).

For navigation purposes, the estimation of the full state vector $\mathbf{x}$ is required whenever an observation becomes available. Therefore, Bayesian filtering should be implemented recursively in order to adapt the state PDF to the new information and quantify its posterior shape (Särkkä, 2013). Generally, the structure of such a filter is divided into two parts: the prediction and the update. During the prediction stage, the INS mechanization equations (i.e., system model) are utilized in tandem with the latest inertial sensor measurements and previous epoch's state knowledge in order to estimate the "predictive" conditional transition PDF of the state at the present time. However, this PDF does not utilize any current moment information and since the measurements used for its estimation are noisy (i.e., inertial sensor observations), especially for the case low-cost and commercial grade equipment, it only natural that it will be deformed. As for the update stage, the information provided by an aiding source like GNSS is utilized along

with the predictive PDF and the Bayes theorem (fundamental statistics formula) in order to estimate a posterior PDF that encompasses all the available information (see (Simon, 2006) for an in-depth discussion).

The aforementioned recursive implementation of the Bayes theorem yields high-dimensional integrals, which according to Doucet, (1998), it is virtually impossible to analytically evaluate unless the system at hand is Gaussian and linear in nature. Furthermore, it is emphasized that the latter case refers to romanticized systems and only nonlinear ones exist in real-life (Noureldin et al., 2013). Therefore, in order to overcome the intractability of these integrals in nonlinear systems, sub-optimal methods have to be utilized, which employ some form of approximation to the inference of their solutions. A brief description of such techniques, including their respective advantages and disadvantages can be found in (Arulampalam et al., 2002).

Nowadays, the most heavily used Bayesian filtering approaches for the purpose of integrated vehicular navigation are:

A) The Extended Kalman Filter (EKF)

B) The Unscented Kalman Filter (UKF)

C) Particle Filter (PF) variants

The primary differences between these Bayesian filters are the manner in which they handle the nonlinearities of the system and measurement models as well as the way that they perceive the state PDF. Furthermore, if the complex stochastic modeling information for the inertial sensor errors provided by the multi-signal GMWM-based stochastic analysis approach is to be considered, then this would cause a considerable increase to the computational cost since the state-space size should be augmented. Consequently, this automatically disqualifies the use of the PFs

from practical applications since due to their inherent curse of dimensionality, the demand for computational resources would be prohibitively large. Therefore, only the EKF and UKF approaches are viable Bayesian filter candidates for the infusion of such stochastic analysis information for the inertial sensor errors. In addition, it should be noted that the UKF, a less restrictive approach than the conventional EKF, has never been utilized before along with GMWM-based stochastic analysis for the inertial sensor errors and thus, it would be worthwhile to investigate the benefits of such synergy to the navigation performance.

With the aforementioned in mind, the subject of this thesis is the robust stochastic modeling of inertial sensor errors as well as its contribution to the integrated vehicular navigation performance while using different information fusion methods. Furthermore, besides the use of GNSS as an aiding source, two motion constraints can also be utilized: (a) the Non-Holonomic Constraints (NHCs), which express the intuitive observation that the velocities along the vertical and transversal direction of a moving car should be equal to zero and (b) the Zero Velocity Updates (ZUPTs), where the velocity of the vehicle along all three dimensions is equal to zero since it has stopped moving. Hence, the following research objectives will be realized in this thesis:

1) Propose a simplified implementation for GMWM-based algorithms that ensures speed, accuracy, and complexity reduction of the final composite stochastic model.

2) Highlight the usefulness of performing the single-signal stochastic analysis of inertial sensor errors in a robust way.

3) Establish and validate a new robust multi-signal stochastic modeling method in the context of the GMWM framework.

4) Modify the EKF-based and UKF-based INS/GNSS/NHC/ZUPT algorithms in order to infuse them with the new stochastic analysis approach's information.

5) Investigate the contributions of the new robust multi-signal stochastic modeling method to the EKF-based and UKF-based INS/GNSS/NHC/ZUPT integrated navigation performance.

6) Compare the performance of the EKF and UKF schemes.

1.2 Thesis Outline

For the purpose of realizing the aforementioned research objectives, this thesis is structured in the manner that is described in the following.

Chapter 2 starts by mentioning the fundamental principles of Inertial Navigation. Then, it proceeds to break down the error budget associated with the measurements provided by the Micro Electronic Mechanical System (MEMS)-based inertial sensors into two main categories: the deterministic and the stochastic. The definition for each error is also provided. Furthermore, the properties that characterize the most common stochastic processes that are being utilized in the literature for modeling the random error behavior are highlighted.

In Chapter 3, the methods of quantifying the deterministic error influence on the inertial sensor measurements are mentioned. Subsequently, a concise literature review is presented for each of the available stochastic modeling techniques, along with their corresponding algorithm and weaknesses that warrant further investigation. Furthermore, it is highlighted that the entirety of past studies exposes the connection between the inertial sensor stochastic modeling quality and the final navigation performance via a small number of practical experiments. However, such an endeavor is not enough to infer reliable conclusions from a purely statistics viewpoint and thus, the use of a recently proposed navigation simulator by Cucci et al., (2023) is suggested for the validation of the new robust GMWM-based multi-signal method that will be presented in this thesis. Finally, it is noticed that the GMWM-based stochastic analysis has only been tested in the

context of an EKF filter and only for INS/GNSS integration, without the assistance of other up-
dates.

Chapter 4 is devoted to main contributions of this thesis, which are related to the stochastic
modeling of low-cost and commercial-grade inertial sensor errors. Firstly, a refined implementa-
tion algorithm for the GMWM is presented. In addition, the mathematical foundation for reduc-
ing the derived stochastic model's complexity under specific conditions is established, along
with ways to assess whether these conditions are satisfied. Second, a simulation study is con-
ducted, in order to investigate whether the robust version of the GMWM can be effectively uti-
lized in every scenario, without requiring confirmation of whether the calibration data at hand
are corrupted or not. Subsequently, a novel robust multi-signal wavelet variance-based stochastic
modeling method that contains two layers of robustness is presented. From that, two estimators
are defined, which are evaluated through a simulation and a case study in order to assess their
efficiency in terms of stochastic model parameter estimation. Moreover, the contribution of the
new robust estimators to the navigation performance was evaluated via a hybrid study by em-
ploying the navigation simulator proposed by Cucci et al., (2023) and real inertial sensor data
that have been artificially contaminated with outliers. Finally, the stochastic analysis of commer-
cial grade inertial sensors was implemented using the newly established approach as well as the
conventional Allan Variance method.

In Chapters 5, the structure of an EKF-based INS/GNSS/NHC/ZUPT loosely coupled integra-
tion algorithm is presented in detail. Furthermore, special focus is given in reporting how the
knowledge derived by the new stochastic analysis method can be properly infused within the fil-
ter.

Chapter 6 contains the description of a novel UKF-based INS/GNSS/NHC/ZUPT loosely coupled integration scheme, in the sense that this is the first time that stochastic modeling information derived by GMWM-based estimators is being infused in the context of such a filter.

In Chapter 7, the stochastic modeling information derived in Chapter 4 is infused within the EKF and UKF filters described in Chapters 5 and 6 respectively and thus 4 filter configurations are created. Then, their performance is evaluated in terms of horizontal positioning and 3d orientation estimation accuracy via a real-life vehicle navigation experiment. In fact, this assessment is conducted under different conditions in order to highlight the improvement that the new stochastic estimators can provide over the classical Allan Variance from multiple aspects. Finally, the computational times of the filters are also calculated in order to provide further evidence for selecting the most appropriate configuration.

Chapter 8 is the final chapter of this thesis, where the derived conclusions from the previous chapters are summarized. In addition, several recommendations are made for expanding the research presented here in order to make further contributions.

Chapter Two: Inertial Sensors and Measurement Error Budget

2.1 Introduction

The measurements provided by MEMS-based inertial sensors, which are primarily utilized for low-cost applications, are typically compromised by a significant error budget. These errors can be classified into two different categories, depending on their nature: the deterministic and stochastic. In this chapter, a listing of the errors that belong to each type as well as their respective properties will be provided, with a particular focus given to the characteristics of the stochastic ones. Before that however, the operational principle, based on which the inertial sensor measurements can be translated to navigation information will be briefly mentioned.

2.2 Inertial Navigation System and Inertial Sensors

An Inertial Navigation System is a self-contained system able to produce high-rate PVA information in the 3d space using inertial sensor measurements and the Dead Reckoning concept. According to that concept, it is possible to determine the navigation states of a moving platform by combining measurements of acceleration and angular rate that sense its motion between subsequent points w.r.t an inertial frame and the knowledge of its initial condition. Specifically, a proper manipulation of the angular rates can infer the transformation between the inertial and the navigation frame (commonly the Local Level Frame (LLF)) and allow the evaluation of the attitude in the new state. In turn, using that information, the acceleration observations can be referred to the navigation frame (n-frame), where a single and a double integration over time would produce the position and velocity of the platform respectively at the end of the sensed movement (El-Sheimy, 2014).

The apparatus that can provide the aforementioned observations in the 3d space and eventually lead to a full navigation solution is called the Inertial Measurement Unit (IMU), which is

comprised by an accelerometer and a gyroscope orthogonal triad. The accelerometers sense the linear motion along three mutually orthogonal directions by measuring the applied specific force (difference between the acceleration w.r.t the inertial frame and the gravitational acceleration), while the gyroscopes perceive the angular motion along mutually orthogonal directions as well through angular rate observations. Ideally, the axes of both sensor triads are aligned with each other, share the same origin (accelerometer triad's) and since they are mounted on the surface of the IMU, they define the so-called body frame (b-frame) (Noureldin et al., 2013).

2.3 MEMS-based Inertial Sensor Error Budget

Conventional INS devices are highly sophisticated, heavy, and particularly high-priced. Therefore, it stands to reason that they are unapproachable by the average consumer. A solution to this problem has been provided by advancements in the MEMS technology, which by combining silicon-based microelectronics and micromachining, has allowed the production of chip-based inertial sensors (e.g., accelerometers, gyroscopes) that are compact, lightweight, cheap, power-efficient and reliable for mass-market applications (Aggarwal, 2010). Regardless, the output from this type of sensors is compromised by errors, with the magnitude and complexity of which being inversely proportional to the value of the sensors, that cause the rapid degradation of the INS standalone performance over time.

Typically, the nature of the errors that govern the inertial sensor measurements (either of accelerometers or gyroscopes) and influence their performance can be divided into two distinct categories: deterministic and stochastic. The deterministic errors are related to the equipment's inherent property and manufacturing defects (Rogers and Schetz, 2003), can be corrected through a calibration procedure (in-lab or in-field) since their effects to the sensor output can be described with a closed-form expression and removed from the measurements prior to the INS

mechanization (i.e., algorithm that translates the inertial sensor output to navigation information). As for the stochastic ones, their randomness forbids the direct calculation of their magnitude but their behaviour over time can be modeled stochastically. Moreover, it should be highlighted that the operating conditions like the temperature and the dynamics have a non-negligible impact to the behaviour of the stochastic errors, which is why their influence should also be considered during the stochastic calibration (Abdel-Hamid, 2005; Stebler et al., 2014a).

In the following section, the errors that belong to each of these two general categories will be briefly discussed.

2.3.1 Deterministic Errors

2.3.1.1 Bias

Practically, the bias is the output of any sensor in the case when there is no external input and it is defined as a long-term average of the measurements under specific operating conditions that is independent of the observable (i.e., specific force, angular rate) (Noureldin et al., 2013). Regarding the gyro bias, it is usually expressed in radians per second (rad/sec), while the accelerometer bias is given in metre per second per second (m/sec^2).

Furthermore, it is possible for the sensor bias to be different for positive and negative inputs. Such dissimilarity is called bias asymmetry and shares the same units as the sensor bias for both inertial sensor types (Hou, 2004).

2.3.1.2 Scale Factor

The scale factor represents the ratio of change in output to a corresponding change in input and it can be mathematically quantified as the slope of the optimally fitted line to the input-output data using the Least Squares (LS) method (Aggarwal, 2010). Given that, it is possible to

define the scale factor error as the divergence of that slope from unity, which is usually expressed in parts per million (ppm).

Similarly to the bias, the scale factor could also present a difference for positive and negative inputs. It is specified as a fraction of the scale factor over the input range and it directly implies that the input-output gradient has a discontinuity at the zero input location (Hou, 2004).

2.3.1.3 Axes Misalignment

Axes misalignment is a consequence of an imperfect sensor mounting during the manufacturing stage and refers to the deviation of the inertial sensors' sensitive axes from the mutually orthogonal axes of the INS b-frame. In turn, this results to a cross-axis signal coupling in the b-frame (Aggarwal, 2010).

2.3.2 Stochastic Errors

The primary expression of the stochastic error category is the noise, which is defined as an unwanted, non-systematic disturbance contained within the output signal and it is related to the sensor itself or to external electronic interference (Hou, 2004). In addition, the inertial sensor noise contains the random fluctuations of the deterministic errors over time, meaning the bias (bias drift) and scale factor (scale factor instability).

As it was mentioned earlier, the stochastic errors cannot be directly quantified. Instead, what can be done is the modeling of their behaviour over time using a stochastic process. A stochastic process is defined as a discrete and finite ensemble of functions of time $\{x(t)\}$, collected with a fixed time interval Δt. This means that at any sampled time t_k, the inertial sensor noise value $x(t_k)$ represents a random variable that has been randomly drawn from a specified probability distribution (Gelb, 1974). Furthermore, such a process is usually assumed to be stationary, mean-

ing that its statistical properties (i.e., the statistics of its probability density) are invariant with respect to absolute time (Brown and Hwang, 2012). In other words, if two different chunks of data with size N are chosen in the manner demonstrated in Figure 2.1, then it should be anticipated that the average signal properties (e.g., means, autocorrelations, etc.) computed based on each of those data chunks are very similar (Orfanidis, 1988).
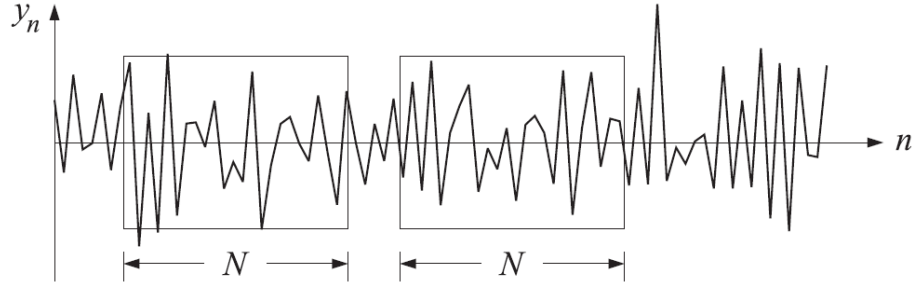
Figure 2.1: Data chunks selected from a stationary signal. (Orfanidis, 1988)

In the following segment, the most common stochastic processes used to describe the random errors of MEMS-based inertial sensors will be presented, along with their respective descriptive differential equation, discrete state-space model, and power spectral density (PSD) representation.

2.3.2.1 Gaussian White Noise (WN)

Gaussian white noise is a stationary stochastic process whose random variables are independent and identically distributed (i.i.d) based on a Gaussian distribution with zero mean and a finite variance (σ^2_{WN}). Furthermore, it has a constant power spectral density (hence the white designation), meaning that its power is uniformly distributed throughout the entirety of the spectrum and it can be utilized as the innovation sequence for the production of other random processes (Gelb, 1974). On another note, it should be mentioned that the WN process is also referred to in the navigation-related literature as angle or velocity random walk (ARW/VRW) depending on

whether it is being used to describe the gyroscope or the accelerometer measurement noise respectively.

The WN process has a correlation time that is shorter than the sampling interval Δt, it represents a high frequency noise term, and it is characterized by the rate PSD function $S_{WN}(f)$, the differential equation $\dot{X}_{WN}(t)$ and the discrete state space model X_{WN_k} (at an arbitrary time k). The mathematical models of these three quantities are provided below by equations (2.1), (2.2) and (2.3) respectively (Gelb, 1974):

$$S_{WN}(f) = \sigma^2{}_{WN}, \qquad \sigma^2{}_{WN} \in \mathbb{R}^+ \tag{2.1}$$

$$\dot{X}_{WN}(t) = W(t) \tag{2.2}$$

$$X_{WN_k} = W_k, \qquad W_k \overset{i.i.d}{\sim} \mathcal{N}(0, \sigma^2{}_{WN}) \tag{2.3}$$

2.3.2.2 Quantization Noise (QN)

The quantization error represents the small deviation between the actual amplitudes of the points that are sampled from the true analog signal (continuous) and the corresponding digitally encoded values (finite) produced by the analog-to-digital (ADC) converter (Widrow and Kollár, 2008).

The quantization error is regarded as a random process with a short correlation time and whose rate PSD expression and discrete state-space model are provided by the following equations (El-Sheimy et al., 2008; Stebler et al., 2014b):

$$S_{QN}(f) = 4q^2{}_{QN} \sin^2\left(\frac{\pi f}{\Delta t}\right)\Delta t, \qquad f < \frac{\Delta t}{2} \; and \; q^2{}_{QN} \in \mathbb{R}^+ \tag{2.4}$$

$$X_{QN_k} = \sqrt{12q^2_{QN}}\,(Y_k - Y_{k-1}), \qquad Y_k \overset{i.i.d}{\sim} U(0,1) \tag{2.5}$$

where q^2_{QN} is the defining parameter of the QN process, f is the frequency, Δt is the data interval and Y_k is a standard (i.i.d) uniform variable.

2.3.2.3 Random Walk (RW)

Random walk takes its name from the analogy of a person that at any moment can potentially move towards any arbitrary direction with a standard step length. It is defined as a zero-mean random process with long correlation time that is generated by integrating a WN process. In other words, RW consists of the sum of a sequence of WN-based random changes in a random variable, meaning that not only there is no pattern to the variations of that random variable but also that such changes cannot be predicted (Gelb, 1974; Ibe, 2013).

Based on that, the state uncertainty of the RW grows linearly with the number of generated samples (Nassar, 2003). This means that such a process is non-stationary and thus a direct derivation of a rate PSD expression is not possible. However, it is reasonable to consider that the RW process is stationary within small time intervals (Mohamed, 1999). With this in mind, an approximation to the rate PSD can be determined for the description of the RW process, the formula of which is given below (Stebler et al., 2014b):

$$\tilde{S}_{RW}(f) = \frac{\gamma^2_{RW}}{(2\pi f)^2}, \qquad \gamma^2_{RW} \in \mathbb{R}^+ \tag{2.6}$$

where γ^2_{RW} is the variance of the RW process. Furthermore, its continuous and discrete mathematical descriptions are provided by the following equations (Stebler et al., 2014b):

$$\dot{X}_{RW}(t) = W(t) \tag{2.7}$$

$$X_{RW_{k+1}} = X_{RW_k} + W_k, \qquad W_k \overset{i.i.d}{\sim} \mathcal{N}\left(0, \gamma^2{}_{RW}\right) \tag{2.8}$$

Finally, it should be highlighted that for accelerometers, the literature refers to the RW as Acceleration Random Walk (AccRW), while for gyros it is called Rate Random Walk (RRW).

2.3.2.4 Drift Ramp (DR)

Before the stochastic modeling of the inertial sensor errors, the deterministic ones must be removed via a deterministic calibration procedure. However, such task cannot realistically be perfect and because of this, there is a small fraction of systematic influence left in the data that affects the random error behaviour. To model that impact, a stochastic process called drift ramp can be utilized, which grows linearly with time, has a random variable as its growth rate and because of those properties, it is a non-stationary process.

Depending on the type of sensor measurements that are modeled, the DR can be designated as Drift Acceleration Ramp (DAccR) for accelerometers and Drift Rate Ramp (DRR) for gyroscopes, while its approximate rate PSD and discrete-state space model are given by the following equations (El-Sheimy et al., 2008):

$$\tilde{S}_{DR}(f) = \frac{\omega^2{}_{DR}}{(2\pi f)^3}, \qquad \omega_{DR} \in \mathbb{R}^+ \text{ or } \omega_{DR} \in \mathbb{R}^- \tag{2.9}$$

$$X_{DR_k} = \omega_{DR}\, \Delta t \tag{2.10}$$

where ω_{DR} is the defining parameter of the DR process and symbolizes the growth rate of the drift.

2.3.2.5 Bias Instability (BI)

Bias instability is a low-frequency noise process originated from random flickering of the sensor's electronics and it causes bias fluctuations in the data over time (Hou, 2004). Furthermore, it is strongly related to the stability of the sensor (its ability to provide the same output to the same input over a period of time for a single run) and it is usually approximated by a first-order Gauss-Markov process (See (Farrell et al., 2022) for how this is implemented in practice).

The rate PSD that describes this stationary random process along with a state-space model that could describe its behaviour are provided below (Stebler et al., 2014b):

$$S_{BI}(f) = \begin{cases} \sigma^2{}_{BI}/(2\pi f), & f \leq f_0 \\ 0, & f > f_0 \end{cases} \tag{2.11}$$

$$X_{BI_{k+1}} = \begin{cases} W_{k+1}, & \text{if } \mathrm{mod}(t_{k+1}, T_{BI}) = 0 \\ X_{BI_k}, & \text{otherwise} \end{cases}, \qquad W_{k+1} \overset{\text{i.i.d}}{\sim} \mathcal{N}(0, \sigma^2{}_{BI}) \tag{2.12}$$

where $(\sigma^2{}_{BI}, T_{BI})$ are the bias instability variance and fluctuation period, f_0 is the cut-off frequency and $\mathrm{mod}(\cdot)$ is the modulo operator.

2.3.2.6 Gauss-Markov (GM)

Random processes that are stationary and have exponential autocorrelation functions are called Gauss-Markov processes (El-Diasty and Pagiatakis, 2008). Generally, they can be used to model the behaviour of a multitude of physical processes with a good enough accuracy. For navigation applications, the 1st order Gauss-Markov (GM1) process is the one that is primarily used for the study of inertial sensor errors due to its mathematical model's simplicity and ability to describe time-correlated random errors.
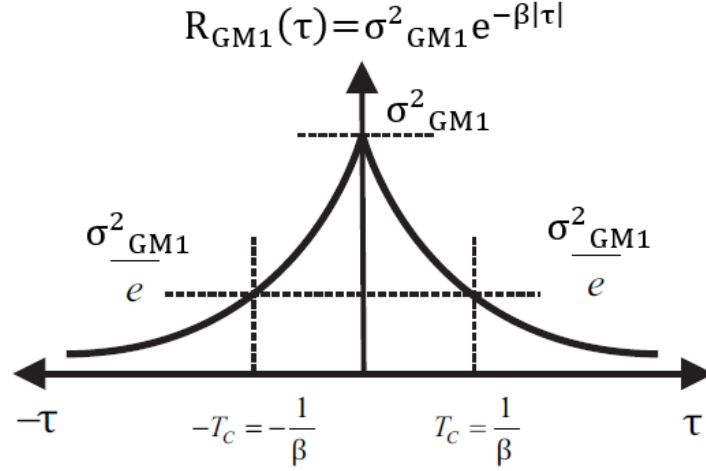
Figure 2.2: Fully characterizing (theoretical) autocorrelation function of the 1st-order Gauss-Markov stochastic process.

The autocorrelation R_{GM1} (See Figure 2.2 for graphical representation) and PSD of such process are provided by the following equations:

$$R_{GM1}(\tau) = \sigma^2{}_{GM1}\ e^{-\beta_{GM1}|\tau|} \tag{2.13}$$

$$S_{GM1}(f) = \frac{2\sigma^2{}_{GM1}\ \beta_{GM1}}{(2\pi f)^2 + \beta_{GM1}{}^2} \tag{2.14}$$

where τ is the shift in time, β_{GM1} is the inverse of the process' correlation time T_c and $\sigma^2{}_{GM1}$ is the variance of the GM1-based state. From equation (2.13 it is evident that the GM1 process it able to represent bounded uncertainty, meaning that the correlation coefficient for any time shift τ can either be less or equal to the correlation coefficient for zero time shift (Gelb, 1974).

The differential equation and discrete state-space model that describes the GM1 stochastic process are given by the equations below:

$$\dot{X}_{GM1}(t) = -\beta_{GM1}\ X_{GM1}(t) + W(t) \tag{2.15}$$

$$X_{GM1_{k+1}} = e^{-\beta_{GM1}\Delta t}\ X_{GM1_k} + W_k, \qquad W_k \overset{i.i.d}{\sim} \mathcal{N}\left(0, \sigma^2{}_{GM1}\left(1 - e^{-2\beta_{GM1}\Delta t}\right)\right) \tag{2.16}$$

where Δt is the time interval of the available data. Finally, by observing equation (2.16), it can be inferred that when the correlation time is small, the GM1 simulates a WN process, while when the correlation time is large, then the GM1 approximates a RW process.

2.3.2.7 Autoregressive (AR)

An autoregressive process is a stationary random process that makes the assumption that a signal's behaviour can be predicted from a linear combination of the past observations plus a gaussian random variable. The autoregressive process of order 1 (AR1), meaning that only one previous observation is used every time to predict the next, is most times chosen to model the time-dependent inertial sensor random error behaviour and it can be described by the following discrete state-space model:

$$X_{AR1_{k+1}} = \varphi_{AR1} X_{AR1_k} + \varepsilon_k, \qquad \varepsilon_k \overset{\text{i.i.d}}{\sim} \mathcal{N}\left(0, \xi^2{}_{AR1}\right) \tag{2.17}$$

where φ_{AR1} is the parameter that refers to the systematic part of the AR1 and $\xi^2{}_{AR1}$ is the variance of gaussian white noise ε_k that drives the process.

At this point, an important note should be made. The AR1 process is essentially a re-parameterization of the GM1 process, and they can be used interchangeably after certain considerations. Assuming that the data interval value is known and equal to Δt, then the relationships between the AR1 and GM1 defining parameters can be written as follows:

$$\varphi_{AR1} = e^{-\beta_{GM1}\Delta t} \longleftrightarrow \beta_{GM1} = -\frac{\ln(\varphi_{AR1})}{\Delta t} \tag{2.18}$$

$$\xi^2{}_{AR1} = \sigma^2{}_{GM1}\left(1 - e^{-2\beta_{GM1}\Delta t}\right) \longleftrightarrow \sigma^2{}_{GM1} = \frac{\xi^2{}_{AR1}}{1 - e^{-2\beta_{GM1}\Delta t}} \tag{2.19}$$

2.4 Summary

This chapter was devoted to a brief description of the deterministic and random errors that characterize MEMS-based inertial sensors. A particular focus however was given to the stochastic processes that are typically used to model the random error behavior. Specifically, their corresponding defining parameters, state-space model and PSD expression were presented, all of which will be used in forthcoming chapters.

Chapter Three: Deterministic and Stochastic Calibration of Inertial Sensors

3.1 Introduction

In the previous chapter it was highlighted that the inertial sensor errors can be divided into two distinct groups: the deterministic and the stochastic. The errors that belong in the first category can be evaluated through a calibration procedure, since their effects can be described in an explicit way and then removed from the measurements. That being said, the first section of this chapter will highlight the characteristics of the major deterministic calibration techniques that are available, such as the *LLF calibration*, the *6-position static and angle rate tests* as well as various *multi-position calibration methods*. As for the second category, a stochastic modeling technique has to be applied on deterministic error-free long static data, so that the behavior of the random errors over time can be modeled and then their influenced mitigated within the navigation (fusion) filter. Therefore, the second part of the chapter will be devoted to the presentation of the methods that can be used for such a task along with their respective weaknesses. Specifically, the *Autocorrelation Function (ACF)*, the *Power Spectral Density (PSD)*, the *Allan Variance Linear Regression (AVLR)*, the *Maximum Likelihood Estimator (MLE)*, the *Generalized Method of Wavelet Moments (GMWM)* and its multi-signal extensions will be mentioned.

3.2 Deterministic Calibration

In general, deterministic calibration can be defined as a procedure that compares sensor measurements with known reference information, evaluates coefficients (i.e., bias, scale factor, non-orthogonality) that force the sensor output to match with the reference values over a desired range and which are then utilized for the removal of the systematic effects from the measurement data (Chatfield, 1997; Noureldin et al., 2013). Usually, such a task is performed with high accuracy in a laboratory environment using specialized equipment (e.g., turntable), while it is also

possible to be conducted in the field, without any equipment requirement but with decreased calibration accuracy. Below, the most commonly used deterministic calibration techniques will be described.

3.2.1 LLF Calibration

This calibration technique was formally defined in the work of Salychev (1998) and in principle, it is conducted in a laboratory environment. Specifically, the IMU device is secured on a multi-axis turntable whose axes are precisely aligned with the ones of the LLF. Then, the table rotates through several different and well-known orientations, in each of which static measurements are collected. Eventually, using the LS estimation method, all the error coefficients can be derived.

Even though this calibration method offers high accuracy in the estimation of the error coefficients, it is unable to calibrate low-cost gyros. The reason behind this is related to the fact that the reference signal used in this case, the Earth's rotation rate (ω_e), is a very weak signal that cannot be detected by the low-cost gyros due to the high levels of noise that they exhibit. In addition, the equipment required for the implementation of this method is very expensive, while its efficiency is highly dependent on the alignment accuracy of the turntable's axes to the LLF, a not at all easy task to accomplish in practice (Shin and El-Sheimy, 2002).

3.2.2 6-Position Static and Angle Rate Tests

The 6-position static test is the standard laboratory technique for the deterministic calibration of inertial sensors (Titterton and Weston, 2004). It requires the placement of the IMU on a levelled surface (usually a turntable), the alignment of the sensitive axis of each inertial sensor towards the upward and downward direction along the local vertical as demonstrated in Figure 3.1

and the collection of static data in each of the 6 resulting positions (if a mutually orthogonal sensor triad is employed).
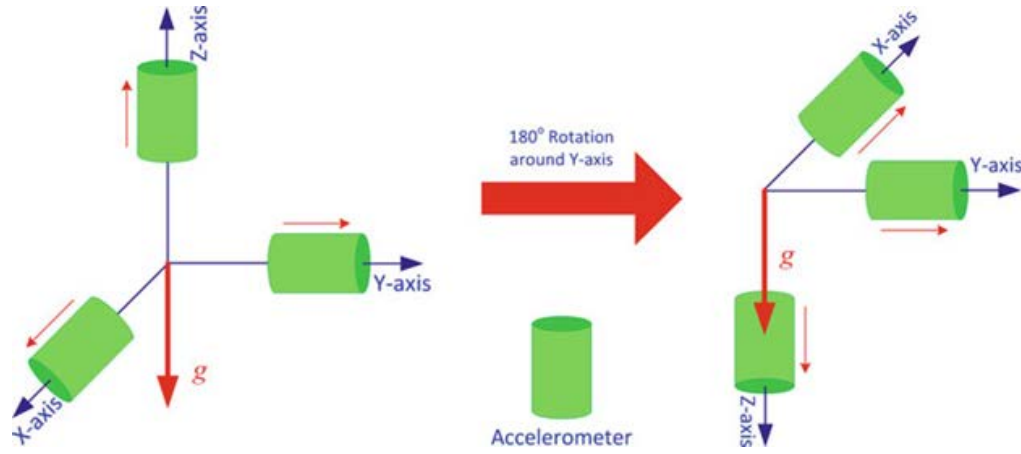
Figure 3.1: Sensitive axes of the accelerometer triad when the Z-axis is pointing upwards (left) and downwards (right), along the direction of gravity (local vertical). (Noureldin et al., 2013)

Eventually, the bias (b) and scale factor error (s) can be calculated from the following expressions (Aggarwal, 2010):

$$b = \frac{\bar{l}^{up} + \bar{l}^{down}}{2} \tag{3.1}$$

$$s = \frac{\bar{l}^{up} - \bar{l}^{down} - 2 \cdot R}{2 \cdot R} \tag{3.2}$$

where $\bar{l}^{up}$ and $\bar{l}^{down}$ are the mean values of the sensor measurements with the sensitive axis pointing upwards and downwards along the local vertical and R is the reference signal. For the case of accelerometers, R is theoretically equal to the value of gravity g at the location of the IMU but in practice, the value of normal gravity γ is utilized, as it is derived from Somigliana's formula (Wei and Schwarz, 1990) with the approximate latitude (ϕ_{IMU}) and ellipsoidal height (h_{IMU}) of the IMU as inputs. As for the gyroscopes, R is equal to the vertical component of the Earth's rotation rate at the location of the IMU ($\omega_e \sin\phi_{IMU}$) (Poddar et al., 2017).

At this point, it should be mentioned that the accuracy of this method is highly dependent on how well the surface that the IMU was placed is aligned with the local vertical. Furthermore, this technique is not only unable to estimate the misalignment (non-orthogonality) angles of the IMU, but it is also incapable of calibrating low-cost gyros due to the masking of the reference signal by the high levels of noise in the measurements (Aggarwal, 2010).

In order to allow the calculation of the non-orthogonalities along with the other error coefficients, El-Diasty and Pagiatakis (2008) proposed an improved 6-position test based on an extended measurement model that includes them and a weighted LS estimation procedure. According to that work, the accelerometer sensor triad measurements can be described in matrix form as follows:

$$
\begin{bmatrix} \tilde{f}_x \\ \tilde{f}_y \\ \tilde{f}_z \end{bmatrix} = \begin{bmatrix} s_{a,x} & m_{a,yx} & m_{a,zx} & b_{a,x} \\ m_{a,xy} & s_{a,y} & m_{a,zy} & b_{a,y} \\ m_{a,xz} & m_{a,yz} & s_{a,z} & b_{a,z} \end{bmatrix} \cdot \begin{bmatrix} f_x \\ f_y \\ f_z \\ 1 \end{bmatrix} \Leftrightarrow \tilde{f} = \mathbf{M}_c \cdot f \tag{3.3}
$$

where (f_x, f_y, f_z) are the true unknown specific force values, $(\tilde{f}_x, \tilde{f}_y, \tilde{f}_z)$ the specific force measurements, $(b_{a,x}, b_{a,y}, b_{a,z})$ the bias errors, $(s_{a,x}, s_{a,y}, s_{a,z})$ the scale factor errors and m_a the non-orthogonalities. Subsequently, the standard 6-position test data collection procedure is conducted, and the following LS problem is formed, with the $\mathbf{M}_c$ error coefficient matrix being the unknown:

$$
\mathbf{A}_{LS} = \begin{bmatrix} g & -g & 0 & 0 & 0 & 0 \\ 0 & 0 & g & -g & 0 & 0 \\ 0 & 0 & 0 & 0 & g & -g \\ 1 & 1 & 1 & 1 & 1 & 1 \end{bmatrix} \tag{3.4}
$$

$$\mathbf{W}_{LS} = \begin{bmatrix} \left(\bar{f}_{x}^{\,up}\right)_{x} - g & \left(\bar{f}_{x}^{\,down}\right)_{x} + g & \left(\bar{f}_{y}^{\,up}\right)_{x} & \left(\bar{f}_{y}^{\,down}\right)_{x} & \left(\bar{f}_{z}^{\,up}\right)_{x} & \left(\bar{f}_{z}^{\,down}\right)_{x} \\ \left(\bar{f}_{x}^{\,up}\right)_{y} & \left(\bar{f}_{x}^{\,down}\right)_{y} & \left(\bar{f}_{y}^{\,up}\right)_{y} - g & \left(\bar{f}_{y}^{\,down}\right)_{y} + g & \left(\bar{f}_{z}^{\,up}\right)_{y} & \left(\bar{f}_{z}^{\,down}\right)_{y} \\ \left(\bar{f}_{x}^{\,up}\right)_{z} & \left(\bar{f}_{x}^{\,down}\right)_{z} & \left(\bar{f}_{y}^{\,up}\right)_{z} & \left(\bar{f}_{y}^{\,down}\right)_{z} & \left(\bar{f}_{z}^{\,up}\right)_{z} - g & \left(\bar{f}_{z}^{\,down}\right)_{z} + g \end{bmatrix} \tag{3.5}$$

$$\hat{\mathbf{x}} = \mathbf{M}_{c} = (\mathbf{W} \cdot \mathbf{P} \cdot \mathbf{A}^{T}) \cdot (\mathbf{A} \cdot \mathbf{P} \cdot \mathbf{A}^{T})^{-1}, \qquad \mathbf{P}_{LS} = \sigma_{0}^{2} \cdot \mathbf{\Sigma}^{-1} \tag{3.6}$$

where $\bar{f}$ is the mean value of the specific force measurements, σ_{0}^{2} is the a-priori variance factor (usually is set to be equal to unity) and $\mathbf{\Sigma}$ is the diagonal sample Variance-Covariance (V-C) matrix.

Even though this improved version of the 6-position static test is capable to fully calibrate the accelerometer triad, it is still unable to do the same for the gyroscope triad in the case of low-cost inertial sensors. To overcome this issue, the so-called angle rate test should be employed to each of the 6 positions, with the IMU being placed on a levelled precise rate rotating table and with the sensitive axis of each sensor aligned with the rotation axis of the table each time. Then, by introducing rotations with a constant rate (e.g., 60 deg/sec) in a clockwise and counter-clockwise manner, a strong reference signal for the gyro calibration is provided and the aforementioned LS adjustment equations can be utilized for the complete low-cost gyroscope triad calibration (El-Diasty and Pagiatakis, 2008).

3.2.3 Multi-Position Calibration

The last method is the multi-position calibration, which is more flexible and cost-effective than the other methods because it does not require expensive equipment to be implemented. The literature contains many versions of this type of calibration, but they are all based on the principle that at any IMU orientation, the total sensor output (norm) should be equal to the magnitude

of the reference signal. However, this creates a problem in the gyro triad calibration because the Earth's rotation rate is a very weak signal and impossible to be sensed by low-cost gyros.

Ferraris et al., (1995) were the first ones to introduce a multi-position in-field technique for the determination of the biases and scale factors of tri-axial accelerometers and gyroscopes, without the need of any kind of equipment. To accomplish this, the authors basically suggested the implementation of a 6-position static test on an arbitrary surface and as a result, the sensitive axis of each sensor is to be very roughly aligned with the local vertical towards the upward and downward direction. However, such a method does not consider the axes misalignment errors and obviously, it cannot provide any guarantees about whether the sensitive axis of each sensor has been accurately aligned with the direction of the reference quantity (gravity or the Earth's rotation rate).

Shin and El-Sheimy (2002) extended the multi-position scheme considering the axes misalignment parameters and suggested that the estimation of the error coefficients should be conducted via an optimization framework using iterative LS adjustment. Furthermore, such a process requires the inversion of a matrix and in order to be able to provide reliable results, the number of different positions needs to be greater than the number of unknown error coefficients that need to be estimated. Therefore, the authors suggested the generation of 26 different positions by placing each face, side and corner of the IMU vertically, towards the upward and downward direction. Even though this method was shown to be highly efficient in fully calibrating the accelerometer triad of low-cost IMUs, it is unable to provide a reliable estimation for the gyro scale factors and non-orthogonalities due to observability issues of the reference quantity.

Later, Zhang et al., (2009) attempted to enhance the preceded multi-position calibration methods by evaluating the misalignments between the accelerometer and the gyroscope triads. To do

so, the differences between the rotational axis direction measurements as they were independently derived from the accelerometer and gyroscope triads were utilized. Moreover, the authors proposed a near-optimal calibration scheme by maximizing the sensitivity of the norm of the IMU measurements with respect to the calibration parameters. Finally, it should be highlighted that although this method was found to outperform the traditional laboratory method described in (Xiao et al., 2008) (24-position scheme for accelerometer parameters and gyro biases and a 3-axis rotation scheme for the gyro scale factors and non-orthogonalities), the calibration of the gyro triad requires the use of a turntable, a fact that makes this method reliant on external equipment.

Nieminen et al., (2010) continued the work of Syed et al., (2007), who utilized a turntable in order to enhance the method of Shin and El-Sheimy (2002) and fully calibrate the low-cost gyro triad, by including cross-axis correlation terms to the considered error coefficients. Specifically, this technique exploits the large range of centripetal accelerations caused by different rotation rates introduced by the employed turntable, while simultaneously compensating many different error sources. In addition, the proposed method considers the IMU as a black box, meaning that it does not require any a-priori knowledge about the properties of the IMU and its characteristics. Finally, the authors state that the suggested approach is less prone to errors, exploits more accurate sensor models and provides a better accuracy than the methods proposed by Syed et al., (2007) and the traditional ones, since it calibrated the IMU for different dynamic ranges.

Finally, a very interesting research by Li et al., (2012) proposes a simple and efficient in-situ calibration method for smartphone low-cost MEMS-based IMUs that requires no expert knowledge on how to perform or specialized equipment. Specifically, the Kalman Filter (KF)-based loosely coupled INS/GNSS navigation algorithm is employed, where when the GNSS ob-

servation is available, it can be used to calibrate the IMU biases and scale factors and when it is not, they are replaced by a kind of pseudo-observations that are related to the limited movement of the IMU in the user's hands. Eventually, the hand motions introduce sufficient dynamic conditions that allow the estimation of the IMU biases and scale factors within just 30 seconds and with sufficient accuracy. However, the non-orthogonalities are not considered, since the modern MEMS manufacturing technology makes these errors smaller than others, relatively time-invariant and possible to control.

3.3 Stochastic Calibration

After the removal of the systematic (deterministic) errors from the inertial sensor measurements, the effects of the random errors should also be considered. The reason for this is because they are a major contributing factor to the rapid drift of the INS standalone performance, especially in the case of low-cost and consumer grade MEMS-based inertial sensors. In addition, the literature suggests that the operating conditions like the temperature and the dynamics have a non-negligible impact on the behaviour of the random errors, which is why their influence should also be taken into account (Aggarwal et al., 2008a; Radi et al., 2018).

The procedure of obtaining knowledge regarding the behaviour of the random errors associated with the inertial sensor (accelerometers, gyroscopes) output is designated as "stochastic calibration". A typical setting for the implementation of such task is: a) the placement of the IMU that contains the sensors on a pre-levelled surface, b) the acquisition of long data (e.g., 3hr) under different temperature and dynamic conditions, c) the removal of the systematic error influence using the calibration coefficients estimated by a deterministic calibration method (See paragraph 3.2) and d) the utilization of the deterministic error-free data in the context of a stochastic

modeling technique in order to quantify and model the error behavior using a stochastic process under each specific condition and for each sensor.

Following that procedure, the derived state-space models characterizing the errors of the sensors are included within the navigation algorithm in order to allow recursive compensation for their effects (Stebler et al., 2011). However, the noise that governs the low-cost inertial sensor measurements presents a rather complex spectral structure. Therefore, it is highly possible that a multitude of stochastic processes would have to be utilized for each individual sensor, since one might not be enough to describe the random error behaviour throughout the entirety of the observed noise's spectrum.

Generally, there are several mathematical tools that can be used to perform the random error analysis of the data collected for stochastic calibration purposes. The most commonly used ones will be presented below, along with their respective characteristics as well as a brief literature review.

3.3.1 Autocorrelation Function (ACF)

The Autocorrelation Function (ACF) is a continuous time-domain statistical metric that describes the behavioral change of the correlation between the signal under analysis and a phased version of itself (*linear convolution*) and it is able to detect repeating patterns in that signal (Smith, 1999). Assuming that the input signal is a stationary random process $X(t)$, then its corresponding ACF would be given by the following formula (Brown and Hwang, 2012):

$$R_X(\tau) = E\{X(t)X(t+\tau)\} = \text{average}\left[\sum_{t=-\infty}^{\infty} X(t)\,X(t+\tau)\right] \qquad (3.7)$$

where R_X is the ACF of the random process $X(t)$, $E\{\cdot\}$ denotes the mathematical expectation, t is an arbitrary time value and τ is the time shift from one sample to another. However, in practice, it is only possible to collect discrete-time signals. Instead, the Autocorrelation Sequence (ACS) should be evaluated, which is derived by replacing the time t in equation (3.7) with the sampling sequence k and the time shift τ with the sampling interval d. Therefore, the equation that provides the ACS is (Orfanidis, 1988):

$$R_X(m) = E\{X(k)\, X(k+d)\} = \text{average}\left[\sum_{k=-\infty}^{\infty} X(k)\, X(k+d)\right] \tag{3.8}$$

The statistical autocorrelation values delivered by equation (3.8) are based on an ensemble averages approach that requires an infinite (discrete) dataset for their calculation, which is impossible to collect in reality. Instead, the stationarity assumption that has already been made permits the calculation of an approximation to the ACS that uses a finite data chunk $(y_0, y_1, \ldots, y_{N-1})$ of length N and *time averages*. Such an approximation is referred as *sample autocorrelation* and it is provided by the following equation (Orfanidis, 1988):

$$\widehat{R}_X(d) = \frac{1}{N}\sum_{k=0}^{N-1-d} y_k\, y_{k+d}, \qquad 0 \leq k \leq N-1 \tag{3.9}$$

In the inertial navigation field, the ACS method has been primarily used for the defining parameter estimation of Gauss-Markov processes (used to model the inertial sensor random errors) by fitting long static inertial sensor measurements (after the deterministic calibration has been conducted and the mean value has been subtracted) to their respective fully characterizing autocorrelation expression (Gelb, 1974). In addition, the ACS can also be used in the context of the Yule-Walker/autocorrelation method, where the parameters of Autoregressive processes (AR) of

any order can be optimally estimated by solving a set of linear normal equations (Makhoul, 1975). However, the choice of the AR order should be made carefully, since if the derived model that is to be included within the navigation algorithm (usually a Kalman Filter) is of a high order, then destabilization is very possible (Nassar and El-Sheimy, 2005).

Generally, there are numerous studies, where the ACS technique and either a GM1 or an AR (of order 1 or higher) was utilized in order to stochastically analyze the inertial sensor measurements produced by tactical-grade, navigation-grade or consumer-grade IMUs (Niu et al., 2002; Nassar and El-Sheimy, 2005; Georgy et al., 2010; Yuksel et al., 2010; Li et al., 2015). Moreover, it can be utilized as a tool to determine the existence of colored noise within the analyzed signal (Guerrier et al., 2012). However, the correlation method suffers from several weaknesses that make it unreliable for the task of stochastic modeling of inertial sensors, especially when dealing with low-cost ones. Specifically, it assumes that the input signal is stationary in nature, something that, as it will be shown in a later chapter, might not always be the case in practice. In addition, Quinchia et al., (2013) identified that the performance of the ACS-based methods depends highly on the size of the signal under analysis and concluded that it is unlikely that an accurate ACS can be obtained from experimental data since they will always be limited and finite. On another note, Nassar, (2003) highlighted the fact that the input sequence to an ACS-based method has to be outlier-free and which is why it has to be pre-filtered (e.g., wavelet de-noising). However, such a procedure always contains the risk of removing useful information along with the outliers. In order to counter this problem, several robust estimators of the autocorrelation have been introduced (e.g., Ma and Genton, 2000), which even though they manage to be less influenced by the existence of extreme measurements (outliers), their efficiency appears to be noticeably decreased. Finally, it should be mentioned that the ACS method does not investigate the in-

put signal in order to study its unique random behavior. Instead, it can only estimate coefficients of a chosen type of stochastic process, whose theoretical ACS expression can be mathematically derived.

3.3.2 Power Spectral Density (PSD)

The PSD is the primary method for representing the frequency-domain expression of any periodic or non-periodic signal as well as for studying its spectral content and variations (Hou, 2004). Assuming a stationary and ergodic (the statistical properties of the stochastic process can be identified from a single realization) random process $X(t)$, its PSD S_X is mathematically defined as the Fourier Transformation (FT) of its fully describing autocorrelation function R_X and thus the following Wiener-Khinchine relation applies (Brown and Hwang, 2012):

$$S_X(f) = \mathcal{F}\{R_X(t)\} = \int_{-\infty}^{\infty} R_X(\tau)e^{-2j\pi f\tau}d\tau, \qquad -\infty < f < +\infty \qquad (3.10)$$

where S_X is in units^2/Hz if X(t) is measured in units, $\mathcal{F}\{\cdot\}$ is the FT operator, j is the imaginary unit and f is the frequency in Hz. However, due to the stationarity of the $X(t)$ process, the integral above does not converge. Instead, in order to ensure integrability, the Fourier transform should be applied to a (finite) sample realization of the truncated process in the interval $[0, T]$ that is denoted as $X_T(t)$. Therefore, while also taking into account the fact that it is generally convenient to specify the PSD as a one-sided function, for any particular sample realization of $X_T(t)$, the following expression is defined as its periodogram (IEEE Std 1293, 2018):

$$\tilde{S}_{X_T}^1(f) = \frac{1}{T}\left|\mathcal{F}\{R_{X_T}\}\right|^2 = \frac{1}{T}|X(f)|^2, \qquad f \geq 0 \qquad (3.11)$$

where T is the data record span and $X(f)$ is the continuous FT of the autocorrelation function and

by averaging over an ensemble of periodograms for a large span of time, the PSD can be derived (Heinzel et al., 2002).

The considerations that have been made so far require the collection of continuous and infinite data, something that is impossible to achieve in practice, on both accounts. Consequently, assuming that x_k $(k = 0,1, ..., N - 1)$ discrete and finite experimental data observing a stationary random process have been collected at uniform time intervals Δt, the one-sided discrete periodogram can be evaluated using the following formulas (IEEE Std 1293, 2018):

$$\tilde{S}_X^1(f_j) = \frac{\Delta t^2}{T} |X_j|^2, \qquad j = 0,1, ..., \left\lfloor \frac{N}{2} \right\rfloor - 1, \qquad f_j = \frac{j}{2T} \tag{3.12}$$

$$\tilde{S}_X^1(f_{\lfloor N/2 \rfloor}) = \begin{cases} \dfrac{\Delta t^2}{T} |X_{\lfloor N/2 \rfloor}|^2, & \text{if } N \text{ is odd} \\ \dfrac{\Delta t^2}{2T} |X_{\lfloor N/2 \rfloor}|^2, & \text{if } N \text{ is even} \end{cases} \tag{3.13}$$

where N is the sample size (let it be a power of 2) and X_j is the Discrete Fourier Transform (DFT) of the autocorrelation sequence, evaluated using the collected x_k data.

In practical applications, one of the most popular methods for the calculation of the PSD from experimental data is the Welch's Overlapped Segmented Average (WOSA) method (Welch, 1967). According to that, a long data record should initially be collected, its corresponding ACS calculated using equation (3.9) and its mean value removed from its entirety (Orfanidis, 1988). Then, the resulting data are subdivided into shorter overlapping segments. The larger the length and amount of these segments, the higher the frequency resolution of the PSD estimate, and the improvement of its statistical stability is achieved. Following that, a *window function* (see Heinzel et al., (2002) for an overview of the available window functions) is applied to each of those segments in order to reduce the impact of the *spectral leakage* phenomenon, caused by the

periodicity assumption of the DFT, which will be utilized in the next step (Orfanidis, 1988). However, it should be highlighted that since these functions involve some form of compromise between the resulting peak in the frequency domain, the amplitude accuracy and the reduction rate of spectral leakage, uncertainty is unavoidably introduced into the evaluated spectrum (Heinzel et al., 2002). Finally, using the DFT equations (3.12) and (3.13), the periodogram of each window segment is computed and the derived periodograms are averaged together (*ensemble averaging*) in order to obtain the final PSD estimate (Heinzel et al., 2002).

For the case of performing stochastic analysis of accelerometer/gyroscope random errors using the PSD method, an acceleration domain PSD for an accelerometer or an angle rate domain PSD for a gyroscope has to be computed, which require a simple modification of the aforementioned PSD estimate (See Hou, (2004) for how this is implemented). Then, the PSD is plotted in a log-log plot where the x-axis shows the frequency values, and the y-axis contains the corresponding discrete (one-sided) PSD values. Using the derived plot, a slope analysis is performed and through which it is possible to identify stochastic processes that describe the random error behaviour in different parts of the spectrum. Specifically, the stochastic processes that can be identified are random walk (rate/acceleration random walk), bias instability, drift ramp, white noise (angle/velocity random walk) and quantization noise, with the characteristic slopes of each shown in Figure 3.2. However, it is highlighted that because the random walk and drift ramp processes have the same theoretical slope in the PSD plot, they cannot be distinguished using frequency domain analysis.
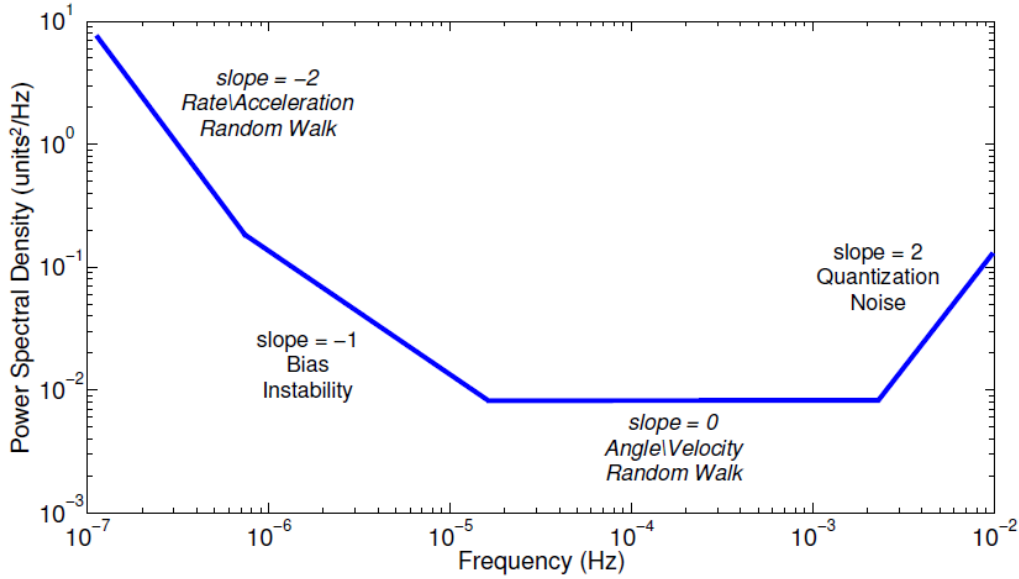
Figure 3.2: Theoretical one-sided PSD slopes of identifiable stochastic processes. (adapted from Quinchia et al., (2013))

In practice, where real data are utilized, gradual transition would exist between the different PSD slopes, rather than the sharp ones shown in Figure 3.2 and the slopes might be different than the -2, -1, 0 and +2 values. Therefore, it is evident that a certain amount of noise would always exist in the plot curve due to the uncertainty of the measured PSD. Furthermore, it is very common that due to the density of the high frequency data points in the log-log PSD plot, challenges might arise in the identification of the random processes. Hence, instead of the ensemble averaging approach, the *frequency averaging* technique (IEEE Std 1293, 2018) can be used instead, which is able to reduce the amount of points in the PSD estimate and thus make the process identification easier. Finally, it should be mentioned that the various slopes of the PSD log-log plot can either be estimated by eye (and thus the frequency averaging technique should be employed) or through a LS fit of the following function to the estimated PSD curve:

$$\frac{A_1}{f^2} + \frac{A_2}{f} + A_3 + A_4 f^2 \tag{3.14}$$

where f is the frequency and A_1, A_2, A_3 and A_4 are the random walk, bias instability, white noise, and quantization noise characteristic parameters respectively.

In the inertial navigation literature, the PSD method has been utilized for the stochastic analysis of inertial sensor measurements provided by low-cost MEMS-based IMUs (Petkov and Slavov, 2010; Quinchia et al., 2012; D'Alessandro et al., 2017) as well as for validating the consistency of higher level stochastic modeling techniques like the AVLR. However, although the PSD method can determine the high frequency noise components (i.e., WN) with great accuracy, it has certain limitations that make it unattractive for applications where high accuracy is required and the signals have a complex spectral structure (low-cost MEMS-based inertial sensor noise). Firstly, the PSD method assumes that the input signal is stationary, something that as it will be shown later, it is not always valid in practice. Secondly, the identification of low-frequency noise parameters is characterized by an estimation accuracy deficit since the low-frequency part of the PSD contains information with significantly elevated uncertainty (Hou, 2004). Third, the PSD method does not have a way to protect its estimation quality from the existence of outliers in the input signal and thus some form of de-noising must be conducted prior to the processing. And finally, the PSD slope analysis is unable to identify correlated noise terms, which can be very impactful to the standalone operation of low-cost and consumer grade inertial sensors if they are not considered.

3.3.3 Maximum Likelihood Estimator (MLE)

Practically, the random errors of inertial sensor measurements are often issued from a latent composite process (i.e., a process composed of a sum different underlying processes). The MLE is a widely used approach, which through the expectation-maximization (EM) algorithm (Demp-

ster et al., 1977) within a KF is able to optimally estimate the coefficients of that composite process (Huang et al., 2007; Zhu et al., 2021).

In the work by Stebler et al., (2011), an automation of this process by maximizing the likelihood function of the assumed state-space models under investigation (i.e., proposals for the true/unknown error generating model) using a constrained version of the EM algorithm was proposed. Furthermore, the authors highlighted the increased generality of the method compared to the AVLR as well as its ability to estimate models (albeit relatively simple) on which the AVLR identification fails. Unfortunately, even though the MLE is a statistically sound and efficient estimator, it was identified that it becomes numerically unstable when the size of the observed random process is large and the complexity of the model increases (e.g., sum of several AR1 processes), meaning that it gets very sensitive to the selection of the initial parameter approximation and that the convergence to a global minimum is no longer guaranteed.

In another research, Zhao et al., (2011) put forward a nonlinear adaptive KF to improve the estimation results, while Nikolic et al., (2016) proposed a log-sampling strategy with the same purpose in mind but without, however, solving either the numerical instability nor the convergence problems.

Finally, with the aforementioned in mind as well as of the fact that such procedure can be very computationally intense (Balamuta et al., 2018), the practical applicability of the MLE to the stochastic modeling of inertial sensor errors is indirectly established (Guerrier et al., 2013a).

3.3.4 Allan Variance Linear Regression (AVLR)

The AVLR is a time-domain technique that was proposed by Allan, (1966) for the purpose of studying the phase and frequency instability of precision oscillators. Later, the IEEE Std, (1999) introduced the AVLR as a method for the identification and quantification of the random noise

exhibited by linear accelerometers, while Hou and El-Sheimy, (2003) were the first to apply it for the stochastic calibration of MEMS-based inertial sensors. Nowadays, datasheets provided by the manufactures typically utilize AVLR-derived information in order to characterize the anticipated IMU performance (Farrell et al., 2022).

Through the AV quantity, the root mean square (RMS) random drift error is expressed as a function of the averaged times and the study of its behaviour permits the knowledge inference about the underlying stochastic processes as well as the study of their individual contribution to the total noise statistics of the analyzed (error) signal.

The calculation of this method's fundamental quantity, the AV, is based on cluster analysis of the data at hand. Generally, there are several different ways for how the clusters can be created (i.e., selection of stride step and cluster length), with each of which leading to a different variant of the method (See (Riley and Howe, 2008) for an overview of the available variants). One of the most frequently used and asymptotically most efficient is the Maximal Overlap Allan Variance (Greenhall, 1991), which although it manages to provide an instability estimate with enhanced confidence, its computational burden is significantly increased compared to the ordinary AV (Li and Fang, 2013a). The algorithm for its calculation is presented below:

1) Assuming that a long inertial sensor measurement sequence $X_1, \ldots, X_T$ has been collected for calibration purposes with sampling time t_0 and length T and that the influence of the deterministic errors has been removed via deterministic calibration. Then, divide this time series into clusters with size τ ($1 \leq \tau \leq T/2$) in the manner shown in Figure 3.3. The calculation of the AV requires the use of different cluster lengths, each of which corresponds to a different AV curve point. A standard choice for them is $\tau = 2^i$, where $i = 1, \ldots, J$ and $J = \lfloor \log_{10}(T)/\log_{10}(2) \rfloor - 1$
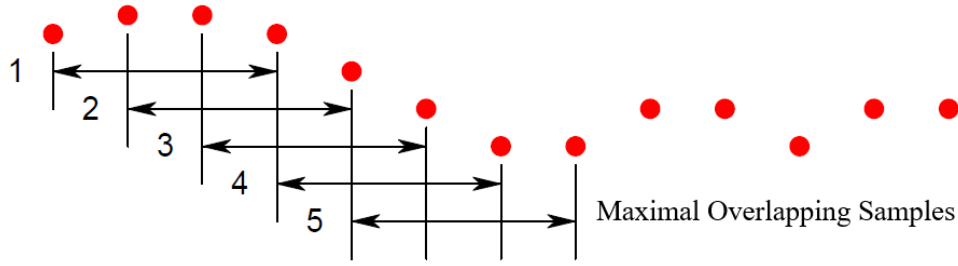
Figure 3.3: Maximal overlap cluster sampling for the evaluation of the AV. (adapted from Riley and Howe, (2008))

2) For the smallest cluster length ($\tau = 2$), calculate the mean value $\bar{y}_j$ of each created cluster

using the formula $\bar{y}_j = (1/\tau)\sum_{t=j}^{\tau+j-1} X_t$, for $j = 1, \dots, T - \tau + 1$

3) Evaluate the total cluster number $M_{AV} = T - 2\tau + 1$

4) Compute the maximal overlapped AV value using the following formula (Greenhall, 1991):

$$\sigma^2{}_{AV}(\tau = 2) = \frac{1}{2M_{AV}} \sum_{k=1}^{M} [\bar{\Omega}_k(\tau) - \bar{\Omega}_{k-\tau}(\tau)]^2 \tag{3.15}$$

where $\bar{\Omega}$ denotes the mean value of the measurements included in the cluster at hand.

5) Repeat steps 2-5 for the different cluster lengths, going from the smallest ($\tau = 2$) to the largest value ($\tau = 2^J$). This permits the instability study for different correlation time scales.

6) Calculate the Allan Standard Deviation (ADEV) by taking the square root of the AV for every scale. Then, determine their pointwise estimation quality through the equation:

$$\text{error}_{ADEV}\left(\tau = 2^{i=1,\dots,J}\right) = \frac{1}{\sqrt{2\left[\frac{T}{\tau} - 1\right]}} \tag{3.16}$$

and from which it is evident that as the number of clusters increases, the more accurate the estimation of the ADEV becomes.

7) Create a log-log plot to represent the ADEV (σ_{AV}) curve with respect to the cluster times τ, which in turn will be used to perform the stochastic analysis of the input signal.

Subsequently, the identification and quantification of the different stochastic processes is conducted by performing independent regressions (based on a LS approach) on the visually identified linear regions of the σ_{AV} log-log plot. The reason why this is possible it because there is a unique relationship between the AV $\left(\sigma^2_{AV}(\tau)\right)$ and the rate PSD $\left(S(f)\right)$ of the underlying stochastic processes (assumed to be stationary), which is given below (El-Sheimy et al., 2008):

$$\sigma^2_{AV}(\tau) = 4 \int_0^\infty S(f) \cdot \frac{\sin^4(\pi f \tau)}{(\pi f \tau)^2} \cdot \mathrm{d}f \qquad (3.17)$$

Generally, the (statistically independent) processes that are considered by this method are the ones that produce power-law noises with linear ADEV representation and more specifically WN, RW, QN, BI and DR. The characteristic σ_{AV} slopes of each of those processes as well as their respective theoretical value (See (Tehrani, 1983; Zhang, 2008) for the detailed derivations) are provided in Table 3.1. Also, it should be mentioned that it is possible to identify the existence of time-correlated and sinusoidal noise through the AVLR. However, due to the fact that such processes have a rather complex AV expression, they cannot be rigorously estimated using this approach (Guerrier et al., 2013b) and thus they will not be considered here.

The relevant research literature regarding the application of the AVLR focuses on either the study of the random error behaviour of the inertial sensor errors with respect to certain conditions (i.e., normal, varying temperature or dynamics) (e.g., see (El-Diasty et al., 2007; Aggarwal et al., 2008b; El-Sheimy et al., 2008; Li and Fang, 2013b; Hussen and Jleta, 2015; Miao et al., 2015; Yuan et al., 2016)) or the investigation of the contribution of such knowledge in a KF-

based INS/GNSS loosely coupled integration practical setting (e.g., see (Zhiqiang Xing and Ge-bre-Egziabher, 2008; Han et al., 2009; Moafipoor et al., 2011; Hidalgo et al., 2012; Zhang et al., 2013; Quinchia et al., 2013; Hidalgo-Carrió et al., 2016)). In the latter case, the results from eve-ry one of these studies show a considerable improvement to the overall performance compared to the conventional considerations (e.g., simple, and manually tuned AR1 models), a fact that par-ticularly highlights the significance of considering accurate modeling of the inertial sensor noise in the navigation algorithms. Finally, it is noticed that all the available works utilize the EKF to include the derived inertial sensor error stochastic modeling knowledge and thus allow for their online compensation. However, it hasn't really been investigated whether the use of a less-restrictive filter like the UKF along with the improved stochastic modeling for the inertial sensor random drift could potentially provide an even better performance.

Table 3.1: Properties of identifiable stochastic processes by the AVLR analysis. (El-Sheimy et al., 2008; Zhang, 2008)

Stochastic Process	Coefficient	$\sigma_{AV}(T)$	Theoretical Slope
QN	Q_z	$Q_z\sqrt{\dfrac{3}{T^2}}$	-1
WN	N	$N\sqrt{\dfrac{1}{T}}$	$-1/2$
BI	B	$B\sqrt{\dfrac{2\ln 2}{\pi}}$	0
RW	K	$K\sqrt{\dfrac{2T^2+1}{6T}}$	$+1/2$
DR	R	$R\left(\dfrac{T\sqrt{2}}{2}\right)$	$+1$

In the research by Li and Fang, (2013), the authors proposed the integration of a not fully overlapping approach for the implementation of the cluster sampling into the calculation algo-

rithm of the Allan Variance and Total Variance (TV) quantities. Briefly, the TV (Han et al., 2007; IEEE Std 1139, 2009) is an extension of the AV that uses the maximal overlapping cluster samples and manages to improve the estimation accuracy in long cluster times but its computational burden is quite heavy. The resulting estimators were shown to be less computationally intensive than their fully overlapping counterparts, while managing to maintain a similar performance. Consequently, this work provides the attribute of computational efficiency to the AV and TV methodologies and thus is very beneficial for the task of stochastically modeling inertial sensor errors, where long datasets must be utilized for the inference of an accurate solution. Furthermore, the authors proposed a way for the additional improvement in analysis efficiency and parameter estimation accuracy by using different AV/TV variants based on their individual advantages in order to study the short, middle, and high cluster times respectively.

A very interesting application of the AVLR was presented by Niu et al., (2014), where positioning solution errors derived by three different processing strategies, Single Point Positioning (SPP), Precise Point Positioning (PPP) and Differential GNSS (DGNSS) were stochastically studied. From that analysis, the authors noticed that the random behavior of each one of them is rather complex as well as that there are considerable differences (both in terms of model structure and parameter value) not only between each processing strategy but also between different data rates. As a result, the common assumption made by the navigation community that the positioning errors are just white noise was formally debunked and highlighted that the adoption of more detailed and complex models instead, can potentially provide significant contributions to the improvement of GNSS positioning methods and applications.

In another research work by Wang et al., (2018), the AVLR was utilized for the purpose of boosting the MEMS-based INS/GNSS navigation performance from two separate aspects. The

first one referred to the stochastic analysis of the inertial sensor errors using the AVLR instead of the regularly used (and manually tuned) AR models and the inclusion of the derived knowledge within the navigation filter (e.g., Kalman Filter) to allow recursive error compensation. As for the second, it was introduced at the level of GNSS for the error covariance adaptive estimation, which subsequently was incorporated within an innovation-based robust KF (Yang et al., 2001; Yang and Gao, 2006). The navigation performance of the fused algorithm that includes both levels of improvement was evaluated in a case study, where information from either DGNSS or SPP mode were used as the auxiliary source within the integration filter. Eventually, from the analysis of the results, the authors observed a considerable improvement compared to the analogous conventional counterparts, something that once again confirmed the importance of using accurate stochastic modeling knowledge in the context of navigation applications.

Despite the apparent popularity of this approach due to its simplicity and straightforwardness in the navigation field, it suffers from certain weaknesses that do not justify its widespread use. Specifically, Guerrier et al., (2016) provided sound mathematical evidence about the statistical inconsistency of the AVLR method when estimating the parameters of composite stochastic processes. This is something that is directly related to the difficulty of the AVLR in separating the random processes in the spectral domain, especially for the case of multiple underlying GM1s (Stebler et al., 2012). And since in low-cost inertial sensor applications, the signals typically present a very complex spectral structure (i.e., existence of multiple time-correlated processes), the utilization of the AVLR should be avoided. In addition to that, the AVLR, just like all the stochastic modeling methods that have been mentioned so far, utilizes a single signal to conduct its analysis. This means that it implicitly makes a stationarity assumption, something that as it will be shown later, might not be the case when stochastically studying signals produced by low-cost

and consumer-grade equipment. And last but not least, it is important to mention that the AVLR does not have a robust feature and thus it is unable to handle data infected with outliers without significantly compromising the accuracy of the derived stochastic modeling information. That is why, in order to evade such an occurrence, it is common practice to pre-filter the available data before they are inputted into the AVLR for processing (Hou, 2004). However, a significant drawback from that would be that along with the removal of the outliers, the useful information carried by the signal will probably be diluted.

3.3.5 Generalized Method of Wavelet Moments (GMWM)

The GMWM[1] was formally proposed by Guerrier et al., (2013a) and it represents the most recent approach for the accurate identification of the underlying stochastic processes that comprise the random drift generating function of a single input (error) signal as well as the efficient estimation of their corresponding defining parameters. It belongs to the Generalized Method of Moments (GMM) estimator family (Hansen, 1982) and it utilizes the Generalized Least Squares (GLS) principle along with wavelet multiresolution analysis in order to optimally estimate the coefficients of a candidate composite stochastic model that can be characterized by high complexity. Moreover, this estimator is statistically consistent (i.e., converges in terms of probability to the truth as the considered sample size tends to infinity) and asymptotically normally distributed (i.e., the distribution of the estimator converges to a normal distribution as the considered sample size increases) with comparable finite sample performance to the MLE (Guerrier et al., 2013a), it has been formally shown to outperform the AVLR in terms of efficiency (Guerrier et al., 2020) and it is also computationally efficient (Balamuta et al., 2018). Finally, it is highlighted that the GMWM makes an intrinsically stationarity assumption, which means that if a suitable transformation of the input dataset is applied, which here is the first-order differences, then the

---

[1]The GMWM "R" package: https://github.com/SMAC-Group/gmwm

outcome would be stationary.

According to Guerrier et al., (2013a), the GMWM operates under the assumption that the true (unknown) error generating function is the summation outcome of multiple independent and additive Gaussian stochastic processes. However, there is a certain condition that applies here. The processes QN, WN, RW and DR can only be included once in the composite model of the generating function, while the AR1/GM1 processes can be included multiple times. Therefore, with this in mind, the two-step algorithm of the GMWM is presented below:

1) Assuming that a long discrete data sequence Y_t of static inertial sensor measurements has been collected at a sufficiently large data rate f (e.g., 100Hz) and that the influence of the deterministic errors has been removed. Then, evaluate the empirical (equation (3.18)) and model-implied wavelet variances (WVs) (equation (3.19)) by utilizing the sequence Y_t and the candidate model correspondingly (Percival, 1995; Serroukh et al., 2000; Percival, 2002):

$$\hat{v}_j^2 = \frac{1}{M_j} \sum_{t=1}^{M_j} W_{j,t}^2 \tag{3.18}$$

where $\hat{v}_j^2$ is the classical empirical WV, T the length of the input signal, $M_j = T - \tau_j + 1$ the wavelet coefficient ($W_{j,t}$) length at scale τ_j, j is the wavelet decomposition level with $j_{max} = \lfloor \log_2 T \rfloor - 1$, $\lfloor \cdot \rfloor$ is the floor operator, $\tau_j = 2^j$ are the Haar wavelet scales, $W_{j,t} = \sum_{l=1}^{\tau_j} h_{j,l} Y_{t-l}$ are the wavelet coefficients derived by applying the Maximal Overlap Discrete Wavelet Transform (MODWT) to the input data sequence Y_t and $h_{j,l} = 1/\tau_j$ are the MODWT Haar wavelet filters (See Mallat, (1999)).

$$v_j^2(\boldsymbol{\theta}) = \int_{-1/2}^{1/2} S_{w_j}(f) df = \int_{-1/2}^{1/2} \text{mod}\left(H_j(f)\right)^2 S_{F_\theta}(f) \, df \tag{3.19}$$

where $v_j^2(\boldsymbol{\theta})$ is the model-implied WV, S_{w_j} is the wavelet coefficient PSD, $\text{mod}(\cdot)$ is the modulus operator, $H_j(f)$ is the transfer function of the MODWT wavelet filter $h_{j,l}$, $\boldsymbol{\theta}(p \times 1)$ is the vector that contains the defining parameters of the candidate model with $\boldsymbol{\theta} \in \boldsymbol{\Theta} \subset \mathbb{R}^p$ and $\boldsymbol{\Theta}$ assumed to be a compact set, $F_{\boldsymbol{\theta}}$ is the candidate/tested random drift generating model and $S_{F_{\boldsymbol{\theta}}}$ its implied PSD expression. The PSD and Haar WV expression for each of the processes considered by the GMWM are provided in Table 3.2.

Table 3.2: Properties of the stochastic processes that are utilized by the GMWM framework.

Stochastic Process	PSD $S(f)$	Theoretical Haar WV $v_j^2(\boldsymbol{\theta})$
QN	$4q^2_{\text{QN}} \sin^2\left(\frac{\pi f}{\Delta t}\right) \Delta t, f < \frac{\Delta t}{2}$	$\dfrac{6q^2_{\text{QN}}}{2^{2j}}$
WN	σ^2_{WN}	$\dfrac{\sigma^2_{\text{WN}}}{2^j}$
RW	$\dfrac{\gamma^2_{\text{RW}}}{(2\pi f)^2}$	$\dfrac{(2^{2j} + 2)\,\gamma^2_{\text{RW}}}{12 \cdot 2^j}$
DR	$\dfrac{\omega_{\text{DR}}}{(2\pi f)^3}$	$\dfrac{2^{2j}\,\omega_{\text{DR}}^2}{16}$
AR1	$\dfrac{\xi^2_{\text{AR1}}}{1 + \varphi_{\text{AR1}}^2 - 2\varphi_{\text{AR1}} \cos(2\pi f)}$	$\dfrac{\left[(\varphi_{\text{AR1}}^2 - 1)2^j + 2\varphi_{\text{AR1}}\left(-4\varphi_{\text{AR1}}^{2^{j-1}} + \varphi_{\text{AR1}}^{2^j} + 3\right)\right]\xi^2_{\text{AR1}}}{(\varphi_{\text{AR1}} - 1)^3(1 + \varphi_{\text{AR1}})\,2^{2j}}$

2) Solve the minimization problem of the distance between the empirical and model-implied WV using the GLS in order estimate (optimally) the defining parameter values of the candidate model. The equation that expresses this problem is given below:

$$\widehat{\boldsymbol{\theta}} = \operatorname{argmin}_{\boldsymbol{\theta} \in \boldsymbol{\Theta}} \left(\widehat{\boldsymbol{v}} - \boldsymbol{v}(\boldsymbol{\theta})\right)^T \widehat{\boldsymbol{\Omega}} \left(\widehat{\boldsymbol{v}} - \boldsymbol{v}(\boldsymbol{\theta})\right), \qquad (3.20)$$

where $\widehat{\boldsymbol{\theta}}$ is the vector that contains the model parameter estimations, $\widehat{\boldsymbol{v}} = \left[\hat{v}_1{}^2 \; ... \; \hat{v}_{j_{max}}{}^2\right]$ is the empirical WV values vector, $\boldsymbol{v}(\boldsymbol{\theta}) = \left[v_1(\boldsymbol{\theta})^2 \; ... \; v_{j_{max}}(\boldsymbol{\theta})^2\right]$ is the model-implied WV values vector and $\widehat{\boldsymbol{\Omega}}$ is the GLS positive definite weight matrix, which is chosen in a way that maximizes the asymptotic efficiency of the GMWM estimator (See (Guerrier et al., 2013a) for more information). For the case of inertial sensor calibration, where the input signal's size is typically quite large, a sensible choice for $\widehat{\boldsymbol{\Omega}}$ can be given by the following equation:

$$\widehat{\boldsymbol{\Omega}}_{i,j} = \begin{cases} \dfrac{1}{\left(CI_{high,j} - CI_{low,j}\right)^2} & \text{if i = j} \\ 0 & \text{if i} \neq \text{j} \end{cases}, \tag{3.21}$$

where $CI_{high,j}$ and $CI_{low,j}$ represent the piecewise 95% confidence intervals (CIs) for the jth wavelet scale of the empirical WV (see Percival and Walden, (2000), eq. 314c).

As it was mentioned above, the optimization/minimization problem that the GMWM attempts to solve is based on the GLS. Therefore, as such, it is sensitive to the selection of the initial condition since if this is not done properly, it is highly possible that the estimation process would get stuck to a local minima (instead of the global one) or even diverge entirely. Balamuta et al., (2018) addressed this issue by infusing the GMWM framework with a heuristic algorithm that performs a grid-search in order to appropriate starting values for the GLS-based optimization.

Another challenge that the GMWM faces is the determination of the composite model's structure which manages to best describe the stochastic behavior of the input (error) signal with the less possible complexity. In order to tackle it, Guerrier et al., (2015) developed a consistent and unbiased estimator for a model selection criterion called the *Wavelet Variance Information Cri-*

terion (WVIC), which was based on theoretical results of Guerrier and Victoria-Feser, (2015) and the mathematical equation that describes it is provided below:

$$\widehat{WVIC} = \left(\hat{\boldsymbol{v}} - \boldsymbol{v}(\boldsymbol{\theta})\right)^T \hat{\boldsymbol{\Omega}} \left(\hat{\boldsymbol{v}} - \boldsymbol{v}(\boldsymbol{\theta})\right) + 2tr\left(\widehat{cov}[\hat{\boldsymbol{v}}, \boldsymbol{v}(\boldsymbol{\theta})] \hat{\boldsymbol{\Omega}}^T\right), \qquad (3.22)$$

The first term of equation (3.22) is designated as the *objective function* of the GMWM. It describes an unbiased estimator of the minimized discrepancy between the data-based empirical WV and the candidate model-implied WV and its value decreases as the complexity of the tested model increases. As for the second term, it is referred to as *optimism* and it expresses the complexity of the candidate model. In fact, it acts as a penalty for overfitting to the empirical behavior and its value increases as the number of individual stochastic processes included into the tested composite model rises. Eventually, the model with the smallest WVIC criterion value is the one that achieves the optimal balance between future error prediction accuracy and simplicity, and it is the one that should be selected.

The computation of the optimism in equation (3.22) is generally a difficult task because it contains the covariance matrix between the empirical and model-implied WV, a quantity which is not a directly observable statistic. According to Guerrier et al., (2015), the most prominent and convenient way to provide an estimation of this covariance is parametric bootstrap. Moreover, the authors proposed an automatic model selection algorithm based on the calculation of the WVIC criterion. Specifically, the user provides the most complicated model that should be considered, and the algorithm evaluates the WVIC for all the nested models with great speed, ranks them and outputs the best one (has the smallest criterion value). However, even though this algorithm provided a statistically rigorous way to find the optimal model structure, the computational burden can be considerable, especially when the nested model number is too high.

The GMWM algorithm that contains all the aforementioned improvements has a significant fundamental weakness, which is related to the fact that its estimation result is particularly prone to the existence of outliers in the analyzed (error) sequence. In order to overcome this limitation without the need for pre-filtering, Guerrier et al., (2022) proposed a natural extension to the GMWM (i.e., maintains its statistical properties) called the *Robust Generalized Method of Wavelet Moments (RGMWM)* which makes the classical one robust in the infinitesimal sense and therefore capable of reducing the effects of the outliers to the estimation solution. Specifically, the way that this is achieved is by using an M-estimator with a bounded Influence Function (IF) (See (Maronna et al., 2019) for an in-depth discussion) for the calculation of the empirical WV, the equation of which is provided below (Guerrier et al., 2022):

$$\tilde{v}_j^2 = \text{argzero}_{v \in \mathbb{R}^+} \left[\frac{1}{M_j} \sum_{t=1}^{M_j} \omega^2 \left(\frac{W_{j,t}}{v}; v^2, c \right) \left(\frac{W_{j,t}}{v} \right)^2 - a(v^2, c) \right], \qquad (3.23)$$

where $\tilde{v}_j^2$ is the robust version of the empirical WV, ω is the weight function that corresponds to the selection of the ψ-function (i.e., the IF), c is a tuning constant that controls the relationship between efficiency and robustness and a is a rectification term that ensures that the true WV will be derived if the estimator is applied to the same data from which the wavelet coefficients were obtained from. A potential option for ω would be the Tukey-Biweight ψ-function (Beaton and Tukey, 1974), which is the one that was used by Guerrier et al., (2022) and it is presented below:

$$\omega_{[Bi]} \left(\frac{W_{j,t}}{v}; v^2, c \right) = \begin{cases} \left(\left(\frac{W_{j,t}}{v} \frac{1}{c} \right)^2 - 1 \right)^2 & \text{if } \left| \frac{W_{j,t}}{v} \right| \leq c \\ 0 & \text{if } \left| \frac{W_{j,t}}{v} \right| > c \end{cases}, \qquad (3.24)$$

Finally, the authors highlighted that in order to make sure that the M-estimator provides the highest level of robustness as possible, they suggested that the tuning constant's value could be set to $c \approx 4.97$, which is the analogous to a 60% efficiency compared to the classical estimator.

Even so, it can be very challenging to detect with absolute certainty whether the data at hand contain outliers or not, which are actually very common in practice. The reason behind this limitation is the fact that even though robust statistics provides us with outlier detection markers (e.g., Mahalanobis distances), it is highly possible that a phenomenon called the "masking effect" is in effect. What this means is that the effects of the outliers in the data at hand interact in such a manner that they are overlooked by those markers (See (Maronna et al., 2019) for an in-depth discussion).

For the case of stochastic analysis using the GMWM, Balamuta et al., (2016) suggested that a visual comparison between the classical and robust WV, in a log-log plot with respect to time scales and where their respective 95% CIs are also included, could be a reasonable contamination test. However, if outliers are indeed present, then the information conveyed by the classical WV would be unreliable and thus incapable of providing a theoretically valid conclusion.

In the research work by Radi et al., (2018), the GMWM and the AVLR were utilized for the investigation of the correlation between the dynamics and the stochastic error behaviour of low-cost MEMS-based inertial sensors included into smartphones. Based on that analysis, it was highlighted that even though the dynamic conditions vary, the model structure remains the same, but the parameter values change as well as that the GMWM has the unique ability to efficiently detect and quantify time-correlated noises in the form of AR1 processes, while the AVLR failed to do so. Furthermore, the authors created an adaptive EKF-based navigation algorithm that is capable of changing the stochastic error model parameter values that describe the inertial sensor

random drift in real-time, depending on the sensed dynamics of the platform. Finally, the proposed filter driven by modeling information from the GMWM and the AVLR using static and multiple dynamic condition data was tested in a simulated INS/GNSS scenario during very small (10sec) GNSS outages. The results from this application confirmed not only the superiority of the GMWM over the AVLR but also the importance of considering the influence of dynamics to the inertial sensor error random behaviour in practice.

In another work by Zhao and Zhao, (2023), an online application and inclusion of the derived information into an EKF-based INS/GNSS filter for vehicular navigation in urban cities was proposed. Specifically, this algorithm utilizes a static state detector with an adaptive threshold in order to identify the times when the vehicle is stopped and uses the collected static IMU data to perform the stochastic modeling of the inertial sensor errors. In fact, the data during the first stop are used to determine the stochastic model structure and then the accumulated data from the stops after that are used to update the model parameter values in real-time. The performance of this algorithm was tested in a real vehicle navigation scenario using the GMWM, AVLR and MLE stochastic methodologies and it was found that not only the GMWM clearly surpasses them in terms of resulting navigation accuracy but also its online performance is also validated.

A very interesting and meaningful contribution has very recently been presented in the research work of Cucci et al., (2023a). Specifically, the authors proposed an extension to the GMWM algorithm for processing daily GNSS positioning solutions in order to simultaneously estimate the parameters of linear functional (geophysical) and stochastic error models, along with their respective uncertainty level. This newly created framework called GMWMX, where X refers to its eXogenous inputs, is a semi-parametric approach (i.e., unspecified underlying data distribution) that can ensure its statistical properties as an estimator like consistency and asymp-

totic normality without the need for strict parametric assumptions like the MLE does. From that framework, the authors defined two estimators, the GMWMX-1 and GMWMX-2, and compared their performance with the standard MLE via simulations with different stochastic model structures, available data length and size of missing information. The analysis of the derived results clearly showed that the GMWMX estimators offer superior computational efficiency that allows the processing of large GNSS networks in mere minutes by just using a personal computer, while in reality, that computational load would prohibit the use of the standard MLE. Furthermore, it was highlighted that the GMWMX estimators provide very similar results with the MLE in terms of stochastic model parameter estimation. As for the functional model, the performance of the GMWMX-1 appears to be slightly worse than the MLE, while the GMWMX-2 sacrifices part of its computational potency in order to equate its efficiency to the MLE.

3.3.6 Multi-signal GMWM Extensions

The methodologies that have been described so far utilize a single signal in order to conduct the analysis of the inertial sensor error drift. This means, that a stationarity assumption is being made, where the parameter vector $\boldsymbol{\theta}_0$ defining the true (unknown) error generating function that fully describes the analyzed signal is constant in time (Figure 3.4a). However, Bakalli et al., (2017) highlighted that when multiple inertial sensor replicate are collected under the same operating conditions, their WV log-log plots (either classical or robust) demonstrate a certain variability but still follow the same general shape.

With the purpose of describing this occurrence, Bakalli et al., (2017) proposed the concept of *near-stationarity*. According to that, it is assumed that every error signal is produced by the same true (composite) stationary generating model $G(\boldsymbol{\theta}_0)$ but with the defining parameter vector of each replicate $\boldsymbol{\theta}_i$ being a random intercept from an unspecified probability distribution (i.e., each

parameter vector component is an independent random variable) (Figure 3.4b). Furthermore, the authors introduced a near-stationarity test with the purpose of determining whether the stationarity assumption is valid (null hypothesis) or not (alternative hypothesis), and with the outcome in mind, choose the proper CI inference method for the estimated stochastic model parameters (See (Radi et al., 2019) for more information).
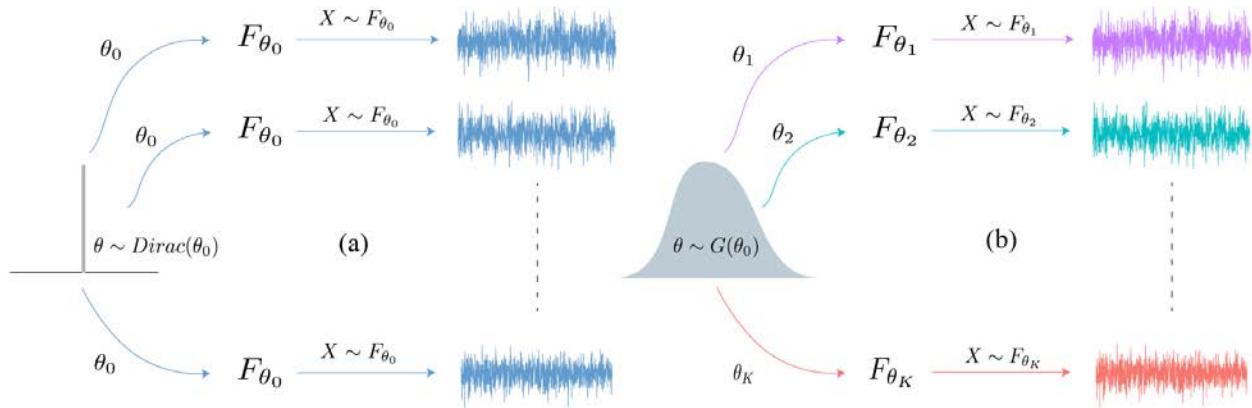
Figure 3.4: Schematic representation of the stationarity (a) and near-stationarity (b) concepts. (Radi et al., 2019)

The near-stationarity setting is actually very common in practice, especially when low-cost equipment is utilized, and thus certain challenges arise. The first one is that if only one signal is used for the stochastic analysis, then it is possible that the derived model will not be optimal for navigation applications. And the second, is the fact that in practice, when numerous replicated have been collected and a single one has to be chosen for the analysis, the selection criterion is somewhat arbitrary. Therefore, there is the danger of picking one that is not representative of the general sensor behaviour (i.e., abnormal replicate).

Given these challenges, it is clear that this parameter variation has to be sufficiently taken into account in order to estimate a model that optimally describes the future behaviour of the inertial sensor random errors. In turn, this will contribute not only to the accuracy enhancement of the final navigation solution but also to increased reliability of the corresponding uncertainty. For

that reason and as extensions of the GMWM framework, 3 multi-signal estimators have been proposed based on the near-stationarity principle and with each having a different minimization criterion: the Average GMWM (AGMWM) (Bakalli et al., 2017), the Multi-signal GMWM (MS-GMWM) (Radi et al., 2019) and the Average Wavelet Variance (AWV) estimator (Bakalli et al., 2023).

Assuming that K independent static inertial sensor signal replicates have been collected using the same IMU under invariant operating conditions and with each signal having a length of T_i. Then, the optimization problem that each of the 3 aforementioned multi-signal estimators solves for the purpose of estimating the true (unknown) parameter vector $\boldsymbol{\theta}_0$ are given below (Bakalli et al., 2023):

$$\widehat{\boldsymbol{\theta}}_{AGMWM}^{o} = \operatorname{argmin}_{\boldsymbol{\theta} \in \boldsymbol{\Theta}} \left\| \sum_{i=1}^{K} w_i \widehat{\boldsymbol{\theta}}_i - \boldsymbol{\theta} \right\|_I^2, \qquad \widehat{\boldsymbol{\theta}}_i = \operatorname{argmin}_{\boldsymbol{\theta}_i \in \boldsymbol{\Theta}} \|\widehat{\boldsymbol{v}}_i - \boldsymbol{v}(\boldsymbol{\theta}_i)\|_{\Omega}^2 \qquad (3.25)$$

$$\widehat{\boldsymbol{\theta}}_{AWV}^{\dagger} = \operatorname{argmin}_{\boldsymbol{\theta} \in \boldsymbol{\Theta}} \left\| \sum_{i=1}^{K} w_i \widehat{\boldsymbol{v}}_i - \boldsymbol{v}(\boldsymbol{\theta}) \right\|_{\Omega}^2 \qquad (3.26)$$

$$\widehat{\boldsymbol{\theta}}_{MS-GMWM} = \operatorname{argmin}_{\boldsymbol{\theta} \in \boldsymbol{\Theta}} \sum_{i=1}^{K} w_i \|\widehat{\boldsymbol{v}}_i - \boldsymbol{v}(\boldsymbol{\theta})\|_{\Omega}^2 \qquad (3.27)$$

where $\left(\widehat{\boldsymbol{\theta}}_{AGMWM}^{o}, \widehat{\boldsymbol{\theta}}_{AWV}^{\dagger}, \widehat{\boldsymbol{\theta}}_{MS-GMWM}\right)$ are the estimations of the stochastic model parameter vector using the AGMWM, AWV and MS-GMWM estimator respectively, $\|Z\|_{\Omega}^2 = Z^T \Omega Z$ with $Z \in \mathbb{R}^J$, $\widehat{\boldsymbol{\theta}}_i$ is the parameter vector derived from processing each available signal individually with the GMWM, $\sum_{i=1}^{K} w_i \widehat{\boldsymbol{v}}_i$ is the AWV wavelet variance, Ω is a positive definite weight matrix and an estimator that maximizes asymptotic efficiency for the case of multi-signal inertial sensor stochastic calibration can be $\widehat{\boldsymbol{\Omega}} = \sum_{i=1}^{K} w_i \widehat{\boldsymbol{\Omega}}_i$ (Guerrier et al., 2013a), $\widehat{\boldsymbol{\Omega}}_i$ is derived using equation

(3.21) for every considered signal and $w_i = T_i / \sum_{j=1}^{K} T_j$ is a weighting factor for each empirical WV based on the signal length, while also satisfying the condition $\sum_{i=1}^{K} w_i = 1$. Practically, this choice for the weighting factor represents the intuitive consideration that the longer the signal, the more knowledge it contains and thus the estimator should perceive its greater importance.

(Bakalli et al., 2023) investigated the statistical properties of all these 3 multi-signal estimators and provided the mathematical explanation and conditions under which they are consistent and asymptotically normal. Furthermore, it was highlighted that the AGMWM aims to estimate the expected value of the G model, which is optimal (and equivalent to the other two estimators) only for the case where the underlying processes have a linear WV representation (i.e., WN, QN, RW, DR). However, if there are processes with nonlinear WV behaviour (AR1/GM1), which is actually very common for the case of stochastically modeling low-cost inertial sensor errors, then this estimator would not provide representative information and thus its use should be avoided for navigation applications. As for the AWV and MS-GMWM, the authors demonstrated their equivalence in targeting the parameter values that optimally predict the future error behaviour (and included within the navigation algorithm) and have no stipulations for doing so about the linearity/nonlinearity of the underlying processes. Nevertheless, they suggested that AWV would be a more preferable choice for inertial sensor stochastic calibration due to practical advantages. The reason for that is because the AWV can make use of the well-established GMWM framework by simply using the weighted average of the WVs and weight matrices of the available signals instead of the single-signal-based quantities. Consequently, it can take advantage of the starting value guessing algorithms that the GMWM employs. On the other hand, if the MS-GMWM is chosen, then the use of GMWM's algorithms for finding initial parameter values will not be possible. Alternatively, a possible choice would be to use the AGMWM solution as a

starting point, which might not be good enough if the underlying processes are heavily nonlinear. Therefore, it is evident that the use of AWV would be the safest choice.

Given these theoretical conclusions, the authors compared the efficiency of the AWV and AGMWM estimators in terms of parameter estimation in two simulation studies, with varying model complexity. From that, they confirmed that the AWV and AGMWM aim for a different quantity altogether, with the AWV targeting the optimal one, based on the observed behaviour. Finally, a case study was also conducted, where models derived by applying the single-signal GMWM to multiple real signal replicates as well as by using the AWV were inputted into an EKF, and several Monte-Carlo (MC) navigation simulations were conducted. The results from this application showed that the AWV model provided (most times) optimal results in terms of position and orientation accuracy as well as of accurate and reliable navigation state uncertainties. Contrarily, the various GMWM-derived models appeared to significantly over or underestimate the state estimations in most cases.

On another note, just like in the GMWM, there is the need for a rigorous determination of the model structure that best describes the sensed behavior with the least possible complexity. For that reason, Radi et al., (2019) proposed an automatic algorithm (See Figure 3.5), in the context of the MS-GMWM estimator, that evaluates an extension of the WVIC criterion to the multi-signal case. This new criterion was named the *Cross-Validated Wavelet Variance Information Criterion (CV-WVIC)* and it was evaluated for every nested model within an inputted complex one in order to eventually determine the optimal, which is the one with the smallest criterion value. However, just like in the single-signal GMWM, such a meticulous investigation for the proper model structure can be very computationally intensive in the case where a large number of

candidate models is considered and eventually, it might also be possible that the obtained "best"

model can be simplified further.
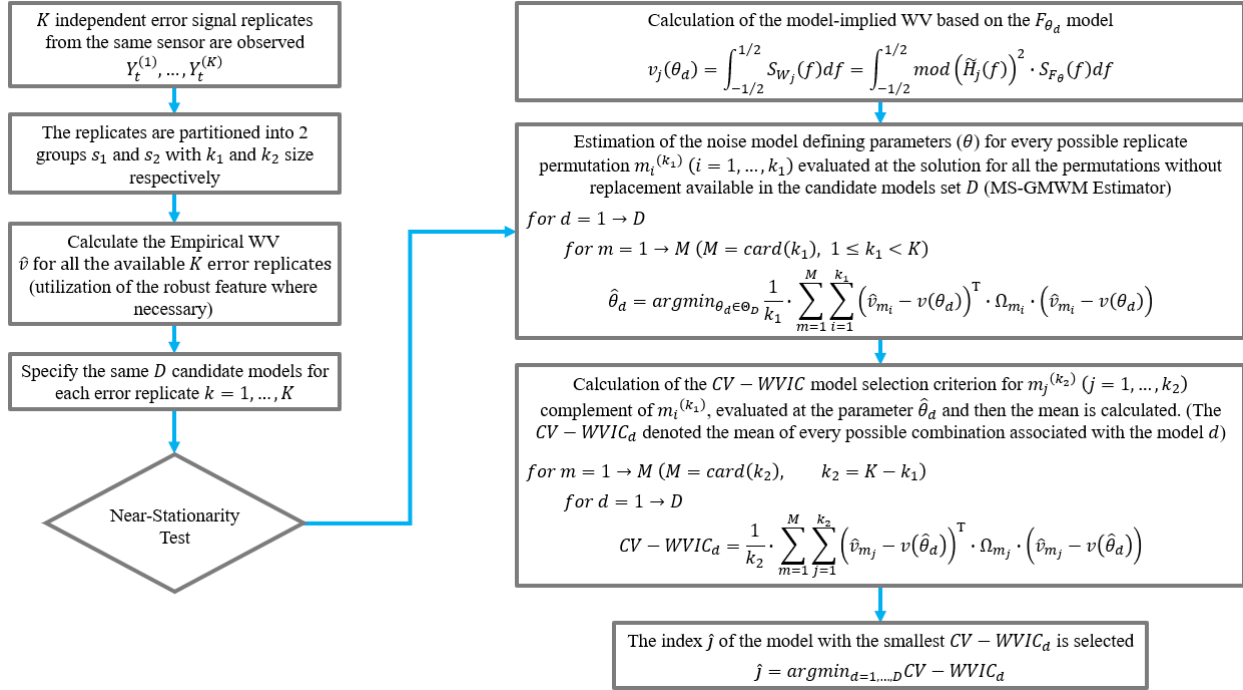
Figure 3.5: The MS-GMWM algorithm that incorporates the CV-WVIC criterion evaluation.

A very interesting application of the MS-GMWM was conducted by Radi, (2018), who utilized this innovative framework to meticulously study the influence of temperature and platform dynamics to the stochastic modeling of low-cost MEMS-based inertial sensor errors. In addition, the author created an environmentally adaptive EKF filter for INS/GNSS integration, which could alter the stochastic model parameter values depending on the applied dynamics and temperature of the IMU. Eventually, the application to a real-life vehicular navigation problem confirmed that by considering the influence of the operating conditions (i.e., temperature, dynamics) to the inertial sensor random drift behavior, it is possible to further improve the 2D positioning accuracy of the INS standalone solution.

Despite the improvement that the multi-signal extension has provided, a very important factor has not been considered, which can compromise the estimation of stochastic model parameter values that optimally predict the future error behavior. That factor is none other than the existence of potential outliers in the considered data, a danger that is logically more likely to occur in the multi-signal case. Therefore, in order to ensure the estimation accuracy and stability of the navigation solution as well as of its corresponding uncertainty, this issue must be addressed. Furthermore, in the past, the connection between stochastic modeling efficiency and navigation performance has only been investigated via a very limited number of practical experiments, which are definitely not enough to infer reliable conclusions from a statistics point of view. On another note, this advanced stochastic modeling knowledge has only been utilized in the context of an EKF for simple INS/GNSS integration, without the provision of any additional updates, that in turn can provide a more frequent compensation for the inertial sensor bias. Finally, it would also be worthwhile to investigate what kind of improvement these additional updates could introduce not only in an EKF but also in the context of a less restrictive filter like the UKF.

3.4 Summary

In this chapter, the existing deterministic calibration methods and stochastic modeling techniques were presented along with a concise description of their algorithms. Moreover, past research works were mentioned, and particular focus was given in highlighting the weaknesses of the stochastic analysis approaches. From that, although it was made apparent that the GMWM-based stochastic modeling approaches represent the latest advances in the field of inertial sensor stochastic calibration, there are still weaknesses that warrant further investigation (main objective of this thesis). Below, these limitations are provided in bullet form, and which will be addressed in the next chapters:

- The WVIC-based model selection algorithm can be very computationally intensive in the case where a large number of models are being investigated. In addition, the selected "best" model might require further simplification.

- The contamination test suggested by Balamuta et al., (2016) for the choice between the classical or robust single-signal GMWM is not theoretically sound.

- The multi-signal GMWM approach does not contain safeguards against the existence of any type of outlier in the considered calibration data.

- In past studies, the connection between the quality of inertial sensor stochastic calibration and navigation performance has only been investigated via a small number of practical experiments, something that is not enough for the inference of well-founded conclusions.

- To this day, the stochastic knowledge about the inertial sensor errors derived from GMWM-based estimators has only been infused within an EKF and only for a simple INS/GNSS integration, without the provision of other, more frequent, updates.

Chapter Four: Robust Stochastic Modeling of MEMS-based Inertial Sensor Errors

4.1 Introduction

In low-budget applications, where MEMS-based IMUs are mostly utilized, the major factor that determines the quality of the provided navigation solution is the available knowledge about the inertial sensor random drift behavior, which is hard to obtain accurately in practice. The primary reason for this is that it is very common that the inertial sensor measurements collected for calibration purposes contain outliers due to either internal or external factors, which cannot be precisely identified. Nevertheless, it is theorized that they are associated with the condition of the IMU (e.g., assembly integrity, ageing, material quality) and/or the surface where the IMU is placed (e.g., turntable), since it is highly likely that any vibration, no matter how small, can affect the output of the inertial sensors. Consequently, stochastic calibration should be implemented using an estimator that can decrease the influence of such outliers in order to efficiently estimate the proper model. In turn, when the derived model is inputted within the navigation algorithm that integrates INS with GNSS and other aiding sources like cameras, magnetometers, etc. and the GNSS information is unobtainable (outage regions), the INS standalone solution would be optimal in terms of accuracy and reliability.

Currently, the modern approach for the effective handling of the complex random error nature displayed by low-cost and consumer grade MEMS-based inertial sensors is the GMWM and its multi-signal extensions (See Sections 3.3.5 and 3.3.6 respectively). However, even though the existent framework is very rigorous regarding the model selection using its automatic algorithm based on the calculation of the WVIC criterion for all the models nested within a very complex one (Guerrier et al., 2015), it can still be computationally intensive when the number of investi-

gated models is large. To counter this issue and make sure that the model selection is conducted in a good enough and fast way, a simplified algorithm for implementing the GMWM will be presented in this chapter. In addition, ways of reducing the complexity of the derived model will be suggested.

On another note, despite the fact that the GMWM has a natural robust version called the RGMWM (Guerrier et al., 2022), it can be difficult to determine whether the analyzed data contain outliers or not and whether the RGMWM should be used instead. The reason behind this is the fact that even though robust statistics provides us with statistical markers (e.g., Interquartile range method, Mahalanobis distance, "three sigma edit" rule, etc.) to probe the existence of outliers, it is highly likely that their effects interact in such a manner that they remain undetected. This phenomenon is designated in the literature as the "masking effect" (See (Maronna et al., 2019) for more details). Therefore, with this in mind, along with the fact that the available contamination test (See Balamuta et al., 2016)) is not theoretically sound, an alternative will be explored.

As for the multi-signal extensions of the GMWM (Bakalli et al., 2017; Radi et al., 2019; Bakalli et al., 2023), none of the available estimators contain any such safeguard and that is why they remain vulnerable to the effects of outliers. To address this limitation, the multi-signal approach will be extended to include a certain level of robustness and its efficiency will be evaluated, both in terms of parameter estimation accuracy and contribution to the reliability of the navigation solution. Finally, the stochastic calibration of a consumer grade MEMS-based IMU will be conducted using the new robust multi-signal method as well as the standard maximal overlapping AVLR and their results will be compared.

4.2 A Simplified GMWM Implementation Algorithm and Model Complexity Reduction Techniques

In this section, a simpler version of the single-signal GMWM-based algorithm for the stochastic calibration of MEMS-based inertial sensors will be presented in a step-by-step fashion through a typical practical example.

First, a MEMS-based IMU is placed on a levelled surface and 1.5hr static measurements are collected with a 100Hz sampling rate under standard conditions. Then, for the data referring to a single inertial sensor, say the Y Gyroscope, the deterministic error influence is removed (using either manufacturer-provided coefficients or by performing a deterministic calibration process) and the corresponding robust empirical WV is evaluated. In turn, the very complicated model $M_1 = 4AR1 + DR + RW + WN + QN$ is fitted to it using the GMWM framework and with starting parameter values for the optimization process provided by the guessing algorithm of Balamuta et al., (2018). From the results of this fit, Figure 4.1 is created that contains the empirical WV and its corresponding 95% CIs, the model-implied WV and the individual contribution of each stochastic process (See Table 3.2) included within the M_1 model (i.e., the WV expression of each process that is characterized by the estimated parameters). Then, from a visual inspection of the individual process contributions, it is possible to remove the redundant ones that are less significant compared to others that describe the same region. Specifically, based on Figure 4.1, it is clear that between the 4th AR1, 1st AR1, WN and QN processes, it is the 4th AR1 that has the most significant contribution to the higher scales and thus the rest can be safely removed.
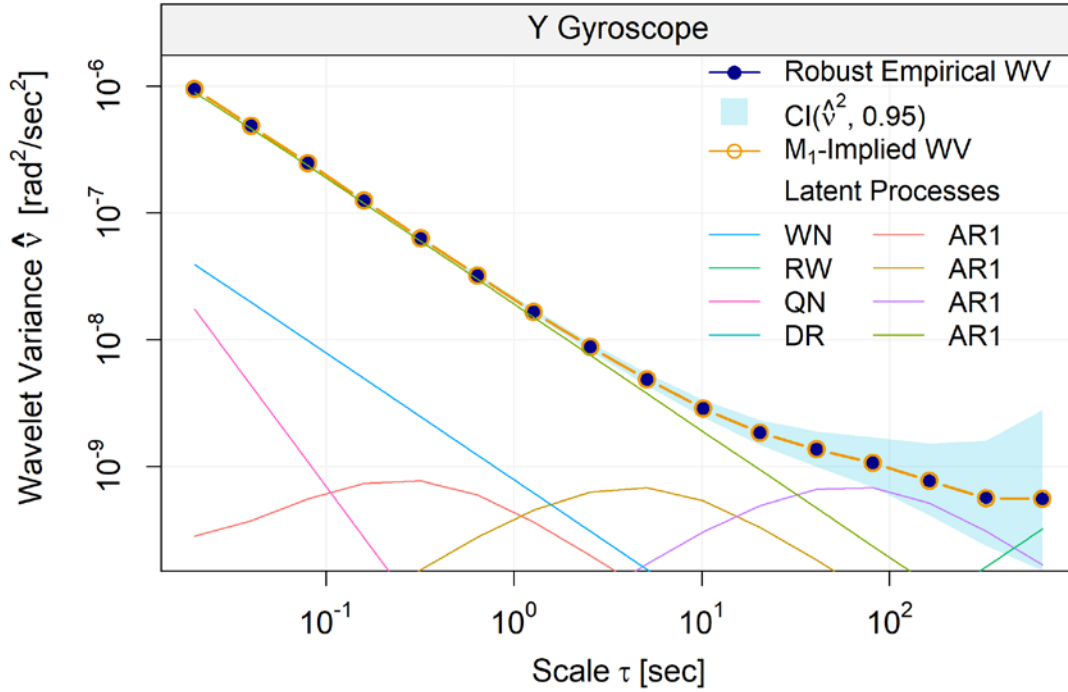
Figure 4.1: Robust empirical WV along with the corresponding 95% CIs and Implied WV constructed from the M_1 model estimated parameters. The individual contribution of each stochastic process to the overall fit is also included.

Furthermore, the DR process can also be removed since it is not important enough to appear somewhere near the region of the RW, which is much more important to the fit for the higher scales. Hence, the simpler model $M_2 = 3AR1 + RW$ is fitted to the empirical WV but with the initial conditions being the parameter values that these specific processes had in the M_1 model fit. The results from this operation are demonstrated in a similar way as before in Figure 4.2.

At this point, it is important to highlight that the contribution shapes of the 5 considered stochastic processes by the GMWM framework are well known and demonstrated in Figure 4.3. In fact, by comparing that with Figure 4.2, it is evident that the 3rd AR1 tends to emulate the WN behavior, something that is also confirmed by the process' small φ value (~ 0.0228). Therefore, since this is actually a very common occurrence when studying the random behavior of inertial sensor error, it is worth investigating whether the model can be simplified by over-bounding such an AR1 process with WN.
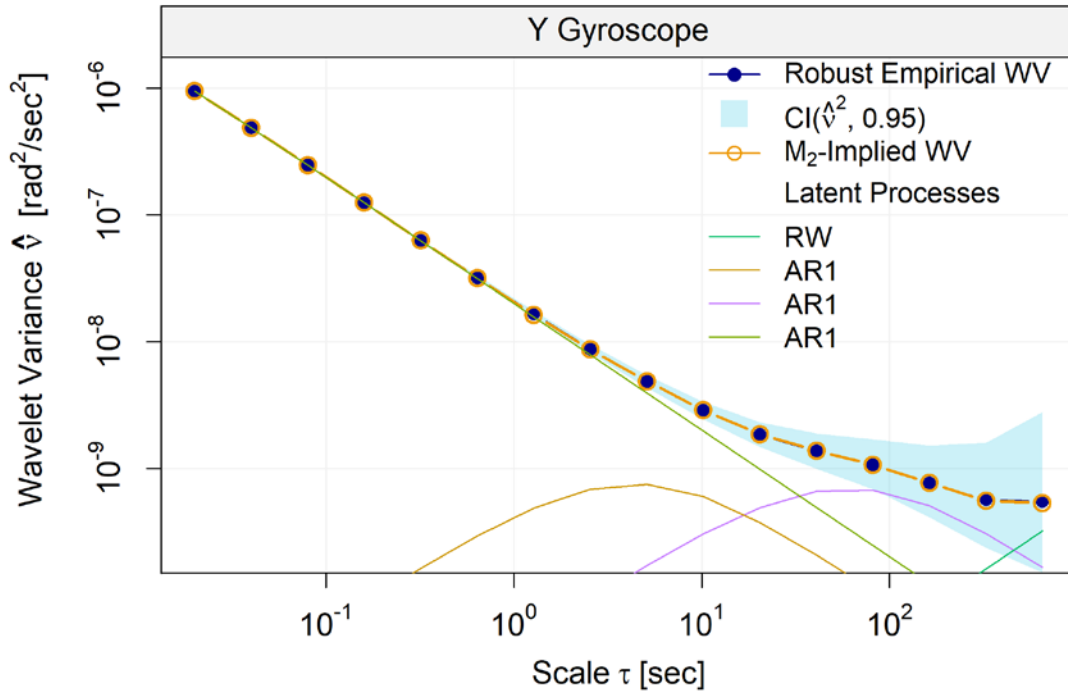
Figure 4.2: M_2 model fit to the robust empirical WV.

At this point, it is important to highlight that the contribution shapes of the 5 considered stochastic processes by the GMWM framework are well known and demonstrated in Figure 4.3. In fact, by comparing that with Figure 4.2, it is evident that the 3rd AR1 tends to emulate the WN behavior, something that is also confirmed by the process' small φ value ($\sim$0.0228). Therefore, since this is actually a very common occurrence when studying the random behavior of inertial sensor error, it is worth investigating whether the model can be simplified by over-bounding such an AR1 process with WN.
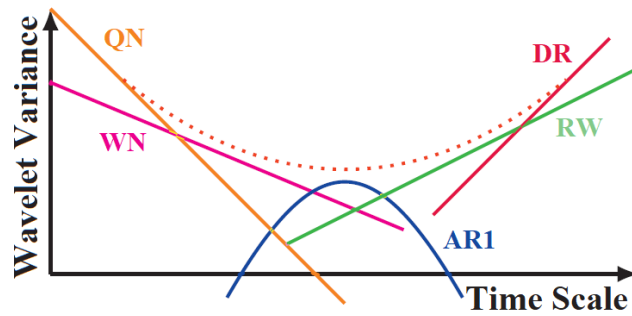
Figure 4.3: Approximate contribution to the WV log-log plot of each of the 5 considered stochastic processes by the GMWM. (Adapted from (Clausen et al., 2018))

The theoretical Haar WV expression of an AR1 process was presented in Table 3.2 and a proper manipulation of that equation yields:

$$v_j^2(\varphi_{AR1}, \xi^2_{AR1}) = \xi^2_{AR1} \left[\frac{1}{(1 - \varphi_{AR1})^2 2^j} + \frac{2\varphi_{AR1}\left(4\varphi_{AR1}^{2^{j-1}} - \varphi_{AR1}^{2^j} - 3\right)}{(1 - \varphi_{AR1})^3(1 + \varphi_{AR1})\,2^{2j}} \right] \quad (4.1)$$

Based on that, let

$$P_1(\varphi_{AR1}) = \frac{1}{(1 - \varphi_{AR1})^2 2^j} \quad (4.2)$$

and

$$P_2(\varphi_{AR1}) = \frac{2\phi_{AR1}\left(4\varphi_{AR1}^{2^{j-1}} - \varphi_{AR1}^{2^j} - 3\right)}{(1 - \varphi_{AR1})^3(1 + \varphi_{AR1})\,2^{2j}} \quad (4.3)$$

Then, since by definition $\varphi_{AR1} \geq 0$, it can be deduced that $P_1(\varphi_{AR1}) > 0$ and $P_2(\varphi_{AR1}) \leq 0$. Therefore, the following is obtained:

$$v_j^2(\varphi_{AR1}, \xi^2_{AR1}) = \xi^2_{AR1}[P_1(\varphi_{AR1}) + P_2(\varphi_{AR1})] \leq \xi^2_{AR1}\,P_1(\varphi_{AR1}), \quad (4.4)$$

$$\xi^2_{AR1}\,P_1(\varphi_{AR1}) = \xi^2_{AR1}\frac{1}{(1 - \varphi_{AR1})^2 2^j} = \frac{\xi^2_{AR1}}{(1 - \varphi_{AR1})^2}\frac{1}{2^j} = \frac{\sigma^2_\varphi}{2^j} \quad (4.5)$$

where the right side of the inequality is basically equal to the WV expression of WN. As a result, any AR1 can be over-bounded by WN with variance σ^2_φ. However, this approximation is not always valid, and it must be applied in cases where the φ_{AR1} is sufficiently small. After a lot of experimentation to find a proper threshold, it was found that a good condition for when to implement this can be $\varphi_{AR1} \leq 0.2$.

Given this conclusion and for the case at hand, the equation (4.5) is utilized for the 3rd AR1 of the M_2 model and the updated model $M_3 = 2AR1 + RW + WN$ can be fitted, where the initial values of the optimization originate from the M_2 model and the over-bounded WN variance. The result from the M_3 model fit is depicted in Figure 4.4 for a final assessment.

On top of that, it was also noticed that there are cases where one or two WV points deviate from the general trend in a local region of the log-log plot and sometimes a more refined fit can be achieved by removing those scales from consideration when estimating the candidate model. Specifically, this can be achieved by setting their corresponding weight value in the Ω to be equal to an extremely high number. Therefore, with this in mind, an improvement was introduced to the GMWM code in order for the framework to provide the option of taking this special circumstance into account.
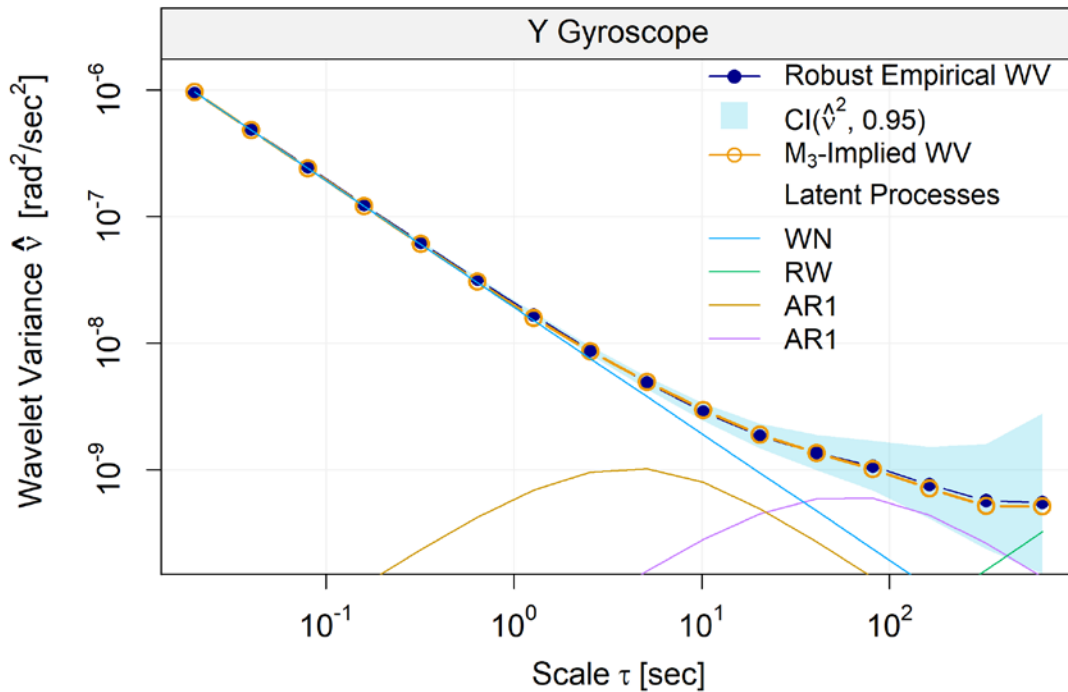
Figure 4.4: M_3 model fit to the robust empirical WV.

Indeed, for the case at hand, the first scale very slightly deviates from a WN behavior and as a result, scales 6-8 seem to not exactly follow the empirical WV. Thus, that scale was removed, the fit was repeated and according to Figure 4.5, the result became slightly better than before. And even though the difference in the final parameter values is not noteworthy, it is still proof that the proposed concept can be beneficial.

Finally, one more simplification is possible and that is the over-bounding of an AR1 characterized by a big correlation time using a RW process. The reason why this might be desirable is the happenstance where the duration of the navigation experiment is not big enough for the effects of such an AR1 to "appear". Therefore, with this in mind, a way to implement this overbound will be presented next.
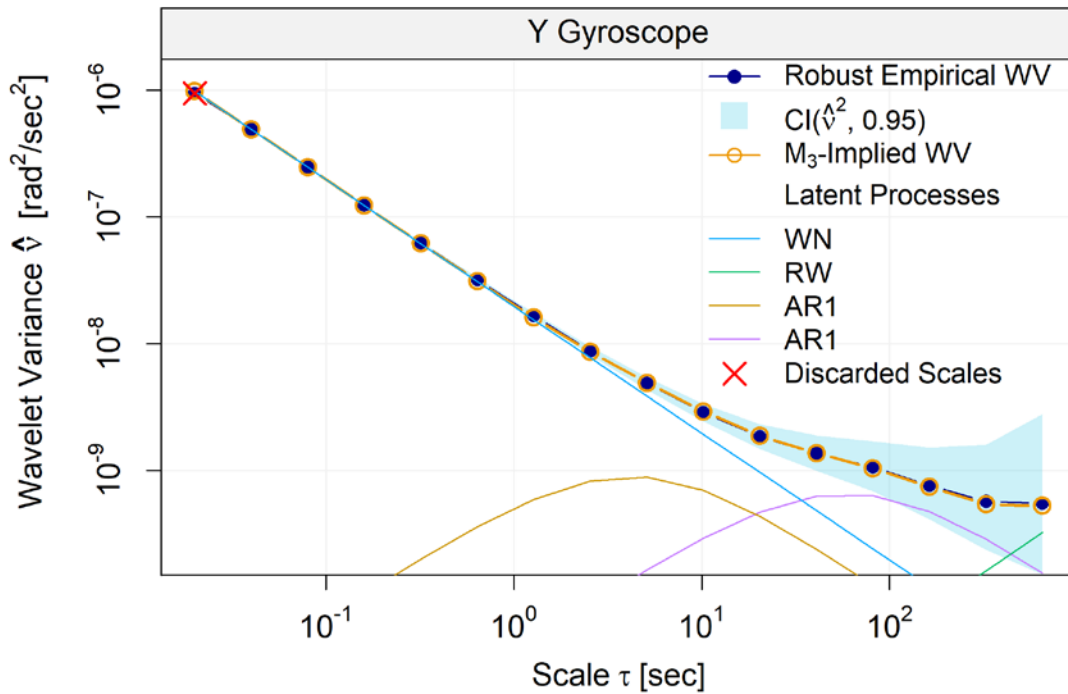
Figure 4.5: Refined M_3 model fit to the robust empirical WV.

According to Table 3.2, the Haar WV representation of a RW stochastic process is:

$$v_j^2\left(\gamma^2_{RW}\right) = \frac{\left(2^{2j} + 2\right)\gamma^2_{RW}}{12 \cdot 2^j} \tag{4.6}$$

and in order to find the proper RW variance that corresponds to an AR1, the following equation should be solved:

$$v_j^2\left(\gamma^2_{RW}\right) = v_j^2\left(\varphi_{AR1}, \xi^2_{AR1}\right) \tag{4.7}$$

Now, the question arises about which scale should be utilized for the derivation. A simple choice would be the first one but due to the fact that there is this $+2$ in the numerator of equation (4.6), the WV expression of the process in the log-log plot presents a break from the linear trend in that scale, and thus it is disqualified. Instead, the 2nd WV point is regarded as a more reasonable choice and the derivation of solving equation (4.7) for $j = 2$ is presented below:

$$v_2^2\left(\gamma^2_{RW}\right) = v_2^2\left(\varphi_{AR1}, \xi^2_{AR1}\right) \Rightarrow$$

$$\gamma^2_{RW}\frac{\left(2^{2 \cdot 2} + 2\right)}{12 \cdot 2^2} = \xi^2_{AR1}\frac{\left(\varphi_{AR1}^2 - 1\right)2^2 + 2\varphi_{AR1}\left(-4\varphi_{AR1}^{2^{2-1}} + \varphi_{AR1}^{2^2} + 3\right)}{\left(\varphi_{AR1} - 1\right)^3\left(1 + \varphi_{AR1}\right)2^{2 \cdot 2}} \tag{4.8}$$

$$\Rightarrow \gamma^2_{RW} = \frac{48}{18} \cdot \xi^2_{AR1}\frac{2\left(\varphi_{AR1}^2 - 1\right) + \varphi_{AR1}\left(-4\varphi_{AR1}^2 + \varphi_{AR1}^4 + 3\right)}{8\left(\varphi_{AR1} - 1\right)^3\left(1 + \varphi_{AR1}\right)}$$

With this in mind, an example is conducted to test the validity of this outcome. Let's assume that an AR1 process has been estimated based on 1 million inertial data points with 100 Hz sampling rate and which is characterized by the model parameter values $\varphi_{AR1} = 0.999985837$ and $\xi^2_{AR1} = 1.21568E - 11$. Then, using equation (4.8), the variance of the over-bounding RW process is evaluated and the implied WVs of the two processes are plotted against each other in a log-log plot, shown in Figure 4.6. Based on that, it can be concluded that the two processes are very close to each other for most scales, meaning that the followed reasoning is validated.
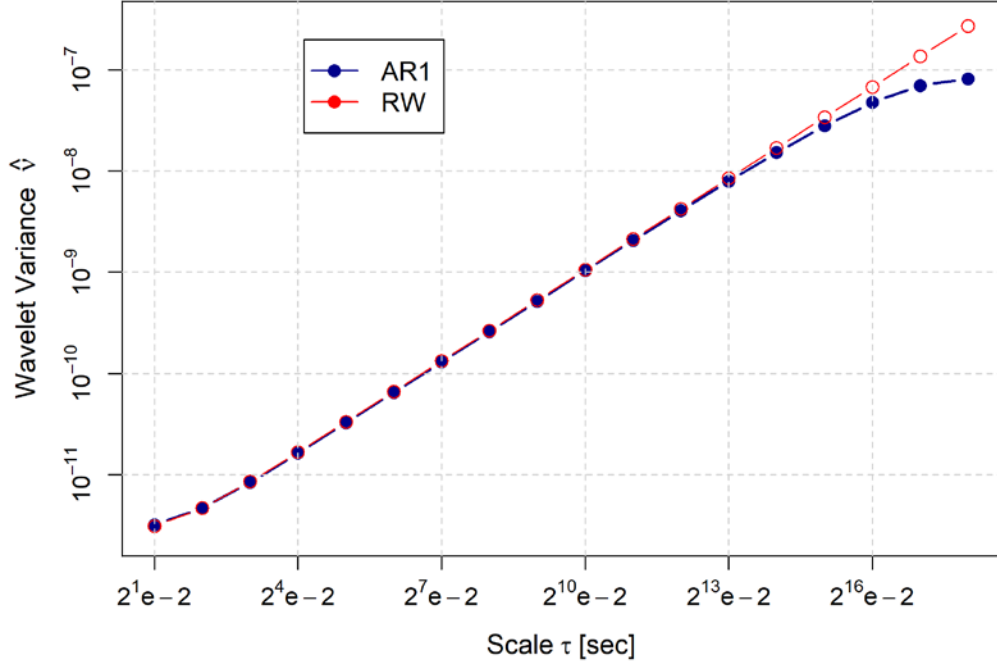
Figure 4.6: WV expression of an AR1 against its over-bounding RW.

However, it is also evident that the fit becomes progressively worse as the time scale value increases. Therefore, in order to investigate the relationship between the elapsed time and approximation accuracy, the following quantity is calculated for each WV scale:

$$\left[\sum_{j=1} v_j^2\left(\varphi_{AR1}, \xi^2_{AR1}\right) \Big/ \sum_{j=1} v_j^2\left(\gamma^2_{RW}\right)\right] 100 \tag{4.9}$$

In turn, this basically represents the over-bound percentage of the AR1 by the RW for an elapsed time equal to the corresponding time scale. Therefore, through a log-log plot, it would be possible to visually match any operation duration with the RW approximation level of the AR1 process at hand. Such a plot, for the case discussed here, is shown in Figure 4.7.
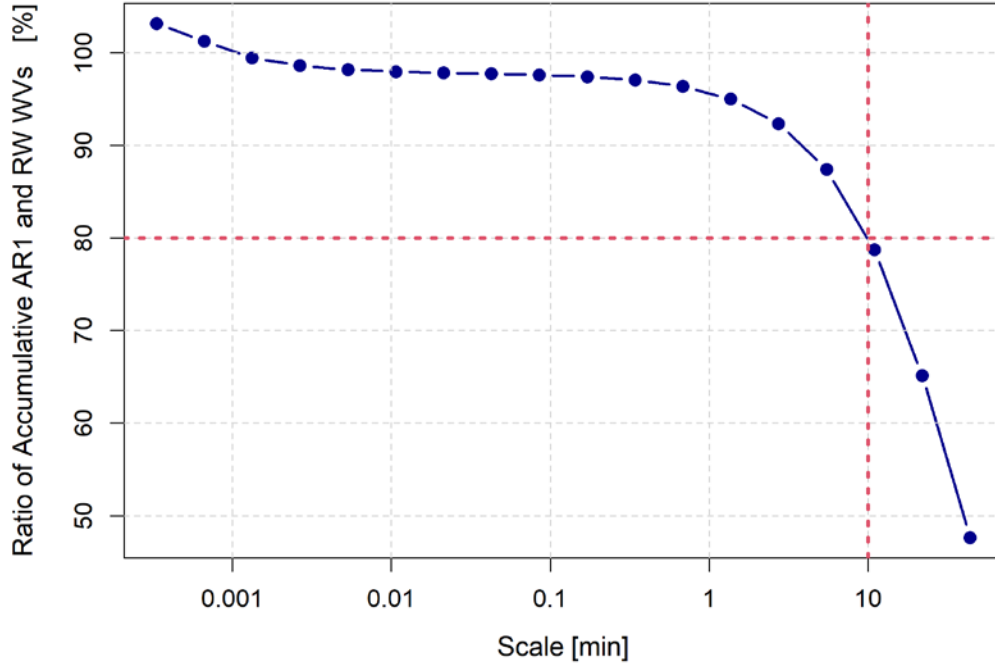
Figure 4.7: Cumulative sum ratio of the AR1-implied WV over the RW-implied WV.

Generally, an adequate over-bound percentage is assumed to be 80%. As a result and based on Figure 4.7 for the example discussed here, the RW can replace the AR1 for any operation with duration less or equal than 10 minutes. And if the investigated model already contains a RW process, then due to the additive noises assumption made by the GMWM, the two variances (existing and over-bounded RW) can be added together and then placed within the navigation algorithm.

4.3 Simulation Study for the Utilization of RGMWM in Every Scenario

In the introduction of this chapter, it was mentioned that it can be very challenging to detect with absolute certainty whether the data at hand are contaminated with outliers or not. The standard practice deals with this issue by conducting a pre-filtering procedure before the stochastic analysis. However, it is almost certain that such a course of action will unavoidably remove some useful information as well. Furthermore, in the case where the classical GMWM is used and outliers are present in the data, then there is very high potential that this will lead to either a

mistaken choice for the model structure or a bad estimation quality of the defining parameters. In fact, this danger is also present when a pre-filtering process is implemented. Hence, a simulation study will be conducted in order to investigate whether the use of the RGMWM in every single scenario without the need for outlier existence confirmation is a worthwhile exchange between reduction in the estimator's efficiency and protection against potential outlier effects. Besides, it is not unrealistic to assume that there is always going to be some form of corruption to the inertial sensor measurements when low-cost or consumer grade equipment is utilized.

Presuming that a signal X_t with sample size $T = 10^6$ has been collected using a 100Hz data rate and that it is fully described by the composite stochastic model $\mathcal{M}$ that consists of one AR1($\varphi = 9.998343 \cdot 10^{-1}$, $\xi^2 = 6.926130 \cdot 10^{-10}$) and one WN($\sigma^2 = 5.921208 \cdot 10^{-5}$). The rationale behind the choice of such a signal length is the fact that commonly 2 to 3 hours of data are necessary for the study of both the short and long-term stochastic characteristics of the noise that typically governs low-cost inertial sensors. And if a 100Hz sampling rate is utilized (standard choice in practice) then 1 million samples would represent almost 3hr of data, thus satisfying the criterion that was mentioned above. Next, $H = 500$ MC simulations are implemented using this information to produce that many signal realizations and then, based on each of them, the $\mathcal{M}$ model parameter inference is conducted by both the GMWM and the RGMWM. In the end, boxplots are created for the purpose of not only displaying the empirical distributions of the derived solutions from both estimators but also for comparing their proximity to the truth. Figure 4.8 contains these boxplots and according to it, both estimators appear to be consistent in targeting the true values. Furthermore, the efficiency loss of the RGMWM against the GMWM does not appear to be noteworthy and thus, either one can be utilized for the derivation of accurate stochastic modeling knowledge in an outlier-free data scenario.
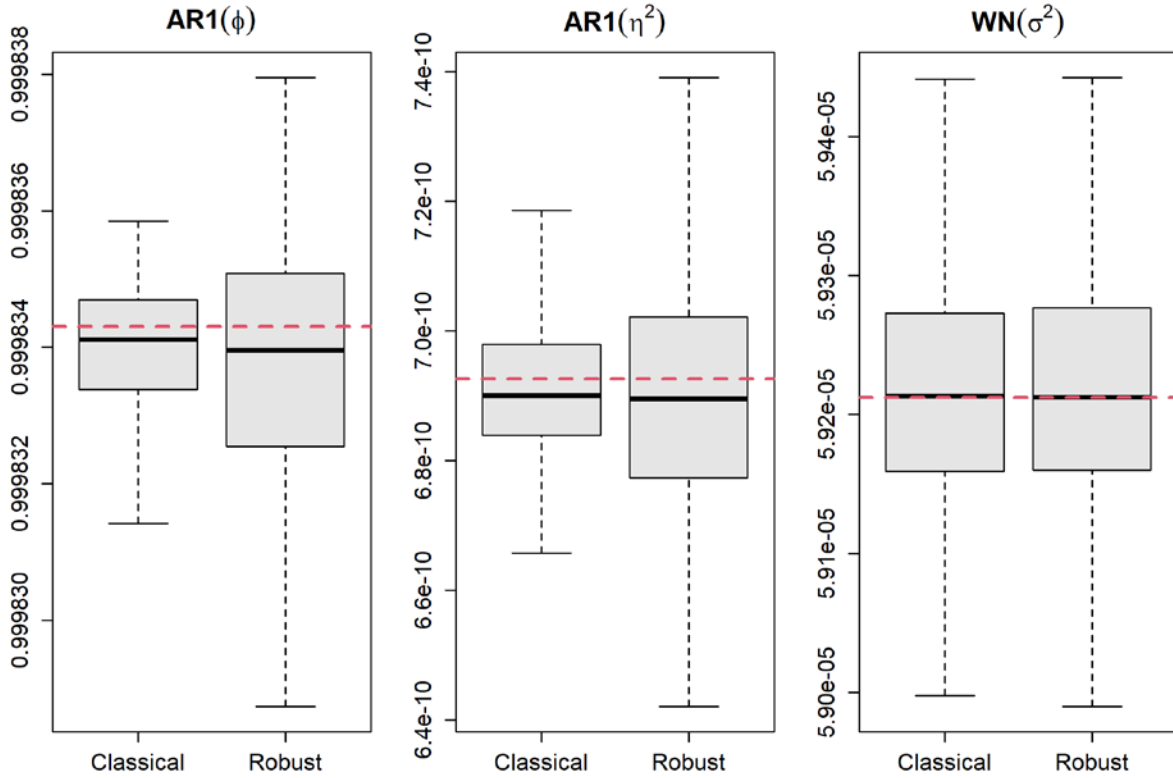
Figure 4.8: Empirical distributions of the GMWM (classical) and RGMWM (robust) estimator $\mathcal{M}$ model parameter solutions using 500 MC-simulated X_t that are outlier-free.

Following that, a second simulation study is conducted, for the purpose of showcasing the superior performance of the RGMWM over the GMWM in the case where outliers are present in the data at hand. Specifically, 1000 data points are randomly selected from each of the H realizations of the X_t signal (0.1% of the total length) and Gaussian white noise is added to them, which is characterized by a standard deviation equal to 4 times the one of the $\mathcal{M}$ model WN process. Eventually, the derived results are again represented with the help of boxplots in Figure 4.9, from which it is evident that unlike the GMWM. the RGMWM manages to remain close to the true value. Therefore, it is confirmed the RGMWM must always be utilized when outliers are present in order to impart some level of protection against their damaging influence.

The results presented in this section have been published in (Minaretzis et al., 2022).
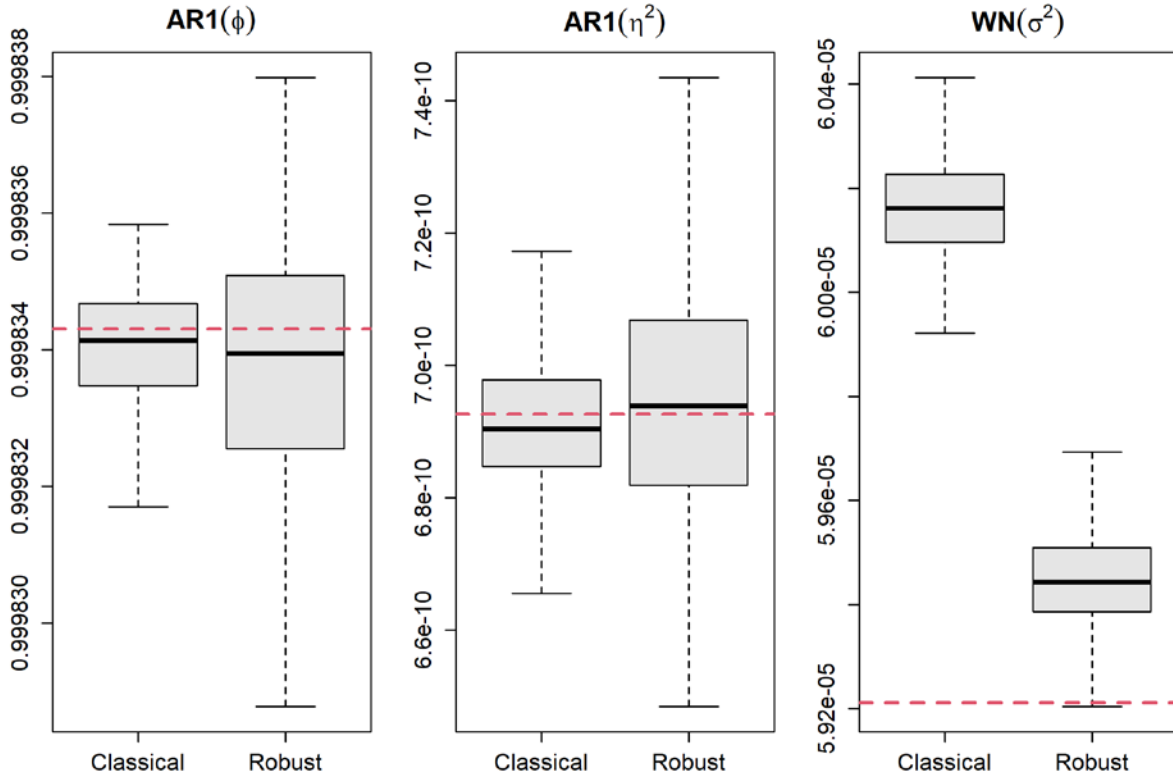
Figure 4.9: Empirical distributions of the GMWM (classical) and RGMWM (robust) estimator M model parameter solutions using 500 MC-simulated X_t that contain outliers.

4.4 Robust Multi-Signal Wavelet Variance-based Stochastic Modeling Approaches

As mentioned in Section 3.3, the standard methods for performing the stochastic analysis of low-cost (and consumer grade) inertial sensor errors utilize only one signal to derive knowledge about their behavior. In past research works, it was observed that some level of variation in terms of model parameter values between replicates is displayed, something that was also confirmed by practical experimentation, as it is apparent in Figure 4.10. Recently, estimators have been proposed to consider this by using multiple signals to conduct the stochastic model parameter estimation in an efficient way and with statistical guarantees (i.e., consistency, asymptotic normality). However, it is possible that outliers might exist in each of those signals, the impact of which has so far been neglected in this context. Henceforth, this kind of contamination will be referred

to with the term "data corruption". Furthermore, according to Figure 4.10, it is also possible to collect signal replicates (e.g., replicate 4) with notably different WV behavior compared to the rest in some regions, a phenomenon that is designated as "sample contamination" and whose effects are also yet to be considered. Therefore, to address these limitations and with the purpose of providing protection to the estimation outcome from both, a new robust multi-signal approach will be presented here. Finally, the efficiency of this new approach will be evaluated in a simulation, a case, and a hybrid case study, with respect to parameter estimation accuracy and contribution to the reliability of the navigation solution.
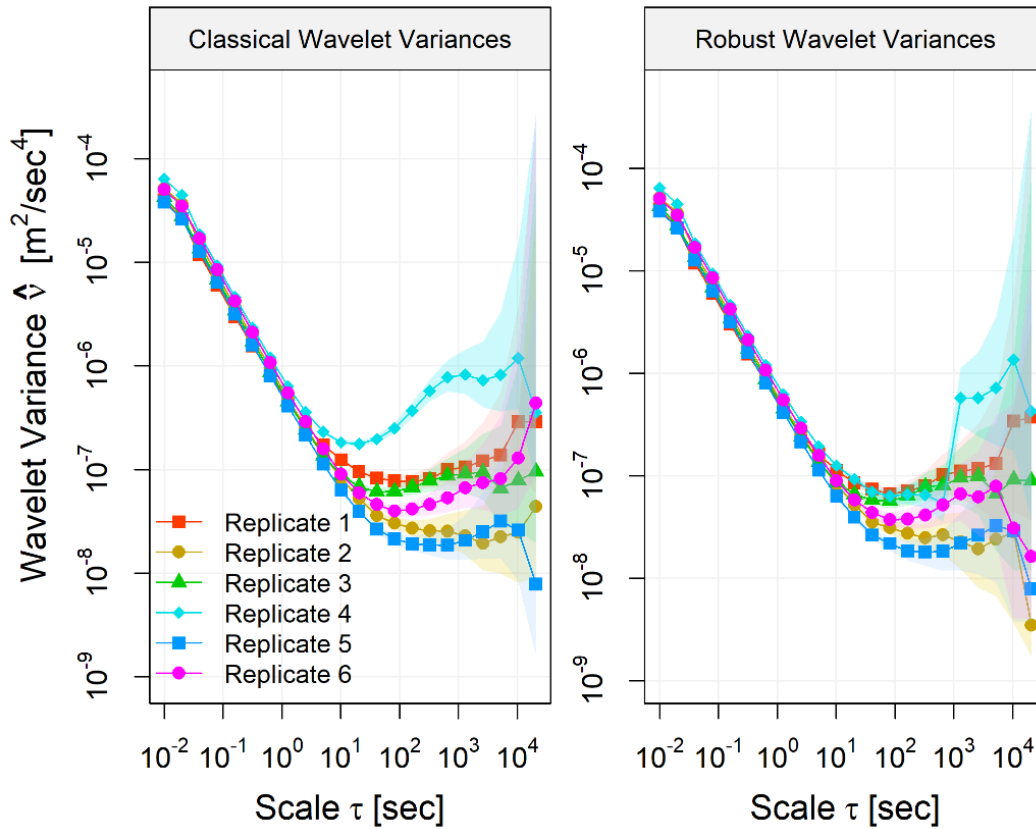
Figure 4.10: Classical (left panel) and robust (right panel) wavelet variances of 12-hour Y-Accelerometer static inertial sensor measurement replicates that were collected using an ultra-low-cost (~10 USD) MEMS-based Bosch Sensortec BMI085 tri-axial IMU[2] with a data rate of 200Hz. Also, deterministic calibration was conducted a-priori.

4.4.1 Definition of the Robust Multi-Signal Method and its Estimators

The new robust multi-signal approach is chosen to be derived as a natural extension to the AWV estimator (Bakalli et al., 2023) described by equation (3.26). Specifically, this is achieved by substituting the classical empirical WV with its robust counterpart in order to account for data corruption and by utilizing the weighted trimmed mean instead of the standard weighted mean in order to consider sample contamination. In the end, the fully describing expression of this two-layered robust multi-signal approach is given by:

$$\overline{\boldsymbol{\theta}} = \text{argmin}_{\boldsymbol{\theta} \in \boldsymbol{\Theta}} \left\| \frac{\sum_{i=p+1}^{K-p} w_i \widetilde{\boldsymbol{v}}_i}{K - 2p} - \boldsymbol{v}(\boldsymbol{\theta}) \right\|_{\Omega}^2 \tag{4.10}$$

where K is the number of available signal replicates, $\sum_{i=p+1}^{K-p} w_i \widetilde{\boldsymbol{v}}_i / K - 2p$ is the method's characteristic empirical WV and $\widetilde{\boldsymbol{v}}_i$ is the robust estimator for the WV (see equations (3.23) and (3.24)) based on the ith replicate. As for how the weighted trimmed mean is implemented, the available WV values for each scale are sorted in ascending order, then based on the trim level $tr \in [0,0.5]$, $p = \lfloor tr \cdot K \rfloor$ number of the lowest and highest values are removed and eventually, the weighted mean of the values left is calculated. In addition, the weight matrix is calculated as a weighted mean of the $\widehat{\boldsymbol{\Omega}}_i$ values for each scale but with the corresponding values to the WV points that remained after the truncation. Finally, the trim level should be selected in a way so that a balance is maintained between the removal of the abnormal replicate(s) and the preservation of as much information as possible.

For the purposes of this study, two estimators are defined. The first one is called the Singly Robust AWV (SR-AWV) estimator, it contains one layer of robustness that accounts of data corruption, and it is derived by equation (4.10) with $p = 0$. And the second is called the Doubly

Robust AWV (DR-AWV), it is equipped with safeguards against both data corruption and sample contamination and it is also given by equation (4.10) with $p \neq 0$.

The detailed mathematical circumstances ensuring the statistical consistency and infinitesimal robustness of the proposed parent estimator given by equation (4.10) are beyond the scope of this dissertation. However, they have been included in (Minaretzis et al., 2023), which is a manuscript that has been submitted for publication.

On another note, an important question arises, concerning the amount of signal replicates K that is considered by the multi-signal estimators. From a logical standpoint, the greater this number is, not only the more representative the resulting stochastic modeling information becomes of the inertial sensor stochastic error behaviour becomes, but also the more replicates can be considered for inference by the DR-AWV estimator, after a reasonable trim level is selected. Nevertheless, in practice, it is only feasible to obtain a relatively limited number of replicates. Hence, considering this constraint and drawing on empirical insights garnered from the experiments conducted for the purposes of this thesis, it is recommended that a minimum of 6, and ideally 10, calibration signal replicates be used for the stochastic modeling of inertial sensor errors.

4.4.2 Simulation Study

The aim of this segment is to showcase the efficiency of the newly proposed robust multi-signal estimators compared to their classical counterpart in accurately estimating the true model coefficients that dictate the random error characteristics of inertial sensor measurements produced by MEMS-based equipment. To that end, a simulation study is implemented for the following 3 data collection scenarios that are based on artificial accelerometer measurements:

1) No outliers are present in the simulated datasets (clean setting-Scenario I),

2) Different kinds of outliers are included in the replicates that affect different parts of the signal spectrum (data corruption setting-Scenario II),

3) The same outliers of the former setting are existent along with a replicate with notably dissimilar random error behavior compared to the rest (sample contamination setting-Scenario III)

Moreover, the evaluation of the estimator statistical performance was chosen to be conducted through a robust variant of the Root Mean Square Error (RMSE), the equation of which is given below (Guerrier et al., 2022):

$$RMSE = \sqrt{\text{med}\left(\frac{\hat{\theta}_i - \theta_{i,o}}{\theta_{i,o}}\right)^2 + \text{mad}\left(\frac{\hat{\theta}_i}{\theta_{i,o}}\right)^2}, \tag{4.11}$$

where $\text{med}(\cdot)$ is the median operator, $\text{mad}(\cdot)$ is the median absolute deviation, $\hat{\theta}_i$ refers to the ith component of the estimated parameter vector that defines the considered stochastic model and $\theta_{i,o}$ is its corresponding true value. As for the reason why such metric was selected, it is to allow for a more meaningful comparison between the classical and robust estimators, since the former's bias is unbounded in the presence of outliers.

With these in mind, let's assume that $K = 8$ signal replicates are generated via a MC simulation approach from the compound model $\mathcal{N}$ with data rate $f = 100Hz$ and length $T = 524284$ data points (~1.5 hrs) apiece. This model consists of one AR1, one RW and one WN stochastic process, while for each replicate, their parameter values are random intercepts from the following beta (β) distributions:

$$\text{AR1}(\varphi) = 0.9835489 + (B_1 \cdot 3.4476489 \cdot 10^{-3}), \qquad B_1 \sim \beta(6,2) \qquad (4.12)$$

$$\text{AR1}(\xi^2) = 1.286053 \cdot 10^{-8} + (B_2 \cdot 9.019592 \cdot 10^{-9}), \qquad B_2 \sim \beta(2.2,6.1) \qquad (4.13)$$

$$\text{RW}(\gamma^2) = 2.904098 \cdot 10^{-11} + (B_3 \cdot 1.279669 \cdot 10^{-11}), \qquad B_3 \sim \beta(1.8,3.5) \qquad (4.14)$$

$$\text{WN}(\sigma^2) = 5.195192 \cdot 10^{-5} + (B_4 \cdot 5.24353 \cdot 10^{-6}), \qquad B_4 \sim \beta(3,4) \qquad (4.15)$$

Regarding Scenario I, after the "clean" replicates have been simulated, the characteristic WV of each multi-signal estimator, AWV, SR-AWV and DR-AWV were evaluated through the equations:

$$\overline{v}_{AWV} = \left[\sum_{i=1}^{K} w_i \hat{v}_{ij} \Big/ K \right], \qquad i = 1, \dots, K \text{ and } j = 1, \dots, j_{max} \qquad (4.16)$$

$$\overline{v}_{SR-AWV} = \left[\sum_{i=1}^{K} w_i \tilde{v}_{ij} \Big/ K \right], \qquad i = 1, \dots, K \text{ and } j = 1, \dots, j_{max} \qquad (4.17)$$

$$\overline{v}_{DR-AWV} = \left[\sum_{i=p+1}^{K-p} w_i \tilde{v}_{ij} \Big/ K - 2p \right], \qquad i = 1, \dots, K \text{ and } j = 1, \dots, j_{max} \qquad (4.18)$$

where the DR-AWV is chosen to utilize a 15% trim level ($p = 1$). Subsequently, each of these WVs as well as their respective weight matrices (see paragraph 4.4.1 for how they are calculated) were utilized in the context of the simplified algorithm presented in Section 4.2 to optimally estimate the parameters of $\mathcal{N}$. This process was repeated for $H = 500$ iterations and from the derived results, the RMSE of equation (4.11) was evaluated. Also, it is noted that the true $\mathcal{N}$ parameter values required for the calculation of the statistical metric were estimated via parametric bootstrap.

As for Scenario II, different kinds of outliers were introduced to the clean replicates, which are described in bullet form below:

- 131 data points (=0.025% of the overall length) were chosen in a random way from every signal and substituted with values produced by a WN process with $\sigma^2 = 0.02\,\text{m}^2/\text{sec}^4$. In this way, the lower scales of the WV are influenced.

- A step function with amplitude $A = 0.002\,\text{m/sec}^2$ and centered right in the middle of every one of those signals was added to their entirety in order to affect the higher WV scales.

- 5 vibrations that last 5 seconds each were introduced to three signal replicates every 15 minutes (i.e., 90000 data points), thus compromising the middle scales.

Given that, the same process as the first scenario was implemented, where all three multi-signal methods estimate the $\mathcal{N}$ model for each of the H simulations and the RMSE quantity was evaluated based on the results.

Finally, concerning Scenario III, it is practically the same as Scenario II but with one key difference. Specifically, the RW parameter value of the $\mathcal{N}$ model that produces one of signals with no vibrations is multiplied by a factor of 4 in order to create an abnormal replicate. In the end, the estimation of the $\mathcal{N}$ model coefficients was conducted using the classical and robust multi-signal estimators for the same number of simulations as before and the corresponding RMSE values were calculated from the solutions.

Using the RMSE produced from the three scenarios, a semi-log plot with respect to the y-axis is constructed and presented in Figure 4.11. From that, it is clear that all the estimators demonstrate a very similar level of efficiency in estimating the stochastic model parameters in Scenario I, where no outliers exist. Furthermore, in regard to Scenario II, the classical estimator appears to

be significantly biased compared to the robust estimators, which manage to maintain their performance at the same level as in the clean scenario, while also being equivalent with each other (just as in scenario I). Finally, in Scenario III, it is evident that the existence of the abnormal replicate has only deteriorated the efficiency of the SR-AWV estimator for the RW(γ^2), something that makes sense, considering the way it was created. As for the DR-AWV, it seems that it has managed to avoid its damaging impact.
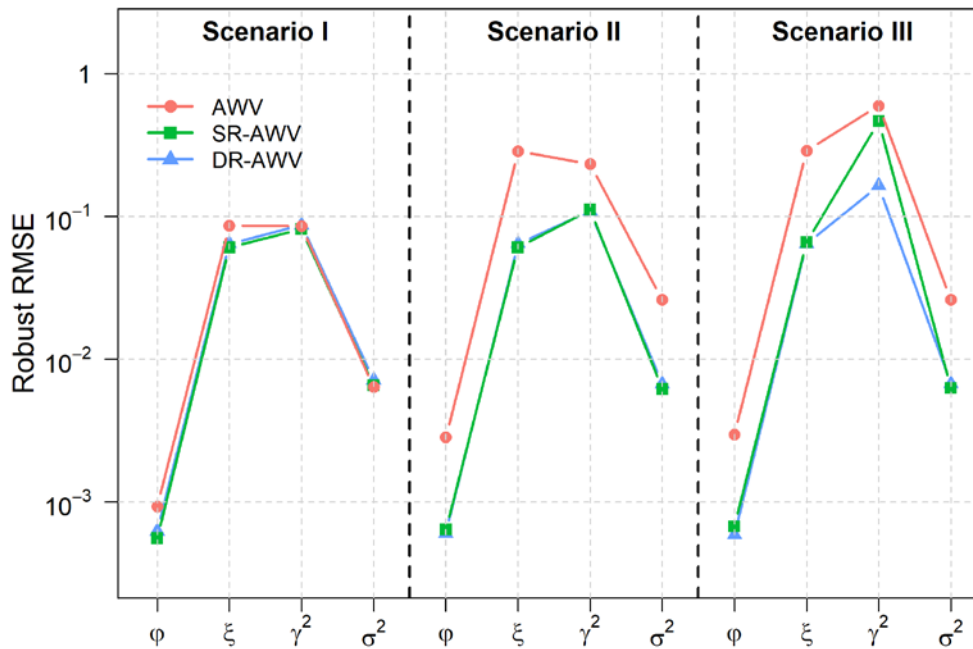
Figure 4.11: Robust RMSE values for each of the utilized multi-signal estimators and for every parameter of the $\mathcal{N}$ composite stochastic model.

Therefore, based on the above observations, it can be inferred that the robust estimators not only are capable of reducing the influence of outliers but also perform in a similar way as the classical one in the clean data scenario. In fact, the latter extends the conclusion derived in subsection 4.3 to the multi-signal case since the robust estimators can be safely used in the case of outlier-free data without meaningful loss in efficiency. Moreover, even though the DR-AWV is performing nicely under both data corruption and sample contamination conditions, the SR-AWV is particularly problematic when there is a replicate distribution problem.

This simulation study has been included within (Minaretzis et al., 2023), a manuscript that has been submitted for publication.

4.4.3 Case Study

In this part, the classical and robust AWV-based estimators will be utilized for the stochastic analysis of real inertial sensor datasets, produced by low-cost equipment. That equipment was chosen to be the MEMS-based Bosch Sensortec BMI085 IMU; a very small (i.e., 3.0mm × 4.5mm × 0.95mm), high performance, chip-based IMU that contains 16-bit accelerometer and gyroscope triads, and it was made for the purpose of Augmented/Virtual Reality applications.

The collection of data was conducted in a lab environment, where the device was positioned on a pre-levelled turntable and 6 static replicates of approximately 8.6 million data points (~12hrs) each were obtained under the same conditions using a 200Hz data rate. Furthermore, the deterministic calibration of the sensor was already implemented beforehand and with the obtained coefficients from that process, their effects were removed from the calibration datasets.

For the sake of demonstrating the importance of using the new robust multi-signal method, the Y-axis accelerometer replicates were chosen to be stochastically analyzed and presented here. Therefore, based on these signals, the characteristic WVs of the AWV (WV-AWV), SR-AWV (WV-SR-AWV) and DR-AWV (WV-DR-AWV) estimators using equations (4.16), (4.17) and (4.18) were calculated and Figure 4.12 was created, where all of them were plotted together for comparison along with their respective 95% CIs, calculated using a percentile parametric bootstrap approach and the chi-squared (χ^2) distribution (Efron and Tibshirani, 1994). From that, it can be inferred that the existence of outliers in each replicate severely compromises the WV-AWV in the mid scales, while the two robust ones are handling it quite well. In addition, it is evident that the abnormal replicate creates a problem on the higher scales, even for the WV-SR-

AWV and that the WV-DR-AWV manages to reduce its effects. Therefore, it is reasonable to select the DR-AWV estimator to stochastically model the random behavior of the Y-accelerometer.

Finally, by utilizing the algorithm presented in Section 4.2, it was identified that a composite model containing 4 AR1 processes is the one that best describes the behavior of WV-DR-AWV. Figure 4.13 demonstrates the fit of that model along with the individual contributions of those processes to the implied WV and which confirms the ability of the DR-AWV estimator to not only select an adequate model structure but also to efficiently estimate its coefficients in such a practical setting.

This case study and its results have been published in (Minaretzis et al., 2022).
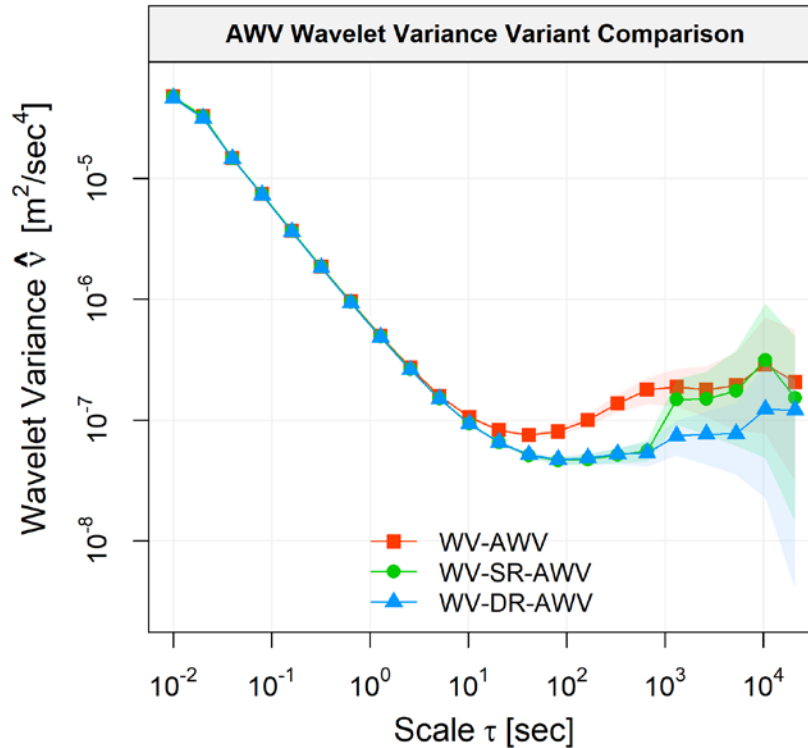
Figure 4.12: Comparison of the characteristic WVs of the multi-signal estimators AWV, SR-AWV and DR-AWV
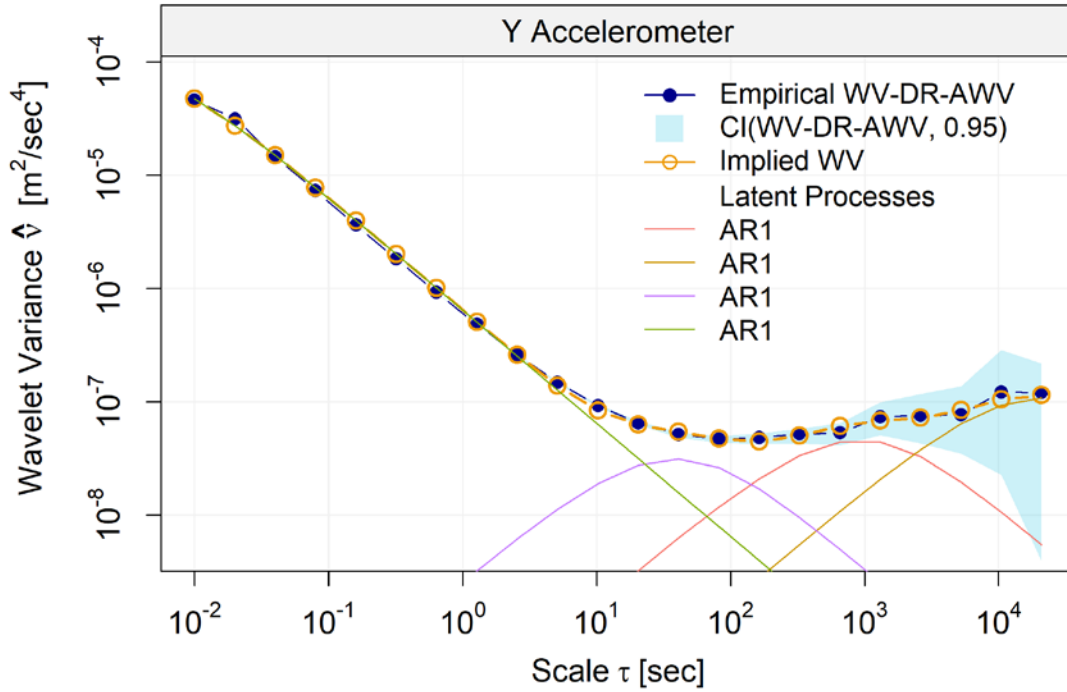
Figure 4.13: Model fit based on the WV-DR-AWV along with the corresponding 95% CIs and Implied WV derived from the estimated model parameters. The contributions to the overall fit of each of the included stochastic processes are also included.

4.4.4 Hybrid Case Study

In the previous two sections, the efficiency of the two new robust multi-signal estimators in targeting the true (unknown) parameter values under different types of contamination in the collected inertial sensor data was established in both a simulation and a case study. However, when the INS system is coupled with other sensors like the GNSS system, the correlation between the efficiency in estimating the true (unknown) stochastic model parameter values and the quality of the final integrated solution in terms of accuracy and validity of the obtained uncertainty is not at all apparent. Commonly, the assessment of a navigation system and thus the exposure of the aforementioned connection is implemented by conducting a small number of real-life experiments and then comparing the derived solution with one produced by a higher-grade system.

Nevertheless, the inference of statistically meaningful conclusions would require the replication of thousands of such experiments, which is not feasible in practice.

With these in mind and with the purpose of combining practical experimentation and strong statistical consideration, a recently proposed navigation simulator[3] in (Cucci et al., 2023b) is utilized. Specifically, this engine makes use of real trajectory information to produce ideal sensor data and along with sensible and programmable error generating algorithms, contaminates them in order to mimic real-life INS/GNSS navigation settings. Subsequently, it employs multiple different realizations of this realistic information within a conventional EKF in order to estimate the navigation solution for each of them. Therefore, in this way, a reasonable approximation to the anticipated system performance can be obtained in a statistically rigorous way since the metrics about the solution accuracy and reasonableness of the estimated confidence intervals are evaluated based on a large number of experiment replicates. Furthermore, given that, it is possible to make an informed decision between possible configurations.
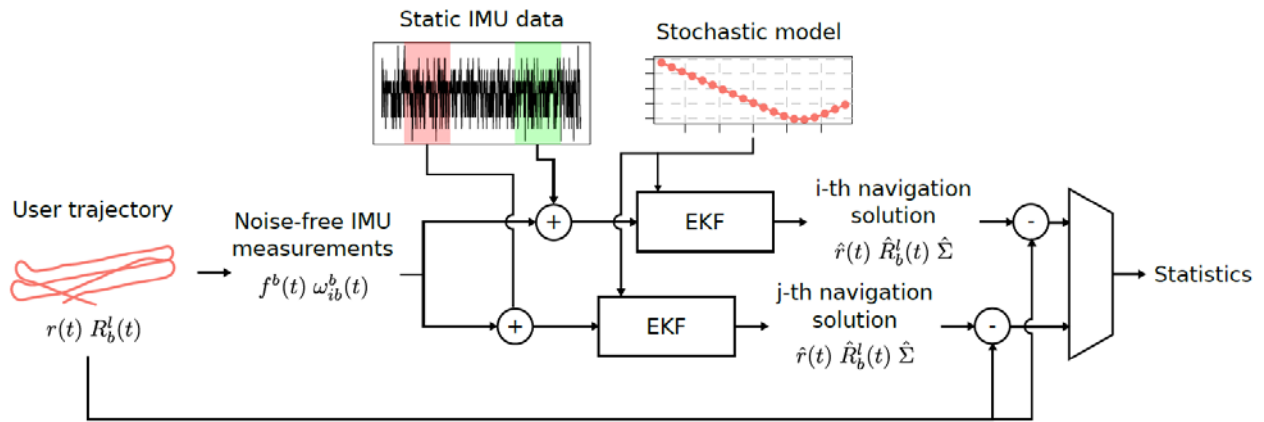
Figure 4.14: Schematic representation of the navigation simulator algorithm.

The algorithm according to which this navigation simulator operates is demonstrated in Figure 4.14 and described below in some detail:

[3]The Nav Simulator "R" package: https://github.com/SMAC-Group/navigation

1) According to the application that is being considered, a trajectory is inputted within the simulator in the form of position r_t and orientation $\mathbf{R}_{b,t}^n$ (direction cosine matrix) datasets with a certain (stable) rate. This trajectory is considered to be the reference solution.

2) For every single MC simulation that will be conducted, the position and orientation data are utilized for the inference of the following quantities:

$$\mathbf{v}_t^n = \frac{r_{t+1} - r_t}{\Delta t} \tag{4.19}$$

$$\boldsymbol{\alpha}_t^n = \frac{\boldsymbol{v}_{t+1}^n - \boldsymbol{v}_t^n}{\Delta t}, \tag{4.20}$$

$$\boldsymbol{\omega}_{nb,t}^b = \frac{log\left(\mathbf{R}_{b,t}^n{}^{\mathrm{T}}\mathbf{R}_{b,t+1}^n\right)}{\Delta t}, \tag{4.21}$$

where $\mathbf{v}_t^n$ is the velocity of the moving platform in the n-frame, $\boldsymbol{\alpha}_t^n$ is the corresponding acceleration, $\boldsymbol{\omega}_{nb,t}^b$ is the angular velocity of the body frame with respect to the n-frame and expressed in the body frame, $log(\cdot)$ expresses the logarithmic mapping in the SO(3) 3D rotation group (see (Solà, 2017) for an in-depth description of this notion) and Δt is the interval of the input data.

Then, error-free inertial sensor measurements are reverse-engineered using the results provided by equations (4.19), (4.20) and (4.21) as well as the orientation data like so:

$$\text{Gyroscope measurements} \rightarrow \boldsymbol{\omega}_{ib,t}^b = \boldsymbol{\omega}_{nb,t}^b + \left(\mathbf{R}_{b,t}^n\right)^{\mathrm{T}}\mathbf{R}_e^n\,\boldsymbol{\omega}_{ne}^e, \tag{4.22}$$

$$\text{Accelerometer measurements} \rightarrow \boldsymbol{f}_t^b = \mathbf{R}_{b,t}^n{}^{\mathrm{T}}(\boldsymbol{\alpha}_t^n + \mathbf{g}^n), \tag{4.23}$$

where $\mathbf{R}_e^n$ is a transformation matrix between the n-frame and the Earth-Centered Earth-Fixed (ECEF) frame (e-frame, position-dependent), $\boldsymbol{\omega}_{ne}^e$ represents the Earth's rate of rota-

tion and $\mathbf{g}^n$ is the gravity vector in the n-frame. Moreover, it is very important to mention that for the inference of the aforementioned quantities, a non-rotating and flat Earth is considered. As a result, the effects of the Earth's rotation, the Coriolis acceleration, the coning and sculling as well as the direction variation of the gravity vector are completely ignored. And despite the fact that such gross simplification is unreasonable for real-world applications, (Cucci et al., 2023b) considered that this assumption has a minimal influence to the assessment of the employed inertial sensor stochastic model, according to a certain accuracy requirement. Besides, in the case where low-cost IMUs are employed, such effects are overshadowed by the significant random drift that typically characterizes such devices.

3) At this point, the simulator assumes that the inertial sensor error behavior is somewhat independent from the environmental conditions (i.e., temperature, platform dynamics), which as mentioned in Section 3.3, is not valid for low-cost and consumer grade IMUs. As a result, static measurements are considered to only contain noise and that this noise has the same characteristics as the one that affects the sensor operation during a standard kinematic operation. Therefore, with this in mind, erroneous inertial sensor measurements are created by adding random parts from real static datasets (different parts for every MC iteration). Furthermore, a noise model is assumed for the GNSS position and velocity information, which for the sake of simplicity is assumed to be WN.

4) A standard EKF is infused with the stochastic modeling knowledge that is to be investigated (See Chapter 5 for how this is implemented) and in turn, processes the erroneous INS and GNSS measurements and estimates the final navigation solution. This procedure is repeated in an MC fashion, with different noise realizations being employed every time.

5) The results from all the simulations are utilized for the computation of statistical metrics (e.g., empirical coverage, mean position, and orientation error) in order to assess the anticipated performance of the system based on the considered scenario.

Based on this INS/GNSS simulator, an experiment is designed to quantify and compare the navigation performance when the EKF is infused with information about the inertial sensor error behavior. As for where this information comes from, it is derived by utilizing each of the three mentioned multi-signal estimators in three different calibration data contamination scenarios. Therefore, in this way, a rigorous investigation will be conducted for the contribution to the navigation solution of different levels of robustness in the multi-signal approach. In the following, the configuration of the simulation-based engine is described in detail.

Initially, a 15-minute car trajectory shown in Figure 4.15 was inputted within the simulator in the form of position and orientation data at a 100Hz rate. In fact, it was produced by NovaTel's high-end Synchronous Position, Attitude and Navigation (SPAN) system by fusing information in a loosely coupled manner from a tactical grade iMAR-FSAS FOG IMU (100Hz data rate) whose specifications are shown in Table 4.1 and a GPS/GLONASS high performance GNSS receiver (1Hz data rate).

In addition, the rate that the simulated GPS position and velocity information is made available was set to 1Hz (very common in practice) and the stochastic models that describe their errors were also set. Specifically, the horizontal and vertical position errors are assumed to be produced from WN processes with variances 4m^2 and 16m^2 respectively, while the horizontal and vertical velocity errors were also set to be defined by WN processes with $0.0016\,\text{m}^2/\text{sec}^2$ and $0.0036\,\text{m}^2/\text{sec}^2$ each.

Trajectory

Altitude profile
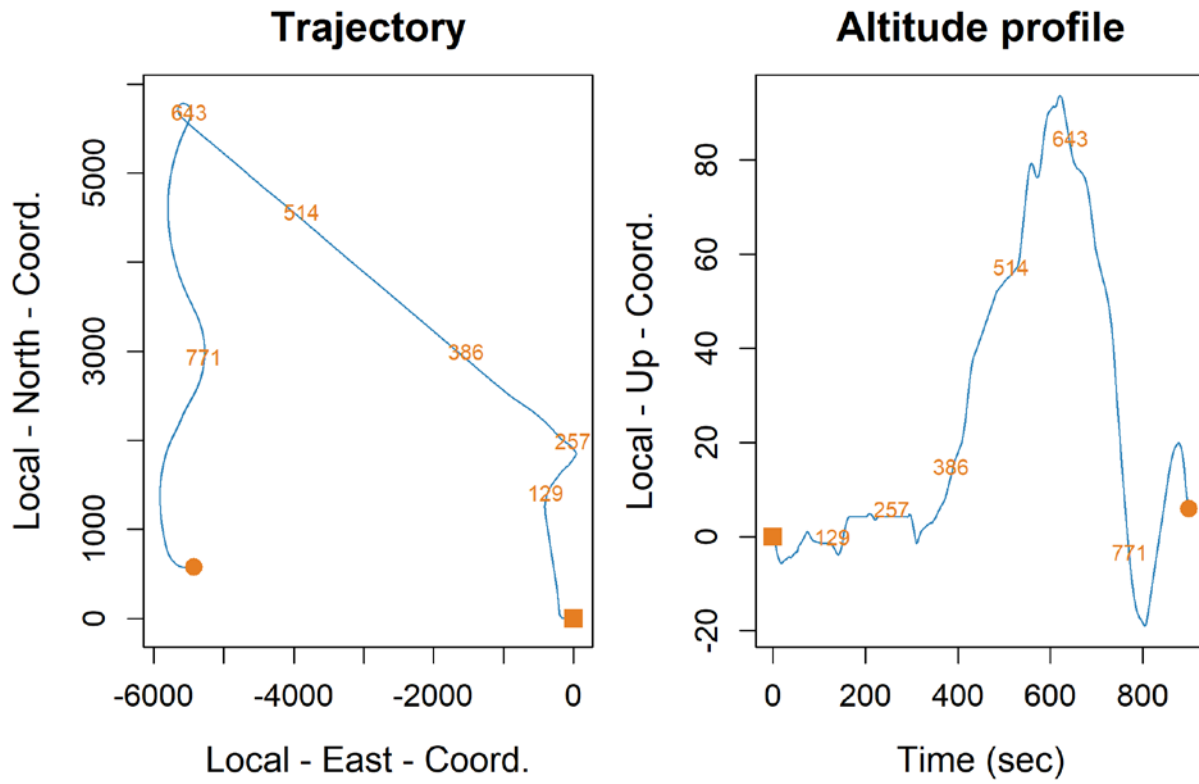
Figure 4.15: Car trajectory provided by the SPAN system.

Table 4.1: iMAR-FSAS IMU technical specifications

Performance Specifications	iMAR-FSAS	
	Gyroscopes	Accelerometers
Maximum Data Rate	200 Hz	200 Hz
Range	$\pm$ 500 deg/sec	$\pm$ 5g
Bias	0.75 deg/hr	1.0 mg
Scale Factor	300 ppm	300 ppm
ARW/VRW	0.16 deg/$\sqrt{hr}$	50 μg/$\sqrt{Hz}$

Subsequently, numerous 1.5hr static datasets at a 100Hz rate (T = 524284 data points) were collected using the consumer-grade MEMS-based Xsens MTi-G-710 IMU (Movella, 2023), which is a small sized device that contains a tri-axial accelerometer and a tri-axial gyroscope, among other sensors (i.e., magnetometers, barometers, temperature sensors) and whose specifications are shown in the Table 4.2.

Table 4.2: Xsens MTi-G-710 technical specifications

Performance Specifications	MTi-G-710	
	Gyroscopes	Accelerometers
Maximum Data Rate	2000 Hz	2000 Hz
Range	$\pm$ 450 deg/sec	$\pm$ 20 g
Bias	0.2 deg/hr	5.0 mg
Scale Factor	0.01 %	0.1 %
Non-orthogonality	0.05 deg	0.05 deg
ARW/VRW	0.6 deg/$\sqrt{\text{hr}}$	60 µg/$\sqrt{\text{Hz}}$

From them, the signals that presented minimal differences between their classical and robust WV were selected as the ones that are more likely to be outlier-free (crude indicator). In addition, the WVs of the "clean" signal replicates were compared with each other and it was identified that the horizontal accelerometers present a very similar behavior with each other, while the same also applies for the horizontal gyroscopes. Therefore, with these in mind, 8 accelerometer and 8 gyroscope replicates were chosen to be used for the stochastic error analysis (see Figure 4.16 for the WVs of the gyroscope signals), while 1 accelerometer and 1 gyroscope replicate were selected as

indicative of the overall behavior in order to be used by the simulator as the contamination source of the "perfect" inertial sensor measurements.
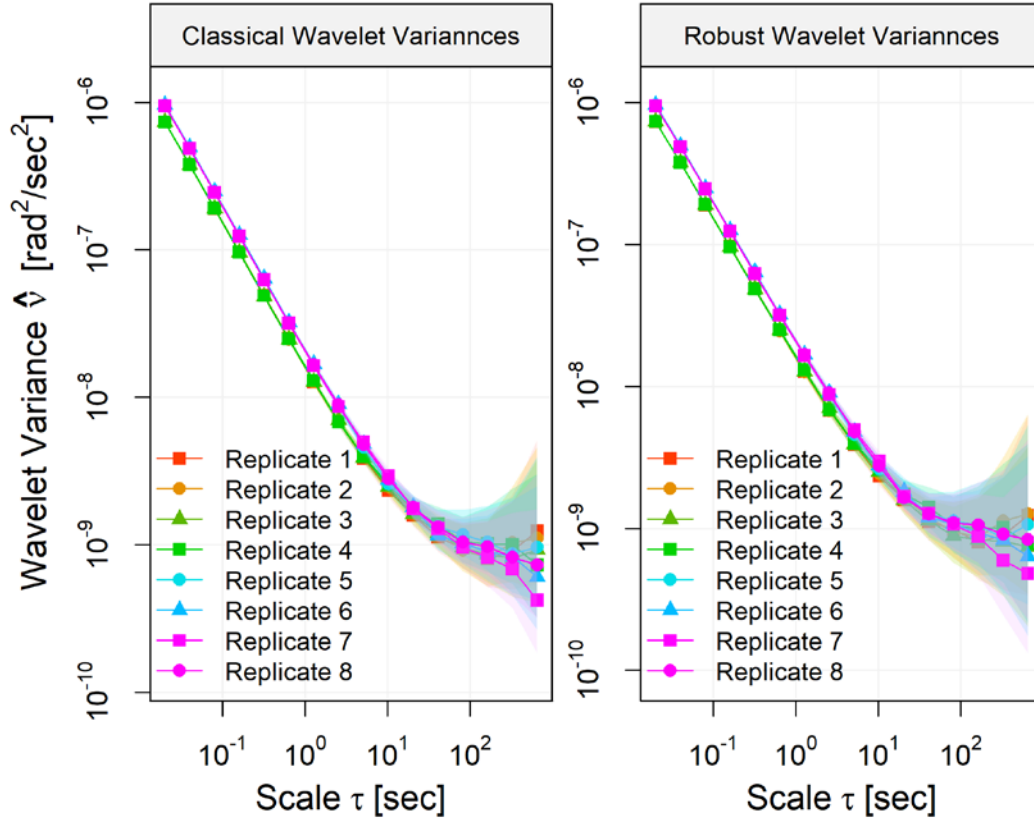
Figure 4.16: Comparison between classical and robust WVs of the 8 selected gyroscope signal replicates.

The selected "clean" signal replicates represent Scenario I and by using equations (4.16), (4.17) and (4.18), the characteristic WV of the AWV, SR-AWV and DR-AWV (with $p = 2$) multi-signal estimators are evaluated. From them, it was identified that the composite model $\mathcal{S}$, comprised of two AR1s, one RW, one WN and one QN stochastic process is capable of sufficiently describing the random behavior of both signal types. Figure 4.17 demonstrates the fit of that model to the WV-AWV along with its respective 95% CIs (evaluated via a percentile parametric bootstrap approach), the model-implied WV, and the individual process contribution.
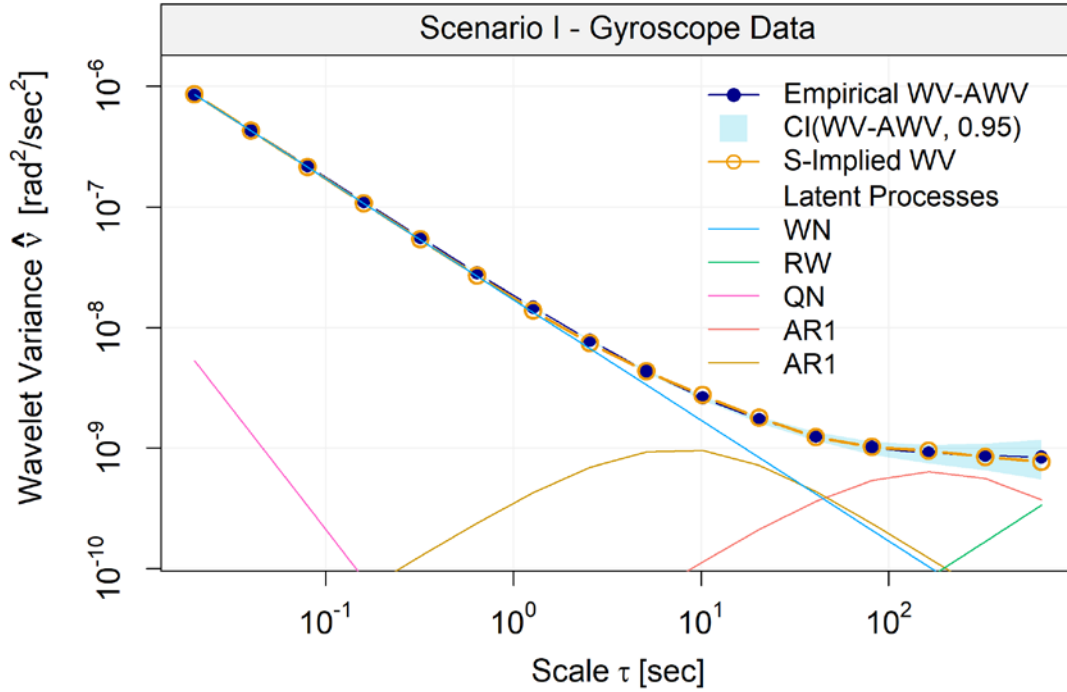
Figure 4.17: $\mathcal{S}$ model fit to the WV-AWV, derived from the gyroscope data.

Regarding Scenario II, the following data corruption-type outliers, whose collective influence affects the entirety of the WV spectrum, are introduced to both types of signals:

- 1% of each signal (accelerometer and gyroscope) is randomly selected and replaced with data points drawn from a WN distribution that is characterized with a variance equal to $0.0256\,\mathrm{m}^2/\mathrm{sec}^4$ for the accelerometer and $0.000676\,\mathrm{rad}^2/\mathrm{sec}^2$ for the gyroscope signals (affects the higher frequencies)

- Small vibrations (500 data points) are introduced to the signals every 90000 samples to every signal. This means that eventually, the total number of these vibrations is equal to 5 (affects the mid frequencies)

- A step function is centered to the middle of each signal and then added to them. Specifically, the amplitude A of that function is $A_{\mathrm{accel}(i)} = \{0.0041, 0.0032, 0.0055, 0.0045, 0.0034,$

$0.0060, 0.0061, 0.0030\}$ m/sec^2 and $A_{\mathrm{gyro}(i)} = \{0.00095, 0.00114, 0.001, 0.00094, 0.0011,$

$0.00085, 0.00055, 0.0009\}$ rad/sec for $i = 1, \dots 8$ (affects the lower frequencies)

Based on that, the characteristic WVs of the three estimators, meaning the WV-AWV, WV-SR-AWV and WV-DR-AWV, are evaluated and plotted in Figure 4.18. By inspecting this figure, it is clear that the characteristic WVs of the robust estimators demonstrate an almost identical behavior, while the WV of the classical one appears to be considerably affected in the lower and higher time scale regions. Moreover, even though the robust estimators are unable to stay unaffected in the mid scales, they do manage to remain close to the "clean" data behavior for the lower (WN part) and higher (RW part) ones. Then, using these WVs and the corresponding estimator, the $\mathcal{S}$ model parameters are estimated.
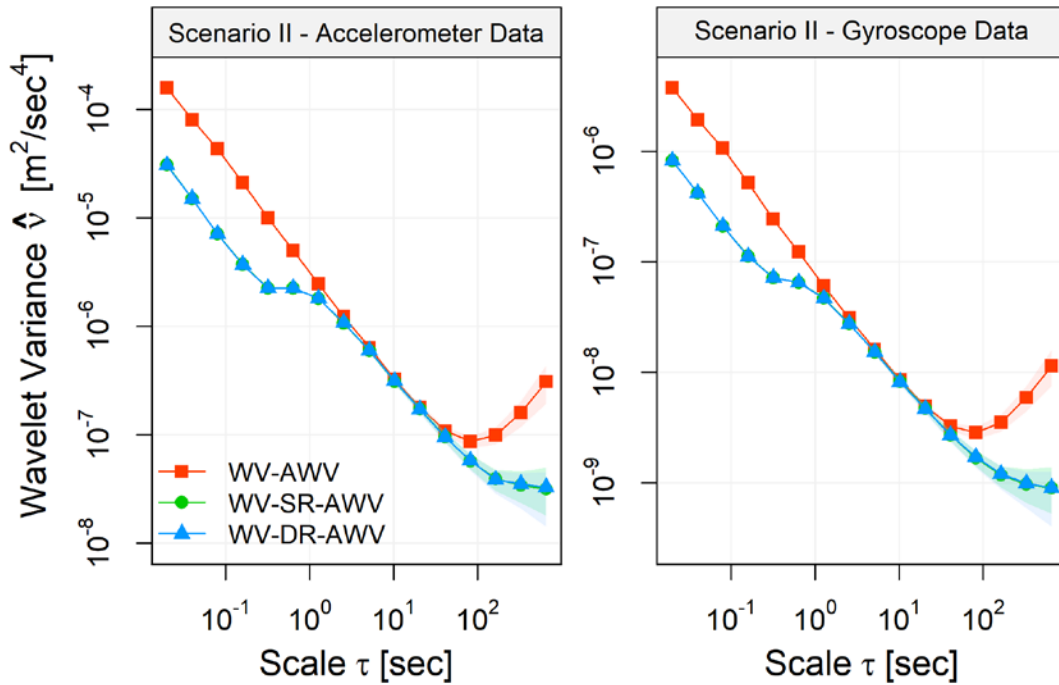
Figure 4.18: Comparison between the WV-AWV, WV-SR-AWV and WV-DR-AWV in a log-log plot with respect to the time scales based on the Scenario II calibration data.

As for Scenario III, a condition where both data corruption and sample contamination are present in the calibration data at hand is created by modifying the Scenario II setting. Specifically,

two signals from both data types are forced to demonstrate an abnormal WV behavior compared to the rest by changing certain outlier attributes and by adding a new outlier type like so:

- The variances for the WN point replacement are set to be $\sigma^2_{accel(i=3,8)} = 0.0324 \, m^2/sec^4$ and $\sigma^2_{gyro(i=2,5)} = \{0.000484, 0.000676\} \, rad^2/sec^2$

- The step function amplitudes are altered to the have the values $A_{accel(i=3,8)} = \{0.0062, 0.0045\} \, m/sec^2$ and $A_{gyro(i=2,5)} = \{0.00114, 0.0011\} \, rad/sec$

- Sequences with the same length as the considered signals are produced by AR1 processes and then added to the entirety of the accelerometer and gyroscope signals that were chosen to be the abnormal ones. The properties of each of these processes are $AR1_{accel(i=3,8)} = (\varphi = 0.975761, \xi^2 = 3.397832 \cdot 10^{-7})$ and $AR1_{gyro(i=2,5)} = \{(\varphi = 0.97239103, \xi^2 = 1.074129 \cdot 10^{-8}), (\varphi = 0.9766580, \xi^2 = 5.313189 \cdot 10^{-9})\}$.

Subsequently, using this data assembly, the WVs used by the three multi-signal estimators are calculated and illustrated in Figure 4.19. Based on that, it is evident that the WV-DR-AWV manages to reduce the impact of the two outlying signal replicates in the mid time scales (AR1 region) and remain in similar levels as in Scenario II, while the same cannot be said for the other two. Therefore, it is confirmed that this scenario fulfills the condition of simultaneous data corruption and sample contamination existence. In turn, the stochastic analysis is conducted by all three estimators based on their corresponding characteristic WV and thus, all the required knowledge to properly configure the navigation simulator for the purposes of this study has been obtained.
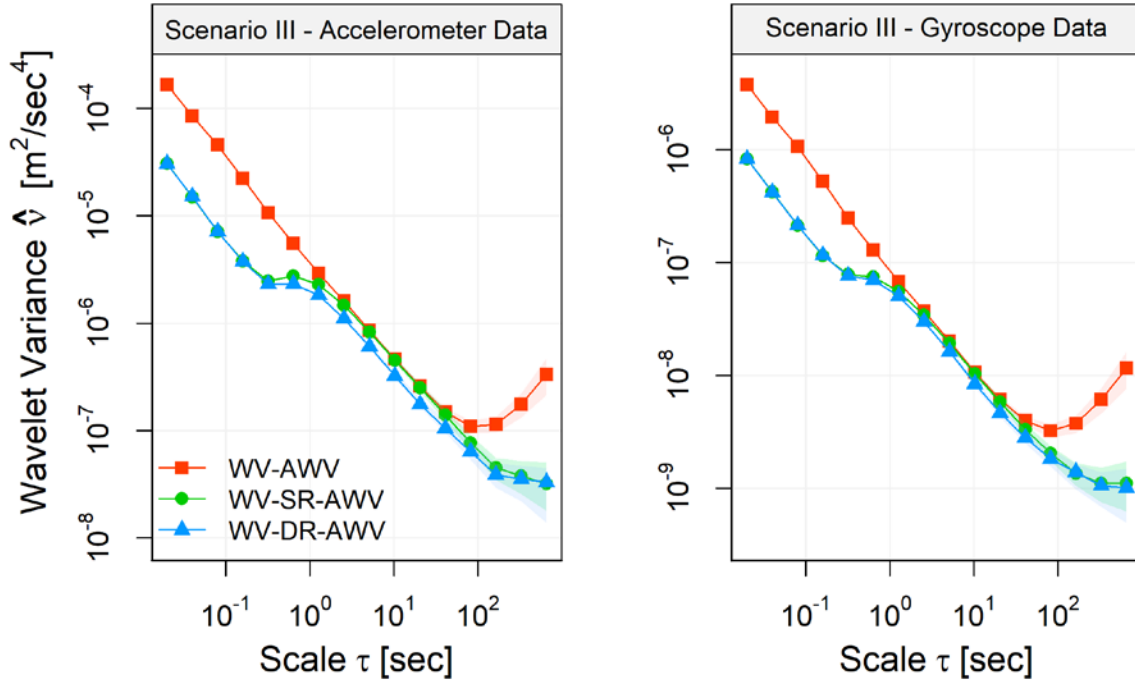
Figure 4.19: Comparison between the WV-AWV, WV-SR-AWV and WV-DR-AWV in a log-log plot with respect to the time scales based on the Scenario III calibration data.

Finally, in order to obtain a direct insight of the contribution of the employed inertial sensor random error modeling knowledge to the INS standalone performance, two 90-second GNSS outages are introduced (300-390sec and 700-790sec). Therefore, the configuration of the INS/GNSS simulator that has been described so far is utilized and $H = 10000$ MC simulations are conducted. Furthermore, this procedure is implemented with the simulator's EKF being infused with the stochastic analysis information inferred from each estimator and calibration data scenario. In the end, 9 different collections of navigation solutions from the H conducted test runs are provided by the simulator's engine.

As it was mentioned earlier, this simulator makes a couple of crude simplifications that make the produced results to be rather unrealistic in terms of real-world navigation performance. Nevertheless, a comparison between statistical metrics obtained under different configurations of the employed stochastic estimator and calibration data, is more than enough to deduce reasonable

conclusions about whether one is better than the other. Furthermore, it should be highlighted that the purpose of robustness in the stochastic modeling of inertial sensor noise is to ensure that the information provided to the EKF will aid the INS standalone performance to maintain stability of the navigation solution and its reliability. Therefore, with these in mind and for the purpose of assessing and comparing the quality of the resulting INS/GNSS solutions driven by different stochastic estimators about the inertial sensor random errors, the empirical coverage (Refer to (Cucci et al., 2023b) for how this quantity is calculated by the simulator's framework) and the standard estimation errors (SEEs) for the position and orientation states (uncertainty estimated by the EKF) are evaluated and studied.

Empirical Coverage Analysis

The empirical coverage, as calculated by the navigation simulator, considers the results of the total number of conducted simulations and allows the evaluation of the estimated position and orientation solutions as well as their respective uncertainty (provided by the EKF) in terms of accuracy and reliability concurrently. Specifically, the empirical coverage (corresponding to the position and orientation states as a whole) expresses the probability that single-sided confidence intervals of level $sl = (1 - a)$ (based on the chi-squared distribution), built using the estimated position and orientation solutions as well as their respective covariance, contain the true values.

For the purposes of this study, a confidence level of $sl = 70\%$ is utilized. The rationale behind this decision is that it is important to have a certain range of behavior above and below the selected level in order to safely determine whether the produced estimates are being either overconfident or pessimistic. Furthermore, if the EKF-provided uncertainties are valid, then the credibility of the previously mentioned confidence intervals is ascertained by the observed empirical coverage residing within a certain range around the theoretical level (i.e., 70%). This range rep-

resents the simulation error and according to (Cucci et al., 2023b), the following formula can be used to provide an estimate of the 95% confidence interval for the empirical coverage:

$$[CI_{low} \quad CI_{high}] = p \pm 1.96 \sqrt{\frac{\text{a} \cdot sl}{H}}, \qquad (4.24)$$

where CI_{low} and CI_{high} is the lower and upper limit of the ideal empirical coverage behavior and H is the number of Monte-Carlo runs that were considered for the calculation of the metric. In this study, this interval is approximately between 69.1% and 70.9%.

Given what has been said, the 70% empirical coverage is calculated for the results from each of the 9 different configurations that were mentioned earlier, and a snapshot of that behavior is provided in Figure 4.20 in percentage units.

According to this figure, and particularly for Scenario I, it can be observed that general behavior of the coverage is not in the desired levels for the entirety of the trajectory and the reasons behind this are related to problems encountered during the data collection, which in turn appear to have influenced the estimation quality of the orientation states. However, despite that, a relative comparison of the metric's behavior between solutions driven by the different estimators can still provide viable conclusions.

With the purpose of making the inference of such conclusions more apparent, the empirical coverage error is calculated as the difference between the theoretical probability (70%) and the ones based on estimations at hand. Then, Table 4.3 is constructed, which contains the mean empirical coverage error for the GNSS outage regions and for each of the three employed stochastic estimators in the three calibration data scenarios. Finally, as to why particular focus is given to these areas, it is where the INS system operates on standalone mode and thus, the full impact of

the provided stochastic modeling knowledge about the inertial sensor errors to the navigation performance can be perceived.
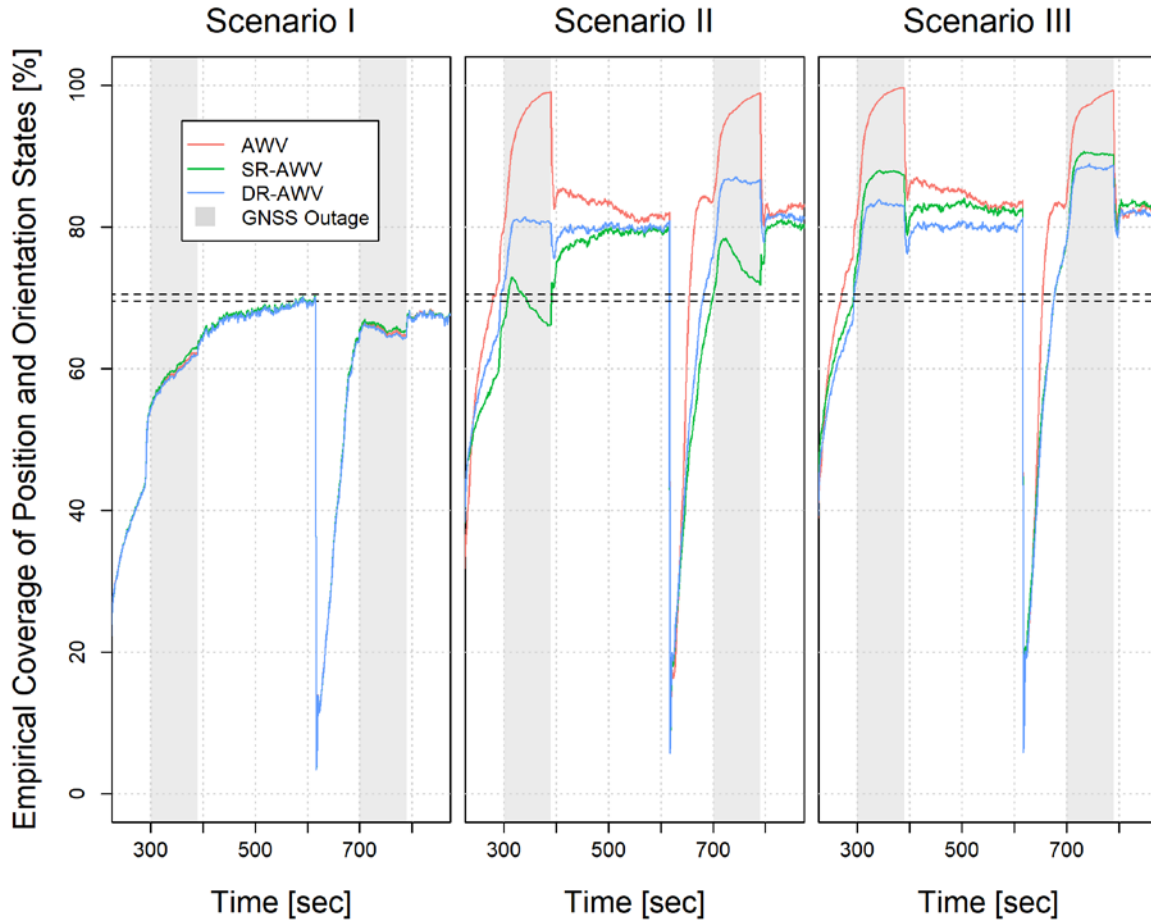
Figure 4.20: 70% Empirical coverage of the combined position and orientation states for each estimator and calibration data contamination scenario.

Table 4.3: Mean empirical coverage error for the two GNSS outage areas and for each of the three estimators used in the different calibration data scenarios.

	Scenario I [%]		Scenario II [%]		Scenario III [%]	
	Outage 1	*Outage 2*	*Outage 1*	*Outage 2*	*Outage 1*	*Outage 2*
AWV	10.75	4.51	-24.82	-25.49	-26.32	-26.32
SR-AWV	**10.30**	**4.15**	**0.97**	**-4.81**	-16.20	-19.04
DR-AWV	11.07	4.84	-9.93	-15.51	**-12.16**	**-17.38**

According to Table 4.3 for Scenario I, all three estimators seem to provide stochastic modeling information about the inertial sensor errors that leads to pessimistic estimations for the position and orientation states. Nevertheless, their resulting navigation solutions have almost the same quality in terms of closeness to the reference and correctness of the derived reliability for both outage regions. Consequently, this confirms the outcomes of the previously conducted simulation and case studies in the navigation setting. In other words, the new robust estimators can be used even in a clean data scenario, without the need for confirmation of outlier existence, and still be equivalent to the classical estimator in terms of implied navigation solution quality.

Regarding Scenario II, the SR-AWV demonstrates the smallest coverage errors, with their values indicating that for the 1st outage, the estimation quality of the position and navigation states is almost optimal, while for the 2nd, such estimations are being a little overconfident. As for the other robust estimator, it appears to be about 10% more overconfident than the SR-AWV for both outages in this scenario. Actually, this partly contradicts the conclusion of the simulation study, because instead of having the two robust estimators performing the same, the SR-AWV appears to be the most dependable in this particular setting by far. Nevertheless, the DR-AWV demonstrates the second smallest coverage error and a much better behavior than the classical estimator-driven solution, which is considerably unreliable in comparison.

Finally, for Scenario III, it is evident that the DR-AWV manages to maintain the empirical coverage error in nearly the same levels as in Scenario II, while the same cannot be said for the SR-AWV. Furthermore, it is noticed that the difference in coverage error between the two robust estimator-driven solutions for Scenario III does not appear to be significant. It is speculated that the reason behind this is related to the way that the abnormal replicates were created, which was with the addition of an AR1 process. As a result, this impacted the estimation quality of the time-

correlated processes of the $\mathcal{S}$ model for the SR-AWV but it had little effect to that of the DR-AWV. Then, by considering this, along with the fact that the trajectory is relatively small (i.e., 15min), there is no adequate time for the influence of the time-correlated processes to become significant enough. Therefore, the superior efficiency of the DR-AWV in estimating them cannot be expressed as a considerable improvement to the navigation performance compared to that implied by the SR-AWV. Nevertheless, this is still a proof of concept that in the case where both data corruption and sample contamination exist in the calibration data, unlike the SR-AWV, the DR-AWV is capable of maintaining the stability of the navigation solution in terms of accuracy and validity of the estimated reliability.

Standard Estimation Error Analysis

The SEE of the position and orientation states, as that is provided by the EKF, is a metric that has been chosen to be utilized for the reliability assessment of the derived navigation solution from the simulator. Furthermore, in order to consider the multiple Monte-Carlo realizations of the same experiment, the SEE should be averaged over the total number of conducted simulations, thus creating the Average Standard Estimation Error (ASEE). However, an inspection of all the available SEEs revealed that the variability of the behavior from one MC run to another is minimal for all the position and orientation states, meaning that a smaller number of simulations can be considered, without affecting the inference of conclusions. Therefore, with this in mind, as well as to reduce the computational load, the calculation of the ASEE is chosen to be conducted based on 100 MC simulation solutions.

What is more, a reasonable assumption is made that the AWV-based solution in Scenario I can be considered to be optimal and as such, the validity of the reliability that the other solutions provide should be evaluated by a comparison with it. Consequently, ratios are evaluated with re-

spect to this reference and for all the available ASEE information. For illustration purposes, Figure 4.21 is created, which contains a snippet of these ratios for the East position (Xe) and the Roll Angle (RA) attitude state, each of which was considered to be representative of all the other position and orientation components. In addition, the mean values of the ASEE ratio errors during the GNSS outages are calculated as the difference of each ratio from unity in percentage units and then provided in Table 4.4 for the East position component and Table 4.5 for the roll angle. In this way, a quantitative analysis of the inspected quantity is brought forth.
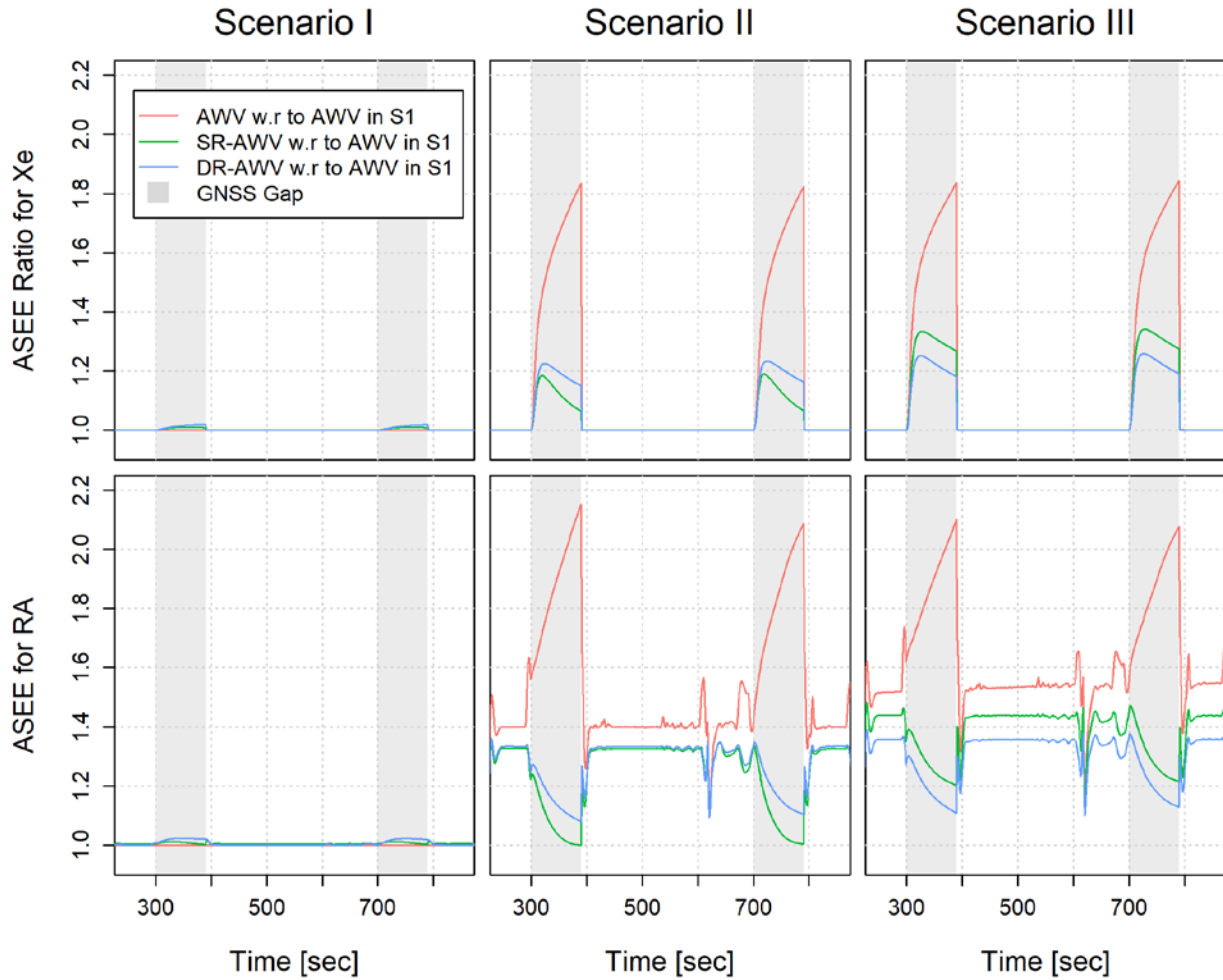
Figure 4.21: ASEE ratios of the East position component (Xe) and roll angle (RA).

Regarding Scenario I and based on Figure 4.21, it is obvious that the robust estimator-based solutions for both position and orientation states are characterized by almost the same reliability

as the reference. As a result, the equivalence of the robust estimators to the classical one in terms of implied navigation performance is once again confirmed in the clean calibration data scenario.

Table 4.4: Mean values of the East position ASEE ratio error for the two GNSS outage regions in each scenario.

	Scenario I [%]		Scenario II [%]		Scenario III [%]	
	Outage 1	*Outage 2*	*Outage 1*	*Outage 2*	*Outage 1*	*Outage 2*
AWV	–	–	75.07	74.05	76.75	77.19
SR-AWV	**0.96**	**0.94**	**9.33**	**9.65**	28.88	29.72
DR-AWV	1.82	1.75	17.23	18.48	**20.24**	**21.24**

Table 4.5: Mean values of the roll angle ASEE ratio error for the two GNSS outage regions in each scenario.

	Scenario I [%]		Scenario II [%]		Scenario III [%]	
	Outage 1	*Outage 2*	*Outage 1*	*Outage 2*	*Outage 1*	*Outage 2*
AWV	–	–	95.46	91.00	93.58	92.45
SR-AWV	**0.74**	**0.75**	**4.24**	**5.36**	25.00	26.86
DR-AWV	2.09	1.97	13.01	15.46	**16.06**	**18.21**

As for Scenario II, it is strongly implied in Figure 4.21 that the estimations provided by the AWV-driven solution are considerably undermined along the entirety of the trajectory and especially during the GNSS outages. On the other hand, the robust estimators manage to remain stable, with the SR-AWV being the one that provides the most realistic estimation confidence by a margin of at least 10% on average for both state types with respect to the DR-AWV (according to Table 4.4 and Table 4.5).

Concerning Scenario III and according to the tables above, the DR-AWV solution provides the most sensible uncertainty information, which has actually only increased by about 3% compared to its respective one in Scenario II, for the position and orientation components in each GNSS outage region. Inversely, the SR-AWV is noticeably problematic since it demonstrates an increase in the estimated uncertainty at a level of 20% in general, compared to Scenario II. Finally, it is worth mentioning that Figure 4.21 suggests that the destabilization of the SR-AWV has not only affected the reliability estimation in the GNSS outage regions but also in the rest of the trajectory.

4.5 Stochastic Calibration of a Consumer-grade MEMS-based IMU Using the New Robust Multi-Signal Method and the Standard AVLR

In this section, the stochastic calibration of consumer-grade MEMS-based inertial sensors is presented, where the newly proposed robust multi-signal approach as well as the conventional single-signal AVLR are utilized.

These sensors were chosen to be the ones included within the Xsens MTi-G-710 device (Movella, 2023), which is a small-sized ($57 \times 42 \times 23.5$mm) assembly of multiple different sensors and it is generally considered to be ideal for visual-inertial systems, UAV navigation and surveying applications. Specifically, this apparatus contains a built-in multi-constellation GNSS receiver (i.e., GPS, GLONASS, BeiDou, and Galileo), accelerometer, gyroscope, and magnetometer triads as well as barometer and temperature sensors. Therefore, by fusing the information from all of them, it can provide high rate (up to 2000Hz) position and orientation solutions of very good quality. Furthermore, it can provide the fundamental observables from each individual sensor type, like for example, 6 Degree of Freedom (DoF) acceleration and angular rate measurements. In this study, only the latter will be utilized for the purpose at hand.

As it was mentioned in Section 3.3, before the stochastic modeling of the inertial sensor errors is conducted, a deterministic calibration process must occur first. In this case, the 6-position static and angle rate tests described in paragraph 3.2.2 were chosen to be implemented in a lab setting. However, because the equipment for accurately aligning the device along those 6 positions was out of commission, certain creative improvisations had to be made with the available hardware. Specifically, the Animatics SmartMotor™ Series 4, a single-axis precise rate turntable, was utilized to introduce the constant rotation required for the calibration of the gyroscopes (i.e., 60 deg/sec) and which is shown in Figure 4.22.
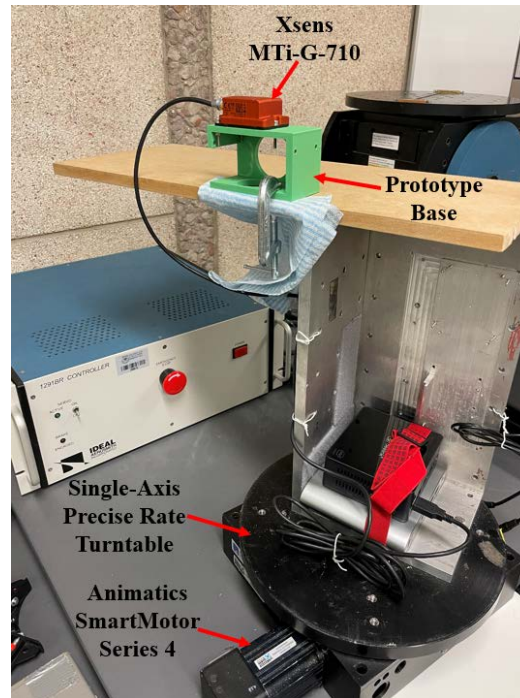
Figure 4.22: The complete apparatus used for the deterministic and stochastic calibration of the Xsens MTi-G-710.

Furthermore, it was noticed that there wasn't a safe way to place the computer and its power source on the table, both of which are required for the collection of the inertial data while the table is rotating. To resolve this issue, a metal construct was mounted onto the levelled turntable, thus allowing the equipment placement for the data retrieval. In turn, a prototype base was built using a 3D printer, where the MTi can be securely bolted on and which in turn can be rotated in

such a way so that alignment with each of the 6-positions can be achieved with an acceptable precision. Finally, a piece of wood was secured on top of the metal construct, where the prototype base can be bolted on[4], along with the MTi. Therefore, given this configuration, the inertial sensor deterministic calibration became feasible, and it was conducted in the manner described in paragraph 3.2.2 to obtain coefficients that describe the deterministic error effects. In the next part, these coefficients will be utilized to create signals that (theoretically) contain only random errors and by using those, implement the stochastic calibration of the MTi inertial sensors using two different methods.

SR/DR-AWV Analysis

For the purpose of modeling the random error behavior of the MTi-G-710 inertial sensors using the newly proposed method, the device was again placed on the apparatus shown in Figure 4.22 (with its Z-axis being parallel to the pre-levelled table's sensitive axis) and 6 static signal replicates were collected using a 100Hz data rate for each inertial sensor. Subsequently, the robust WVs were calculated based on the deterministic error-free data and then, they were compared with each other (for each sensor) in order to determine whether the SR-AWV or the DR-AWV estimator is more suitable for the analysis. These WVs are presented in Figure 4.23 along with the characteristic WV of the estimator that was chosen to be utilized for their behavioural modeling. In fact, the SR-AWV was selected for the Y accelerometer and all three gyroscopes, while the DR-AWV, with 20% trim, was deemed necessary only for the X and Z accelerometers.

Therefore, given these decisions, the optimal composite models were determined for each inertial sensor by following the steps described in Section 4.2 and Figure 4.24 is provided below, where representative examples of the achieved high quality fits to the empirical behavior can be witnessed.

---

[4]The prototype base was also levelled as precisely as possible to make sure that the turntable sensitive axis is parallel to the axis of the gyro aligned with the local gravity direction. In this way, the entirety of the rotation rate signal can be sensed with negligible leaks to the other two directions.
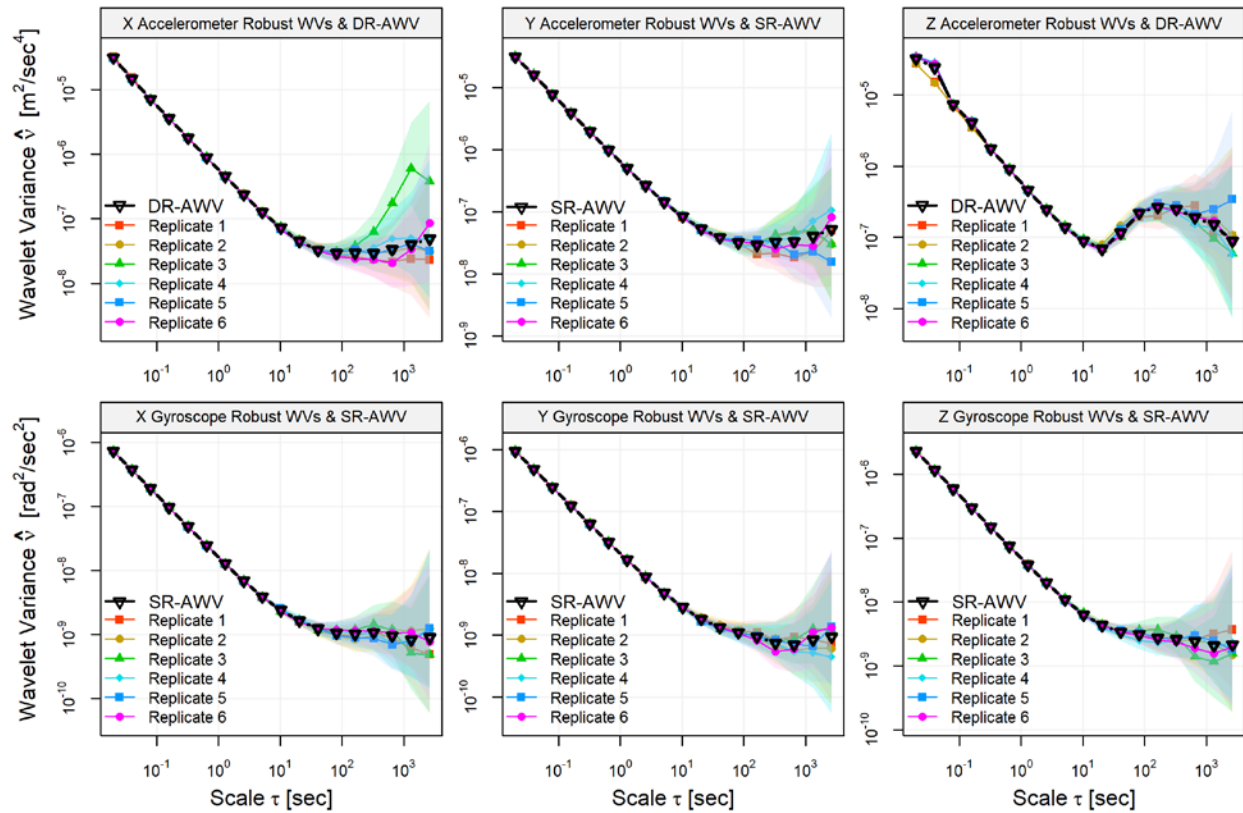
Figure 4.23: Robust empirical WVs of 6 static (deterministic error-free) signal replicates along with their respective 95% CIs as well as the characteristic WV of the selected multi-signal estimator
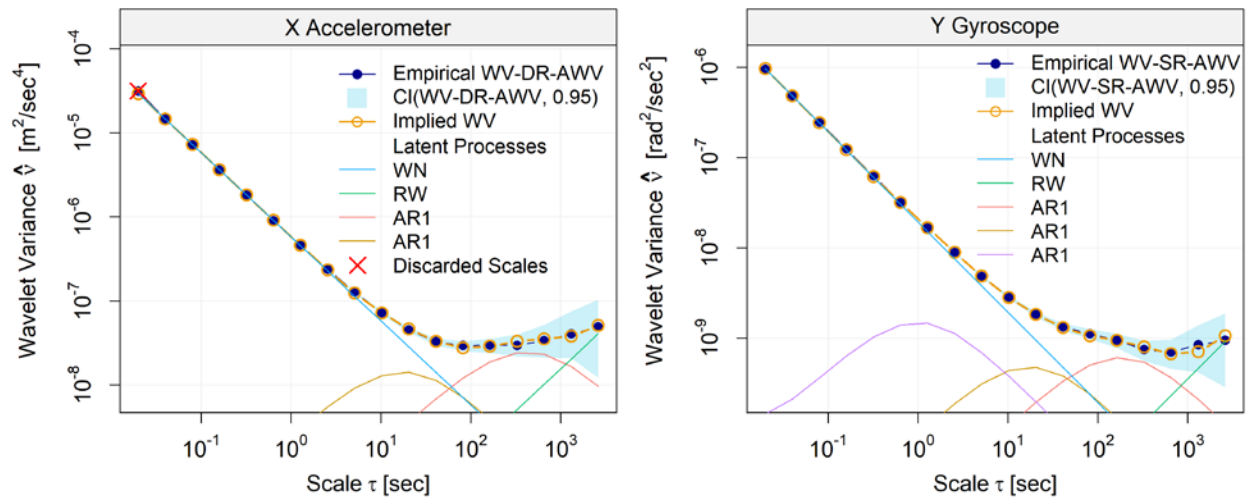
Figure 4.24: Composite stochastic model fits to the X accelerometer (left panel) and Y gyroscope (right panel) random error empirical behavior using the DR-AWV and SR-AWV estimators respectively.

Furthermore, it is worth mentioning that 4 Z-accelerometer replicates presented breaks from the WN behaviour in the 2nd and 4th WV scale, an influence which was also transmitted to the characteristic WV of the DR-AWV estimator. It is speculated that the reason behind these breaks is the existence of some sort of high frequency noise to the collected data, while the cause of this noise could not be pinpointed. Nevertheless, this issue did not create a problem in the stochastic analysis since the capability to remove certain scales from the GMWM-based parameter estimation became possible in this thesis (see Section 4.2). In the following, the parameter values of the identified optimal models are given in Table 4.6 for the accelerometers and Table 4.7 for the gyroscopes, just as they were provided by the method's GMWM-based framework.

Table 4.6: Composite stochastic model parameter values for the accelerometer sensors derived using the SR/DR-AWV multi-signal estimators.

Stochastic Process	X Accelerometer	Y Accelerometer	Z Accelerometer
	DR-AWV	SR-AWV	DR-AWV
$\varphi_{AR1,1}$ [number]	9.9991118934E-01	9.9997413124E-01	9.9988222369E-01
$\xi^2_{AR1,1}$ [m^2/sec^4]	2.3025623378E-11	6.3063130766E-12	3.2376979539E-10
$\varphi_{AR1,2}$ [number]	9.9788236122E-01	9.9956962851E-01	–
$\xi^2_{AR1,2}$ [m^2/sec^4]	3.1698883744E-10	7.8018328644E-11	–
$\varphi_{AR1,3}$ [number]	–	9.9231814672E-01	–
$\xi^2_{AR1,3}$ [m^2/sec^4]	–	1.5325490982E-09	–
γ^2_{RW} [m^2/sec^4]	1.8740855308E-12	1.2769134172E-12	–
σ^2_{GWN} [m^2/sec^4]	5.8001699746E-05	6.2646525277E-05	5.6677308168E-05

Table 4.7: Composite stochastic model parameter values for the gyroscope sensors derived using the SR/DR-AWV multi-signal estimators.

Stochastic Process	X Gyroscope	Y Gyroscope	Z Gyroscope
	SR-AWV	SR-AWV	SR-AWV
$\varphi_{AR1,1}$ [number]	9.9987552667E-01	9.9979175186E-01	9.9991854699E-01
$\xi^2_{AR1,1}$ [rad^2/sec^2]	1.2071600252E-12	1.3239167141E-12	1.6330417865E-12
$\varphi_{AR1,2}$ [number]	9.9575328313E-01	9.9786425451E-01	9.9904712588E-01
$\xi^2_{AR1,2}$ [rad^2/sec^2]	4.1704676405E-11	1.0676557808E-11	1.7600027320E-11
$\varphi_{AR1,3}$ [number]	–	9.6315054006E-01	9.6083305506E-01
$\xi^2_{AR1,3}$ [rad^2/sec^2]	–	5.6366165463E-10	1.0010941006E-09
γ^2_{RW} [rad^2/sec^2]	2.3442744506E-14	4.2139821371E-14	5.8629278092E-14
σ^2_{WN} [rad^2/sec^2]	1.5241658764E-06	1.9294205678E-06	4.6200914915E-06

Finally, it is highlighted that according to the results shown in the above tables, the MTi inertial sensor random error behavior is partially characterized by multiple time-correlated processes. As a result, this confirms the requirement for an alternative to the standard AVLR when dealing with low-cost equipment, since it is very difficult for the latter to even detect noise with time-correlated properties.

AVLR Analysis

In contrast with the previous analysis, the AVLR utilizes only a single signal in order to implement the inertial sensor stochastic calibration. To that end, the MTi was placed on the apparatus demonstrated in Figure 4.22 and the required static data were collected at a 100Hz data rate. Subsequently, the maximal overlapping ADEV quantity (σ_{AV}) was evaluated and its behav-

iour for each inertial sensor is demonstrated in Figure 4.25 along with the 95% CIs for each σ_{AV}

data point, which were evaluated via the following formula:

$$CI_{high,low}\left(\tau = 2^{i=1,...,J}\right) = \sigma_{AV}(\tau) \pm \left(2 \cdot \text{error}_{ADEV}(\tau) \cdot \sigma_{AV}(\tau)\right) \qquad (4.25)$$
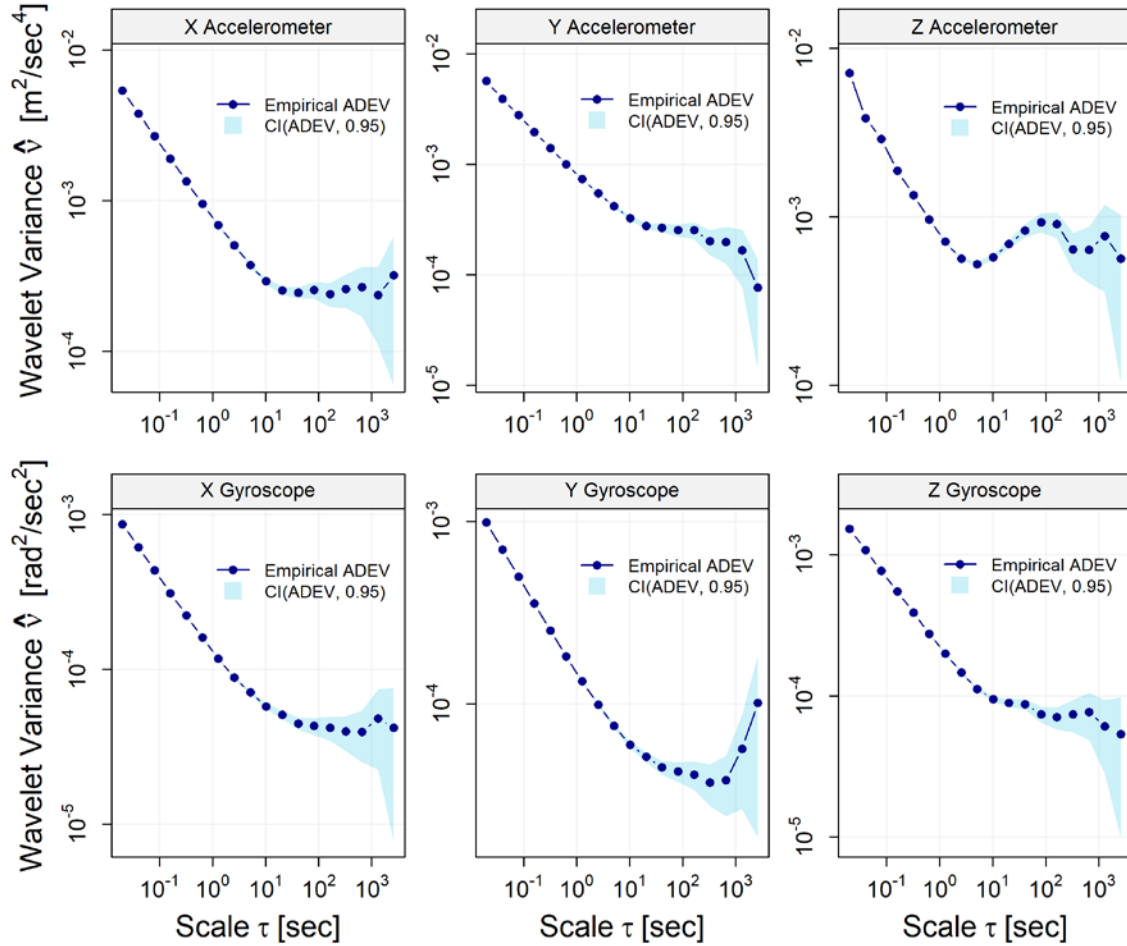
Figure 4.25: Maximal overlapping ADEV for the three accelerometer and three gyroscope sensors along with their respective 95% CIs

At this point, it is worth mentioning that even though the theoretical slopes of each of the

identifiable processes (i.e., RW, WN, BI, QN, DR) in the ADEV plots is known (see Table 3.1),

the empirical behavior can deviate significantly and thus, it is not at all clear which scales should

be utilized for the inference of their respective parameters via linear regression. To tackle this

issue, the process described below can be followed:

1) Inspect the ADEV plot and based on the known stochastic process slopes, identify which of them are present in the empirical behavior.

2) Choose the data points that probably correspond to each of those processes and perform individual linear regressions to evaluate their defining parameter values.

3) For every identified process, utilize its estimated parameter value(s) along with its corresponding theoretical ADEV expression (see Table 3.1) in order to determine the contribution to the overall fit.

4) Create the implied ADEV by adding the individual contributions of the included sub-processes to the composite model (assuming that they are additive) and plot it against its empirical version.

5) Repeat steps 1-4 by selecting different point combinations until the least possible difference between the empirical and implied ADEV can be achieved.

On another note, although it is evident by inspecting Figure 4.25 that there are areas where BI can be identified, such a process cannot be expressed by a state-space model that can in turn be included within the navigation algorithm. Furthermore, according to the literature, the BI can be approximated by either a single AR1/GM1 or a higher order autoregressive process, an operation that can be done in various different ways (see (Farrell et al., 2022) for an overview). Nevertheless, the choice of alternatives to the BI process is somewhat of an artform that depends on multiple factors, including the subjective opinion of the user and thus, it does not depend on a pure statistical reasoning (i.e., a reliable estimator). For the purposes of this thesis, it has been decided that only processes that can be described via a state-space model will be investigated (i.e., RW, WN and DR) and by using the step-by-step process that was described earlier, obtain the best fit

possible to the observed behavior. In turn, when these models are inputted within the navigation algorithm, their parameter values will be tuned in order to achieve the optimal performance. In fact, by doing this, the BI process that was omitted will essentially be over-bounded by the inflated processes. Therefore, with these in mind, the AVLR analysis was implemented and characteristic examples of the achieved fits to the sensed behavior are provided in Figure 4.26 for the X accelerometer and Y gyroscope.
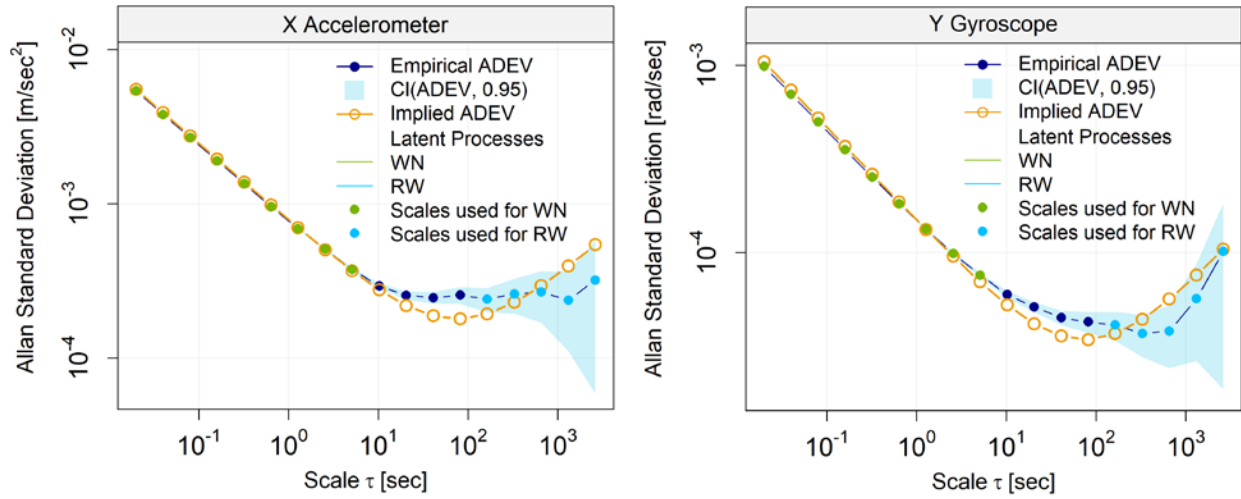
Figure 4.26: AVLR-derived model fits to the empirical behavior for the X accelerometer and Y gyroscope sensors

On top of that, the composite model parameter values are also provided in Table 4.6 and Table 4.7 for the accelerometer and gyroscope sensors respectively, which will be used in by the navigation algorithms in the next chapters for the recursive compensation of the inertial sensor random errors.

able 4.8: Model parameter values for the accelerometer sensors as they were derived from the AVLR analysis.

Stochastic Process	X Accelerometer	Y Accelerometer	Z Accelerometer
	AVLR	AVLR	AVLR
γ^2_{RW} [m^2/sec^4]	3.1683974534E-12	2.6794563541E-12	7.7755862066E-11
σ^2_{WN} [m^2/sec^4]	6.0292810318E-05	6.5565113721E-05	6.3043472951E-05

Table 4.9: Model parameter values for the gyroscope sensors as they were derived from the AVLR analysis.

Stochastic Process	X Gyroscope	Y Gyroscope	Z Gyroscope
	AVLR	AVLR	AVLR
γ^2_{RW} [rad^2/sec^2]	1.1573253607E-13	1.1654416498E-13	2.0258073166E-13
σ^2_{WN} [rad^2/sec^2]	1.6328684006E-06	2.1710272523E-06	5.0172266282E-06

4.6 Summary

In this chapter, a more practical implementation of the single-signal GMWM was presented along with a mathematical reasoning that permits the complexity reduction of the identified composite stochastic model by over-bounding AR1 processes with either using WN or RW under certain conditions. On top of that, the capability to remove certain WV scales from consideration when fitting the models was added to the existing framework, a feature that can be very useful when dealing with low-cost and consumer-grade equipment. Furthermore, the idea of utilizing the RGMWM in every scenario without the need for a contamination test was investigated in a simulation setting and from which it was established that this is a worthwhile trade-off between reduction in model parameter estimation efficiency and safeguarding the estimation process from the harmful influence of outliers.

Subsequently, a robust multi-signal method based on the AWV estimator was proposed, containing two layers of robustness. The first one accounts for the existence of outliers in the individual signal replicates that are being considered and the second protects the estimation process from the collection of abnormal signal replicates, while preserving as much information from them as possible. Based on this approach, two estimators were formally defined: the SR-AWV, which contains protection against data corruption (one layer of robustness) and the DR-AWV, that includes safeguards against sample contamination as well (two layers of robustness).

In turn, the efficiency of the new estimators was evaluated in a simulation and a case study in terms of model parameter estimation under different calibration data contamination settings, from which their robustness to the effects of different types of outliers was established and it was also confirmed that they have an equivalent performance to the classical estimation in a clean data setting (just as in the single-signal GMWM approach).

In addition, an innovative evaluation of their contribution to the navigation performance was also conducted by the means of a recently proposed MC simulation-based navigation simulator. Based on the results from a huge number of simulated trajectories, it was identified that the robust estimators manage to maintain stability under contamination in terms of not only navigation state estimation accuracy but also of correctness of the provided reliability information. Finally, the stochastic analysis of consumer-grade inertial sensors was performed using the proper robust multi-signal estimator as well as the conventional AVLR, the information from which will be used later in the context of different types of navigation algorithms.

Chapter Five: Extended Kalman Filter-based Navigation Algorithm for Loosely Coupled Integration

5.1 Introduction

In this chapter, the EKF, a continuous recursive Bayesian filter will be employed for the solution of the navigation problem and the infusion of the advanced stochastic modeling for the inertial sensor random error drift, which will help making the predictive PDF less noisy. Specifically, this is a linearized unbiased estimator that utilizes an analytical approximation to solve the aforementioned multi-dimensional integrals. In the end, it provides a single optimal solution for the system states, based on the Minimum Mean Square Error (MMSE) criterion, as well as information about the quality of its estimation (i.e., covariance) (Gelb, 1974).

Next, the characteristics and structure of an EKF used for loosely integrating the INS system with GNSS and other update sources will be described. In addition, special attention will be given to the way that the advanced stochastic modeling knowledge about the inertial sensor error drift that was derived in the previous chapter can be encompassed into it.

5.2 The Extended Kalman Filter

As it was mentioned earlier, the navigation equations are nonlinear in nature and this, the standard KF cannot be utilized directly. Instead, its algorithm should be altered in order to be able to handle this nonlinear system and analytically propagate the state PDF. This modification leads to a sub-optimal estimator called the *Extended Kalman Filter*, where the system model is linearized using the Taylor series expansion, usually up to the first order, around the trajectory implied by the INS mechanization (Noureldin et al., 2013). As a result, the filter no longer utilizes the absolute state values like the standard KF does. Instead, it employs the state errors with respect to the nominal solution around which the linearization occurred, and after each iteration,

these errors are used to correct the nominal solution and obtain the optimal estimate, given all the available information. Therefore, it is evident that the quality of the EKF estimation is highly dependent on the validity of that linearization.

According to Gelb, (1974), the continuous time system and measurement models utilized by the EKF (for navigation purposes) are given by the following equations:

$$\delta\dot{\mathbf{x}}(t) = \mathbf{F}(t) \cdot \delta\mathbf{x}(t) + \mathbf{G}(t) \cdot \mathbf{w}(t), \qquad \mathbf{Q}(t) \tag{5.1}$$

$$\delta\mathbf{z}(t) = \mathbf{H} \cdot \delta\mathbf{x}(t) + \boldsymbol{v}(t), \qquad \mathbf{R}(t) \tag{5.2}$$

where $\delta\dot{\mathbf{x}}$ is the first derivative of the $\delta\mathbf{x}$ error-state vector, $\mathbf{F}(t)$ the dynamic matrix that describes the rate that the errors from the INS mechanization evolve over time, $\mathbf{G}(t)$ the random forcing matrix that defines the system noise distribution, $\mathbf{w}(t)$ the system noise vector, $\mathbf{Q}(t)$ a continuous-time V-C matrix that is associated with the characteristics of the system noise, $\delta\mathbf{z}(t)$ the continuous-time measurement error vector, $\mathbf{H}$ the design matrix that provides the ideal connection between measurement error and error state vector and $\boldsymbol{v}(t)$ the measurement noise that is characterized by $\mathbf{R}(t)$.

However, in practice, it is impossible to collect continuous data. Therefore, the aforementioned equations have to be converted into discrete time expressions, which are given below (Noureldin et al., 2013):

$$\delta\mathbf{x}_k = \boldsymbol{\Phi}_{k-1\to k} \cdot \delta\mathbf{x}_{k-1} + \mathbf{G}_k \cdot \mathbf{w}_k, \qquad \boldsymbol{\Phi}_{k-1\to k} = e^{\mathbf{F}\Delta t}, \qquad \mathbf{w}_k \sim \mathcal{N}(0, \mathbf{Q}_k) \tag{5.3}$$

$$\delta\mathbf{z}_k = \mathbf{H}_k \cdot \delta\mathbf{x}_k + \boldsymbol{v}_k, \qquad \boldsymbol{v}_k \sim \mathcal{N}(0, \mathbf{R}_k) \tag{5.4}$$

where $\mathbf{\Phi}_{k-1\to k}$ is the state transition matrix that represents how the INS errors are related to the error state of the EKF, Δt is the time interval between the previous and current epoch, $\mathbf{G}_k$ the noise distribution matrix that describes the error connection between state components, $\mathbf{w}_k$ the process noise vector with $\mathbf{Q}_k$ variance matrix (diagonal, no covariances considered), $\delta \mathbf{z}_k$ the vector that contains the difference between the INS-implied and the auxiliary source's absolute state information and $\mathbf{v}_k$ the random noise vector that describes the update with $\mathbf{R}_k$ variance matrix (diagonal, no covariances considered). In addition, it is highlighted that the EKF assumes that $\mathbf{w}_k$ and $\mathbf{v}_k$ are completely independent with each other and that they are both described by a Gaussian WN stochastic process that is characterized by their respective variance matrices.

With this in mind, the complete error-state EKF algorithm is presented below in two stages (Brown and Hwang, 2012; Noureldin et al., 2013):

A. Prediction

$$\delta \hat{\mathbf{x}}_k^- = \mathbf{\Phi}_{k-1\to k}\, \delta \hat{\mathbf{x}}_{k-1}^+ \tag{5.5}$$

$$\mathbf{P}_k^- = \mathbf{\Phi}_{k-1\to k}\, \mathbf{P}_k^-\, \mathbf{\Phi}_{k-1\to k}^{\mathrm{T}} + \mathbf{Q}_k,$$
$$\mathbf{Q}_k \approx \frac{1}{2}\left[\mathbf{\Phi}_{k-1\to k}\, \mathbf{G}_k\, \mathbf{Q}_s\, \mathbf{G}_k^{\mathrm{T}} + \mathbf{G}_k\, \mathbf{Q}_s\, \mathbf{G}_k^{\mathrm{T}}\, \mathbf{\Phi}_{k-1\to k}^{\mathrm{T}}\right]\Delta t \tag{5.6}$$

B. Update

$$\mathbf{K}_k = \mathbf{P}_k^-\, \mathbf{H}_k^{\mathrm{T}}\left[\mathbf{H}_k\, \mathbf{P}_k^-\, \mathbf{H}_k^{\mathrm{T}} + \mathbf{R}_k\right]^{-1} \tag{5.7}$$

$$\delta \hat{\mathbf{x}}_k^+ = \delta \hat{\mathbf{x}}_k^- + \mathbf{K}_k\left[\delta \mathbf{z}_k - \mathbf{H}_k\, \delta \hat{\mathbf{x}}_k^-\right] \tag{5.8}$$

$$\mathbf{P}_k^+ = [\mathrm{I} - \mathbf{K}_k\, \mathbf{H}_k]\, \mathbf{P}_k^-\, [\mathrm{I} - \mathbf{K}_k\, \mathbf{H}_k]^{\mathrm{T}} + \mathbf{K}_k\, \mathbf{R}_k\, \mathbf{K}_k^{\mathrm{T}} \tag{5.9}$$

where $\delta\hat{\mathbf{x}}_k^-$ is the a-priori estimation of the error state vector based only on the INS operation, $\mathbf{P}_k^-$ the matrix that contains the a-priori state estimation uncertainty, $\mathbf{Q}_s$ the spectral densities matrix of the system noises, Δt is the data interval of the inertial sensor data, $\delta\hat{\mathbf{x}}_{k-1}^+$ the vector of the updated error state estimation from the previous epoch, $\mathbf{K}_k$ is designated as the Kalman gain, $[\delta\mathbf{z}_k - \mathbf{H}_k\,\delta\hat{\mathbf{x}}_k^-]$ is called the innovation sequence, I is an identity matrix, $\delta\hat{\mathbf{x}}_k^+$ is the updated error state vector and $\mathbf{P}_k^+$ is the latter's covariance matrix.

Furthermore, it should be mentioned that in practice, the INS system that drives the EKF integration filter is characterized by a much higher data rate compared to the auxiliary sensors. Consequently, there are times where the INS is operating on standalone mode and thus there is no information for the update stage to be triggered. Therefore, in this case, the updated error state and covariance take the following forms:

$$\delta\hat{\mathbf{x}}_k^+ = \delta\hat{\mathbf{}}_k^- \qquad (5.10)$$

$$\mathbf{P}_k^+ = \mathbf{P}_k^- \qquad (5.11)$$

5.3 Filter Design

In this section, the manner in which each component of the EKF is formulated in order to correspond to a filter that performs the loosely coupled integration of the INS and GNSS systems, while also utilizes updates from the NHCs and ZUPTs will be described. Furthermore, particular focus will be given to the infusion of that algorithm with advanced knowledge about the random drift of the inertial sensor error errors (derived in the previous chapter) in order to allow their recursive online compensation.

5.3.1 Error State Vector

Generally, the way to encompass the stochastic modeling information about the inertial sensor bias instability within a Bayesian-type filter is by utilizing the state-space augmentation technique (Gelb, 1974). Therefore, with this in mind, the general structure of the EKF error state vector $\delta \mathbf{x}$ is provided by the expression:

$$\delta \hat{\mathbf{x}} = [\delta \mathbf{r} \quad \delta \mathbf{v} \quad \boldsymbol{\psi} \quad \delta \boldsymbol{\omega}^{\mathrm{b}} \quad \delta \boldsymbol{f}^{\mathrm{b}}]^{\mathrm{T}} \tag{5.12}$$

where $\delta \mathbf{r} = [\delta \phi \quad \delta \lambda \quad \delta h]$ is the geodetic position (latitude, longitude, ellipsoidal height) error vector, $\delta \mathbf{v} = [\delta v_{\mathrm{n}} \quad \delta v_{\mathrm{e}} \quad \delta v_{\mathrm{d}}]$ the velocity error vector expressed in the NED LLF that is chosen to be the n-frame, $\boldsymbol{\psi} = [\delta r \quad \delta p \quad \delta A]$ the attitude error vector in terms of Euler angles (roll, pitch, azimuth) that correspond to the same NED frame, $\delta \boldsymbol{\omega}^{\mathrm{b}}$ the random bias vector for the 3 gyroscopes and $\delta \boldsymbol{f}^{\mathrm{b}}$ the random bias vector for the 3 accelerometers.

At this point, it should be noted that the dimension of the two latter vectors depends on the complexity of the model that has either been chosen arbitrarily (e.g., a single GM1) or identified by a stochastic modeling methodology (e.g., GMWM) in order to describe each sensor's random error behavior. Here, for illustration purposes, it is assumed that a model $\mathcal{Z}$ that is constituted by the summation of three GM1s, one RW, one WN and one DR stochastic process has been chosen to describe each sensor. As a result, the $\delta \boldsymbol{\omega}^{\mathrm{b}}$ and $\delta \boldsymbol{f}^{\mathrm{b}}$ vectors are expressed as follows:

$$\delta \boldsymbol{\omega}^{\mathrm{b}} = \left[\delta \boldsymbol{\omega}^{\mathrm{b}}_{\mathrm{GM1}(1)} \quad \delta \boldsymbol{\omega}^{\mathrm{b}}_{\mathrm{GM1}(2)} \quad \delta \boldsymbol{\omega}^{\mathrm{b}}_{\mathrm{GM1}(3)} \quad \delta \boldsymbol{\omega}^{\mathrm{b}}_{\mathrm{RW}} \quad \delta \boldsymbol{\omega}^{\mathrm{b}}_{\mathrm{WN}}\right]^{\mathrm{T}} \tag{5.13}$$

$$\delta \boldsymbol{f}^{\mathrm{b}} = \left[\delta \boldsymbol{f}^{\mathrm{b}}_{\mathrm{GM1}(1)} \quad \delta \boldsymbol{f}^{\mathrm{b}}_{\mathrm{GM1}(2)} \quad \delta \boldsymbol{f}^{\mathrm{b}}_{\mathrm{GM1}(3)} \quad \delta \boldsymbol{f}^{\mathrm{b}}_{\mathrm{RW}} \quad \delta \boldsymbol{f}^{\mathrm{b}}_{\mathrm{WN}}\right]^{\mathrm{T}} \tag{5.14}$$

where each element is a (1×3) vector that contains the random bias errors for the measurements of the three inertial sensors (along the x, y, and z directions of the b-frame), as they are dictated by the corresponding stochastic process. Consequently, the dimension of the error state vector becomes equal to 39.

5.3.2 System Model

The system model can be divided into two parts; one that refers to the navigation states and one about the inertial sensor random biases.

Concerning the former, it is based on the errors created from the motion between the previous and the current epoch, a process that is implemented by the INS mechanization algorithm. For the purposes of this study, the quaternion-based INS mechanization described in (Shin, 2005) and used by the Aided Inertial Navigation System (AINS)® software (Shin and El-Sheimy, 2004a) was adopted as well as its corresponding error differential equations, that were derived based on the "*psi-angle error model*" (Benson, 1975). Specifically, this error analysis is resolved with respect to the *computer frame* (c-frame), which is what the mechanization perceives as the true n-frame (i.e., the NED) and in the following, the resulting linearized equations with respect to it are given in matrix form (Scherzinger and Reid, 1994):

$$
\underbrace{\begin{bmatrix} \delta\dot{\phi} \\ \delta\dot{\lambda} \\ \delta\dot{h} \end{bmatrix}}_{\delta\dot{r}^c} = \underbrace{\begin{bmatrix} 0 & -v_E\tan\phi/(R_N+h) & v_N/(R_M+h) \\ v_E\tan\phi/(R_N+h) & 0 & v_E/(R_N+h) \\ -v_N/(R_M+h) & -v_E/(R_N+h) & 0 \end{bmatrix}}_{F_{r,1}} \underbrace{\begin{bmatrix} \delta\phi \\ \delta\lambda \\ \delta h \end{bmatrix}}_{\delta r^c}
$$

$$
+ \underbrace{\begin{bmatrix} 1 & 0 & 0 \\ 0 & 1 & 0 \\ 0 & 0 & 1 \end{bmatrix}}_{F_{r,2}} \underbrace{\begin{bmatrix} \delta v_n \\ \delta v_e \\ \delta v_d \end{bmatrix}}_{\delta v^c}, R_N = \frac{\alpha_e}{(1-e^2\sin^2\phi)^{1/2}}, R_M = \frac{\alpha_e(1-e^2)}{(1-e^2\sin^2\phi)^{3/2}}
$$

(5.15)

where $\alpha_e = 6378137m$ is the semi-major axis (equatorial radius) of the WGS84 reference ellipsoid, $e = 0.08181919$ is its first eccentricity, R_N is the radius of curvature in the prime vertical, R_M is the radius of curvature in the meridian, v_E and v_N are the horizontal velocities with respect to the c-frame (i.e., what the INS mechanization engine perceives as the NED frame), while the latitude ϕ and ellipsoidal height h are provided by the INS mechanization.

$$
\underbrace{\begin{bmatrix} \dot{\delta v_n} \\ \dot{\delta v_e} \\ \dot{\delta v_d} \end{bmatrix}}_{\dot{\delta v}^c} = \underbrace{\begin{bmatrix} -\gamma/(R_M + h) & 0 & 0 \\ 0 & -\gamma/(R_N + h) & 0 \\ 0 & 0 & -2\gamma/(R_e + h) \end{bmatrix}}_{F_{v,1}} \underbrace{\begin{bmatrix} \delta\phi \\ \delta\lambda \\ \delta h \end{bmatrix}}_{\delta r^c}
$$

$$
+ \left(\underbrace{\begin{bmatrix} 0 & -2\omega_e\sin\phi & 0 \\ 2\omega_e\sin\phi & 0 & 2\omega_e\cos\phi \\ 0 & -2\omega_e\cos\phi & 0 \end{bmatrix}}_{F_{v,2}} \right.
$$

$$
\left. + \underbrace{\begin{bmatrix} 0 & -v_E\tan\phi/(R_N + h) & v_N/(R_M + h) \\ v_E\tan\phi/(R_N + h) & 0 & v_E/(R_N + h) \\ -v_N/(R_M + h) & -v_E/(R_N + h) & 0 \end{bmatrix}}_{F_{v,2}} \right) \underbrace{\begin{bmatrix} \delta v_n \\ \delta v_e \\ \delta v_d \end{bmatrix}}_{\delta v^c}
$$

$$
\underbrace{\begin{bmatrix} 0 & -\tilde{f}_d & \tilde{f}_e \\ \tilde{f}_d & 0 & -\tilde{f}_n \\ -\tilde{f}_e & \tilde{f}_n & 0 \end{bmatrix}}_{F_{v,3}} \underbrace{\begin{bmatrix} \delta r \\ \delta p \\ \delta A \end{bmatrix}}_{\psi} + \underbrace{\widehat{\mathbf{R}}_b^n}_{F_{v,4}} \underbrace{\begin{bmatrix} \delta f_x \\ \delta f_y \\ \delta f_z \end{bmatrix}}_{\delta f^b}
$$

$$(5.16)$$

where γ is the normal gravity value based on Somigliana's formula (Wei and Schwarz, 1990) with ϕ and h as inputs, $R_e = \sqrt{R_M R_N}$ the Gaussian mean Earth radius of curvature, $\omega_e = 7.292115147 \cdot 10^{-5}$ rad/sec the Earth's rotation rate, $(\tilde{f}_e, \tilde{f}_n, \tilde{f}_d)$ the specific forces expressed in the c-frame and $\widehat{\mathbf{R}}_b^n$ the attitude-describing DCM of the IMU with respect to the n-frame as it was provided by the INS mechanization. In addition, the full expression of the latter matrix is also given, along with the formulas that can be used to extract the attitude angles of the moving platform from it:

$$\widehat{R}_b^n = \begin{bmatrix} \cos p\,\cos A & -\cos r\,\sin A + \sin r\,\sin p\,\cos A & \sin r\,\sin A + \cos r\,\sin p\,\cos A \\ \cos p\,\sin A & \cos r\,\cos A + \sin r\,\sin p\,\sin A & -\sin r\,\cos A + \cos r\,\sin p\,\sin A \\ -\sin p & \sin r\,\cos p & \cos r\,\cos p \end{bmatrix},$$

$$\hat{p} = \tan^{-1}\left(\frac{-R_{31}}{\sqrt{R_{32}^2 + R_{33}^2}}\right), \qquad \hat{r} = \tan^{-1}\left(\frac{R_{32}}{R_{33}}\right), \qquad \widehat{A} = \tan^{-1}\left(\frac{R_{21}}{R_{11}}\right)$$

(5.17)

$$\underbrace{\begin{bmatrix} \delta\dot{r} \\ \delta\dot{p} \\ \delta\dot{A} \end{bmatrix}}_{\dot{\psi}} = \left(\underbrace{\begin{bmatrix} 0 & -\omega_e\sin\phi & 0 \\ \omega_e\sin\phi & 0 & \omega_e\cos\phi \\ 0 & -\omega_e\cos\phi & 0 \end{bmatrix}}_{F_{\psi,1}} \right.$$

$$+ \underbrace{\begin{bmatrix} 0 & -v_E\tan\phi/(R_N+h) & v_N/(R_M+h) \\ v_E\tan\phi/(R_N+h) & 0 & v_E/(R_N+h) \\ -v_N/(R_M+h) & -v_E/(R_N+h) & 0 \end{bmatrix}}_{F_{\psi,1}} \left.\right) \underbrace{\begin{bmatrix} \delta r \\ \delta p \\ \delta A \end{bmatrix}}_{\psi}$$

(5.18)

$$+ \underbrace{\widehat{R}_b^n}_{F_{\psi,2}} \underbrace{\begin{bmatrix} \delta\omega_x \\ \delta\omega_y \\ \delta\omega_z \end{bmatrix}}_{\delta\omega^b}$$

Regarding the second part, it is built based on state-space model of the stochastic process(es) that have been selected to describe the bias instability of each inertial sensor. Furthermore, it should be mentioned that only processes that have such a representation can be included within the EKF algorithm, meaning the GM1, RW, WN and DR. Therefore, with this in mind, an example is provided below about the gyroscope sensor triad, where the differential equation of each of these processes are shown in matrix form:

$$\underbrace{\begin{bmatrix} \delta\dot{\omega}_x \\ \delta\dot{\omega}_y \\ \delta\dot{\omega}_z \end{bmatrix}}_{\delta\dot{\omega}_{GM1}^b} = \underbrace{\begin{bmatrix} -\beta_{\omega_x} & 0 & 0 \\ 0 & -\beta_{\omega_y} & 0 \\ 0 & 0 & -\beta_{\omega_z} \end{bmatrix}}_{F_{GM1}^{\delta\omega}} \underbrace{\begin{bmatrix} \delta\omega_x \\ \delta\omega_y \\ \delta\omega_z \end{bmatrix}}_{\delta\omega^b} + W_{GM1}, \qquad W_{GM1} \sim \mathcal{N}(0, \mathbf{Q}_{GM1})$$

(5.19)

$$
\underbrace{\begin{bmatrix} \delta\dot{\omega}_x \\ \delta\dot{\omega}_y \\ \delta\dot{\omega}_z \end{bmatrix}}_{\delta\dot{\boldsymbol{\omega}}^b_{RW}} = \underbrace{\begin{bmatrix} 0 & 0 & 0 \\ 0 & 0 & 0 \\ 0 & 0 & 0 \end{bmatrix}}_{F^{\delta\omega}_{RW}} \underbrace{\begin{bmatrix} \delta\omega_x \\ \delta\omega_y \\ \delta\omega_z \end{bmatrix}}_{\delta\boldsymbol{\omega}^b} + W_{RW,\delta\boldsymbol{\omega}}, \qquad W_{RW} \sim \mathcal{N}(0, \mathbf{Q}_{RW}) \tag{5.20}
$$

$$
\underbrace{\begin{bmatrix} \delta\dot{\omega}_x \\ \delta\dot{\omega}_y \\ \delta\dot{\omega}_z \end{bmatrix}}_{\delta\dot{\boldsymbol{\omega}}^b_{WN}} = \underbrace{\begin{bmatrix} 0 & 0 & 0 \\ 0 & 0 & 0 \\ 0 & 0 & 0 \end{bmatrix}}_{F^{\delta\omega}_{WN}} \underbrace{\begin{bmatrix} \delta\omega_x \\ \delta\omega_y \\ \delta\omega_z \end{bmatrix}}_{\delta\boldsymbol{\omega}^b} + W_{WN,\delta\boldsymbol{\omega}}, \qquad W_{WN} \sim \mathcal{N}(0, \mathbf{Q}_{WN}) \tag{5.21}
$$

where β is one of the two parameters of the GM1 process. As for the DR process, its discrete-time state-space expression (see equation (2.10)) indicates that its value is a linear function of time and uncorrelated with the error state vector's evolution. Hence, its contribution is chosen to be added to the WN components in the discrete time space, after the completion of the prediction stage. Specifically, this means that equation (5.5) should be modified as follows:

$$
\delta\hat{\mathbf{x}}_k^- = \boldsymbol{\Phi}_{k-1 \rightarrow k}\, \delta\hat{\mathbf{x}}_{k-1}^+ + \boldsymbol{\omega}_{DR}\, \Delta t \tag{5.22}
$$

where $\boldsymbol{\omega}_{DR}$ is a vector with the same dimensions as the error state and only has values ($\omega_{DR}\, \Delta t$) for the index that corresponds to the WN process of the inertial sensor where the DR process exists.

Subsequently, based on what has been described so far and considering the $\mathcal{Z}$ model for the random drift of the inertial sensor errors, the $\mathbf{F}$, $\boldsymbol{\Phi}$, $\mathbf{G}$ and $\mathbf{Q}_s$ system model matrices are structured as follows:

$$\mathbf{F} = \begin{bmatrix}
\boldsymbol{F}_{\mathrm{r},1} & \boldsymbol{F}_{\mathrm{r},2} & 0_{3\times3} & 0_{3\times3} & 0_{3\times3} & 0_{3\times3} & 0_{3\times3} & 0_{3\times3} & 0_{3\times3} & 0_{3\times3} & 0_{3\times3} & 0_{3\times3} & 0_{3\times3} \\
\boldsymbol{F}_{\mathrm{v},1} & \boldsymbol{F}_{\mathrm{v},2} & \boldsymbol{F}_{\mathrm{v},3} & 0_{3\times3} & \boldsymbol{F}_{\mathrm{v},4} & 0_{3\times3} & \boldsymbol{F}_{\mathrm{v},4} & 0_{3\times3} & \boldsymbol{F}_{\mathrm{v},4} & 0_{3\times3} & \boldsymbol{F}_{\mathrm{v},4} & 0_{3\times3} & \boldsymbol{F}_{\mathrm{v},4} \\
0_{3\times3} & 0_{3\times3} & \boldsymbol{F}_{\psi,1} & \boldsymbol{F}_{\psi,2} & 0_{3\times3} & \boldsymbol{F}_{\psi,2} & 0_{3\times3} & \boldsymbol{F}_{\psi,2} & 0_{3\times3} & \boldsymbol{F}_{\psi,2} & 0_{3\times3} & \boldsymbol{F}_{\psi,2} & 0_{3\times3} \\
0_{3\times3} & 0_{3\times3} & 0_{3\times3} & \boldsymbol{F}^{\delta\boldsymbol{\omega}}_{\mathrm{GM1,1}} & 0_{3\times3} & 0_{3\times3} & 0_{3\times3} & 0_{3\times3} & 0_{3\times3} & 0_{3\times3} & 0_{3\times3} & 0_{3\times3} & 0_{3\times3} \\
0_{3\times3} & 0_{3\times3} & 0_{3\times3} & 0_{3\times3} & \boldsymbol{F}^{\delta f}_{\mathrm{GM1,1}} & 0_{3\times3} & 0_{3\times3} & 0_{3\times3} & 0_{3\times3} & 0_{3\times3} & 0_{3\times3} & 0_{3\times3} & 0_{3\times3} \\
0_{3\times3} & 0_{3\times3} & 0_{3\times3} & 0_{3\times3} & 0_{3\times3} & \boldsymbol{F}^{\delta\boldsymbol{\omega}}_{\mathrm{GM1,2}} & 0_{3\times3} & 0_{3\times3} & 0_{3\times3} & 0_{3\times3} & 0_{3\times3} & 0_{3\times3} & 0_{3\times3} \\
0_{3\times3} & 0_{3\times3} & 0_{3\times3} & 0_{3\times3} & 0_{3\times3} & 0_{3\times3} & \boldsymbol{F}^{\delta f}_{\mathrm{GM1,2}} & 0_{3\times3} & 0_{3\times3} & 0_{3\times3} & 0_{3\times3} & 0_{3\times3} & 0_{3\times3} \\
0_{3\times3} & 0_{3\times3} & 0_{3\times3} & 0_{3\times3} & 0_{3\times3} & 0_{3\times3} & 0_{3\times3} & \boldsymbol{F}^{\delta\boldsymbol{\omega}}_{\mathrm{GM1,3}} & 0_{3\times3} & 0_{3\times3} & 0_{3\times3} & 0_{3\times3} & 0_{3\times3} \\
0_{3\times3} & 0_{3\times3} & 0_{3\times3} & 0_{3\times3} & 0_{3\times3} & 0_{3\times3} & 0_{3\times3} & 0_{3\times3} & \boldsymbol{F}^{\delta f}_{\mathrm{GM1,3}} & 0_{3\times3} & 0_{3\times3} & 0_{3\times3} & 0_{3\times3} \\
0_{3\times3} & 0_{3\times3} & 0_{3\times3} & 0_{3\times3} & 0_{3\times3} & 0_{3\times3} & 0_{3\times3} & 0_{3\times3} & 0_{3\times3} & \boldsymbol{F}^{\delta\boldsymbol{\omega}}_{\mathrm{RW}} & 0_{3\times3} & 0_{3\times3} & 0_{3\times3} \\
0_{3\times3} & 0_{3\times3} & 0_{3\times3} & 0_{3\times3} & 0_{3\times3} & 0_{3\times3} & 0_{3\times3} & 0_{3\times3} & 0_{3\times3} & 0_{3\times3} & \boldsymbol{F}^{\delta f}_{\mathrm{RW}} & 0_{3\times3} & 0_{3\times3} \\
0_{3\times3} & 0_{3\times3} & 0_{3\times3} & 0_{3\times3} & 0_{3\times3} & 0_{3\times3} & 0_{3\times3} & 0_{3\times3} & 0_{3\times3} & 0_{3\times3} & 0_{3\times3} & \boldsymbol{F}^{\delta\boldsymbol{\omega}}_{\mathrm{WN}} & 0_{3\times3} \\
0_{3\times3} & 0_{3\times3} & 0_{3\times3} & 0_{3\times3} & 0_{3\times3} & 0_{3\times3} & 0_{3\times3} & 0_{3\times3} & 0_{3\times3} & 0_{3\times3} & 0_{3\times3} & 0_{3\times3} & \boldsymbol{F}^{\delta f}_{\mathrm{WN}}
\end{bmatrix} \tag{5.23}$$

$$\boldsymbol{\Phi} = \mathrm{e}^{\mathbf{F}\Delta t} \tag{5.24}$$

$$\mathbf{G} = \mathrm{I}_{39\times39} \tag{5.25}$$

$$\mathbf{Q}_{\mathrm{s}} = \mathrm{diag}\Big(\Big[\mathbf{q}^{\mathbf{r}}_{\mathrm{s}\,3\times1} \quad \mathbf{q}^{\mathbf{v}}_{\mathrm{s}\,3\times1} \quad \mathbf{q}^{\boldsymbol{\psi}}_{\mathrm{s}\,3\times1} \quad \mathbf{q}^{\mathrm{GM1,1}}_{\mathrm{s},\delta\boldsymbol{\omega}\,3\times1} \quad \mathbf{q}^{\mathrm{GM1,1}}_{\mathrm{s},\delta f\,3\times1} \quad \mathbf{q}^{\mathrm{GM1,2}}_{\mathrm{s},\delta\boldsymbol{\omega}\,3\times1} \quad \mathbf{q}^{\mathrm{GM1,2}}_{\mathrm{s},\delta f\,3\times1} \cdots$$
$$\mathbf{q}^{\mathrm{GM1,3}}_{\mathrm{s},\delta\boldsymbol{\omega}\,3\times1} \quad \mathbf{q}^{\mathrm{GM1,3}}_{\mathrm{s},\delta f\,3\times1} \quad \mathbf{q}^{\mathrm{RW}}_{\mathrm{s},\delta\boldsymbol{\omega}\,3\times1} \quad \mathbf{q}^{\mathrm{RW}}_{\mathrm{s},\delta f\,3\times1} \quad \mathbf{q}^{\mathrm{WN}}_{\mathrm{s},\delta\boldsymbol{\omega}\,3\times1} \quad \mathbf{q}^{\mathrm{WN}}_{\mathrm{s},\delta f\,3\times1}\Big]\Big) \tag{5.26}$$

where the calculation of the exponential in equation (5.24) can be implemented via the *expm* MATLAB built-in function, which utilizes the Padé approximation with scaling and squaring (Gene H. Golub, 2013). Furthermore, it is noted that after the calculation of the $\boldsymbol{\Phi}$ using this method, the diagonal elements that correspond to WN will all be equal to 1, which does not satisfy the discrete state-space expression of the process. Therefore, to counter this issue, these elements should always be manually set to be equal to 0. Finally, it is highlighted that in order to avoid numerical instability of the EKF filter, if a sensor has a more simplified model than the general one, like for example two GM1s, one RW and one WN, then the rows and columns that correspond to the redundant GM1 process in the above matrices should be deleted.

At this point, a special discussion should be made about the values that the $\mathbf{Q}_s$ spectral densities matrix elements should take and in what units. Specifically, $\mathbf{q}_s^r$ is usually set to be equal to a zero vector, $\mathbf{q}_s^v$ should be in $m^2 Hz$ units and it could be set as the squared value of the accelerometer noise density (i.e., VRW) that has been pre-multiplied with Δt, while $\mathbf{q}_s^\psi$ should be provided in $rad^2 Hz$ and be equal to the squared value of the gyroscope noise density (i.e., ARW) that has been pre-multiplied with Δt. Furthermore, it is noted that both these densities can be retrieved from the specifications of the sensor, provided by the manufacturer. As for the values that correspond to the inertial sensor random bias states, there is a great deal of confusion among practitioners about how they should be properly set, considering the outcome from the stochastic analysis techniques (e.g., GMWM).

In the previous chapter, where the stochastic analysis was conducted, the defining parameters of the identified stochastic processes were given in discrete time units. However, the $\mathbf{Q}_s$ matrix requires its values to be in continuous time, meaning that they have to be expressed as a function of the sensor frequency f (i.e., data rate). Furthermore, both the stochastic modeling techniques

that were used in Section 4.5, consider AR1 processes, not GM1s. Therefore, a unique considera-

tion has to be made in order to determine the GM1 parameters in the form required by the EKF.

Let's consider a continuous time system with the general form $\dot{\mathbf{x}}(t) = \mathbf{F}(t)\,\mathbf{x}(t) + \mathbf{G}(t)\,\mathbf{w}(t)$,

where $\mathbf{w}(t)$ the (continuous time) system (Gaussian and white) noise with q_{KF} spectral density.

Then, the variance of the corresponding discrete time process noise σ^2_{DISC} would be given by

the following formula (Bar-Shalom et al., 2004):

$$\sigma^2_{DISC} = \int_0^{\Delta t} e^{(\Delta t - \tau)\mathbf{F}(t)}\,\mathbf{G}(t)\,q_{KF}\,\mathbf{G}(t)^T\,e^{(\Delta t - \tau)\mathbf{F}(t)}d\tau \tag{5.27}$$

which can be used to infer the q_{KF} value of the GM1, RW and WN stochastic processes. The

derivations for each of them are provided up next.

1st-order Gauss-Markov

First, the β_{DISC} parameter of the GM1 process is determined from the φ_{GMWM} parameter of

the AR1 process (the reason why GMWM is included in the subscript is because of its frame-

work's capability to accurately infer knowledge about time-correlated processes) via equation

(2.18). In turn, using their respective discrete state-space models, the following derivations are

conducted:

$$
\begin{aligned}
\text{var}(x_t) &= \text{var}(\varphi_{GMWM}\,x_{t-1} + \varepsilon_{t-1}) \Rightarrow \\
\text{var}(x_t) &= \varphi_{GMWM}{}^2\,\text{var}(x_{t-1}) + \text{var}(\varepsilon_{t-1}) \Rightarrow \\
\text{var}(x_t) &= \varphi_{GMWM}{}^2\,\text{var}(x_{t-1}) + \xi^2{}_{GMWM}
\end{aligned}
\tag{5.28}
$$

$$
\begin{aligned}
\text{var}(x_t) &= \text{var}\left(e^{-\beta_{DISC}/f}\,x_{t-1} + w_{t-1}\right) \Rightarrow \\
\text{var}(x_t) &= e^{-2\beta_{DISC}/f}\,\text{var}(x_{t-1}) + \text{var}(w_{t-1}) \Rightarrow \\
\text{var}(x_t) &= e^{-2\beta_{DISC}/f}\,\text{var}(x_{t-1}) + \sigma^2{}_{DISC}
\end{aligned}
\tag{5.29}
$$

Furthermore, the observations are made that both these processes are stationary in time, which means that $\text{var}(x_t) = \text{var}(x_{t-1})$ as well as that their variances in discrete time should be equal. Hence, the expression below is obtained:

$$\frac{\xi^2_{\text{GMWM}}}{1 - \varphi_{\text{GMWM}}{}^2} = \frac{\sigma^2_{\text{DISC}}}{1 - e^{-2\beta_{\text{DISC}}/f}} \rightarrow \xi^2_{\text{GMWM}} = \sigma^2_{\text{DISC}} \tag{5.30}$$

Finally, by setting $\mathbf{F}(t) = -\beta_{\text{DISC}}$ and $\mathbf{G}(t) = I$ to equation (5.27), the $q_{\text{KF}}^{\text{GM1}}$ is derived as follows:

$$\sigma^2_{\text{DISC}} = \int_0^{\Delta t} e^{-(\Delta t - \tau)\beta_{\text{DISC}}} q_{\text{KF}}^{\text{GM1}} e^{-(\Delta t - \tau)\beta_{\text{DISC}}} d\tau \Longrightarrow$$

$$\sigma^2_{\text{DISC}} = q_{\text{KF}}^{\text{GM1}} \int_0^{\Delta t} e^{-2(\Delta t - \tau)\beta_{\text{DISC}}} d\tau \Longrightarrow$$

$$\sigma^2_{\text{DISC}} = q_{\text{KF}}^{\text{GM1}} \int_0^{\Delta t} e^{-2\beta_{\text{DISC}}\Delta t} e^{2\tau\beta_{\text{DISC}}} d\tau \Longrightarrow \tag{5.31}$$

$$\sigma^2_{\text{DISC}} = q_{\text{KF}}^{\text{GM1}} e^{-2\beta_{\text{DISC}}\Delta t} \int_0^{\Delta t} e^{2\tau\beta_{\text{DISC}}} d\tau \Longrightarrow$$

$$\sigma^2_{\text{DISC}} = q_{\text{KF}}^{\text{GM1}} \frac{e^{-2\beta_{\text{DISC}}\Delta t}}{2\beta_{\text{DISC}}} \left[e^{2\beta_{\text{DISC}}\Delta t} - 1 \right] \Longrightarrow$$

$$q_{\text{KF}}^{\text{GM1}} = \frac{2\beta_{\text{DISC}} \sigma^2_{\text{DISC}}}{1 - e^{-2\beta_{\text{DISC}}/f}}, \qquad f = 1/\Delta t$$

where $q_{\text{KF}}^{\text{GM1}}$ is expressed in either $m^2 Hz/sec^4$ for an accelerometer or in $rad^2 Hz/sec^2$ for a gyroscope sensor.

Random Walk

The RW process can be considered as a special case of the GM1 process with $\beta_{\text{DISC}} \rightarrow 0$. As a result, the $q_{\text{KF}}^{\text{RW}}$ can be obtained by taking the limit of equation (5.31) and by setting $\sigma^2_{\text{DISC}} =$

$\gamma^2{}_{RW}$, where $\gamma^2{}_{RW}$ is the RW discrete time parameter value, as that is produced by the GMWM/AVLR frameworks. This derivation is provided below:

$$q_{KF}^{RW} = \lim_{\beta \to 0} \frac{2\beta_{DISC}\,\gamma^2{}_{RW}}{1 - e^{-2\beta_{DISC}\Delta t}} = \lim_{\beta \to 0} \frac{(2\beta_{DISC}\,\gamma^2{}_{RW})'}{(1 - e^{-2\beta_{DISC}\Delta t})'} = \lim_{\beta \to 0} \frac{2\gamma^2{}_{RW}}{2\Delta t\, e^{-2\beta_{DISC}\Delta t}}$$
$$= \frac{\gamma^2{}_{RW}}{\Delta t} \lim_{\beta \to 0} \frac{1}{e^{-2\beta_{DISC}\Delta t}} \Longrightarrow q_{KF}^{RW} = \gamma^2{}_{RW}f \tag{5.32}$$

where q_{KF}^{RW} is in either $m^2 Hz/sec^4$ for an accelerometer or in $rad^2 Hz/sec^2$ for a gyroscope.

White Noise

After the GMWM/AVLR framework produces the σ_{WN}^2 defining parameter for the WN process, its corresponding q_{KF}^{WN} can be calculated by setting $\mathbf{F}(t) = 0$ and $\mathbf{G}(t) = I$ in equation (5.27) as follows:

$$\sigma_{WN}^2 = \int_0^{\Delta t} q_{KF}^{WN}\, d\tau \Longrightarrow q_{KF}^{WN} = \sigma_{WN}^2/f \tag{5.33}$$

where q_{KF}^{WN} is in either $m^2/sec^4/Hz$ for an accelerometer or in $rad^2/sec^2/Hz$ for a gyroscope.

5.3.3 Linearized Measurement Model

As it was mentioned earlier, the measurement model relates the update information with the navigation error states and it is expressed by the $\delta\mathbf{z}$, $\mathbf{H}$ and $\mathbf{R}$ matrices within the EKF algorithm. In this study, where focus is given on vehicular navigation, three update sources will be utilized: the GNSS system, the NHCs and ZUPTs. Furthermore, it is noted that the updates of each source are introduced to the filter independently from each other, depending on the conditions below:

- GNSS availability: 3d position and velocity updates from the GNSS system,

- GNSS outage and vehicle in-motion: velocity updates based on the NHCs,

- GNSS outage and stationary vehicle: 3d velocity updates based on the ZUPTs.

Therefore, with this in mind, the linearized measurement model matrices for each update will be presented next.

GNSS System Updates

First, the matrices that correspond to the position updates from the GNSS system are presented below (Shin, 2005):

$$\delta \mathbf{z}_r = \mathbf{R}_e^n \left(\hat{\mathbf{r}}_{IMU}^e - \tilde{\mathbf{r}}_{GNSS}^e \right) + \hat{\mathbf{R}}_b^n \, \boldsymbol{l}_{GNSS}^b,$$

$$\mathbf{R}_e^n = \begin{bmatrix} -\sin\tilde{\phi} \cos\tilde{\lambda} & -\sin\tilde{\phi} \sin\tilde{\lambda} & \cos\tilde{\phi} \\ -\sin\tilde{\lambda} & \cos\tilde{\lambda} & 0 \\ -\cos\tilde{\phi} \cos\tilde{\lambda} & -\cos\tilde{\phi} \sin\tilde{\lambda} & -\sin\tilde{\phi} \end{bmatrix} \tag{5.34}$$

$$\mathbf{H}_r = \begin{bmatrix} \mathbf{I}_{3\times3} & \mathbf{0}_{3\times3} & \left(\hat{\mathbf{R}}_b^n \, \boldsymbol{l}_{GNSS}^b \times \right) & \mathbf{0}_{3\times30} \end{bmatrix} \tag{5.35}$$

$$\mathbf{R}_r = \mathrm{diag}\left(\begin{bmatrix} \sigma^2_{\tilde{\phi}} & \sigma^2_{\tilde{\lambda}} & \sigma^2_{\tilde{h}} \end{bmatrix} \right) \tag{5.36}$$

where $\mathbf{R}_e^n$ is the DCM matrix that describes the transformation from the e-frame to the n-frame and it is a function of the GNSS-provided latitude $\tilde{\phi}$ and longitude $\tilde{\lambda}$, $\hat{\mathbf{r}}_{IMU}^e$ and $\tilde{\mathbf{r}}_{GNSS}^e$ are the e-frame 3d position vectors from the INS mechanization and the GNSS system respectively, $\boldsymbol{l}_{GNSS}^b$ is referred to as the *lever arm* and represents the 3d vector between the GNSS antenna phase center and the IMU's center with respect to the b-frame and $\left(\sigma^2_{\tilde{\phi}}, \sigma^2_{\tilde{\lambda}}, \sigma^2_{\tilde{h}} \right)$ are the variances provided by the separate EKF filter that estimated the GNSS position information.

Subsequently, the linearized model regarding the velocity updates is presented as well (Shin, 2005):

$$\delta\mathbf{z}_v = \hat{\mathbf{v}}_{IMU}^c - \tilde{\mathbf{v}}_{GNSS}^c - [(\hat{\omega}_{ie}^n \times) + (\hat{\omega}_{en}^n \times)] \, \hat{\mathbf{R}}_b^n \, \boldsymbol{l}_{GNSS}^b - \hat{\mathbf{R}}_b^n (\boldsymbol{l}_{GNSS}^b \times) \, \tilde{\boldsymbol{\omega}}_{ib}^b \implies$$

$$\delta\mathbf{z}_v = \hat{\mathbf{v}}_{IMU}^c - \mathbf{R}_e^c \, (\mathbf{R}_e^n)^T \, \tilde{\mathbf{v}}_{GNSS}^n - (\hat{\omega}_{in}^n \times) \, \hat{\mathbf{R}}_b^n \, \boldsymbol{l}_{GNSS}^b - \hat{\mathbf{R}}_b^n (\boldsymbol{l}_{GNSS}^b \times) \, \tilde{\boldsymbol{\omega}}_{ib}^b,$$

$$\mathbf{R}_e^c = \begin{bmatrix} -\sin\phi\cos\lambda & -\sin\phi\sin\lambda & \cos\phi \\ -\sin\lambda & \cos\lambda & 0 \\ -\cos\phi\cos\lambda & -\cos\phi\sin\lambda & -\sin\phi \end{bmatrix} \tag{5.37}$$

$$\omega_{ie}^n = [\omega_e \cos\phi \quad 0 \quad -\omega_e \sin\phi]^T,$$

$$\omega_{en}^n = [v_E/(R_N + h) \quad -v_N/(R_M + h) \quad -v_E \tan\phi/(R_N + h)]^T$$

$$\mathbf{H}_v = \begin{bmatrix} 0_{3\times3} & I_{3\times3} & -(\omega_{in}^n \times) \, \hat{\mathbf{R}}_b^n \, (\boldsymbol{l}_{GNSS}^b \times) - (\hat{\mathbf{R}}_b^n \, (\boldsymbol{l}_{GNSS}^b \times \tilde{\boldsymbol{\omega}}_{ib}^b) \times) \dots \end{bmatrix}$$
$$\hat{\mathbf{R}}_b^n \, (\boldsymbol{l}_{GNSS}^b \times) \quad 0_{3\times3} \quad \hat{\mathbf{R}}_b^n \, (\boldsymbol{l}_{GNSS}^b \times) \quad 0_{3\times3} \quad \hat{\mathbf{R}}_b^n \, (\boldsymbol{l}_{GNSS}^b \times) \quad 0_{3\times3} \dots \tag{5.38}$$
$$\begin{bmatrix} \hat{\mathbf{R}}_b^n \, (\boldsymbol{l}_{GNSS}^b \times) & 0_{3\times3} & \hat{\mathbf{R}}_b^n \, (\boldsymbol{l}_{GNSS}^b \times) & 0_{3\times3} \end{bmatrix}$$

$$\mathbf{R}_v = \text{diag}\left([\sigma^2_{\tilde{v}_N} \quad \sigma^2_{\tilde{v}_E} \quad \sigma^2_{\tilde{v}_D}]\right) \tag{5.39}$$

where $\hat{\omega}_{ie}^n$ is the Earth's rotation rate in the n-frame, $\hat{\omega}_{en}^n$ is referred to as the transport rate (it is based on the latitude and longitude provided by the INS mechanization), $(\cdot\times)$ constitutes the skew-symmetric representation of a (3×1) vector, $\tilde{\boldsymbol{\omega}}_{ib}^b$ are the gyroscope measurement vector, $\tilde{\mathbf{v}}_{GNSS}^n$ the velocities derived by the GNSS system in the n-frame, $\mathbf{R}_e^c$ the rotation matrix from the e-frame to the c-frame and $(\sigma^2_{\tilde{v}_N}, \sigma^2_{\tilde{v}_E}, \sigma^2_{\tilde{v}_D})$ are the estimated variances by the GNSS filter that describe the velocity value variability.

Eventually, the aforementioned equations are combined in order to constitute the total measurement model matrices for both the position and velocity updates from the GNSS sensor:

$$\delta\mathbf{z} = [\delta\mathbf{z}_r \quad \delta\mathbf{z}_v]^T, \qquad \mathbf{H} = [\mathbf{H}_r \quad \mathbf{H}_v]^T, \qquad \mathbf{R} = [\mathbf{R}_r \quad \mathbf{R}_v]^T \tag{5.40}$$

Non-Holonomic Constraint Updates

The NHCs are two artificial velocity updates that can be provided to the EKF filter when dealing with vehicular navigation or robot localization. Specifically, these updates represent the intuitive observation that when a car or a robot is in motion and not skidding, the upwards and sideways velocities should be equal to zero, or at least very close to it. Below, the linearized measurement model that corresponds to these updates and be used in the context of the EKF is presented (Shin, 2005):

$$
\delta \mathbf{z}_{\text{NHC}} = \left[\mathbf{R}_b^v \left(\widehat{\mathbf{R}}_b^n \right)^T \widehat{\mathbf{v}}_{\text{IMU}}^c + \mathbf{R}_b^v \left(\widehat{\omega}_{nb}^b \times \right) \mathbf{l}_{\text{wheel}}^b \right]_{2:3} ,
$$

$$
\widehat{\omega}_{nb}^b = \widetilde{\boldsymbol{\omega}}_{ib}^b - \left(\widehat{\mathbf{R}}_b^n \right)^T (\widehat{\omega}_{ie}^n + \widehat{\omega}_{en}^n)
$$

(5.41)

$$
\mathbf{H}_{\text{NHC}} = \big[0_{3\times3} \quad \left(\widehat{\mathbf{R}}_b^n \right)^T \quad -\mathbf{R}_b^v \left(\widehat{\mathbf{R}}_b^n \right)^T \left(\widehat{\mathbf{v}}_{\text{IMU}}^c \times \right) \quad -\mathbf{R}_b^v \left(\mathbf{l}_{\text{wheel}}^b \times \right) \quad 0_{3\times3} \cdots
$$

$$
-\mathbf{R}_b^v \left(\mathbf{l}_{\text{wheel}}^b \times \right) \quad 0_{3\times3} \quad -\mathbf{R}_b^v \left(\mathbf{l}_{\text{wheel}}^b \times \right) \quad 0_{3\times3} \quad -\mathbf{R}_b^v \left(\mathbf{l}_{\text{wheel}}^b \times \right) \quad 0_{3\times3} \cdots
$$

$$
-\mathbf{R}_b^v \left(\mathbf{l}_{\text{wheel}}^b \times \right) \quad 0_{3\times3} \big]_{2:3}
$$

(5.42)

$$
\mathbf{R}_{\text{NHC}} = \text{diag}\left(\left[\sigma^2_{v_{\text{E,NHC}}} \quad \sigma^2_{v_{\text{D,NHC}}} \right] \right)
$$

(5.43)

where $\mathbf{R}_b^v$ is referred to as the *boresight* matrix and it describes the relationship between the b-frame of the IMU and the vehicle frame (v-frame), $\mathbf{l}_{\text{wheel}}^b$ is the lever arm between the IMU and the vehicle frame's origin and $\left(\sigma^2_{v_{\text{E,NHC}}}, \sigma^2_{v_{\text{D,NHC}}} \right)$ are the variances associated with the discrepancies of the side and vertical velocities from the nominal value (i.e., zero), which are reasonably selected in order to maximize the navigation performance.

Zero Velocity Updates

The last update source that will be utilized in this study is related to the situation where the vehicle has stopped moving. Consequently, all three of its velocity navigation state components should be equal to zero, or just very close to it due to the vibrations created by the operation of the static vehicle. As for how it is determined whether the vehicle has stopped moving, there are two main ways to do it; one that relies on the utilization of the vehicle's speedometer and one that is based on the analysis of the raw inertial sensor measurements (for example, see (Aggarwal, 2010) for an accelerometer sensor-based stop detection algorithm). Therefore, the EKF measurement model matrices that should be used for the consideration of the ZUPTs would receive the following form:

$$\delta \mathbf{z}_{\text{ZUPT}} = \hat{\mathbf{v}}_{\text{IMU}}^{c} \tag{5.44}$$

$$\mathbf{H}_{\text{ZUPT}} = \begin{bmatrix} 0_{3\times3} & I_{3\times3} & 0_{3\times33} \end{bmatrix} \tag{5.45}$$

$$\mathbf{R}_{\text{ZUPT}} = \text{diag}\left(\begin{bmatrix} \sigma^2_{v_{N,\text{ZUPT}}} & \sigma^2_{v_{E,\text{ZUPT}}} & \sigma^2_{v_{D,\text{ZUPT}}} \end{bmatrix}\right) \tag{5.46}$$

where $(\sigma^2_{v_{N,\text{ZUPT}}}, \sigma^2_{v_{E,\text{ZUPT}}}, \sigma^2_{v_{D,\text{ZUPT}}})$ are logically selected variances, affiliated with the ZUPT-implied velocities.

5.4 Filter Initialization

This section is devoted to the description of the manner in which the aforementioned recursive EKF filter can be initialized. Specifically, this refers to the selection of proper starting values for the absolute state vector $\mathbf{x}_0$ and its corresponding V-C matrix $\mathbf{P}_0$. Typically, the navigation algorithm is initiated from the first epoch that the GNSS information becomes available. Therefore, with this in mind and for the purposes of this study, the state vector $\mathbf{x}_0$ is chosen as follows:

- The position (ϕ_0, λ_0, h_0) and velocity $(v_{N,0}, v_{E,0}, v_{D,0})$ components are set to be equal to the first GNSS-derived solutions,

- the initial attitude (r_0, p_0, A_0) is evaluated via a 10-minute static alignment process, conducted prior to the beginning of the navigation experiment (i.e., GNSS information starting time),

- and the random biases for each inertial sensor are set to zero.

As for the corresponding uncertainty matrix $\mathbf{P}_0$, it is set to be diagonal and to have the following values:

- The position and velocity elements (i.e., variances) are obtained from the separate EKF that estimated the GNSS solutions (that's why this is a loosely coupled integration algorithm).

- The initial attitude angle variances are given by the following formulas (Britting, 1971):

$$\sigma^2_{r_0} = \frac{b_{f_y}}{g} \tag{5.47}$$

$$\sigma^2_{p_0} = \frac{1}{2}\left[-\frac{b_{f_x}}{g} + \frac{b_{f_z}}{g}\tan\phi - \frac{b_{\omega_z}}{\omega_e\cos\phi}\right] \tag{5.48}$$

$$\sigma^2{}_{A_0} = -\frac{b_{f_z}}{g}\tan\phi + \frac{b_{\omega_y}}{\omega_e\cos\phi} \tag{5.49}$$

where $(b_{f_x}, b_{f_y}, b_{f_z}, b_{\omega_y}, b_{\omega_z})$ are the inertial sensor deterministic biases, evaluated via deterministic calibration.

- The variances that correspond to each stochastic process type that is included within the EKF's system model are:

$$\sigma^2(\text{GM1}) = \frac{\xi^2{}_{\text{GMWM}}}{1 - \varphi_{\text{GMWM}}{}^2} \tag{5.50}$$

$$\sigma^2(\text{RW}) = \gamma^2{}_{\text{RW}} \tag{5.51}$$

$$\sigma^2(\text{WN}) = \sigma^2{}_{\text{WN}} \tag{5.52}$$

where $(\varphi_{\text{GMWM}}, \xi^2{}_{\text{GMWM}})$ are the AR1 parameters as they were provided by the GMWM analysis (the AR1 parameters can be used here due to equation (5.30)) and $(\gamma^2{}_{\text{RW}}, \sigma^2{}_{\text{WN}})$ are the parameters for the RW and WN processes respectively, as they were given by the GMWM/AVLR frameworks.

5.5 Error Feedback

A final consideration that must be made is about how $\delta\hat{\mathbf{x}}_k{}^+$ is utilized to enhance the integrated navigation performance. Specifically, after the filter has completed an iteration at time k of both prediction and update, the absolute (navigation) state vector from the previous time $\mathbf{x}_{k-1}$ is updated as follows:

$$\mathbf{x}_k = \mathbf{x}_{k-1} + \delta\hat{\mathbf{x}}_k{}^+ \tag{5.53}$$

In turn, the components of $\mathbf{x}_k$ that correspond to corrections for the same sensor are added together and then utilized to correct next epoch's measurement in the manner that is shown by the formula below the gyroscope sensor triad:

$$
\widetilde{\boldsymbol{\omega}}_{k+1}^b = \begin{bmatrix} 1 + s_{g,x} & m_{g,yx} & m_{g,zx} \\ m_{g,xy} & 1 + s_{g,y} & m_{g,zy} \\ m_{g,xz} & m_{g,yz} & 1 + s_{g,z} \end{bmatrix}^{-1} \begin{bmatrix} \omega_{x,k+1}^b - b_{g,x}' \\ \omega_{x,k+1}^b - b_{g,y}' \\ \omega_{x,k+1}^b - b_{g,z}' \end{bmatrix},
$$

$$
\begin{bmatrix} b_{g,x}' \\ b_{g,y}' \\ b_{g,z}' \end{bmatrix} = \begin{bmatrix} b_{g,x} + \delta\omega_{x,GM1,1} + \delta\omega_{x,GM1,2} + \delta\omega_{x,GM1,3} + \delta\omega_{x,RW} + \delta\omega_{x,WN} \\ b_{g,y} + \delta\omega_{y,GM1,1} + \delta\omega_{y,GM1,2} + \delta\omega_{y,GM1,3} + \delta\omega_{y,RW} + \delta\omega_{y,WN} \\ b_{g,z} + \delta\omega_{z,GM1,1} + \delta\omega_{z,GM1,2} + \delta\omega_{z,GM1,3} + \delta\omega_{z,RW} + \delta\omega_{z,WN} \end{bmatrix}
$$

(5.54)

where $(s_{g,x}, s_{g,y}, s_{g,z})$ and $(m_{g,yx}, m_{g,zx}, m_{g,xy}, m_{g,zy}, m_{g,xz}, m_{g,yz})$ are the gyroscope scale factor errors and non-orthogonality angles that have been estimated by deterministic calibration, $(b_{g,x}, b_{g,y}, b_{g,z})$ are the gyro biases at time k and $(b_{g,x}', b_{g,y}', b_{g,z}')$ the gyro biases at time $k+1$. In fact, for $k = 0$, the $(b_{g,x}, b_{g,y}, b_{g,z})$ quantities are equal to the bias values determined via calibration. Furthermore, when there is no update to the system, the corrected biases $(b_{g,x}', b_{g,y}', b_{g,z}')$ from the last time there was one is still being utilized to correct the measurements until a new update becomes available.

This scheme, where the bias corrections are fed back to correct the inertial sensor measurements before they are used by the INS mechanization is called the "closed-loop integration scheme" and as a result, the quantity $\delta\hat{\mathbf{x}}_{k-1}^+$ is set to be equal to zero at the start of every iteration.

5.6 Summary

In this chapter, an EKF-based INS/GNSS/NHC/ZUPT navigation algorithm was presented via a thorough description of the matrices that express its linearized system and measurement models. Furthermore, the way that the stochastic modeling knowledge about the inertial sensor errors, obtained from either the GMWM or the AVLR, can be infused within the EKF and more specifically within the dynamic and spectral density matrices was highlighted. Finally, instructions on how to properly initialize the filter were given along with an explanation on how the employed closed-loop scheme works, which is related to the manner that the EKF applies the corrections it estimates to the inertial measurements of the next epoch(s).

Chapter Six: Unscented Kalman Filter-based Navigation Algorithm for Loosely Coupled Integration

6.1 Introduction

This chapter is devoted to another recursive Bayesian-type filter that has been widely utilized for a variety of different applications, called the *Unscented Kalman Filter* (Julier et al., 1995). The UKF is a nonlinear estimator that is based on the MMSE criterion and it attempts to better support the notion under which KF variants operate, that it is easier to approximate Gaussian distributions instead of arbitrary nonlinear PDFs (Julier and Uhlmann, 1997a). Consequently, just like the EKF, it assumes the states as Gaussian Random Variables (GRVs), meaning that their respective PDF follows the Gaussian distribution. The primary difference however with the EKF lies in the fact that the mean and covariance characterizing the state distribution are no longer specified by single values. Instead, they are captured with a set of deterministically sampled and appropriately weighted points called the *Sigma Points* (SPs), which are calculated by the Unscented Transformation (UT). In turn, these SPs are propagated through the true nonlinear system and measurement models and they manage to recursively estimate the posterior PDF's characteristics with an accuracy up to at least the 2nd order for any nonlinearity (Wan and Van Der Merwe, 2000; Van Der Merwe et al., 2001). Therefore, in this way, the UKF achieves a better fitting of a Gaussian distribution to the true state PDF than the standard EKF, something that is visually demonstrated in Figure 6.1.
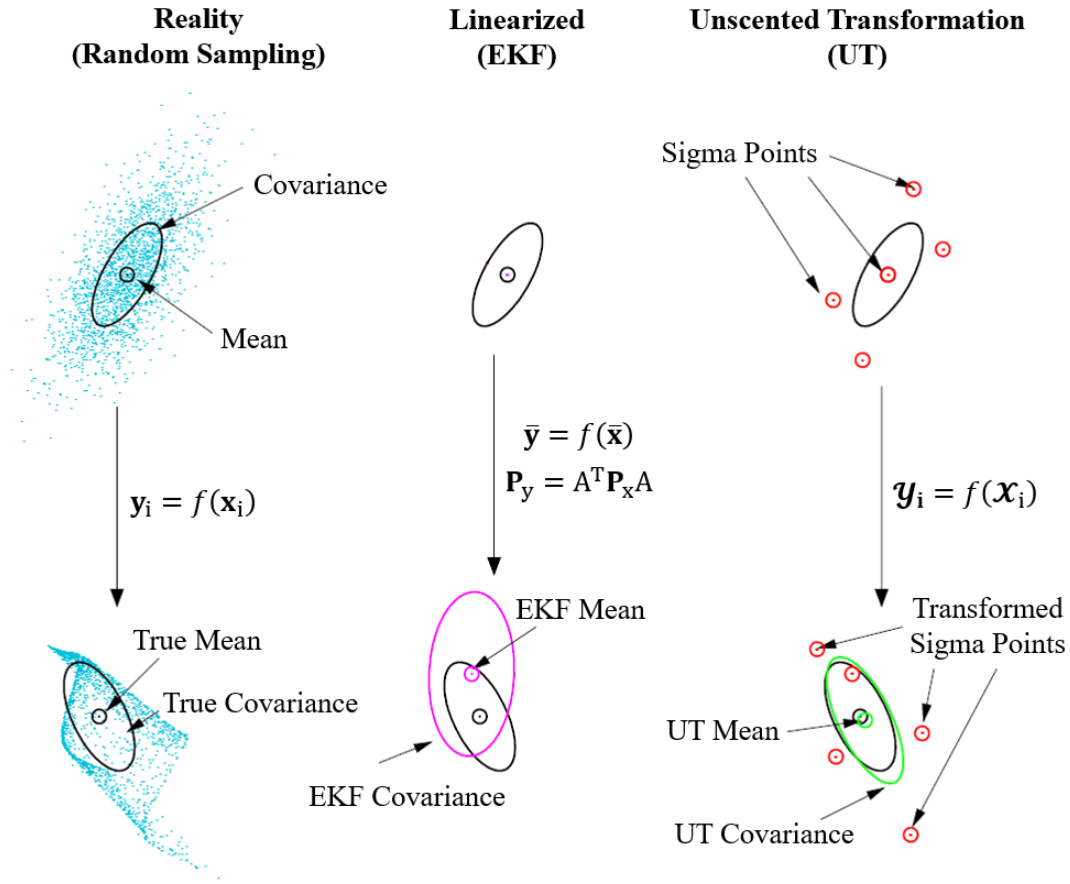
Figure 6.1: Schematic representation of how the mean and covariance are propagated in (a) reality, (b) a first-order truncated Taylor series expansion-based scheme (EKF) and (c) the UT-driven UKF (adapted from Wan and Van Der Merwe, (2002))

Given the aforementioned, it is important to mention that the UKF does not require the linearization of the models based on which the filter is structured and as a result, there is no need for neither the selection of a state error model, nor the calculation of Jacobian matrices. In fact, this makes the UKF to be a much more straightforward approach compared to the EKF and any possible errors from complex derivations or model linearization are avoided (Julier et al., 1995). Furthermore, when the nonlinearity of the system and/or the measurement models is significant, the UKF will not have as significant nonlinear truncation errors as the EKF would have and thus, better estimation accuracy and more reliable uncertainty information can be obtained (Brown and Hwang, 2012).

Shin and El-Sheimy, (2004) were the first to adapt the UKF for navigation purposes, while they also demonstrated the filter's prowess in handling attitude errors of any magnitude with great efficiency. Nevertheless, due to the fact that the authors utilized Euler angles to describe and propagate the attitude, the proposed approach was vulnerable to the occurrence of singularities, while the way that the attitude differences were being evaluated was insufficient. To resolve these issues, Shin, (2005) developed a quaternion-based UKF for multiple navigation sensor integration based on the approach established by Kraft, (2003), where the noises were assumed to be non-additive in nature and the random drift of the inertial sensor biases, scale factors and non-orthogonalities was considered. As a matter of fact, the resulting filter structure is being utilized by the UKF that is included within the AINS® software (Shin and El-Sheimy, 2004a). Finally, it should be noted that the UKF has been utilized in a multitude of applications in the navigation field with great success (e.g., see (Shin and El-Sheimy, 2007; Yi, 2007; Bogdanski and Best, 2018; Liu, 2019)).

Next, a UKF algorithm for INS/GNSS/NHC/ZUPT integration that utilizes the AINS® software's version as a base and only accounts for the bias instability of the inertial sensors will be presented. In addition, it is highlighted that this consideration will be based on the advanced stochastic modeling information derived from the new multi-signal GMWM-based framework as well as the standard AVLR, presented in Section 4.5.

6.2 The Unscented Transformation

The core element of the UKF filter is the Unscented Transformation (UT), the procedure through which the mean $\bar{\mathbf{x}}$ and covariance $\mathbf{P}$ of the (presumed) Gaussian state PDF are utilized in order to produce the SPs $\mathcal{X}_i$ along with their corresponding weights w_i^{m} (for the mean) and w_i^{c} (for the covariance), based on the three conditions presented below (Julier and Uhlmann, 1997b):

$$\sum_{i=0}^{p-1} w_i^{\mathrm{m}} = \sum_{i=0}^{p-1} w_i^{\mathrm{c}} = 1 \tag{6.1a}$$

$$\sum_{i=0}^{p-1} w_i^{\mathrm{m}} \, \boldsymbol{X_i} = \bar{\mathbf{x}} \tag{6.2b}$$

$$\sum_{i=0}^{p-1} w_i^{\mathrm{c}} \, (\boldsymbol{X_i} - \bar{\mathbf{x}})(\boldsymbol{X_i} - \bar{\mathbf{x}})^{\mathrm{T}} = \mathbf{P} \tag{6.3c}$$

where p is the number of SPs that capture the mean and covariance. Generally, the literature contains several schemes for the manner that these points are generated, the choice of which also determines their number. An overview of these methods can be found in (Van Der Merwe, 2004).

In order to select the proper UT scheme, the characteristics of the problem at hand have to be considered. Specifically, the INS information that drives the filter has a very high data rate (resulting to an increased computational load), the introduction of the advanced stochastic modeling knowledge about the inertial sensor error random drift requires the increase of the state dimension n (the absolute minimal number of SPs is desirable to maintain computational efficiency in logical levels) and that it has to be ensured that the SPs will be sampled in a region close to the uncertainty level of the PDF's mean. Therefore, with these in mind, the Scaled Spherical Simplex UT (SSS-UT) was chosen to be utilized. In fact, according to Julier, (2003), the SSS-UT is capable of producing SPs that achieve a 2nd order accuracy in terms of both the mean and the covariance of the propagated/transformed state PDF, while also having the advantage of being numerically better compared to SPs derived using other schemes. Nevertheless, before the algorithm of the selected UT is presented, it is worth explaining what each component of its designation practically means.

The spherical part in the SSS-UT refers to the fact that the SPs (satisfying the UT conditions) are geometrically dispersed on a hypersphere with radius $\sqrt{n/(1-w_0)}$ (w_0 the 0th point's weight and n is the dimension of the state vector) and centred at the state mean, apart from one, which is located at the exact center of that sphere. However, in high dimensional systems, which is the case in this study, even though the mean and covariance of the prior state distribution (before the propagation and update consideration) are captured correctly, the SP distribution radius (i.e., hypersphere) is increased to such a extent that it becomes possible to sample non-local effects (region far away from the state's true uncertainty region) (Van Der Merwe, 2004). Consequently, in the case where the nonlinearities are acute, this would potentially result to considerable difficulties, especially with regards to orientation-related sigma point generation, propagation and estimation, due to the angle periodicity (Shin, 2004). Therefore, to counter this issue, the scaled part is included to the selected UT's designation, which refers to the appropriate adjustment of the SP sampling area's size in order to ensure that it will more accurately approximate the (true) state uncertainty region, despite the high dimensionality of the system (Julier, 2003). Finally, regarding the simplex part, it indicates that not only the produced SPs have been selected in such a way that not only they are the absolute necessary (minimal) in number, but also, they capture the first two moments of the state PDF's mean and covariance correctly and minimize the third order moment influence (i.e., skewness) (Julier, 2002).

Having presented the reasons why the SSS-UT has been selected as well as the corresponding practical implications, its complete algorithm is presented below, where the SPs are derived from the absolute state vector $\hat{\mathbf{X}}$ and its corresponding covariance matrix $\mathbf{P}$ (Shin, 2005):

1) Select w_0, with the condition $0 \leq w_0 \leq 1$ in mind.

According to Shin, (2005), the transformed state variance after its propagation through the nonlinear system model will correspond to the true quantity if $w_0 = 2/3$.

2) Evaluate the weight series:

$$w_i = (1 - w_0)/(n + 1), \qquad i = 1, \dots, n + 1 \tag{6.4}$$

where n is the dimension of the $\hat{\mathbf{X}}$ state vector.

3) Initialize the vector sequence of the SPs (for $j = 1$):

$$\mathcal{X}^1_{u,0} = [0], \qquad \mathcal{X}^1_{u,1} = \left[\frac{-1}{\sqrt{2w_1}}\right], \qquad \mathcal{X}^1_{u,2} = \left[\frac{1}{\sqrt{2w_1}}\right] \tag{6.5}$$

4) Complete the vector sequence of the SPs (for $j = 2, \dots, n$):

$$\mathcal{X}^j_{u,i} = \begin{cases} \begin{bmatrix} \mathcal{X}^{j-1}_{u,0} \\ 0 \end{bmatrix} & i = 0 \\[2ex] \begin{bmatrix} \mathcal{X}^{j-1}_{u,i} \\ -1/\sqrt{j(j+1)w_1} \end{bmatrix} & i = 1, \dots, j \\[2ex] \begin{bmatrix} 0^{j-1} \\ j/\sqrt{j(j+1)w_1} \end{bmatrix} & i = j + 1 \end{cases} \tag{6.6}$$

where $\mathcal{X}^j_{u,i}$ indicates the SPs that correspond to $\hat{\mathbf{X}} = 0$ and $\mathbf{P} = \mathbf{I}$, j denotes the SP element and i is the sequence indicator of each SP.

5) Determine the weights for the mean (1st moment of the state PDF):

$$w_i^m = \begin{cases} (w_0 - 1)/\alpha^2 + 1 & i = 0 \\ w_i^2/\alpha^2 & i \neq 0 \end{cases} \tag{6.7}$$

where α is a small positive constant $(10^{-4} \leq \alpha \leq 1)$ that scales the size of the SP distribution and prevents the sampling from non-local effects (Van Der Merwe, 2004).

According to Shin, (2004), this parameter can be set to be equal to the reciprocal of the hypersphere's radius $\alpha = \sqrt{(1 - w_0)/n}$ within which the SPs are conditioned to exist in. Thus, the SPs will be sampled within the $(\pm 1\sigma)$ range from the sphere's center (i.e., state PDF mean).

6) Evaluate the weights for the covariance (2nd moment of the state PDF):

$$w_i^c = \begin{cases} (w_0 - 1)/\alpha^2 + 2 + \beta - \alpha^2 & i = 0 \\ w_i^2/\alpha^2 & i \neq 0 \end{cases} \tag{6.8}$$

where β is a positive parameter that incorporates higher order moment knowledge to the state distribution (Van Der Merwe, 2004).

According to Julier, (2002), for Gaussian distributions, the optimal value would be $\beta = 2$.

7) Apply the Cholesky factorization to the state covariance matrix **P** in order to obtain the lower triangular square root matrix $\mathbf{S}(1 \times n)$. In turn, compute the SSS-UT SPs based on the input state vector $\hat{\mathbf{X}}$:

$$\mathcal{X}_i = \hat{\mathbf{X}} + \alpha \, \mathbf{S} \, \mathcal{X}_{u,i}, \qquad i =, \dots, n + 1 \tag{6.9}$$

From a practical standpoint, in order for the Cholesky factorization to be implemented, the **P** matrix has to be positive definite. Therefore, in order to ensure that during the recursive estimation process the positive definiteness of the covariance matrix is not violated, a very small quantity must be added to its elements (e.g., 10^{-25}).

6.3 The Unscented Kalman Filter

Having described the cornerstone of the UKF, its complete discrete-time algorithm that is to be utilized for the purposes of this thesis can now be presented. Furthermore, it should be mentioned that the form of this Bayesian-type filter changes slightly depending on whether the system and measurement noises are assumed to be additive or non-additive in nature. Here, considering the characteristics of the INS/GNSS/NHC/ZUPT integration problem, it is realistic to presume the system noises to be non-additive and the measurement noises to be additive in nature. Therefore, with this in mind, the two-step recursive algorithm (prediction and update) of the UKF that incorporates the SSS-UT is provided in the following:

Prediction

1) Given the prior (Gaussian) state PDF's mean $\widehat{\mathbf{X}}_{k-1|k-1}$ and covariance $\mathbf{P}_{k-1|k-1}$, the SSS-UT SPs and their corresponding weights are derived:

$$\left\{\boldsymbol{\mathcal{X}}_{i,k-1|k-1}, w_i^m, w_i^c\right\} = \text{SSS} - \text{UT}\left\{\widehat{\mathbf{X}}_{k-1|k-1}, \mathbf{P}_{k-1|k-1}, \alpha, \beta, w_0\right\} \qquad (6.10)$$

2) The SPs are transformed through the original nonlinear system model SM:

$$\boldsymbol{\mathcal{X}}_{i,k-1|k} = SM\left(\boldsymbol{\mathcal{X}}_{i,k-1|k-1}, \mathbf{u}_{k-1}, \mathbf{w}_{i,k-1}\right), \qquad i = 0, \dots, n+1 \qquad (6.11)$$

where i is the SP index, $\mathbf{u}_{k-1}$ the control input that drives the transition from the previous to the current time, $\mathbf{w}_{i,k-1}$ the process noise and n is the dimension of the state vector.

3) Using the basic conditions of the UT (equations (6.2b) and (6.3c)), the mean and covariance of the predicted state PDF are evaluated from the SPs:

$$\widehat{\mathbf{X}}_{k-1|k}(-) = \sum_{i=0}^{n+1} w_i^m \, \mathcal{X}_{i,k-1|k} \tag{6.12}$$

$$\mathbf{P}_{k-1|k}(-) = \sum_{i=0}^{n+1} w_i^c \left(\Delta \mathcal{X}_{i,k-1|k}\right)\left(\Delta \mathcal{X}_{i,k-1|k}\right)^T \tag{6.13}$$

where $\Delta \mathcal{X}_{i,k-1|k} = \mathcal{X}_{i,k-1|k} - \widehat{\mathbf{X}}_{k-1|k}(-)$.

4) From the predicted state vector and covariance matrix, the SSS-UT SPs and associated weights are calculated:

$$\left\{\mathcal{X}'_{i,k-1|k}, w_i^{m'}, w_i^{c'}\right\} = \text{SSS} - \text{UT}\left\{\widehat{\mathbf{X}}_{k-1|k}(-), \mathbf{P}_{k-1|k}(-), \alpha, \beta, w_0\right\} \tag{6.14}$$

Update

1) The SPs are transformed through the original nonlinear measurement model:

$$\mathcal{Z}_{i,k-1|k} = h\left[\mathcal{X}'_{i,k-1|k}\right] \tag{6.15}$$

2) Using the UT property of equation (6.2b), the predicted measurements are evaluated from the transformed SPs:

$$\widehat{\mathbf{z}}_{k-1|k} = \sum_{i=0}^{n+1} w_i^{m'} \mathcal{Z}_{i,k-1|k} \tag{6.16}$$

3) The cross-covariance between the states and the measurements is derived from the following formula:

$$\mathbf{P}_{xz,k} = \sum_{i=0}^{n+1} w_i^{c'} \left(\Delta \mathcal{X}'_{i,k-1|k}\right)\left(\Delta \mathcal{Z}_{i,k-1|k}\right)^T \tag{6.17}$$

where $\Delta \mathcal{X}'_{i,k-1|k} = \mathcal{X}'_{i,k-1|k} - \widehat{\mathbf{X}}_{k-1|k}(-)$ and $\Delta Z_{i,k-1|k} = Z_{i,k-1|k} - \widehat{\mathbf{z}}_{k-1|k}$.

4) The covariance of the innovation sequence, considering the additivity of the measurement noises, is computed:

$$\mathbf{P}_{vv,k} = \sum_{i=0}^{n+1} w_i^{c'} \left(\Delta Z_{i,k-1|k} \right) \left(\Delta Z_{i,k-1|k} \right)^{\mathrm{T}} + \mathbf{R}_k \tag{6.18}$$

5) Using the previously evaluated covariance matrices, the Kalman gain $\mathbf{K}$ is derived from the equation below:

$$\mathbf{K}_k = \mathbf{P}_{xz,k} \, \mathbf{P}_{vv,k}^{-1} \tag{6.19}$$

6) The updated mean $\widehat{\mathbf{X}}$ and covariance $\mathbf{P}$ of the (posterior) state PDF are determined:

$$\widehat{\mathbf{X}}_{k|k}(+) = \widehat{\mathbf{X}}_{k-1|k}(-) + \mathbf{K}_k \underbrace{\left(z_k - \widehat{\mathbf{z}}_{k-1|k} \right)}_{v_k} \tag{6.20}$$

$$\mathbf{P}_{k|k}(+) = \mathbf{P}_{k-1|k}(-) - \mathbf{K}_k \, \mathbf{P}_{vv,k} \, \mathbf{K}_k^{\mathrm{T}} \tag{6.21}$$

where z_k is the auxiliary source information and v_k the innovation sequence.

7) The SPs that correspond to the updated state PDF's characteristics are evaluated based on the SSS-UT:

$$\left\{ \mathcal{X}''_{i,k|k}, w_i^{m''}, w_i^{c''} \right\} = \mathrm{SSS} - \mathrm{UT} \left\{ \widehat{\mathbf{X}}_{k|k}(+), \mathbf{P}_{k|k}(+), \alpha, \beta, w_0 \right\} \tag{6.22}$$

6.4 Filter Structure

This section is dedicated to the way that each part of the aforementioned UKF has to be constructed in order to perform the INS/GNSS/NHC/ZUPT information fusion in a loosely coupled

manner. In addition, the modifications required for the incorporation of the sophisticated stochastic modeling information regarding the inertial sensor bias instability, as that was derived by the robust multi-signal GMWM-based method as well as the AVLR in Section 4.5, will be highlighted.

6.4.1 Absolute State Vector

Similarly to the EKF, the infusion of the UKF's algorithm with the advanced stochastic modeling for the inertial sensor measurement random errors will be conducted through the state-space augmentation technique (Gelb, 1974). Moreover, since the process noises are considered to be non-additive, this augmentation has to be expanded in order to include them as well and thus allow their natural propagation (integration) through the nonlinear system model. Therefore, with this in mind and by considering the same $\mathcal{Z}$ model that was utilized in Chapter 5 to structure the EKF state vector, the augmented UKF state $\mathbf{X}^a$ is given below:

$$\mathbf{X}^a = [\mathbf{X} \quad \mathbf{w}]^T \tag{6.23}$$

$$\mathbf{X} = [\mathbf{r}^n \quad \mathbf{v}^n \quad \mathbf{q}_b^n \quad \mathbf{b}_{\omega,GM1(1)} \quad \mathbf{b}_{f,GM1(1)} \quad \mathbf{b}_{\omega,GM1(2)} \quad \mathbf{b}_{f,GM1(2)}$$
$$\mathbf{b}_{\omega,GM1(3)} \quad \mathbf{b}_{f,GM1(3)} \quad \mathbf{b}_{\omega,RW} \quad \mathbf{b}_{f,RW} \quad \mathbf{b}_{\omega,WN} \quad \mathbf{b}_{f,WN}] \tag{6.24}$$

$$\mathbf{w} = [\mathbf{w}_v \quad \mathbf{w}_\varphi \quad \mathbf{w}_{b_{\omega,GM1(1)}} \quad \mathbf{w}_{b_{f,GM1(1)}} \quad \mathbf{w}_{b_{\omega,GM1(2)}} \quad \mathbf{w}_{b_{f,GM1(2)}}$$
$$\mathbf{w}_{b_{\omega,GM1(3)}} \quad \mathbf{w}_{b_{f,GM1(3)}} \quad \mathbf{w}_{b_{\omega,RW}} \quad \mathbf{w}_{b_{f,RW}} \quad \mathbf{w}_{b_{\omega,WN}} \quad \mathbf{w}_{b_{f,WN}}] \tag{6.25}$$

where $\mathbf{X}(1 \times 40)$ contains the absolute navigation states and inertial sensor random biases, $\mathbf{w}(1 \times 36)$ the corresponding zero-meaned, uncorrelated and white process (system) noises vector (not including the position components) with covariance $\mathbf{Q} = \mathbb{E}[\mathbf{w} \, \mathbf{w}^T]$, $\mathbf{r}^n$ the 3d position in terms of geodetic coordinates vector, $\mathbf{v}^n$ the NED velocities vector, $\mathbf{q}_b^n$ the Hamilton convention-based orientation quaternion (Shuster, 1993) that corresponds to the $\mathbf{R}_b^n$ DCM matrix, $\{\mathbf{b}_\omega, \mathbf{b}_f\}$

the b-frame gyro and accelerometer bias vectors respectively (based on the stochastic processes included within the $\mathcal{Z}$ model), $\mathbf{w}_v$ the velocity noises, $\mathbf{w}_\varphi$ the attitude noises and $\{\mathbf{w}_{b_\omega}, \mathbf{w}_{b_f}\}$ the gyro and accelerometer bias noises respectively.

6.4.2 System and Measurement Models

System Model

Regarding the system model of the UKF, which drives its prediction stage, it has to be structured in such a way that it considers the augmented state vector of equation (6.23). Specifically, this means that it has to be comprised by both the INS mechanization and the sensor error state-space model expressions. Consequently, the discrete-time nonlinear system model takes the following form:

$$\mathbf{X}_{k-1|k}^a(11{:}40,1) = SE\left(\mathbf{X}_{k-1|k-1}(11{:}40,1), \mathbf{w}_{k-1}(7{:}36,1)\right) \tag{6.26}$$

$$\mathbf{X}_{k-1|k}^a(1{:}10,1) = SM\big(\mathbf{X}_{k-1|k-1}(1{:}10,1), \mathbf{X}_{k-1|k}^a(11{:}40,1), \ldots$$
$$\left\{\tilde{\mathbf{f}}^b(t_k), \tilde{\boldsymbol{\omega}}_{ib}^b(t_k)\right\}, \mathbf{w}_{k-1}(1{:}6,1)\big) \tag{6.27}$$

where SE symbolizes a function of the non-linearized state-space models (i.e., equations (2.3), (2.8) and (2.16) for the WN, RW and GM1 respectively) that fully describe each stochastic process that is included within the $\mathcal{Z}$ composite model and every inertial sensor, SM is the INS mechanization procedure as that was simplified by Shin, (2005) from the works of Savage, (2000a, 2000b) and $\left(\tilde{\mathbf{f}}^b, \tilde{\boldsymbol{\omega}}_{ib}^b\right)$ are the accelerometer and gyroscope measurements, from which the deterministic error effects have been removed.

Building more on the above equations, it is highlighted that for each SP, the effects of the propagated biases (by the SE function) are removed from the inertial sensor measurements and

which in turn, are plugged into the INS mechanization process (*SM* function) for the inference of the navigation solution (i.e., position, velocity, attitude). Furthermore, with this structure, the change of the sensor errors is tracked internally, which means that they are adjusted based on the updated information and they maintain their values during their absence. Finally, it should be mentioned that in equation (6.26), the GM1, RW and WN stochastic processes can be taken into account. As for the DR process, in a similar manner as in the EKF, its contribution should be added to the WN components of the augmented state vector $\mathbf{X}^a_{k-1|k}$ after they have been propagated from the m function. For illustration purposes, this notion is expressed by the following formula, which refers to the gyroscope triad:

$$\mathbf{X}^a_{k-1|k}(35:37,1) = \mathbf{X}^a_{k-1|k}(35:37,1) + \omega_{DR}\,\Delta t \qquad (6.28)$$

where Δt is the data interval of the inertial sensor measurements that drive the navigation filter.

Given this system model structure, there are certain things that should be clarified. First, the latitude and longitude position components are expressed in degrees and thus, due to their periodicity, the averaging described in equation (6.12) of the UKF's prediction stage will be problematic. Instead, the position averaging process of the transformed SPs $\hat{\mathbf{r}}^n_{i,k-1|k}$ can be implemented in the e-frame like so:

$$\hat{\mathbf{r}}^e_{k-1|k} = \sum_{i=0}^{p-1} w^m_i \left(\mathbf{R}^e_n\,\hat{\mathbf{r}}^n_{i,k-1|k}\right) \qquad (6.29)$$

And second, since the attitude of the moving platform is described by a quaternion, the corresponding SP generation and averaging should be modified properly. Regarding the former, the error vector $\delta\mathbf{X}$ (i.e., estimation minus truth) is considered only for the attitude:

$$\delta \mathbf{X} = [\cdots \quad \boldsymbol{\varphi} \quad \cdots]^{\mathrm{T}} \tag{6.30}$$

where $\boldsymbol{\varphi}$ is the implied rotation vector to the resulting quaternion from $(\hat{\mathbf{q}}_b^n) \otimes (\mathbf{q}_b^n)^{-1}$ (see (Shin, 2005, p. 14) for how the quaternion can be converted to a rotation vector). Subsequently, step 7 of the SSS-UT algorithm (equation (6.9)) is adjusted as follows:

$$\Delta \boldsymbol{\mathcal{X}}_i = \alpha \, \mathbf{S} \, \boldsymbol{\mathcal{X}}_{u,i} = \left[\cdots \quad (\boldsymbol{\varphi}_i)^{\mathrm{T}} \quad \cdots \right]^{\mathrm{T}}, \qquad i =, \dots, n+1 \tag{6.31}$$

$$\boldsymbol{\mathcal{X}}_i = \left[\cdots \quad \left(\mathbf{q}_{\phi_i} \otimes \hat{\mathbf{q}}_b^n \right)^{\mathrm{T}} \quad \cdots \right] \tag{6.32}$$

where $\mathbf{q}_{\phi_i}$ is the corresponding quaternion to the $\boldsymbol{\varphi}_i$ rotation vector and $\hat{\mathbf{q}}_b^n$ the quaternion that expresses the prior state orientation.

Furthermore, the quantities provided by equation (6.31) are utilized in equations (6.13) and (6.17) of the UKF prediction and update stages respectively. Finally, concerning the averaging of the quaternions, the direct implementation of such a process would not result in a quaternion. Hence, to overcome this issue, the iterative intrinsic gradient descent algorithm presented by Kraft, (2003) is chosen to be utilized for the evaluation of the weighted mean quaternion, which is based on the principles of Riemannian geometry (see (Shin and El-Sheimy, 2007) for a compact presentation of this algorithm).

Measurement Model

Contrarily to the EKF, the measurement model of the UKF navigation algorithm is comprised of a set of nonlinear equations h. In turn, these equations are utilized to transform the INS-based SPs in such a way that they become comparable with the external information that is fed into the

filter as updates. As it was mentioned earlier, the errors of the auxiliary information are considered to be additive. Therefore, the general expression of the measurement model has the form:

$$\mathbf{Z}_k = h(\mathbf{X}_k) + \mathbf{V}_k, \qquad \mathbf{R}_k = \mathbb{E}\left[\mathbf{V}_k \, \mathbf{V}_k{}^T\right] \tag{6.33}$$

where $\mathbf{Z}$ is the measurement vector, h the nonlinear vector function of the absolute state vector and $\mathbf{V}$ the zero meaned, uncorrelated, and white measurement noises vector with covariance $\mathbf{R}$.

In this study, the 3d position and velocity components from the GNSS system, the transversal and vertical velocities from the NHCs and the 3d velocity components from the ZUPTs will be the updates and their respective measurement model matrices are provided below:

A) GNSS position

$$\mathbf{Z}_k(\mathbf{r}_{GNSS}) = \text{diag}([1 \quad 1 \quad -1]) \left[\mathbf{R}_e^n\left(\tilde{\mathbf{r}}_{GNSS}^e - \hat{\mathbf{r}}_{IMU_{i,k-1|k}}^e\right) - \hat{\mathbf{R}}_{b_{i,k-1|k}}^n \, l_{GNSS}^b\right] \tag{6.34}$$

$$\mathbf{v}_k = z_k - \hat{z}_{k-1|k} = \sum_{i=0}^{n+1} w_i^m \, \mathcal{Z}_{i,k-1|k} \tag{6.35}$$

$$\Delta \mathcal{Z}_{i,k-1|k} = \mathbf{v}_k - \mathcal{Z}_{i,k-1|k} \tag{6.36}$$

$$\mathbf{R}_r(\mathbf{r}_{GNSS}) = \text{diag}\left(\left[\sigma^2{}_{\phi_{GNSS}} \quad \sigma^2{}_{\lambda_{GNSS}} \quad \sigma^2{}_{h_{GNSS}}\right]\right) \tag{6.37}$$

where $\tilde{\mathbf{r}}_{GNSS}^e$ is the GNSS-derived e-frame position vector and $\hat{\mathbf{r}}_{IMU_{i,k-1|k}}^e$ the predicted position based on the inertial sensor measurements for each SP.

B) GNSS velocities

$$\begin{aligned}
\mathbf{Z}_k(\mathbf{v}_{GNSS}) &= \hat{\mathbf{v}}_{IMU_{i,k-1|k}}^n - (\hat{\omega}_{in}^n \times)_{i,k-1|k} \, \hat{\mathbf{R}}_{b_{i,k-1|k}}^n \, l_{GNSS}^b - \\
&\quad \hat{\mathbf{R}}_{b_{i,k-1|k}}^n \left(l_{GNSS}^b \times\right) \omega_{ib}^b
\end{aligned} \tag{6.38}$$

$$z_k = \tilde{\mathbf{v}}_{GNSS}^n \tag{6.39}$$

$$\mathbf{R}_v = \text{diag}\left(\begin{bmatrix} \sigma^2{}_{vN,GNSS} & \sigma^2{}_{vE,GNSS} & \sigma^2{}_{vD,GNSS} \end{bmatrix}\right) \tag{6.40}$$

C) Non-Holonomic Constraints

$$\mathbf{Z}_k(\mathbf{v}_{NHC}) = \left[\mathbf{R}_b^v \left(\hat{\mathbf{R}}_{b_{i,k-1|k}}^n\right)^T \hat{\mathbf{v}}_{IMU_{i,k-1|k}}^n + \mathbf{R}_b^v \left(\hat{\omega}_{nb}^b \times\right)_{i,k-1|k} \boldsymbol{l}_{wheel}^b\right]_{2:3} \tag{6.41}$$

$$z_k = 0 \tag{6.42}$$

$$\mathbf{R}_{NHC} = \text{diag}\left(\begin{bmatrix} \sigma^2{}_{vE,NHC} & \sigma^2{}_{vD,NHC} \end{bmatrix}\right) \tag{6.43}$$

D) Zero Velocity Updates

$$\mathbf{Z}_{k,ZUPT} = \hat{\mathbf{v}}_{IMU_{i,k-1|k}}^n \tag{6.44}$$

$$\mathbf{v}_k = z_k - \hat{z}_{k-1|k} = -\hat{\mathbf{v}}_{k-1|k}^n \tag{6.45}$$

$$\Delta Z_{i,k-1|k} = {}_{i,k-1|k} - \hat{z}_{k-1|k} = \Delta \mathcal{X}_{i,k-1|k}(4:6,1:n+2) \tag{6.46}$$

$$\mathbf{R}_{ZUPT} = \text{diag}\left(\begin{bmatrix} \sigma^2{}_{vN,ZUPT} & \sigma^2{}_{vE,ZUPT} & \sigma^2{}_{vD,ZUPT} \end{bmatrix}\right) \tag{6.47}$$

6.5 Filter Initialization

This part of the chapter is dedicated to how the augmented state vector $\hat{\mathbf{X}}_{0|0}^a$ and its corresponding covariance matrix $\mathbf{P}_{0|0}^a$ are initialized. In fact, their general form is provided by the following expressions:

$$\hat{\mathbf{X}}_{0|0}^a = \begin{bmatrix} \hat{\mathbf{X}}_{0|0} \\ 0 \end{bmatrix} \tag{6.48}$$

$$\mathbf{P}_{0|0}^a = \begin{bmatrix} \mathbf{P}_{0|0} & 0 \\ 0 & \mathbf{Q}_0 \end{bmatrix} \tag{6.49}$$

where $\widehat{\mathbf{X}}_{0|0}$ refers to the initial position, velocity, and attitude (expressed through a quaternion) of the moving platform, $\mathbf{P}_{0|0}$ the navigation state covariance matrix and $\mathbf{Q}_0$ the covariance of the system noises. In fact, by augmenting the state with the noise vector, the influence of the system noises on the covariance evolution can be expressed in a more natural way compared to the EKF, since there is no need for the utilization of an approximation to the integration of the $\mathbf{Q}$ matrix.

Regarding $\widehat{\mathbf{X}}_{0|0}$, its values are exactly the same as those of the EKF (see Section 5.4), with the only difference being that the Euler angles are now expressed as a quaternion. In addition, the initial values for the biases and noises are set to be equal to zero. As for $\mathbf{P}_{0|0}^a$, modifications should be made compared to the EKF's version, which are provided below in bullet form:

- The initial position variances are modified as follows:

$$\mathbf{P}_{0|0}(\phi_0) = \frac{\sigma^2_{\phi_0}}{(R_M + h_0)^2} \tag{6.50}$$

$$\mathbf{P}_{0|0}(\lambda_0) = \frac{\sigma^2_{\lambda_0}}{[(R_N + h_0)\cos\phi_0]^2} \tag{6.51}$$

$$\mathbf{P}_{0|0}(h_0) = \sigma^2_{h_0} \tag{6.52}$$

- The initial velocity variances are obtained directly from the separate filter that derived the GNSS position and velocity solutions.

- The dimension of a quaternion is 4, while its degrees of freedom are equal to 3. Therefore, the size of the corresponding covariance matrix should be one less than the augmented state vector and its components will be the attitude variances given by equations (5.47), (5.48), and (5.49).

- The covariance matrix elements that refer to the initial bias variation for the GM1, RW and WN stochastic processes are given by equations (5.50), (5.51), and (5.52) respectively.

- The $\mathbf{Q}_0$ matrix is given by the following formula:

$$\mathbf{Q}_0 = \mathbf{Q}_s \, \Delta t \tag{6.53}$$

where Δt is the data interval of the INS measurements and $\mathbf{Q}_s$ is the EKF's spectral densities matrix of equation (5.26). Furthermore, it is highlighted that the position components are removed, since they are typically set to zero and their removal ensures that the implementation of the Cholesky factorization of the $\mathbf{P}^a$ matrix will always be possible (i.e., its positive definiteness is preserved).

Finally, concluding this section, it is extremely important to highlight that in order for the implementation of the UKF to be possible, the diagonal of the $\mathbf{P}^a$ matrix should be fully populated (i.e., no zeros included) to ensure its positive definiteness. As a result, if according to the stochastic analysis, a sensor is found to be characterized by a model with less complexity than the one of the $\mathcal{Z}$ model, then the rows and columns that correspond to the processes that are not included within the simpler model should be removed.

6.6 Summary

In this chapter, a navigation algorithm for INS/GNSS/NHC/ZUPT integration was presented, based on the UKF filter. Moreover, in the context of this Bayesian filter, the system noises were considered to be non-additive and thus, the state vector was augmented in order to allow their natural propagation through the original nonlinear models. As for the measurement noises, given the nature of the estimation problem at hand, it was deemed more logical to presume them as additive in nature. Finally, an in-depth description of this algorithm was provided along with the

required adjustments for the incorporation of the advanced stochastic modeling knowledge regarding the inertial sensor error random behavior that was inferred in Section 4.5. In fact, this is the first time that such a UKF filter is used in tandem with GMWM-based stochastic analysis and more specifically with modeling information derived from using the new SR/DR-AWV robust multi-signal estimators.

Chapter Seven: Empirical Evaluation of EKF and UKF-based Navigation Algorithms Infused with SR/DR-AWV Stochastic Modeling Information for the Inertial Sensor Random Errors

7.1 Introduction

In this chapter, the stochastic modeling analysis of a commercial grade IMU, derived using the proposed robust multi-signal GMWM-based framework as well as the conventional AVLR method, will be infused within the EKF and UKF-based INS/GNSS/NHC/ZUPT integration algorithms, described in Chapter Five and Chapter Six. In turn, their performance will be evaluated in a real-life land vehicle navigation setting and compared with each other. Consequently, in this way, the impact of this new and improved stochastic modeling methodology about the inertial sensor errors on the overall navigation performance will be explored, in contrast to the classical approach and in the context of the two aforementioned Bayesian filter variants.

7.2 Equipment Setup

The commercial grade Xsens MTi-G-710, whose inertial sensor random errors were studied in Section 4.5 (after a deterministic calibration process was previously performed), was placed on a wooden platform that has been bolted in the back of a car. For the purposes of this experiment, the reference with respect to which the performance of the MTi will be validated was chosen to be NovAtel's SPAN system. Hence, its components, meaning the high-end iMAR-FSAS IMU and the high-quality dual frequency SPAN-SE GNSS (it can detect signals from the GPS and GLONASS constellations) receiver, were secured on the very same platform as the MTi, in the manner demonstrated in Figure 7.1. On top of that, a high-end GNSS antenna was stuck on the top of the car and connected with the SPAN-SE receiver. Finally, it is highlighted that in order to allow a direct comparison between the reference and the MTi, the same GNSS information that

the SPAN system uses to infer its navigation solution will also be used by the MTi-driven integration schemes. However, these two sources of information are not synchronized with each other and generally, the best way to match them is via GPS time. Hence, with this in mind, a low-cost GNSS antenna was connected to the MTi device and stuck on top of the car. Consequently, the inertial sensor measurements will be able to receive a GPS timestamp and thus, allow the synchronization with the GNSS information used by the SPAN system.
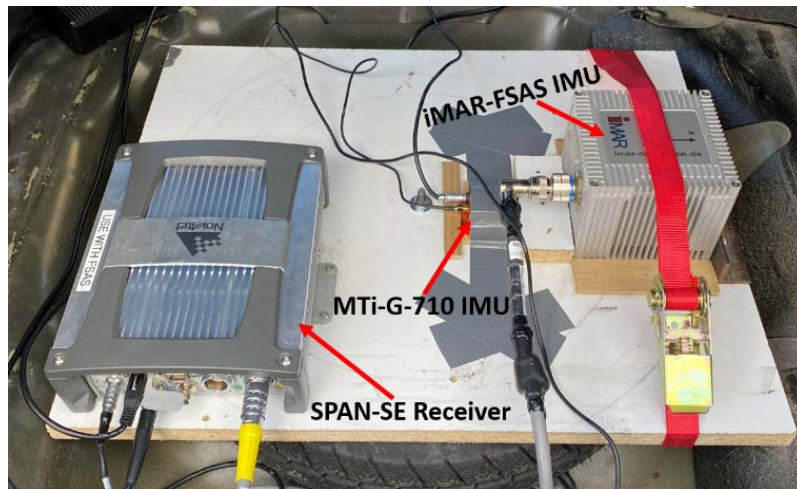

Figure 7.1: Equipment placement at the trunk of the vehicle

Following the completion of the equipment placement on the vehicle, a TCR803 3" reflector-less total station was utilized to measure (with the highest possible accuracy) the quantities mentioned below and which are also shown in Figure 7.2:

1) Lever arm between the MTi's center (its exact location was identified from the manufacture's CAD drawings) and the GNSS antenna phase center.

2) Lever arm between the MTi's center and the vehicle frame's origin, with the latter being defined as the center point of the rear drive axle's ground projection.

3) MTi body frame and vehicle frame axes.

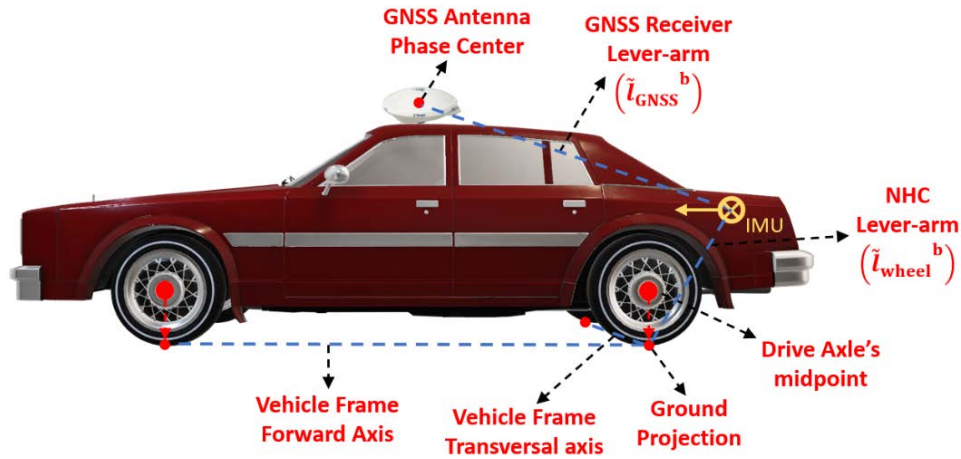4) Boresight (indirect inference by comparing the MTi body frame and vehicle frame axes).

Figure 7.2: Sideview representation of the lever arms, MTi IMU body frame and vehicle frame

7.3 Data Collection

In order to empirically evaluate the contributions of the new robust multi-signal GMWM-based framework to the navigation performance in the context of both the EKF and UKF-based algorithms described in Chapter Five and Chapter Six, a 20-min trajectory located in a suburban area (since open sky conditions and minimal multipath are desired) of NW Calgary was designed and demonstrated in Figure 7.3.
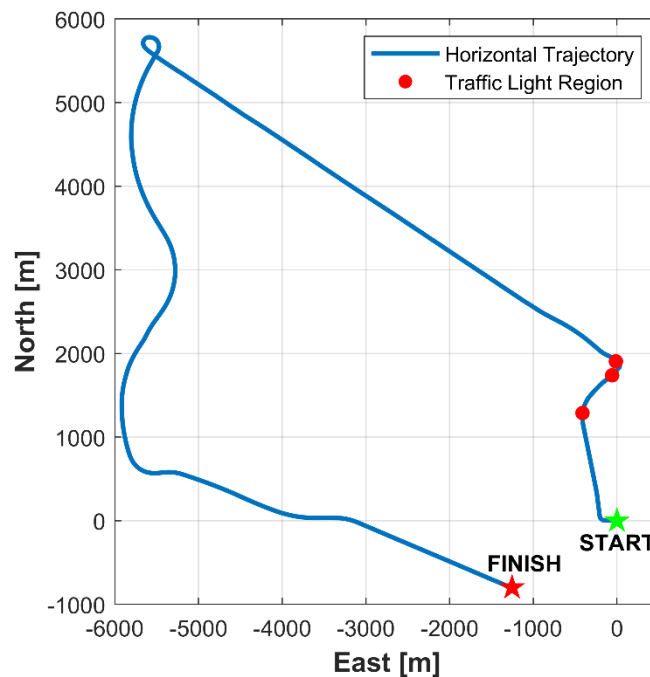

Figure 7.3: Designed trajectory in the horizontal plane

In the following section, the reasons behind the inclusion of multiple stops and turns in the trajectory will be presented in bullet form:

- One of the major improvements that the new robust multi-signal GMWM-based framework provides compared to the conventional AVLR method is the high accuracy in identifying the characteristics of the time-correlated noises that govern the inertial sensor random errors. Furthermore, it is noted that the importance of the time-correlated noises starts becoming significant to the navigation performance when the moving platform experiences complex dynamics. And since here focus is given to vehicular navigation, this means that there have to be moments where the vehicle is turning.

- As it was mentioned in Chapter Six:, the UKF is capable of handling the nonlinearities to the system and measurement models in a better way than the EKF. Ergo, the UKF's advantages can be more clearly seen when the nonlinearities become significant, which again occurs during vehicle turns.

- The NHCs are a very useful tool in vehicular navigation, and it is especially important when the INS system operates on standalone mode during complex vehicle movements. Therefore, it would be very interesting to investigate what the combination of NHCs, the UKF and the improved stochastic modeling information about the inertial sensor errors can contribute to the INS performance when the vehicle performs a turn and there is a GNSS outage at the same time.

- The ZUPTs, which are also included within the tested algorithms, prevent the navigation solution from deteriorating during vehicle stops. Therefore, it would be worthwhile to investigate whether the use of advanced stochastic modeling information for the inertial sensor er-

rors in the context of the EKF and UKF filters can further improve the ZUPTs usefulness. As a result, regions where traffic lights exist should be included in order to increase the chance for a ZUPT to occur.

Given the aforementioned equipment configuration and trajectory planning, this vehicular navigation experiment was implemented on November 15th, 2021. Specifically, regarding the MTi, GPS timestamped inertial sensor measurements were collected at a 100Hz data rate using the 4.8.2 version of the MT Software Suite. As for the reference system, NovAtel's Inertial Explorer software was utilized to collect iMAR's inertial sensor data at a 100Hz rate, while position and velocity information from SPAN's GNSS receiver in SPP mode were retrieved at a 1Hz rate. In turn, the same software was also utilized for the loosely coupled integration of the SPAN system's INS and GNSS information and the estimation of the reference solution, which will be used up next to validate the performance of the MTi.

7.4 Tests and Results Discussion

In this section, the EKF and UKF filters described in Chapter Five and Chapter Six respectively will each be infused with the stochastic modeling knowledge for the Xsens MTi-G-710 IMU, which was derived in Section 4.5 using the new SR/DR-AWV estimators and the classical AVLR method.

Since the duration of the trajectory has been set, it is now possible to investigate whether there are any time-correlated stochastic processes within the SR/DR-AWV stochastic analysis that can be over-bounded using a RW process, based on the procedure introduced in Section 4.2. Specifically, this will be accomplished by calculating the correlation times of each AR1 process shown in Table 4.6 for the accelerometers and Table 4.7 for the gyroscopes and then, by inspecting which processes have a large enough correlation time with respect to the total trajectory duration,

determine the likely candidates. From such a process, it was found that only one process can be a valid possibility for over-bounding since its correlation time is equal to approximately 387sec. Actually, this process is the 1st AR1 that refers to the Y-Accelerometer (i.e., AR1,1) and whose parameters are shown in Table 4.4. Subsequently, using these parameter values, the duration of the trajectory (i.e., 20 min) and the inertial sensor data rate (i.e., 100Hz) in the context of the approach described in Section 4.2, Figure 7.4 is obtained and presented below:
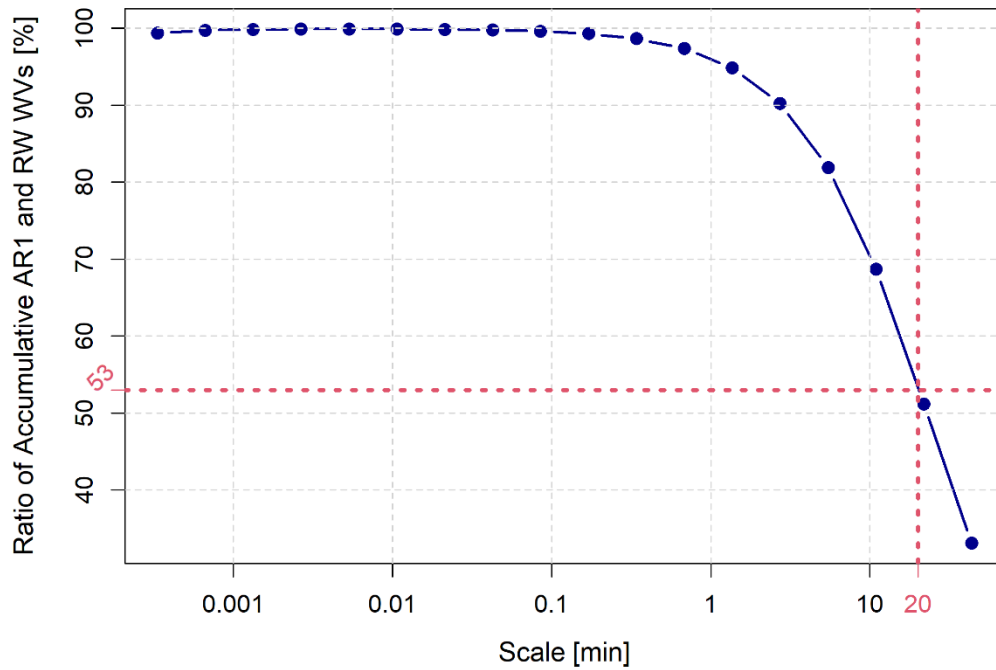

Figure 7.4: Accumulative sum ratio of the AR1-implied WV over the RW-implied WV

Based on this figure, it is clear that if this process is to be over-bounded with a RW for the trajectory at hand, the approximation level would be equal to 53%, which is not enough to justify such course of action. Consequently, no changes can be applied to the SR/DR-AWV stochastic analysis, and it will be used for the purposes of the experimental evaluation described in this chapter.

With the stochastic modeling information for this experiment now finalized and in order to gain a more comprehensive insight into the performance of the MTi provided by the aforementioned filter configurations, two realistic scenarios were devised. In fact, each of these scenarios

was set to contain one 1min and one 30sec artificial GNSS outages at different locations along the trajectory that are far apart from each other. Specifically, the 1min outages were chosen to initially contain a straight path trajectory, then encounter a vehicle stop and finally continue on a straight path again. In this way, the performance of the ZUPTs can be evaluated. As for the 30sec outages, to which more focus will be given since they are the most likely to occur in reality, those were placed in regions where both straight course (linear) and vehicle turns (nonlinear) are included in order to assess the efficiency of the NHCs. Hence, it becomes possible to:

1) Evaluate the performance of the algorithms when transitioning from a linear to a nonlinear trajectory.

2) Investigate the improvement that the information provided by the new robust multi-signal GMWM-based framework regarding the inertial sensor random errors can have over the commonly used AVLR method.

3) Inspect whether the use of a UKF filter instead of an EKF one along with the knowledge provided by the newly proposed SR/DR-AWV estimators about the inertial sensor noise can further enhance the navigation performance.

With the aforementioned in mind, and concerning Scenario I, Outage 1 was chosen to be between the 80th and 140th second of the trajectory, covering the area of before and after the first traffic light region that is shown in Figure 7.3, where there is a 26 second stop (i.e., ZUPT should be applied). As for Outage 2, it was set to start at the 590th second and end at the 620th and it contains a sharp right turn.

Regarding Scenario II, its first outage, designated as Outage 3, was placed partially before and after the second traffic light region (see Figure 7.3), where a 33 second stop occurs. In addition,

the second outage, hereinafter referred to as Outage 4, was established between the 750th and 780th second of the trajectory, where the car performs a wide right turn.

At this point, it should be mentioned that the EKF infused with AVLR information represents the conventional method and thus, it is considered as the base solution to which improvement is sought after. Furthermore, it is common practice for the AVLR information that is included within the EKF and UKF-based navigation algorithms to be tuned in order to achieve adequately good results. However, it was found that the modeling information provided by the SR/DR-AWV estimators does not require any such process. As for the metrics that were chosen to evaluate the performance of the MTi in the context of these filters with respect to the reference solution, those were the RMS of the 2D positioning errors (RMS_2D), the percentage of RMS_2D with respect to the traveled distance ($\text{P}_{\text{RMS}_\text{2D}}$) and the RMS of the 3D orientation errors (RMS_3D), the formulas for which are given below:

$$\text{RMS}_\text{2D} = \text{rms}\left(\sqrt{\left(u_{r_\text{E}}\right)^2 + \left(u_{r_\text{N}}\right)^2}\right) \tag{7.1}$$

$$\text{P}_{\text{RMS}_\text{2D}} = (\text{RMS}_\text{2D}/\text{Traveled distance}) \cdot 100 \tag{7.2}$$

$$\text{RMS}_\text{3D} = \text{rms}\left(\sqrt{(u_\text{r})^2 + \left(u_\text{p}\right)^2 + (u_\text{A})^2}\right) \tag{7.3}$$

where $\left(u_{r_\text{E}}, u_{r_\text{N}}\right)$ are the East and North position error time series (w.r.t the SPAN system's reference solution) and $\left(u_\text{r}, u_\text{p}, u_\text{A}\right)$ are the error time series of the roll, pitch, and azimuth attitude angles.

Finally, it is underlined that the NHCs were chosen to be applied at a 10Hz rate with a variance equal to $0.25(\text{m/sec})^2$, while the ZUPTs were selected to be performed at a 20Hz rate with

$0.4(\text{m/sec})^2$ variance. In the following, the results from each of the two scenarios will be provided and discussed.

Scenario I

The statistical metrics for the Scenario I outage regions are provided in Table 7.1.

Table 7.1: RMS_{2D}, percentage of RMS_{2D} w.r.t the traveled distance and RMS_{3D} values for the outages of Scenario I

Outage Designation	Duration [sec]	Approx. Traveled Distance [m]	Integration Filter	Stochastic Estimator	RMS_{2D} [m]	$P_{RMS_{2D}}$ [%]	RMS_{3D} [deg]
Outage 1 (80-140sec)	60	370.724	EKF	AVLR	2.884	0.778	0.995
				SR/DR	**2.816** **(-2.3%)**	**0.760**	0.898 (-9.7%)
			UKF	AVLR	2.894 (+0.3%)	0.781	0.883 (-11.2%)
				SR/DR	2.950 (+2.3%)	0.796	**0.828** **(-16.8%)**
Outage 2 (590-620sec)	30	552.915	EKF	AVLR	5.803	1.049	0.907
				SR/DR	5.323 (-8.3%)	0.962	0.801 (-11.7%)
			UKF	AVLR	5.436 (-6.3%)	0.982	0.822 (-9.4%)
				SR/DR	**4.954** **(-14.7%)**	**0.897**	**0.799** **(-11.9%)**

According to that, and for Outage 1, both the EKF and UKF demonstrate equivalent error levels in terms of horizontal positioning, when either the AVLR or the SR/DR-AWV stochastic modeling information is utilized. On the other hand, the EKF with the SR/DR-AWV analysis and the UKF with the classical AVLR-derived knowledge provide a very similar orientation estimation improvement, with the latter having the edge compared to the conventional setting. Finally, the UKF infused with SR/DR-AWV modeling information appears to be the one with the best performance. Therefore, based on this, it can be concluded that in a condition where the car is most-

ly static, the choice of stochastic modeling estimator does not have any effect on the horizontal positioning estimation accuracy. However, the same cannot be said for the orientation determination quality, which does appear to be correlated with the previously mentioned dilemma.

Concerning Outage 2 and based on Table 7.1, it is confirmed that with respect to the filters that are infused with AVLR stochastic modeling knowledge, the reliable handling of the nonlinearities up to the 2nd order that the UKF offers is capable of providing a meaningful improvement compared to the conventional filter from the aspects of both positioning and orientation when the vehicle is turning. In fact, the UKF with the SR/DR-AWV information manages to obtain a significant boost of the order of 14.7% in terms of horizontal positioning, which corresponds to 0.897% of the total outage distance, while the EKF appears to be comparable to it with an 8.3% enhancement that translates to 0.962% of the outage distance. As for the orientation, both the EKF and UKF introduce a considerable and almost equivalent improvement of approximately 12%. Therefore, based on the aforementioned, it can be deduced that the combination of an improved inertial sensor random error understanding and a better handling of the system model nonlinearities can enhance the navigation performance not only in terms of 2D positioning but also in terms of the orientation of the moving platform. Finally, the influence of the stochastic modeling information choice as well as of the integration filter implied by the stats of Table 7.1 is also confirmed by Figure 7.5 and Figure 7.6, where snapshots from the sharp turn that the vehicle performs during the outage are depicted. In fact, it is worth mentioning that the orientation error quality is primarily dependent on the azimuth estimation.
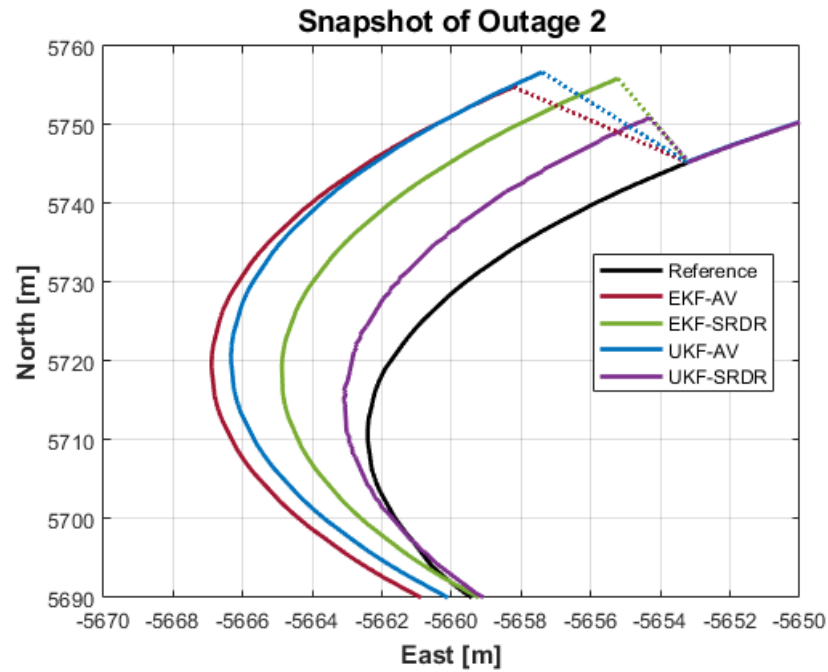
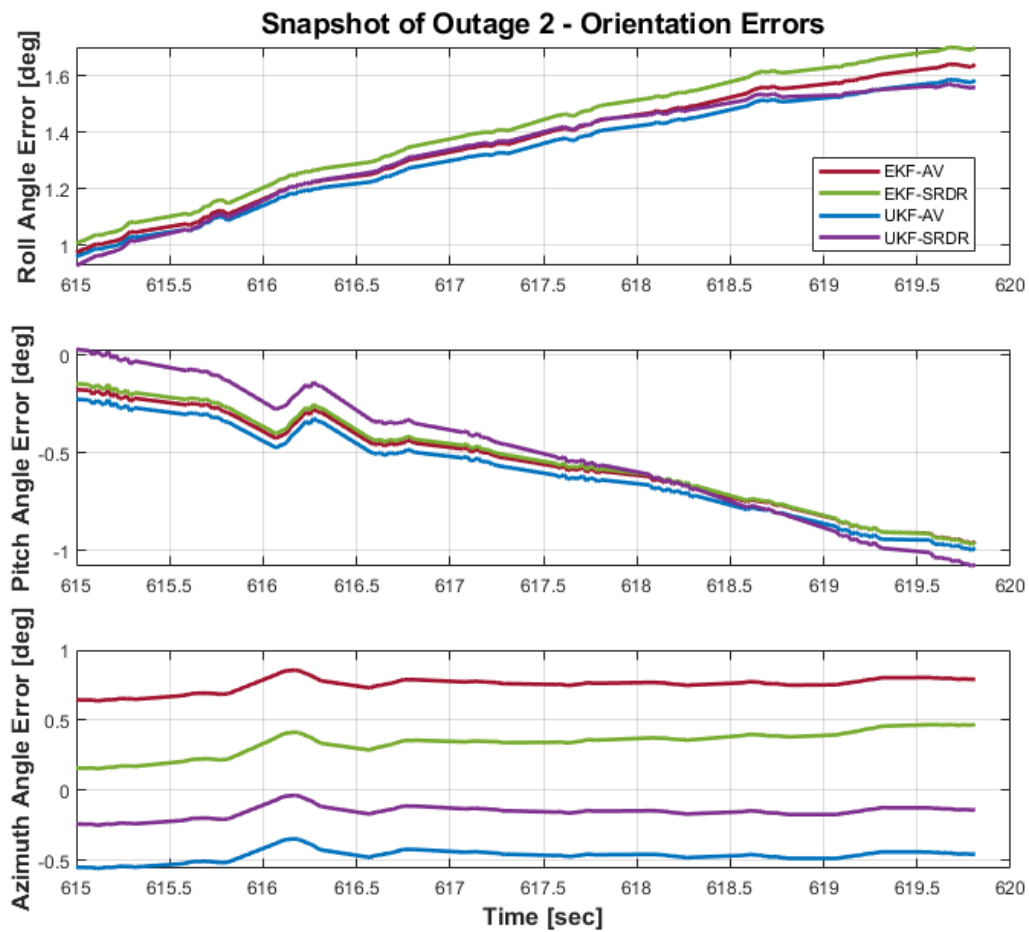Figure 7.5: Snapshot of the Outage 2 horizontal positioning solutions

Figure 7.6: Snapshot from the Outage 2 orientation angle estimation errors

Scenario II

Regarding Scenario II, the EKF and UKF filters infused with both the SR/DR-AWV and AVLR stochastic analysis for the inertial sensor errors were implemented and Table 7.2 was formed, where the statistics of the derived solutions for the artificial GNSS outage regions are included.

According to Table 7.2, a very similar behavior to Outage 1 is observed for Outage 3, both in terms of horizontal position as well as orientation estimation quality. Specifically, all four filter configurations appear to be equivalent with respect to horizontal positioning. Moreover, the EKF containing the SR/DR-AWV analysis exhibits an almost equivalent performance to the UKF that is infused with AVLR information from the orientation determination standpoint (7.5 and 9.1% respectively). As for the UKF containing the new robust multi-signal method's modeling for the inertial sensor errors and just like in Outage 1, it is the optimal one since it manages to enhance the estimation quality of the orientation compared to the standard scheme by 17.3%.

Based on Table 7.2, and for Outage 4, it seems that the filters containing the SR/DR-AWV stochastic modeling information are the ones to provide a meaningful improvement compared to the standard configuration. In fact, the UKF provides a positioning quality improvement compared to the conventional setting at order of 17.8% (i.e., 0.887% of the total outage distance) that is better than the EKF by a small but noticeable 5%, while their orientation estimation prowess is at more or less the same level. Finally, a more rigorous inspection of the filter's performance in Outage 4 was deemed worthwhile in order to further validate the results provided in Table 7.2 and thus, Figure 7.7 and Figure 7.8 were created, where snapshots of the horizontal solution and attitude angle errors are depicted.

Table 7.2: RMS_{2D}, percentage of RMS_{2D} w.r.t the traveled distance and RMS_{3D} values for the outages of Scenario II

Outage Designation	Duration [sec]	Approx. Traveled Distance [m]	Integration Filter	Stochastic Estimator	RMS_{2D} [m]	$P_{RMS_{2D}}$ [%]	RMS_{3D} [deg]
Outage 3 (160-220sec)	60	196.652	EKF	AVLR	1.393	0.708	1.300
				SR/DR	**1.379** (-1.0%)	**0.701**	1.203 (-7.5%)
			UKF	AVLR	1.407 (+1.0%)	0.715	1.182 (-9.1%)
				SR/DR	1.405 (0.8%)	0.714	**1.075** (-17.3%)
Outage 4 (750-780sec)	30	711.731	EKF	AVLR	7.682	1.079	0.958
				SR/DR	6.696 (-12.8%)	0.940	0.849 (-11.4%)
			UKF	AVLR	7.355 (-4.3%)	1.033	0.912 (-4.8%)
				SR/DR	**6.318** (-17.8%)	**0.887**	**0.839** (-12.5%)

From a visual inspection of Figure 7.7, it can be deduced that an accurate knowledge of the time-correlated noises can certainly be beneficial to the navigation performance, especially when the moving platform is under nonlinear trajectory conditions and it can be maximized when it is combined with a better handling of the system model nonlinearities through the UKF.

As for Figure 7.8, it is evident that the much harsher turn that the moving platform performs, compared to Outage 2, results to a more noticeable difference in all three attitude angle estimations from one filter configuration to another. Nevertheless, it is once again confirmed that the filters containing the SR/DR-AWV analysis manage to not only enhance the horizontal positioning performance but at the same time improve the orientation estimation in a meaningful way, with the UKF maintaining the edge on both accounts.
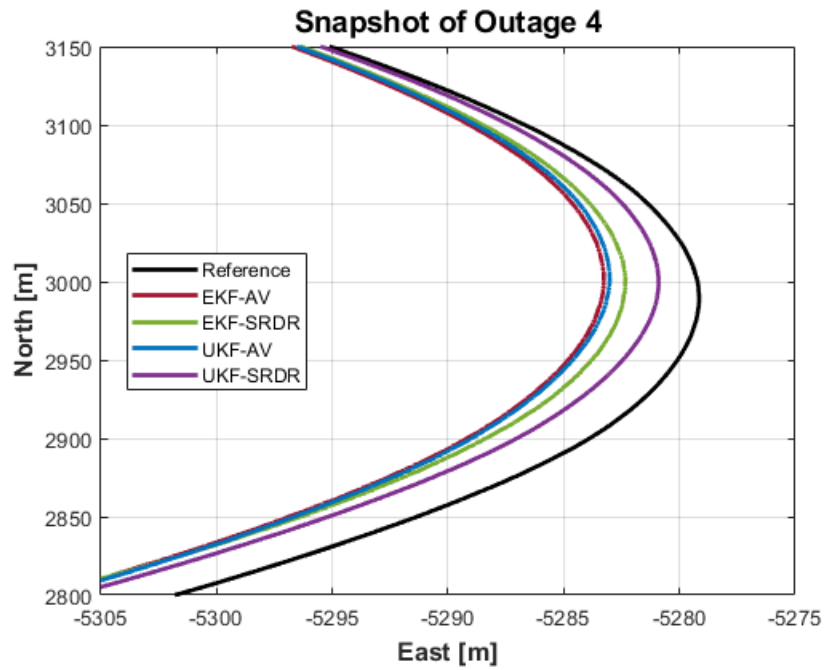
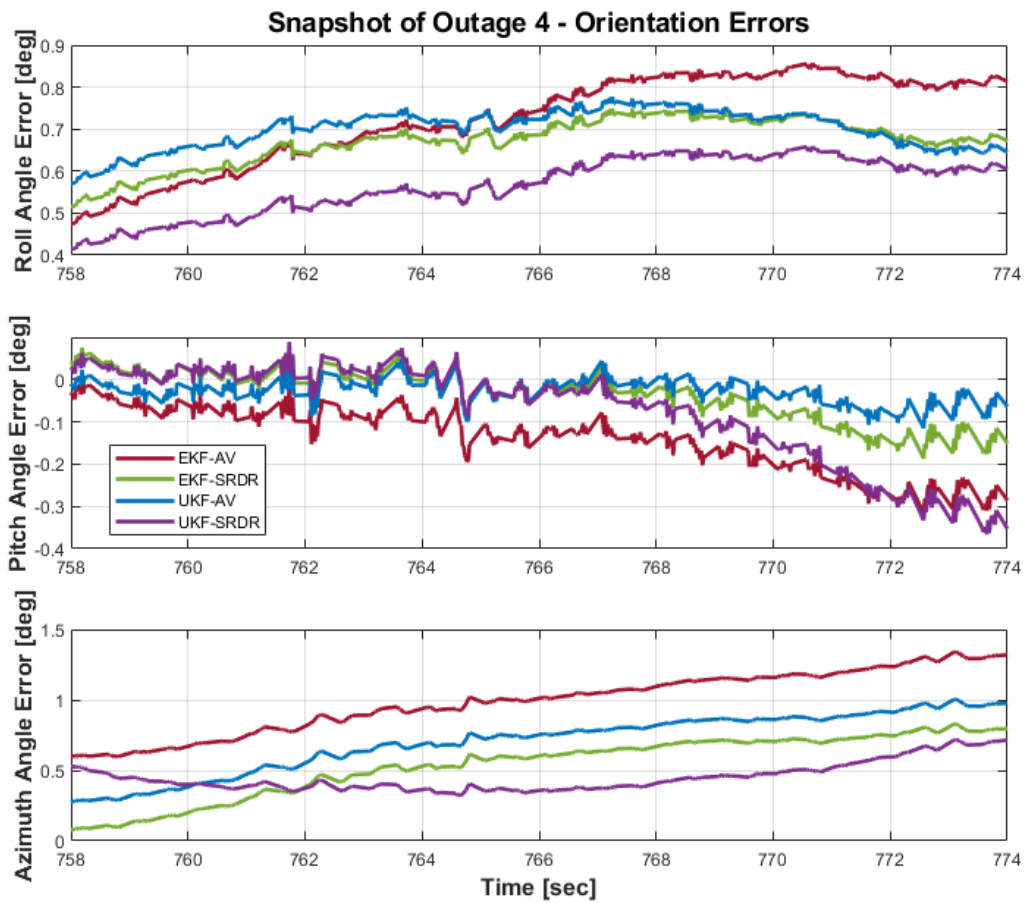Figure 7.7: Snapshot of the Outage 4 horizontal positioning solutions

Figure 7.8: Snapshot from the Outage 4 orientation angle estimation errors

Based on the aforementioned, it is clear that under nonlinear trajectory conditions, the UKF with the SR/DR-AWV analysis is the one that provides the best horizontal positioning and orientation estimation performance, while the EKF with the same stochastic modeling information is a close second. As for the static circumstances, the UKF-based filters are shown to be able to handle the orientation determination in a more efficient way than the EKF-based schemes.

Computational time

Another very important aspect that should be considered is the time that it takes to process the 20-minute trajectory at hand with each of the 4 filter configurations that have been discussed here. Therefore, given that the tests were conducted using MATLAB 2023a on an AMD Ryzen 7 4800H 2.90GHz processor and 16GB RAM, the following table with each filter's state dimension and computational time in minutes was constructed.

Table 7.3: State dimensions and computational times for each filter design

Integration Filter	Stochastic Estimator	State Dimension	Processing Time [min]
EKF	AVLR	21	3.60
	SR/DR	34	**3.62** **(+0.6%)**
UKF	AVLR	40	10.98 (+205.0%)
	SR/DR	66	17.14 (+376%)

According to the information provided in Table 7.3, several observations can be made. Firstly, regarding the EKF filters, the utilization of the SR/DR-AWV stochastic analysis instead of the standard AVLR does not seem to impact the computational time, despite the increase in the state dimension. This can be attributed to efforts made for the avoidance of including spare stochastic

processes in the filter matrices, which in turn resulted to the filter maintaining numerical stability. Secondly, and with the aforementioned test results in mind, the EKF algorithm with SR/DR-AWV information is proven to be suitable for general-purpose and real-time applications, assuming that modern equipment is being utilized. In addition, it is blatantly apparent that a strong correlation exists between the processing time and the state vector dimension of the UKF filters. Consequently, both of them exhibit considerably long computational times, which come very close to the total duration of the trajectory (55 and 86% of the total time length when using the AVLR and SR/DR-AWV respectively). In fact, with respect to the AVLR, the UKF requires 3 times more processing time than the EKF, whereas with the SR/DR-AWV, it demands nearly five times more. Therefore, ultimately, the decision to incorporate the (proven to be superior) SR/DR-AWV analysis within either the EKF or UKF depends on the available computational capabilities and the specific application at hand.

7.5 Summary

In this chapter, tests were conducted in order to assess the impact of the Xsens MTi-G-710 inertial sensor random error analysis on the quality of horizontal positioning and orientation estimation. This evaluation was performed in the context of an INS/GNSS/NHC/ZUPT navigation algorithm, where the contribution of the analysis derived using the new robust multi-signal GMWM-based stochastic modeling method was compared to the one provided by the conventional AVLR method. Through that, it became possible to examine the effectiveness of the synergy between the inertial sensor stochastic error modeling information, the NHCs and the ZUPT updates. In fact, particular focus was given in regions where GNSS outages have been artificially introduced and the moving platform is under either linear-static or dynamic conditions. Furthermore, the potential benefits of utilizing an alternative and less restrictive Bayesian filter like the

UKF, instead of the standard EKF, were explored with the purpose of achieving a better collaboration with the new inertial sensor error stochastic analysis and further improving the navigation performance. Finally, the computational times for implementing the EKF and UKF-filters, infused with the SR/DR-AWV stochastic analysis information for the inertial sensor random errors were discussed.

Chapter Eight: Conclusions and Recommendations

8.1 Summary and Conclusions

In this thesis, it has been highlighted that the measurements of low-cost and commercial-grade MEMS sensors are characterized by significant systematic biases and random errors, the significance of which tends to get magnified as they are integrated over time for the derivation of the navigation solution. Particular focus, however, was given to the random errors, whose level, complexity, and behavioral variability from one experimental run to another tends to increase as the cost of the sensor drops. Hence, in order to avoid significant degradation of the INS standalone performance due to their influence, their precise stochastic calibration is necessary. Furthermore, it was pointed out that it is highly possible that their measurements are contaminated with outliers, whose impact also increases as the cost of the sensor drops and which can create problems in the analysis and modeling of the random errors.

In order to take all the aforementioned characteristics of the measurements provided by low-cost and commercial-grade MEMS sensors into account (i.e., stochastic error behavioral complexity and variability from replicate to replicate, outlier existence), a multi-signal stochastic analysis framework has been brought forward that contains two levels of robustness and it is fundamentally based on the GMWM framework and its multi-signal extension, the AWV estimator. In turn, from this new approach, two estimators were defined: the SR-AWV and the DR-AWV, with the first containing a single layer of robustness against data corruption in each considered signal replicate and with the latter reinforcing that protection against sample contamination as well. Finally, based on the aforementioned, a logical deduction is be noted, that the contribution of this new method gets more important as the cost of the sensor drops since the behavioral variability of the errors from run-to-run raises along with the outlier influence.

On another note, it should be highlighted that the publicly available framework for the implementation of the GMWM/ RGMWM single-signal stochastic analysis was utilized as a base for the development of the new robust multi-signal framework; in the near future, its code will also be incorporated in the context of the GMWM engine and thus be made available to practitioners for open use. Furthermore, it is reminded that although this new method targets the problem of inertial sensor error stochastic modeling, it is characterized by generality and it can be used for the stochastic analysis of any observable, as long as intrinsically stationary error sequences can be collected.

Before testing the capabilities of the new estimators, a straightforward and fast to implement algorithm for analyzing the calibration data at hand using the single-signal GMWM method and by extension, the new multi-signal estimators was presented in Section 4.2. In addition, a mathematical reasoning was provided that permits the simplification of time-correlated stochastic processes that have been identified and estimated by the algorithm, based on certain conditions.

Next, the efficiency of the two new estimators in terms of model parameter estimation was evaluated in a simulation and a case study setting in Section 4.4, from which the importance of their robustness to the effects of different types of outliers was highlighted and established. On top of that, it was found that both robust multi-signal estimators perform in an almost equivalent way to the classical approach in the clean calibration data setting and thus, either of them can be used without the need for confirmation for the outlier existence. In fact, this conclusion was also found to be valid for the robust single-signal GMWM method in Section 4.3, where it was established that its use in every scenario is a worthwhile trade-off between reduction in model parameter estimation efficiency and safeguarding the estimation process from the harmful influence of outliers.

Building on these two studies, an innovative hybrid study was also conducted using a recently proposed navigation simulator in order to investigate the link between the quality of the stochastic modeling provided by these new robust estimators and the implied INS/GNSS navigation performance (during INS standalone operation) in different calibration data contamination scenarios. Specifically, based on the results from a huge number of simulated trajectories and the implied empirical coverage and standard estimation error metrics, it was found that by introducing robustness to the multi-signal stochastic calibration of inertial sensor errors, stability is maintained under contamination (of the calibration datasets) in terms of not only navigation state point estimation accuracy but also of correctness of the provided reliability information.

Given the prowess establishment of the two new robust estimators under different calibration data contamination settings, it is highlighted that there has to be a careful inspection of the available data for the selection between which of the two should be utilized in order to maximize the final modeling solution accuracy. Specifically, the SR-AWV is the standard choice and the DR-AWV should be employed whenever the available data contain signal replicate(s) with noticeably different random error behavior compared to the rest.

The final section of this dissertation has been devoted to a real-life vehicle navigation experiment, where the stochastic analysis derived in Section 4.5 for the consumer-grade Xsens MTi-G-710 inertial sensors using the new SR/DR-AWV estimators and the standard AVLR method is infused within the conventional EKF and (for the first time) the less restrictive UKF-based filter for INS/GNSS/NHC/ZUPT loosely coupled integration. As for the manner that this was performed, that is detailed in Chapter Five and Chapter Six. However, in the context of such process, a very interesting fact was noticed. Specifically, unlike the conventional AVLR method, the stochastic modeling information provided by the SR/DR-AWV estimators, did not require any

tuning process in order to achieve an adequately good performance. Consequently, this constitutes a very beneficial advantage that this new approach offers over the conventional AVLR method.

Having said that, the purpose of such an experiment was the performance evaluation of these filters under different conditions as well as to highlight the contribution that the new robust multi-signal stochastic modeling method provides to the navigation performance compared to the classical AVLR, when it is combined with update sources like the NHCs and ZUPTs. Towards that end, artificial GNSS outages were introduced in regions where the car performs either linear-static trajectory or is under dynamic conditions. The former was introduced with the intent of evaluating the collaboration between the employed inertial sensor stochastic error analysis and the ZUPT update, while the latter was to inspect the synergy with the NHCs.

The performance of the aforementioned 4 filter configurations was evaluated with reference to a high-end navigation system and from the point of view of horizontal positioning and orientation estimation quality. Moreover, an additional comparison was conducted with respect to the conventional setting, which is none other than the EKF infused with the AVLR stochastic analysis for the inertial sensor errors. The derived results were presented in Section 7.4 and the conclusions that can be inferred from them are summarized below:

Linear-static conditions (Outage 1 and Outage 3)

- All 4 filter configurations provided the same horizontal positioning estimation performance.

- The UKF with AVLR-based information and the EKF infused with SR/DR-AWV knowledge for the inertial sensor measurement noise demonstrated a similar 3D orientation quality with 11.2%-9.1% and 9.7%-7.5% enhancement compared to the standard setting.

- The UKF encompassing the analysis provided by the new robust multi-signal method gave the highest improvement in both outages with 16.8% and 17.3% respectively.

- When utilizing the new approach's knowledge for the MTi's inertial sensor errors, the UKF provided 7.1% for Outage 1 and 9.8% for Outage 3 more improvement to the conventional filter compared to the EKF.

- Overall, the SR/DR-AWV is the best option during linear-static conditions.

Dynamic conditions (Outage 2 and Outage 4)

- In terms of horizontal positioning, the UKF infused with the SR/DR-AWV information was the optimal one for both Outage 2, where the trajectory involved a straight path and a sharp right turn and Outage 4, where the car performed a much harsher and longer right turn. Specifically, its improvement to the standard filter was 14.7% and 17.8% respectively.

- The EKF with SR/DR-AWV provided horizontal positioning solutions that were close to the ones provided by its UKF counterpart with enhancements at the level of 8.3% for Outage 2 and 12.8% for Outage 4. This means that the UKF was better by 6.4% and 5% respectively.

- It can be deduced that the higher the significance of the nonlinearities, the better the horizontal positioning performance of both filters becomes compared to the standard setting due to incorporation of accurate knowledge for the correlated errors.

- Regarding the quality of the orientation estimation, both EKF and UKF filters infused with the SR/DR-AWV stochastic modeling provide an approximately 12% improvement compared to the standard configuration.

- Compared to the standard setting, which provides a horizontal error at the order of 1% of the total GNSS outage distance (i.e., 1.049 and 1.079%), the UKF infused with SR/DR-AWV stochastic analysis information manages to reduce that at the order of 0.89% (i.e., 0.897 and 0.887%) and the EKF to 0.95% (i.e., 0.962 and 0.940%).

- Overall, with respect to dynamic conditions, the SR/DR-AWV clearly outperforms the standard AVLR and thus it should be the one to be utilized.

Finally, the computational times of the 4 filter configurations were also calculated. From their inspection, it was found that although the state dimension was increased significantly when using the SR/DR-AWV instead of the AVLR, the processing time of the EKF-based filter was unaffected. Thus, the numerical stability of this scheme has been confirmed. On the other hand, the UKF-based filters appeared to be particularly vulnerable to the state-space augmentation, despite their good performance. Therefore, it could be inferred that the EKF infused with SR/DR-AWV stochastic modeling information could be a serious candidate for real-time applications, while the UKF can certainly be used for applications where post-processing is possible to optimize the navigation performance.

8.2 Recommendations for Further Research

Given contributions to the overall navigation performance provided by the new multi-signal GMWM-based stochastic modeling framework when it is used for the behavioral analysis of the inertial sensor measurement noise, this approach can also be utilized in the context of the following research ideas to provide further improvements:

- In the context of inertial sensor stochastic calibration, consider signal replicates that have been collected under different operating conditions (i.e., temperature, dynamics) in order to

eventually estimate a model that, on average, describes the sensor's behaviour while also taking into account the influence of those conditions.

- Explore possible contributions in the context of a Reduced Inertial Sensor System (RISS)

- Analysis of the GNSS positioning solutions provided by low-cost receivers through the various different processing strategies (i.e., SPP, DGNSS, PPP, RTK) that exist in the literature in order to obtain an in-depth insight to their random behavior.

- Utilize the analysis of low-cost GNSS receiver-derived SPP positioning solutions to describe the stochastic part of an EKF filter for GNSS-only positioning based on the SPP processing strategy. Subsequently, it can be investigated whether this complex stochastic analysis can provide a meaningful improvement compared to the standard use of a single RW process with arbitrarily chosen (tuned) characteristics.

- The GNSS-only filter mentioned above can be used in tandem with the loosely coupled INS/GNSS/NHC/ZUPT algorithms described in this thesis in order to create a navigation system that takes full advantage of the newly proposed stochastic modeling method.

- Study the low-cost GNSS receiver clock oscillator instability. In turn, the derived modeling may allow the upgrade of the GNSS receiver' performance.

Bibliography

Abdel-Hamid, W., 2005. Accuracy enhancement of integrated MEMS-IMU/GPS systems for land vehicular navigation applications (PhD Thesis). University of Calgary, Calgary, Alberta, Canada. http://dx.doi.org/10.11575/PRISM/23496

Aggarwal, P., 2010. MEMS-based Integrated Navigation. Artech House.

Aggarwal, P., Syed, Z., El-Sheimy, N., 2008a. Thermal Calibration of Low Cost MEMS Sensors for Land Vehicle Navigation System, in: VTC Spring 2008 - IEEE Vehicular Technology Conference. Presented at the VTC Spring 2008 - IEEE Vehicular Technology Conference, pp. 2859–2863. https://doi.org/10.1109/VETECS.2008.623

Aggarwal, P., Syed, Z., Niu, X., El-Sheimy, N., 2008b. A Standard Testing and Calibration Procedure for Low Cost MEMS Inertial Sensors and Units. The Journal of Navigation 61, 323–336. https://doi.org/10.1017/S0373463307004560

Allan, D.W., 1966. Statistics of atomic frequency standards. Proceedings of the IEEE 54, 221–230. https://doi.org/10.1109/PROC.1966.4634

Arulampalam, M.S., Maskell, S., Gordon, N., Clapp, T., 2002. A tutorial on particle filters for online nonlinear/non-Gaussian Bayesian tracking. IEEE Transactions on Signal Processing 50, 174–188. https://doi.org/10.1109/78.978374

Bakalli, G., Cucci, D.A., Radi, A., El-Sheimy, N., Molinari, R., Scaillet, O., Guerrier, S., 2023. Multi-Signal Approaches for Repeated Sampling Schemes in Inertial Sensor Calibration. IEEE Transactions on Signal Processing 1–12. https://doi.org/10.1109/TSP.2023.3262179

Bakalli, G., Radi, A., El-Sheimy, N., Molinari, R., Guerrier, S., 2017. A Computational Multivariate-based Technique for Inertial Sensor Calibration, in: Proceedings of the 30th International Technical Meeting of the Satellite Division of The Institute of Navigation. Presented at the ION GNSS+ 2017, Portland, Oregon, pp. 3028–3038. https://doi.org/10.33012/2017.15255

Balamuta, J., Molinari, R., Guerrier, S., Yang, W., 2016. The gmwm R package: A comprehensive tool for time series analysis from state-space models to robustness. arXiv:1607.04543 [stat].

Balamuta, J.J., Molinari, R., Guerrier, S., Yang, W., 2018. A Computationally Efficient Framework for Automatic Inertial Sensor Calibration. IEEE Sensors Journal 18, 1636–1646. https://doi.org/10.1109/JSEN.2017.2773663

Bar-Shalom, Y., Li, X.R., Kirubarajan, T., 2004. Estimation with Applications to Tracking and Navigation: Theory Algorithms and Software. John Wiley & Sons.

Beaton, A.E., Tukey, J.W., 1974. The Fitting of Power Series, Meaning Polynomials, Illustrated on Band-Spectroscopic Data. Technometrics 16, 147–185. https://doi.org/10.1080/00401706.1974.10489171

Benson, D.O., 1975. A Comparison of Two Approaches to Pure-Inertial and Doppler-Inertial Error Analysis. IEEE Transactions on Aerospace and Electronic Systems AES-11, 447–455. https://doi.org/10.1109/TAES.1975.308106

Bogdanski, K., Best, M.C., 2018. Kalman and particle filtering methods for full vehicle and tyre identification. Vehicle System Dynamics 56, 769–790. https://doi.org/10.1080/00423114.2017.1337914

Britting, K.R., 1971. Inertial Navigation Systems Analysis, 1st ed. John Wiley & Sons Inc.

Brown, R.G., Hwang, P.Y.C., 2012. Introduction to random signals and applied Kalman filtering: with MATLAB exercises, 4th ed. ed. John Wiley, Hoboken, NJ.

Chatfield, A.B., 1997. Fundamentals Of High Accuracy Inertial Navigation. American Institute of Aeronautics and Astronautics, Reston ,VA. https://doi.org/10.2514/4.866463

Clausen, P., Skaloud, J., Molinari, R., Lee, J., Guerrier, S., 2018. Use of a new online calibration platform with applications to inertial sensors. IEEE Aerospace and Electronic Systems Magazine 33, 30–36. https://doi.org/10.1109/MAES.2018.170153

Cucci, D.A., Voirol, L., Kermarrec, G., Montillet, J.-P., Guerrier, S., 2023a. The Generalized Method of Wavelet Moments with eXogenous inputs: a fast approach for the analysis of GNSS position time series. J Geod 97, 14. https://doi.org/10.1007/s00190-023-01702-8

Cucci, D.A., Voirol, L., Khaghani, M., Guerrier, S., 2023b. On Performance Evaluation of Inertial Navigation Systems: The Case of Stochastic Calibration. IEEE Transactions on Instrumentation and Measurement 72, 1–17. https://doi.org/10.1109/TIM.2023.3267360

D'Alessandro, A., Vitale, G., Scudero, S., D'Anna, R., Costanza, A., Fagiolini, A., Greco, L., 2017. Characterization of MEMS accelerometer self-noise by means of PSD and Allan Variance analysis, in: 2017 7th IEEE International Workshop on Advances in Sensors and Interfaces (IWASI). Presented at the 2017 7th IEEE International Workshop on Advances in Sensors and Interfaces (IWASI), pp. 159–164. https://doi.org/10.1109/IWASI.2017.7974238

Dempster, A.P., Laird, N.M., Rubin, D.B., 1977. Maximum Likelihood from Incomplete Data Via the EM Algorithm. Journal of the Royal Statistical Society: Series B (Methodological) 39, 1–22. https://doi.org/10.1111/j.2517-6161.1977.tb01600.x

Doucet, A., 1998. On sequential simulation-based methods for bayesian filtering.

Efron, B., Tibshirani, R.J., 1994. An Introduction to the Bootstrap, Monographs on statistics and applied probability. Chapman and Hall/CRC. https://doi.org/10.1201/9780429246593

El-Diasty, M., El-Rabbany, A., Pagiatakis, S., 2007. Temperature variation effects on stochastic characteristics for low-cost MEMS-based inertial sensor error. Meas. Sci. Technol. 18, 3321–3328. https://doi.org/10.1088/0957-0233/18/11/009

El-Diasty, M., Pagiatakis, S., 2008. Calibration and Stochastic Modelling of Inertial Navigation Sensor Erros. Journal of Global Positioning Systems 7, 170–182. https://doi.org/10.5081/jgps.7.2.170

El-Sheimy, N., 2014. Inertial Techniques and INS/DGPS Integration [Lecture Notes]. Department of Geomatics Engineering, University of Calgary.

El-Sheimy, N., Hou, H., Niu, X., 2008. Analysis and Modeling of Inertial Sensors Using Allan Variance. IEEE Transactions on Instrumentation and Measurement 57, 140–149. https://doi.org/10.1109/TIM.2007.908635

Farrell, J.A., Silva, F.O., Rahman, F., Wendel, J., 2022. Inertial Measurement Unit Error Modeling Tutorial: Inertial Navigation System State Estimation with Real-Time Sensor Calibration. IEEE Control Systems Magazine 42, 40–66. https://doi.org/10.1109/MCS.2022.3209059

Ferraris, F., Grimaldi, U., Parvis, M., 1995. Procedure for effortless in-field calibration of three-axial rate gyro and accelerometers. Sensors and Materials 7(5), 311–330.

Gelb, A., 1974. Applied Optimal Estimation. MIT Press.

Gene H. Golub, C.F.V.L., 2013. Matrix Computations, 4th ed, Johns Hopkins Studies in the Mathematical Sciences. Johns Hopkins University Press.

Georgy, J., 2010. Advanced nonlinear techniques for low cost land vehicle navigation (PhD Thesis). Queen's University, Kingston, Ontario, Canada.

Georgy, J., Noureldin, A., Korenberg, M.J., Bayoumi, M.M., 2010. Modeling the Stochastic Drift of a MEMS-Based Gyroscope in Gyro/Odometer/GPS Integrated Navigation. IEEE Transactions on Intelligent Transportation Systems 11, 856–872. https://doi.org/10.1109/TITS.2010.2052805

Greenhall, C.A., 1991. Recipes for degrees of freedom of frequency stability estimators. IEEE Transactions on Instrumentation and Measurement 40, 994–999. https://doi.org/10.1109/19.119780

Groves, P.D., 2013. Principles of GNSS, Inertial, and Multi-sensor Integrated Navigation Systems, 2nd ed. Artech House.

Guerrier, S., Jurado, J., Khaghani, M., Bakalli, G., Karemera, M., Molinari, R., Orso, S., Raquet, J., Schubert, C., Skaloud, J., Xu, H., Zhang, Y., 2020. Wavelet-Based Moment-Matching Techniques for Inertial Sensor Calibration. IEEE Transactions on Instrumentation and Measurement 69, 7542–7551. https://doi.org/10.1109/TIM.2020.2984820

Guerrier, S., Molinari, R., Skaloud, J., 2015. Automatic Identification and Calibration of Stochastic Parameters in Inertial Sensors. NAVIGATION 62, 265–272. https://doi.org/10.1002/navi.119

Guerrier, S., Molinari, R., Stebler, Y., 2016. Theoretical Limitations of Allan Variance-based Regression for Time Series Model Estimation. IEEE Signal Processing Letters 23, 597–601. https://doi.org/10.1109/LSP.2016.2541867

Guerrier, S., Molinari, R., Victoria-Feser, M.-P., Xu, H., 2022. Robust Two-Step Wavelet-Based Inference for Time Series Models. Journal of the American Statistical Association 117, 1996–2013. https://doi.org/10.1080/01621459.2021.1895176

Guerrier, S., Skaloud, J., Stebler, Y., Victoria-Feser, M.-P., 2013a. Wavelet-Variance-Based Estimation for Composite Stochastic Processes. Journal of the American Statistical Association 108, 1021–1030. https://doi.org/10.1080/01621459.2013.799920

Guerrier, S., Stebler, Y., Skalud, J., Victoria-Feser, M.-P., 2013b. Limits of the Allan Variance and Optimal Tuning of Wavelet Variance based Estimators.

Guerrier, S., Victoria-Feser, M.-P., 2015. A Prediction Divergence Criterion for Model Selection. arXiv:1511.04485 [stat].

Guerrier, S., Waegli, A., Skaloud, J., Victoria-Feser, M.-P., 2012. Fault Detection and Isolation in Multiple MEMS-IMUs Configurations. IEEE Transactions on Aerospace and Electronic Systems 48, 2015–2031. https://doi.org/10.1109/TAES.2012.6237576

Han, J., Ge, S., Shen, Y., 2007. Research on the random error properties of FOG based on total variance. J. Harbin Inst. Technol. 30, 708–711.

Han, S., Wang, J., Knight, N., 2009. Using allan variance to determine the calibration model of inertial sensors for GPS/INS integration. Presented at the 6th Interational Symposium on Mobile Mapping Technology.

Hansen, L.P., 1982. Large Sample Properties of Generalized Method of Moments Estimators. Econometrica 50, 1029–1054. https://doi.org/10.2307/1912775

Haug, A.J., 2005. A Tutorial on Bayesian Estimation and Tracking Techniques Applicable to Nonlinear and Non-Gaussian Processes (Technical Report). MITRE.

Heinzel, G., Rudiger, A., Schilling, R., 2002. Spectrum and spectral density estimation by the Discrete Fourier transform (DFT), including a comprehensive list of window functions and some new at-top windows (Technical Report).

Hidalgo, J., Poulakis, P., Köhler, J., Del-Cerro, J., Barrientos, A., 2012. Improving Planetary Rover Attitude Estimation via MEMS Sensor Characterization. Sensors 12, 2219–2235. https://doi.org/10.3390/s120202219

Hidalgo-Carrió, J., Arnold, S., Poulakis, P., 2016. On the Design of Attitude-Heading Reference Systems Using the Allan Variance. IEEE Transactions on Ultrasonics, Ferroelectrics, and Frequency Control 63, 656–665. https://doi.org/10.1109/TUFFC.2016.2519268

Hou, H., 2004. Modeling inertial sensors errors using Allan variance (PhD Thesis). University of Calgary, Calgary, Alberta, Canada. http://dx.doi.org/10.11575/PRISM/21729

Hou, H., El-Sheimy, N., 2003. Inertial Sensors Errors Modeling Using Allan Variance. Presented at the Proceedings of the 16th International Technical Meeting of the Satellite Division of The Institute of Navigation (ION GPS/GNSS 2003), pp. 2860–2867.

Huang, D., Leung, H., EL-SHEIMY, N., 2007. Expectation Maximization Based GPS/INS Integration for Land-Vehicle Navigation. IEEE Transactions on Aerospace and Electronic Systems 43, 1168–1177. https://doi.org/10.1109/TAES.2007.4383607

Hussen, A.A., Jleta, I.N., 2015. Low-Cost Inertial Sensors Modeling Using Allan Variance. International Journal of Electrical and Computer Engineering 9, 1230–1235.

Ibe, O., 2013. Markov processes for stochastic modeling. Newnes.

IEEE Standard Definitions of Physical Quantities for Fundamental Frequency and Time Metrology—Random Instabilities, 2009. IEEE Std 1139-2008 c1-35. https://doi.org/10.1109/IEEESTD.2008.4797525

IEEE Standard Specification Format Guide and Test Procedure for Linear Single-Axis, Nongyroscopic Accelerometers, 2019. . IEEE Std 1293-2018 (Revision of IEEE Std 1293-1998) 1–271. https://doi.org/10.1109/IEEESTD.2019.8653544

IEEE Standard Specification Format Guide and Test Procedure for Linear, Single-Axis, Non-Gyroscopic Accelerometers, 1999. IEEE Std 1293-1998 1–252. https://doi.org/10.1109/IEEESTD.1999.89857

Julier, S.J., 2003. The spherical simplex unscented transformation, in: Proceedings of the 2003 American Control Conference, 2003. Presented at the Proceedings of the 2003 American Control

Conference, 2003., Denver, CO, U.S, pp. 2430–2434. https://doi.org/10.1109/ACC.2003.1243439

Julier, S.J., 2002. The Scaled Unscented Transformation, in: Proceedings of the 2002 American Control Conference (IEEE Cat. No.CH37301). Presented at the Proceedings of the 2002 American Control Conference (IEEE Cat. No.CH37301), Anchorage, AK, U.S, pp. 4555–4559. https://doi.org/10.1109/ACC.2002.1025369

Julier, S.J., Uhlmann, J.K., 1997a. A New extension of the Kalman filter to nonlinear systems, in: Signal Processing, Sensor Fusion, and Target Recognition VI. Presented at the AeroSense '97, International Society for Optics and Photonics, Orlando, FL, U.S, pp. 182–193. https://doi.org/10.1117/12.280797

Julier, S.J., Uhlmann, J.K., 1997b. Consistent debiased method for converting between polar and Cartesian coordinate systems, in: Acquisition, Tracking, and Pointing XI. Presented at the Acquisition, Tracking, and Pointing XI, SPIE, pp. 110–121. https://doi.org/10.1117/12.277178

Julier, S.J., Uhlmann, J.K., Durrant-Whyte, H.F., 1995. A new approach for filtering nonlinear systems, in: Proceedings of 1995 American Control Conference - ACC'95. Presented at the Proceedings of 1995 American Control Conference - ACC'95, pp. 1628–1632 vol.3. https://doi.org/10.1109/ACC.1995.529783

Kraft, E., 2003. A quaternion-based unscented Kalman filter for orientation tracking, in: Sixth International Conference of Information Fusion, 2003. Proceedings of The. Presented at the Sixth International Conference of Information Fusion, 2003. Proceedings of the, pp. 47–54. https://doi.org/10.1109/ICIF.2003.177425

Li, J., Fang, J., 2013a. Not Fully Overlapping Allan Variance and Total Variance for Inertial Sensor Stochastic Error Analysis. IEEE Transactions on Instrumentation and Measurement 62, 2659–2672. https://doi.org/10.1109/TIM.2013.2258769

Li, J., Fang, J., 2013b. Sliding Average Allan Variance for Inertial Sensor Stochastic Error Analysis. IEEE Transactions on Instrumentation and Measurement 62, 3291–3300. https://doi.org/10.1109/TIM.2013.2272841

Li, Y., Lan, H., Zhuang, Y., Zhang, P., Niu, X., El-Sheimy, N., 2015. Real-time attitude tracking of mobile devices, in: 2015 International Conference on Indoor Positioning and Indoor Navigation (IPIN). Presented at the 2015 International Conference on Indoor Positioning and Indoor Navigation (IPIN), pp. 1–7. https://doi.org/10.1109/IPIN.2015.7346770

Li, Y., Niu, X., Zhang, Q., Zhang, H., Shi, C., 2012. An in-situ hand calibration method using a pseudo-observation scheme for low-end inertial measurement units. Meas. Sci. Technol. 23, 105104. https://doi.org/10.1088/0957-0233/23/10/105104

Liu, Z., 2019. Vision Sensor Aided Navigation for Ground Vehicle Applications (PhD Thesis). University of Calgary, Calgary, Alberta, Canada.

Ma, Y., Genton, M.G., 2000. Highly Robust Estimation of the Autocovariance Function. Journal of Time Series Analysis 21, 663–684. https://doi.org/10.1111/1467-9892.00203

Makhoul, J., 1975. Linear prediction: A tutorial review. Proceedings of the IEEE 63, 561–580. https://doi.org/10.1109/PROC.1975.9792

Mallat, S., 1999. A Wavelet Tour of Signal Processing, 2nd ed, Wavelet Analysis & Its Applications. Academic Press.

Maronna, R.A., Martin, R.D., Yohai, V.J., Salibián-Barrera, M., 2019. Robust Statistics: Theory and Methods (with R). John Wiley & Sons.

Miao, Z., Shen, F., Xu, D., He, K., Tian, C., 2015. Online Estimation of Allan Variance Coefficients Based on a Neural-Extended Kalman Filter. Sensors 15, 2496–2524. https://doi.org/10.3390/s150202496

Minaretzis, C., Cucci, D.A., El-Sheimy, N., Sideris, M., Guerrier, S., Victoria-Feser, M.-P., 2023. Robust Multi-signal Estimation Framework with Applications to Inertial Sensor Stochastic Calibration. Manuscript submitted for publication.

Minaretzis, C., Cucci, D.A., Guerrier, S., Radi, A., El-Sheimy, N., Sideris, M., 2022. Robust Wavelet Variance-based Approaches for the Stochastic Modeling of Inertial Sensor Measurement Noise, in: Proceedings of the 2022 International Technical Meeting of The Institute of Navigation. Presented at the International Technical Meeting 2022, Long Beach, California, pp. 1444–1456. https://doi.org/10.33012/2022.18193

Misra, P., Enge, P., 2011. Global Positioning System: Signals, Measurements, and Performance. Ganga-Jamuna Press.

Moafipoor, S., Bock, L., Fayman, J.A., Mader, G., de Jonge, P.J., 2011. Development and Assessment of a Low Dynamic Vehicle Navigation System. Presented at the Proceedings of the 2011 International Technical Meeting of The Institute of Navigation, pp. 895–907.

Mohamed, A.H., 1999. Optimizing the estimation procedure in INS/GPS integration for kinematic applications. University of Calgary. http://dx.doi.org/10.11575/PRISM/11319

Movella, 2023. MTi-G-710 GNSS/INS [Online Document]. URL https://www.movella.com/products/sensor-modules/xsens-mti-g-710-gnss-ins

Nassar, S., 2003. Improving the Inertial Navigation System (INS) error model for INS and INS/DGPS applications (PhD Thesis). University of Calgary, Calgary, Alberta. http://dx.doi.org/10.11575/PRISM/24131

Nassar, S., El-Sheimy, N., 2005. Accuracy improvement of stochastic modeling of inertial sensor errors. Zeitschrift tfur Geodäsie Geoinformation und Landmanagement (ZfV) 130, 146–155.

Nieminen, T., Kangas, J., Suuriniemi, S., Kettunen, L., 2010. An enhanced multi-position calibration method for consumer-grade inertial measurement units applied and tested. Meas. Sci. Technol. 21, 105204. https://doi.org/10.1088/0957-0233/21/10/105204

Nikolic, J., Furgale, P., Melzer, A., Siegwart, R., 2016. Maximum Likelihood Identification of Inertial Sensor Noise Model Parameters. IEEE Sensors Journal 16, 163–176. https://doi.org/10.1109/JSEN.2015.2476668

Niu, X., Chen, Q., Zhang, Q., Zhang, H., Niu, J., Chen, K., Shi, C., Liu, J., 2014. Using Allan variance to analyze the error characteristics of GNSS positioning. GPS Solutions 18, 231–242. https://doi.org/10.1007/s10291-013-0324-x

Niu, X., Gao, Z., Zhang, R., Chen, Z., Dong, J., 2002. Micro-machined attitude measurement unit with application in satellite TV antenna stabilization. Presented at the Symposium Gyro Technology, Stuttgart, Germany, p. 2002.

Noureldin, A., Karamat, T.B., Georgy, J., 2013. Fundamentals of Inertial Navigation, Satellite-based Positioning and their Integration. Springer Science & Business Media.

Orfanidis, S.J., 1988. Optimum signal processing. Collier Macmillan.

Percival, D., 2002. An Introduction to the Wavelet Variance and Its Statistical Properties.

Percival, D.B., Walden, A.T., 2000. Wavelet Methods for Time Series Analysis, Cambridge Series in Statistical and Probabilistic Mathematics. Cambridge University Press, Cambridge. https://doi.org/10.1017/CBO9780511841040

Percival, D.P., 1995. On estimation of the wavelet variance. Biometrika 82, 619–631. https://doi.org/10.1093/biomet/82.3.619

Petkov, P., Slavov, T., 2010. Stochastic modeling of MEMS inertial sensors. Cybernetics and information technologies 10, 31–40.

Poddar, S., Kumar, V., Kumar, A., 2017. A Comprehensive Overview of Inertial Sensor Calibration Techniques. J. Dyn. Sys., Meas., Control 139. https://doi.org/10.1115/1.4034419

Quinchia, A.G., Falco, G., Falletti, E., Dovis, F., Ferrer, C., 2013. A comparison between different error modeling of MEMS applied to GPS/INS integrated systems. Sensors (Basel) 13, 9549–9588. https://doi.org/10.3390/s130809549

Quinchia, A.G., Ferrer, C., Falco, G., Falletti, E., Dovis, F., 2012. Analysis and modelling of MEMS inertial measurement unit, in: 2012 International Conference on Localization and GNSS. Presented at the 2012 International Conference on Localization and GNSS, pp. 1–7. https://doi.org/10.1109/ICL-GNSS.2012.6253129

Rabiner, L., Juang, B., 1986. An introduction to hidden Markov models. IEEE ASSP Magazine 3, 4–16. https://doi.org/10.1109/MASSP.1986.1165342

Radi, A., 2018. Non-linear Error Modeling for MEMS-based IMUs (PhD Thesis). University of Calgary.

Radi, A., Bakalli, G., Guerrier, S., El-Sheimy, N., Sesay, A.B., Molinari, R., 2019. A Multisignal Wavelet Variance-Based Framework for Inertial Sensor Stochastic Error Modeling. IEEE Transactions on Instrumentation and Measurement 68, 4924–4936. https://doi.org/10.1109/TIM.2019.2899535

Radi, A., Nassar, S., El-Sheimy, N., 2018. Stochastic Error Modeling of Smartphone Inertial Sensors for Navigation in Varying Dynamic Conditions. Gyroscopy Navig. 9, 76–95. https://doi.org/10.1134/S2075108718010078

Riley, W., Howe, D.A., 2008. Handbook of Frequency Stability Analysis, Special Publication (NIST SP) - 1065.

Rogers, R.M., Schetz, J.A., 2003. Applied mathematics in integrated navigation systems, 2nd ed, AIAA Education Series. AIAA (American Institute of Aeronautics & Astronautics).

Salychev, O.S., 1998. Inertial systems in navigation and geophysics. Bauman MSTU Press Moscow, Russia.

Särkkä, S., 2013. Bayesian Filtering and Smoothing. Cambridge University Press.

Savage, P.G., 2000a. Strapdown Analytics - Part 1. Strapdown Associates, Inc., Maple Plain, Minnesota.

Savage, P.G., 2000b. Strapdown Analytics - Part 2. Strapdown Associates, Inc., Maple Plain, Minnesota.

Scherzinger, B.M., Reid, D.B., 1994. Modified strapdown inertial navigator error models, in: Proceedings of 1994 IEEE Position, Location and Navigation Symposium - PLANS'94. Presented at the Proceedings of 1994 IEEE Position, Location and Navigation Symposium - PLANS'94, pp. 426–430. https://doi.org/10.1109/PLANS.1994.303345

Serroukh, A., Walden, A.T., Percival, D.B., 2000. Statistical Properties and Uses of the Wavelet Variance Estimator for the Scale Analysis of Time Series. Journal of the American Statistical Association 95, 184–196. https://doi.org/10.1080/01621459.2000.10473913

Shin, E.-H., 2005. Estimation techniques for low-cost inertial navigation (PhD Thesis). University of Calgary, Calgary, Alberta, Canada.

Shin, E.-H., 2004. A Quaternion-Based Unscented Kalman Filter for the Integration of GPS and MEMS INS. Presented at the Proceedings of the 17th International Technical Meeting of the Satellite Division of The Institute of Navigation (ION GNSS 2004), pp. 1060–1068.

Shin, E.-H., El-Sheimy, N., 2007. Unscented Kalman Filter and Attitude Errors of Low-Cost Inertial Navigation Systems. Journal of The Institute of Navigation 54, 1–9. https://doi.org/10.1002/j.2161-4296.2007.tb00390.x

Shin, E.-H., El-Sheimy, N., 2004a. Aided Inertial Navigation System (AINS^TM) Toolbox for MatLab® Software.

Shin, E.-H., El-Sheimy, N., 2004b. An unscented Kalman filter for in-motion alignment of low-cost IMUs, in: PLANS 2004. Position Location and Navigation Symposium (IEEE Cat. No.04CH37556). Presented at the PLANS 2004. Position Location and Navigation Symposium (IEEE Cat. No.04CH37556), pp. 273–279. https://doi.org/10.1109/PLANS.2004.1309005

Shin, E.-H., El-Sheimy, N., 2002. A New Calibration Method for strapdown Inertial Navigation Systems. ZfV - Zeitschrift für Geodäsie, Geoinformation und Landmanagement.

Shuster, M.D., 1993. Survey of attitude representations. Journal of the Astronautical Sciences 41, 439–517.

Simon, D., 2006. Optimal State Estimation: Kalman, H Infinity, and Nonlinear Approaches, 1st ed. John Wiley & Sons, Hoboken, New Jersey.

Smith, S.W., 1999. The Scientist & Engineer's Guide to Digital Signal Processing, Second. ed. California technical Publishing, San Diego, California.

Solà, J., 2017. Quaternion Kinematics for the Error-state Kalman Filter. CoRR arXiv:1711.02508 [cs].

Stebler, Y., Guerrier, S., Skaloud, J., Molinari, R., Victoria-Feser, M.-P., 2014a. Study of MEMS-based inertial sensors operating in dynamic conditions. Presented at the 2014 IEEE/ION Position, Location and Navigation Symposium - PLANS 2014, pp. 1227–1231. https://doi.org/10.1109/PLANS.2014.6851497

Stebler, Y., Guerrier, S., Skaloud, J., Victoria-Feser, M.-P., 2014b. Generalized method of wavelet moments for inertial navigation filter design. IEEE Transactions on Aerospace and Electronic Systems 50, 2269–2283. https://doi.org/10.1109/TAES.2014.120751

Stebler, Y., Guerrier, S., Skaloud, J., Victoria-Feser, M.-P., 2012. A framework for inertial sensor calibration using complex stochastic error models, in: Proceedings of the 2012 IEEE/ION Position, Location and Navigation Symposium. Presented at the 2012 IEEE/ION Position, Location and Navigation Symposium, pp. 849–861. https://doi.org/10.1109/PLANS.2012.6236827

Stebler, Y., Guerrier, S., Skaloud, J., Victoria-Feser, M.-P., 2011. Constrained expectation-maximization algorithm for stochastic inertial error modeling: study of feasibility. Meas. Sci. Technol. 22, 085204. https://doi.org/10.1088/0957-0233/22/8/085204

Syed, Z.F., Aggarwal, P., Goodall, C., Niu, X., El-Sheimy, N., 2007. A new multi-position calibration method for MEMS inertial navigation systems. Meas. Sci. Technol. 18, 1897–1907. https://doi.org/10.1088/0957-0233/18/7/016

Tehrani, M.M., 1983. Ring Laser Gyro Data Analysis With Cluster Sampling Technique, in: Fiber Optic and Laser Sensors I. Presented at the Fiber Optic and Laser Sensors I, SPIE, pp. 207–220. https://doi.org/10.1117/12.935818

Titterton, D.H., Weston, J.L., 2004. Strapdown inertial navigation technology, Second. ed. Institution of Electrical Engineers and the American Institute of Aeronautics and Astronautics.

Van Der Merwe, R., 2004. Sigma-point Kalman filters for probabilistic inference in dynamic state -space models (Ph.D.). Oregon Health & Science University, United States -- Oregon.

Van Der Merwe, R., Doucet, A., Freitas, N., Wan, E., 2001. The Unscented Particle Filter. Advances in neural information processing systems 13, 584–590.

Wan, E.A., Van Der Merwe, R., 2002. The Unscented Kalman Filter, in: Kalman Filtering and Neural Networks. John Wiley & Sons, Ltd, pp. 221–280. https://doi.org/10.1002/0471221546.ch7

Wan, E.A., Van Der Merwe, R., 2000. The unscented Kalman filter for nonlinear estimation, in: Proceedings of the IEEE 2000 Adaptive Systems for Signal Processing, Communications, and Control Symposium (Cat. No.00EX373). Presented at the Proceedings of the IEEE 2000 Adaptive Systems for Signal Processing, Communications, and Control Symposium (Cat. No.00EX373), pp. 153–158. https://doi.org/10.1109/ASSPCC.2000.882463

Wang, D., Dong, Y., Li, Q., Li, Z., Wu, J., 2018. Using Allan variance to improve stochastic modeling for accurate GNSS/INS integrated navigation. GPS Solut 22, 53. https://doi.org/10.1007/s10291-018-0718-x

Wei, M., Schwarz, K.P., 1990. A Strapdown Inertial Algorithm Using an Earth-Fixed Cartesian Frame. NAVIGATION 37, 153–167. https://doi.org/10.1002/j.2161-4296.1990.tb01544.x

Welch, P., 1967. The use of fast Fourier transform for the estimation of power spectra: A method based on time averaging over short, modified periodograms. IEEE Transactions on Audio and Electroacoustics 15, 70–73. https://doi.org/10.1109/TAU.1967.1161901

Widrow, B., Kollár, I., 2008. Quantization noise: roundoff error in digital computation, signal processing, control, and communications. Cambridge University Press.

Xiao, L., Wei, S., Sun, W., 2008. Research on the high accuracy rapid test method of IMU. Journal of Astronautics 1, 030.

Yang, Y., Gao, W., 2006. An Optimal Adaptive Kalman Filter. J Geodesy 80, 177–183. https://doi.org/10.1007/s00190-006-0041-0

Yang, Y., He, H., Xu, G., 2001. Adaptively robust filtering for kinematic geodetic positioning. Journal of Geodesy 75, 109–116. https://doi.org/10.1007/s001900000157

Yi, Y., 2007. On Improving the Accuracy and Reliability of GPS/INS-Based Direct Sensor Georeferencing (PhD Thesis). Ohio State University, Columbus, Ohio.

Yuan, D., Ma, X., Liu, Y., Shang, Z., Yan, S., 2016. Statistical Modeling of Random Walk Errors for Triaxial Rate Gyros. IEEE Transactions on Instrumentation and Measurement 65, 286–296. https://doi.org/10.1109/TIM.2015.2450358

Yuksel, Y., El-Sheimy, N., Noureldin, A., 2010. Error modeling and characterization of environmental effects for low cost inertial MEMS units, in: IEEE/ION Position, Location and Navigation Symposium. Presented at the IEEE/ION Position, Location and Navigation Symposium, pp. 598–612. https://doi.org/10.1109/PLANS.2010.5507180

Zhang, H., Wu, Y., Wu, W., Wu, M., Hu, X., 2009. Improved multi-position calibration for inertial measurement units. Meas. Sci. Technol. 21, 015107. https://doi.org/10.1088/0957-0233/21/1/015107

Zhang, N.F., 2008. Allan variance of time series models for measurement data. Metrologia 45, 549–561. https://doi.org/10.1088/0026-1394/45/5/009

Zhang, Q., Niu, X., Chen, Q., Zhang, H., Shi, C., 2013. Using Allan variance to evaluate the relative accuracy on different time scales of GNSS/INS systems. Meas. Sci. Technol. 24, 085006. https://doi.org/10.1088/0957-0233/24/8/085006

Zhao, Luodi, Zhao, Long, 2023. An Algorithm for Online Stochastic Error Modeling of Inertial Sensors in Urban Cities. Sensors 23, 1257. https://doi.org/10.3390/s23031257

Zhao, Y., Horemuz, M., Sjöberg, L.E., 2011. Stochastic modelling and analysis of IMU sensor errors. Archives of Photogrammetry, Cartography and Remote Sensing 22, 437–449.

Zhiqiang Xing, Gebre-Egziabher, D., 2008. Modeling and bounding low cost inertial sensor errors, in: 2008 IEEE/ION Position, Location and Navigation Symposium. Presented at the 2008 IEEE/ION Position, Location and Navigation Symposium, pp. 1122–1132. https://doi.org/10.1109/PLANS.2008.4569999

Zhu, C., Cai, S., Yang, Y., Xu, W., Shen, H., Chu, H., 2021. A Combined Method for MEMS Gyroscope Error Compensation Using a Long Short-Term Memory Network and Kalman Filter in Random Vibration Environments. Sensors 21, 1181. https://doi.org/10.3390/s21041181